Development of functionalized silica-based nanoparticle tracers for geo-reservoirs

Zur Erlangung des akademischen Grades einer

DOKTORIN DER NATURWISSENSCHAFTEN (Dr. rer. nat.)

von der KIT Fakultät für
Bauingenieur-, Geo- und Umweltwissenschaften

des Karlsruher Instituts für Technologie (KIT)

genehmigte

DISSERTATION

von

M. Sc. Laura Spitzmüller
aus Achern

Tag der mündlichen Prüfung:	23. Januar 2025
Referent:	Prof. Dr. Thomas Kohl
Korreferent:	Prof. Dr. Thomas Schimmel
Korreferent:	Prof. Dr. Peter Rose

Karlsruhe (2025)

Abstract

Tracer tests are essential tools for assessing hydraulic reservoir conditions in both shallow groundwater aquifers and deep geothermal reservoirs. However, the current conventional tracer technology is limited in the range of measurable reservoir properties, the conditions under which it can be applied, and the accuracy and reproducibility of the results obtained. Among the main problems that hinder better tracer performance are lack of reference values and uncontrollable interaction of the tracer molecules (e.g., fluorescent dyes, ions) with the reservoir environment. A recent promising approach progressing the state-of-the-art tracer technology originates from the synergy of geoscience with nanoscience comprising nanoparticle-based tracers. These aim to take advantage of the modular and adaptable nature of nanoparticles to extend the toolbox of available tracers and enable customized behavior, increasingly elaborate functions, more measurable properties, higher accuracy in quantitative analysis and better predictability. The focus is mainly on silica nanoparticles, as silica is an abundant and natural geomaterial that is facile to synthesize and modify. A necessary aspect in developing functional and applicable nanotracers concerns ensuring the transferability of these silica nanoparticle-based tracers to geological-relevant environments. Further remaining open questions concern the (thermal) stability, integrity, functionality and detectability of the nanoparticle tracers.

In this thesis, these research questions are addressed by an interdisciplinary combination of geoscience with nanoscience, chemistry and physics. More precisely, silica-based fluorescently labeled nanoparticle tracers are developed, enhanced and adapted to provide high stability and integrity, and their functionality, detectability and transportability are tested and proven under geological-relevant conditions.

The main challenges and limitations of conventional fluorescent molecular tracers are attributed to the interaction of the tracer with the environment, namely sorption tendency, (thermal) degradation, detection limitations and instability of the measurement function. To overcome these restrictions, the approach pursued in this thesis encompasses the encapsulation of molecular tracers inside silica nanoparticle carriers in order to restrict the interaction of the tracers with the environment. To fulfill their task the silica-based nanoparticles should endure harsh conditions (e.g., high salinities, elevated temperatures), possess long-term integrity, be identifiable and have favorable transport properties. It is first shown that existing approaches on silica-based nanoparticle tracers are not viable as they are prone to disintegration as a result of silica dissolution under reservoir conditions, similar to amorphous silica. This

challenge is then overcome by applying chemical procedures to enhance the stability of the silica nanoparticles. To further improve the protective function of the nanoparticles, mesoporous silica nanoparticles (MSN) with a stable pore-blocking and surface coating made of titania are used as carriers for fluorescent dyes. This procedure prevents both dye leaching and silica nanoparticle dissolution. With this method, the toolbox of available tracers is augmented as the encapsulated dyes are shielded and protected from the environment. Hence, also molecules that are normally unusable as tracers, such as certain rhodamines, are made applicable as their unfavorable properties (e.g., sorption tendency) dissipate upon encapsulation, thus improving their performance and long-term stability.

Nanoparticles, unlike molecular tracers, offer the possibility of adjusting their interaction with the environment through chemical surface modifications. Applying physi- and chemisorbed surfactant and polymers to the silica-based nanotracers enhances transportability, improves dispersion stability and reduces sorption and retention within geological media. These positive effects are attributed to the formation of a steric layer on the surface of the particles that impacts the particle-particle and particle-surface interactions by affecting the ζ-potential and giving rise to an additional repulsive force: the steric force. Theoretical predictions conducted here based on the (extended) Derjaguin-Landau-Verwey-Overbeek theory (XDLVO theory) and filtration theory reaffirm the benefits surface modifications provide to the functionality of the nanoparticle tracers.

To transfer this system to geological applications, special considerations must be made of the complex and challenging environments – reservoirs differ from each other in parameters such as pH, salinity level, rock charge and chemical composition. However, nanoparticles stand out from other tracers in that they are adaptable and offer a wide possibility of surface modifications, thus enabling application under different reservoir conditions, as well as performing more reliable tracer tests or multi-tracer tests. Further, due to the ease of tailored design, using different particle sizes could help gain information about pore throat sizes and pore size apertures. The studies presented in this thesis lay the ground to allow further progress toward novel smart and functional tracers, thus paving the way to holistic and customized reservoir management.

Kurzfassung

Tracertests sind ein essentielles Werkzeug zur Beurteilung hydraulischer Reservoirbedingungen, sowohl in flachen Grundwasserleitern als auch in tieferen geothermischen Reservoiren. Die Anwendung der aktuellen konventionellen Tracertechnologie ist in Bezug auf die messbaren Reservoir-Eigenschaften, die Anwendungsbedingungen sowie die Genauigkeit und Reproduzierbarkeit der erzielten Ergebnisse begrenzt. Zu den Hauptproblemen zählen das Fehlen von Referenzwerten und die unkontrollierbare Wechselwirkung der Tracer-Moleküle (z. B. fluoreszierende Farbstoffe, Ionen) mit der Reservoirumgebung. Ein vielversprechender Ansatz, der die Tracer-Technologie signifikant erweitert kann, entsteht aus der Synergie von Geowissenschaften und Nanotechnologie und umfasst nanopartikelbasierte Tracer. Diese nutzen die modulare und anpassungsfähige Natur von Nanopartikeln, um das Spektrum der verfügbaren Tracer zu erweitern und ein maßgeschneidertes Verhalten, zunehmend komplexere Funktionen, mehr messbare Eigenschaften, eine höhere Genaugikeit bei der quantitativen Analyse und eine bessere Vorhersagbarkeit zu ermöglichen. Der Fokus liegt hauptsächlich auf Silica-Nanopartikeln, da Silica ein natürliches Geomaterial ist, das kostengünstig zu synthetisieren und einfach zu modifizieren ist. Ein grundlegender Aspekt bei der Entwicklung funktionaler und verlässlicher Nanotracer betrifft die Gewährleistung der Übertragbarkeit auf geologisch relevante Umgebungen. Offene Fragen umfassen die (thermische) Stabilität, Integrität, Funktionalität und Nachweisbarkeit der Nanopartikel-Tracer.

In dieser Arbeit werden diese Forschungsfragen durch eine interdisziplinäre Kombination von Geowissenschaften mit Nanotechnologie, Chemie und Physik angegangen. Genauer gesagt werden fluoreszierende Nanopartikel-Tracer auf Silica-Basis entwickelt, verbessert und angepasst, um hohe Stabilität und Integrität zu gewährleisten. Ihre Funktionalität, Nachweisbarkeit und Transportfähigkeit werden unter geologisch relevanten Bedingungen getestet und bewiesen.

Die Einschränkungen herkömmlicher fluoreszierender molekularer Tracer sind auf die Wechselwirkung der Tracer mit der Umgebung zurückzuführen und umfassen Sorptionstendenz, (thermischer) Abbau, Nachweisgrenzen und Instabilität der Messfunktion. Um diese Schwierigkeiten zu überwinden, wird in dieser Arbeit der Ansatz verfolgt, molekulare Tracer in Silica-Nanopartikeln einzuschließen, um die Tracer vor Umwelteinflüssen abzuschirmen. Die Nanopartikel auf Siliziumdioxidbasis sollten rauen Bedingungen standhalten (z. B. hohe Salzgehalte, hohe Temperaturen), langfristig stabil bleiben, identifizierbar sein und günstige Transporteigenschaften haben. Zunächst wird gezeigt, dass bestehende Ansätze

zu Silica-Nanopartikel-Tracern nicht praktikabel sind, da sie unter Reservoirbedingungen, ähnlich wie amorphes Silica, zur Auflösung neigen. Diese Herausforderung wird durch die Anwendung chemischer Verfahren zur Verbesserung der Stabilität der Silica-Nanopartikel bewältigt. Um die Schutzfunktion der Nanopartikel weiter zu optimieren, werden mesoporöse Silica-Nanopartikel (MSN) mit einer stabilen, porenverschließenden Oberflächenbeschichtung aus Titandioxid als Träger für Fluoreszenzfarbstoffe verwendet. Dieses Verfahren verhindert sowohl die Diffusion der Farbstoffe als auch die Auflösung der Silica-Nanopartikel. Auf diese Weise wird die Palette der verfügbaren Tracer erweitert, da die eingekapselten Farbstoffe vor der Umwelt abgeschirmt und geschützt werden. Somit werden auch Moleküle, die normalerweise als Tracer ungeeignet sind, wie bestimmte Rhodamine, durch die Verkapselung anwendbar, da ihre ungünstigen Eigenschaften (z. B. Sorptionstendenz) an Bedeutung verlieren und ihre Leistung und Langzeitstabilität verbessert werden.

Nanopartikel bieten im Gegensatz zu molekularen Tracern die Möglichkeit, ihre Wechselwirkung mit der Umwelt durch chemische Oberflächenmodifikationen anzupassen. Das Aufbringen von physi- und chemisorbierten Tensiden und Polymeren auf die Silica-basierten Nanotracer erhöht die Transportfähigkeit, verbessert die Dispersionsstabilität und verringert Sorption sowie Retention in geologischen Medien. Diese positiven Effekte werden der Bildung einer sterischen Schicht auf der Oberfläche der Partikel zugeschrieben, die die Partikel-Partikel- und Partikel-Oberflächen-Interaktionen durch Beeinflussung des ζ-Potenzials beeinflusst und eine zusätzliche abstoßende Kraft erzeugt: die sterische Kraft. Theoretische Vorhersagen, basierend auf der (erweiterten) Derjaguin-Landau-Verwey-Overbeek-Theorie (XDLVO-Theorie) und der Filtrationstheorie, bestätigen die Vorteile, die Oberflächenmodifikationen für die Funktionalität der Nanopartikel-Tracer bieten.

Um dieses System auf geologische Anwendungen zu übertragen, müssen die komplexen und herausfordernden Umgebungen besonders berücksichtigt werden – Reservoire unterscheiden sich in Parametern wie pH-Wert, Salzgehalt, mineralischer und chemischer Zusammensetzung. Nanopartikel heben sich jedoch von anderen Tracern ab, da sie anpassbar sind und zahlreiche Möglichkeiten der Oberflächenmodifikation bieten, was ihren Einsatz unter unterschiedlichen Reservoirbedingungen sowie verlässlichere Tracer-Tests oder Multi-Tracer-Tests ermöglicht. Zudem könnte durch die einfache Möglichkeit des maßgeschneiderten Designs, die Verwendung unterschiedlicher Partikelgrößen dazu beitragen, Informationen über die Poren-/Kluftöffnungsweiten zu gewinnen. Die in dieser Arbeit vorgestellten Studien bilden die Grundlage für die weitere Entwicklung in Richtung neuartiger, intelligenter und funktionaler Tracer und ebnen somit den Weg zu einem umfassenden und individuellen Reservoirmanagement.

Contents

Acronyms and symbols

Symbol	Name	Unit
A	Area	m^2
A_H	Hamaker constant	J
A_S	Porosity dependent number	
C/c	Concentration	$mg\,L^{-1}$
C_0	Input concentration	$mg\,L^{-1}$
d	Diameter	m
D	Diffusion coefficient	$m^2\,s^{-1}$
ESC	Excess silica concentration	$mg\,L^{-1}$
f	Porosity	
g	Gravitation constant	$m\,s^{-2}$
h	Separation distance	m
$\hbar$	Reduced Planck constant	J s or eV s
I/IS	Ionic strength	$mol\,L^{-1}$
K	Hydraulic conductivity	$m\,s^{-1}$
k	Permeability	m^2
k_B	Boltzmann constant	$m^2\,kg\,s^{-2}\,K^{-1}$ or $J\,K^{-1}$
$K_{d/D}$	Dissociation constant	$L\,kg^{-1}$
M_W	Molecular weight	Da
N_A	Avogadro constant	mol^{-1}
N_{Att}	Attraction number	
n_e	Effective porosity	
N_G	Gravitation number	
N_{Pe}/Pe	Péclet number	
N_R	Aspect ratio	
N_{vdW}	Van der Waals number	
pK	Dissociation constant	
Q	(Volumetric) flow rate	m^3/s
r	Radius	m
SSC	Silica saturation concentration	$mg\,L^{-1}$
T	Temperature	K
U/u	Velocity	$m\,s^{-1}$

Symbol	Name	Unit
U_e	Electrophoretic mobility	$\mu m\ cm\ V^{-1}\ s^{-1}$
v_a	Mean flow velocity	m/s
V_B	Born force	J
V_e	Elastic force	J
V_{EDL}	Electric double layer force	J
V_{LJ}	Lennard-Jones potential	
V_{LvdW}	London-van der Waals force	J
V_O	Osmotic force	J
V_S	Steric force	J
V_t	Total interaction energy	J
z	Ion valence	
α	Attachment efficiency	
ϵ	$\epsilon_0 * \epsilon_r$	$A\ s\ V^{-1}\ m^{-1}$
ϵ_0	Absolute permittivity of vacuum	$A\ s\ V^{-1}\ m^{-1}$
ϵ_r	Relative permittivity of solvent	
ϵ_E	Depth of primary minimum	
ζ	Zeta potential	V
η_0	Single grain collector contact efficiency	
η	Single grain collector removal efficiency	
κ^{-1}	Debye length	m
λ	Characteristic wavelength of a medium	m
λ_B	Bjerrum length	m
μ	Viscosity	$N\ s\ m^{-2}$
ν_1	Volume of solvent molecule	m^3
ρ	Density	$kg\ m^{-3}$
σ	Born collision diameter	m
ϕ_p	Volume fraction	
χ	Flory-Huggins parameter	
ω	Characteristic dispersion frequency	s^{-1}

Abbreviation	Name
BET	Brunauer-Emmett-Teller specific surface measurement
(X)DLVO	(Extended) Derjaguin-Landau-Verwey-Overbeek theory
FT-IR ATR	Fourier Transform Infrared Spectroscopy - Attenuated Total Reflectance
IAP	Ion activity product
MSN	Mesoporous Silica Nanoparticle(s)
SEM	Scanning Electron Microscopy

Abbreviation	Name
SI	Saturation index
SiNP	Silica nanoparticle(s)
(S)TEM	(Scanning) Transmission Electron Microscopy
TiNP	Titania nanoparticle(s)
TGA	Thermogravimetric Analysis
UV-Vis	Ultraviolet - visible (light)
XRD	X-Ray Diffraction

Abbreviation	Chemical formula	Name
C18	$C_{21}H_{46}O_3Si$	n-Octadecyltrimethoxysilane
CTAB	$C_{19}H_{42}BrN$	Cetrimonium bromide
EDTA	$C_{10}H_{16}N_2O_8$	Ethylenediaminetetraacetic acid
MPTS	$C_6H_{16}O_3SSi$	(3-mercaptopropyl) trimethoxysilane
PEG	$C_{2n}H_{4n+2}O_{n+1}$	Polyethylene glycol
PBS		Phosphate buffered saline
SDS	$NaC_{12}H_{25}SO_4$	Sodium dodecyl sulfate
TBOT	$Ti(C_4H_9O)_4$	Tetrabutyl orthotitanate
TEOS	$SiC_8H_{20}O_4$	Tetraethyl orthosilicate
TMOS	$SiC_4H_{12}O_4$	Tetramethyl orthosilicate
ZI/SB3-14	$C_{19}H_{41}NO_3S$	Zwitterion/Sulfobetaine 3-14
1,3,6-NTS	$C_{10}H_7NaO_9S_3$	1,3,6-Naphthalenetrisulfonic acid
C307	$C_{13}H_{12}F_3NO_2$	Coumarin 307
FITC	$C_{21}H_{11}NO_5S$	Fluorescein isothiocyanate
NBA	$2C_{20}H_{20}N_{30}\cdot SO_4$	Nile blue A
R6G	$C_{28}H_{31}N_2O_3Cl$	Rhodamine 6G
R800	$C_{26}H_{26}ClN_3O_5$	Rhodamine 800
RhB	$C_{28}H_{31}ClN_2O_3$	Rhodamine B
$Ru(bpy)_3^{2+}$	$C_{30}H_{24}N_6Cl_6Ru\cdot 6H_2O$	Tris(bipyridine)ruthenium(II) chloride
Saf O	$C_{20}H_{19}ClN_4$	Safranin O
SG	$C_{25}H_{25}N_2NaO_7S_2$	Sulforhodamine G
Uranine	$C_{20}H_{10}Na_2O_5$	Sodium fluorescein

CHAPTER 1

Introduction

Climate change and the need for an energy transition toward renewable and sustainable energy sources are undeniable facts. The Earth itself has the potential to cover human energy demand in a sustainable and renewable way. The thermal energy stored in Earth's crust up to a depth of 10 km amounts to $1.3 \cdot 10^{27}$ J (Davies and Davies 2010, Lund et al. 2008). For comparison, the current annual energy consumption of humanity is approximately $0.62 \cdot 10^{21}$ J (2023, Energy Institute (2024)). The thermal energy of the Earth originates from two primary sources: the accretion heat remaining from the Earth's formation and radioactive decay processes (Barbier 2002). Using this geothermal energy bears the potential to significantly contribute to the energy transition as a renewable, nearly CO_2-neutral and base-load capable energy source available in most areas. Depending on the temperature, geothermal energy is either used directly for heating/cooling purposes or transformed into electrical energy. Nevertheless, geothermal energy currently accounts for only 0.5 % of renewable energies (IRENA and IGA 2023).

To guarantee a safe and sustainable operation of a geothermal power plant, adequate monitoring and characterization of the reservoir must take place (U.S. Department of Energy 2011). Exploration processes can be subdivided into initial exploration methods that can be performed before drilling, such as geological mapping and geophysical monitoring and operational assessment methods, for example, geochemical analyses and hydraulic testing. These methods pursue gaining information about the reservoir geometry, fluid composition and temperature to ensure a long-term operation and minimize the risk of failure. Due to the inaccessibility of underground reservoirs, one of the most effective methods is the usage of natural or artificial tracers such as isotopic fluid composition, certain anions and, most importantly, fluorescent molecular dyes (Chrysikopoulos 1993). Conducting tracer tests is the best practice for obtaining information about reservoir geometry, fluid pathways, fluid

residence time, fluid velocity and interconnections (Ren et al. 2023). The major drawback of molecular fluorescent dyes lies in their limited variety (e.g., in hydrogeology, mainly restricted to uranine, eosin and sodium naphthionate) and the impracticality of modifying their properties without affecting fluorescence or sorption behavior (Käß 2004, Schaffer et al. 2013). Furthermore, the interpretation of tracer response curves is an intricate task that is based on many assumptions, such as the ideal (conservative) behavior of the tracers. Many tracers suffer from (ir)reversible sorption, degradation and instability of the measurement signal, making tracer tests less predictable and reliable.

1.1 Motivation

While fluorescent dye tracers are particularly useful in providing information about connectivity and fluid velocity, their applicability is limited as they need to be suitable for the specific reservoir conditions to be reliable. For example, it can not be distinguished between tracers lost due to irreversible sorption and degradation processes or due to escaping of the connected fluid pathways. Further, due to degradation or dilution processes in the reservoir, it is possible to miss the breakthrough of a tracer altogether if the detection limit is too high, leading to misinterpretation of the reservoir conditions (Behrens et al. 2009). Finally, for an improved reservoir assessment, additional information can be of great importance, such as data on spatial temperature distribution, fracture sizes, and other critical reservoir characteristics, that could facilitate the interpretation of tracer tests (e.g., Dashti et al. 2023, Sanjuan et al. 2006). However, conventional tracers offer little to no direct possibilities of gathering such data.

In conclusion, there is a necessity for novel tracer types that are ideally more reliable and comparable, are adaptable to suit the conditions prevalent in specific reservoirs, have the possibility to overcome the drawbacks of classical tracer types such as sorption and degradation and permit further development, for example, to record and transport information about in-situ conditions such as temperature distribution or pH values. Promising candidates to form such a novel class of tracers are nanoparticle tracers, which emerged from nanoscientific-based approaches to address geoscientific research questions (e.g., Rudolph et al. 2020). Nanoscience, a relatively new science branch, might be a key technology for advancing the field of tracer technology. It focuses on materials and technologies on the nanometer scale and may offer new approaches and techniques to address the complex issue of tracer tests in the relevant size ranges that enable access also to pathways inside fractured rock (Bayda et al. 2020).

This study is based on four main scientific hypotheses:

1. Nanoparticle-based tracers can be designed to maintain particle integrity and functionality throughout a tracer test, especially in challenging environments.

2. Functionalization of nanoparticle tracers can ensure a straightforward and robust detectability function.
3. Nanoparticle tracer performance can be optimized in geological environments.
4. Nanoparticles offer the opportunity of surface modifications to restrict interaction with the environment, resulting in minimized sorption and retention.

The approach for novel tracer design pursued in this study involves encapsulating molecular dye tracers inside silica nanoparticle carriers. The advantage of this method over others, such as DNA-labeled silica nanoparticles introduced by Paunescu et al. (2013), is that the dye tracers are embedded inside the carrier and not incorporated into the structure or bound to the outside. This results in only the properties of the carriers themselves and not the properties of the dye being decisive for transport behavior and sorption tendency and governing the interactions with the fluid and reservoir matrix. Consequently, also the fluorescence signal is not dependent on the surroundings any more. Using nanoparticles as carriers has several advantages: they are small enough to follow streamlines, they are modular and can be easily customized. While some uses of nanoparticle carriers are already better established, such as bioimaging and drug delivery (Manzano and Vallet-Regí 2020, Vallet-Regí et al. 2001), transferring the application field from well-constrained environments like biological systems to challenging geothermal environments involves considering and adapting multiple factors such as temperature stability and regulating interactions of nanoparticles with the environment. This study aims to advance the design of specialized nanoparticle-based tracers for hydro- and geothermal reservoir exploration and increase the understanding of the behavior and fate of engineered nanoparticles in these environments. Further, this study provides fundamental research that is pivotal for the future application of nanoparticle tracers and is a step toward the development of "smart" and functionalized nanoparticle tracers. Finally, these sophisticated tracers could be used in future to guarantee sustainable reservoir management and prediction of thermal breakthroughs or indications about pH distribution, hence assessing scaling potential.

This thesis pursues an interdisciplinary approach combining geoscience, nanotechnology, chemistry and physics to develop and improve the applicability of nanoparticle-based tracers to address geoscientific research questions. In detail, silica-based fluorescent nanoparticle tracers are synthesized and modified to suit prevalent reservoir conditions. This includes enhancing the stability and functionality of the silica nanoparticles and ensuring the possible application as a reliable tracer in geo-reservoirs.

1.2 Thesis structure

This thesis is organized to address the interdisciplinary nature of the research, encompassing geoscience, nanoscience, chemistry and physics. Due to interconnectedness of these fields, the structure inevitably involves some initial gaps that will be filled in the subsequent chapters. The first three chapters explain the motivation, fundamentals of tracer technology and nanoparticle-based tracers, the role of silica and silica nanoparticles in geosciences and chemical synthesis routes for designing of silica-based nanoparticle tracers. Chapters 4 to 7 are in-depth studies which have been partly published. Chapter 8 summarizes the advances achieved in this thesis and provides an outlook on future research topics.

Chapter 2 provides an overview of current tracer methods in geosciences, focusing on their challenges and limitations. Further, the concept of using nanoparticle tracers as carriers/shuttles for tracer molecules is introduced and the transport processes for nanoparticles/colloids are discussed, as well as the importance of factors like ζ-potential, DLVO and XDLVO theory, which are crucial for understanding nanoparticle behavior in the underground. In **Chapter 3**, silica as a natural geomaterial is presented and its prevalence in natural environments is explained. A special focus lies on solubility, saturation and behavior of silica in geothermal environments. Additionally, the potential of silica nanoparticles as engineered nanoparticle tracer carriers is discussed and an outline of current application fields and the challenges of nanoparticle tracers associated with usage in geothermal reservoirs is given.

Silica appears to be an intriguing option as a tracer shuttle due to its ease of synthesis, functionalization and natural abundance. Yet, several obstacles in applying silica nanoparticles as tracers in geo-environments need to be addressed:

- The solubility of natural and engineered silica nanoparticles depends on various factors such as temperature, pH, and salinity, which necessitates ensuring particle integrity before application.
- The tracer dyes must be protected from the environment by encapsulation in a nanoparticle carrier. Consequently, the flow-through properties and sorption affinity must be independent of the payload and governed only by the properties of the carriers.
- The stability of the dispersion must be guaranteed to prevent nanoparticle aggregation and deposition in geological media.

These constraints are addressed in the following Chapters, some of which have already been published. First, in **Chapter 4**, factors contributing to silica nanoparticle solubility are investigated and strategies to control the dissolution and increase the stability are presented. Based on the findings from this study, **Chapter 5** focuses on enhancing nanoparticle tracer design by utilizing mesoporous silica nanoparticles as tracer shuttles with a stable surface coating made from titania, preventing both nanoparticle dissolution and loss of

the encapsulated payload. This design approach is transferred to a geological environment in **Chapter 6**. By testing the sorption affinity and determining transport properties in porous media, the suitability of the nanoparticle tracer design is shown. In **Chapter 7**, theoretical predictions are made to assess the dispersion stability and predict particle behavior in different environments, as well as particle-reservoir mineral interactions. Additionally, particle deposition in porous media is studied and predicted. Finally, recommendations on suitable tracer design and enhancement of properties are given, such as having a steric barrier to increase dispersion stability and decrease sorption affinity toward reservoir minerals. **Chapter 8** summarizes the advancements and developments achieved during this thesis and provides an outlook on future research questions.

This thesis provides a comprehensive overview of potential nanoparticle-based tracer carriers made of silica for geo-reservoir characterization. Challenges such as the solubility of silica are addressed and solutions developed. The nanoparticle tracer concept is tested in simulated natural environments and theoretical predictions are performed to increase the understanding of the behavior and fate of engineered nanoparticles in geological environments.

Parts of this thesis have been published or are under preparation for submission.

Section 3.3 Nanoparticle-based tracing techniques in geothermal reservoirs: Advances, challenges and prospects

This Section provides an overview of state-of-the-art nanoparticle-based tracing techniques, with a special focus on silica nanoparticle-based approaches such as those by Paunescu et al. (2013) and Rudolph et al. (2020), as well as recent advances. Further, the challenges related to the application of the silica nanoparticle-based tracers are addressed, such as hydrothermal instability and sorption in geo-environments. Additionally, the possibilities of nanoparticles are highlighted: the modifiability of their surface.

This Section has been published as: Spitzmüller, L., Nitschke, F., Maercks, A., Berson, J., Rudolph, B., Schimmel, T. and Kohl, T. (2023a). Nanoparticle-based tracing techniques in geothermal reservoirs: Advances, challenges and prospects. *Proceedings 48th Workshop on Geothermal Reservoir Engineering, Stanford University*, SGP-TR-224. `https://doi.org/10.5445/IR/1000156430`.

Chapter 4 Dissolution Control and Stability Improvement of Silica Nanoparticles in Aqueous Media

In this Chapter, factors governing the dissolution behavior of silica nanoparticles in aqueous environments are investigated. The effects of temperature, pH value, salinity and ion valence, silica concentration and availability of silica on the dissolution rate and solubility of engineered silica nanoparticles are studied. The results indicate that acidic pH values lower the dissolution rate and high salinities reduce the solubility. However, in natural environments, engineered silica nanoparticles are prone to disintegrate and dissolve rapidly,

especially at elevated temperatures within hours, making them unsuitable as geothermal tracer carriers. Nevertheless, several strategies to increase the resistance against dissolution are examined. The most effective approach to improve the stability is to transform the silanol (Si-OH) bonds on the surface of the silica nanoparticles into siloxane (Si-O-Si) bonds by heat treatment (calcination). This process increases the degree of condensation, thereby reducing the solubility.

This chapter has been published as: Spitzmüller, L., Nitschke, F., Rudolph, B., Berson, J., Schimmel, T. and Kohl, T. (2023b). Dissolution Control and Stability Improvement of Silica Nanoparticles in Aqueous Media. *Journal of Nanoparticle Research*, 25. `https://doi.org/10.1007/s11051-023-05688-4`.

Chapter 5 Titania-Mediated Stabilization of Fluorescent Dye Encapsulation in Mesoporous Silica Nanoparticles

Silica nanoparticle-based tracers can be used if they are stabilized to withstand harsh conditions such as high temperatures. As shown in the previous study (Chapter 4), the most effective way to improve stability is through calcination. This process exposes the incorporated organic dyes to high temperatures, causing them to degrade. Therefore, a new approach involves using a stable titania layer to encapsulate fluorescent dyes within calcined mesoporous silica nanoparticles (dye-MSN@TiO_2). This approach entails three major enhancements: allowing calcination before encapsulation by synthesizing mesoporous silica nanoparticles, increasing the range of possible encapsulated dyes and using the titania layer to prevent dye leakage and to ensure the stability of the silica nanoparticle carriers.

This Chapter has been published as: Spitzmüller, L., Berson, J., Nitschke, F., Kohl, T. and Schimmel, T. (2024a). Titania-Mediated Stabilization of Fluorescent Dye Encapsulation in Mesoporous Silica Nanoparticles. *Nanoscale Advances*, 6. `https://doi.org/10.1039/D4NA00242C`.

Chapter 6 Temperature stability and enhanced transport properties by surface modifications of silica nanoparticle tracers for geo-reservoir exploration

The novel developed dye-MSN@TiO_2 nanoparticles undergo rigorous proof of applicability as tracers. They are exposed to increased temperatures to demonstrate the protective measure of the titania layer and their sorption behavior and transport properties are tested. Three different dyes are encapsulated and compared to the behavior of the respective free dyes. Specifically, the behavior of the cationic dye can significantly be improved by encapsulation. It is further shown that the encapsulated dyes show a more uniform transport behavior governed by the carrier particles rather than by the tracer dyes. Additionally, the advantages of using nanoparticle-based tracers are underscored through the application of various surface modification techniques and examination of their effects on sorption behavior.

This Chapter has been published as: Spitzmüller, L., Berson, J., Schimmel, T., Kohl, T. and Nitschke, F. (2024b): Temperature stability and enhanced transport properties by surface modifications of silica nanoparticle tracers for geo-reservoir exploration. *Scientific Reports*, 14. https://doi.org/10.1038/s41598-024-70132-z.

Chapter 7 Dispersion Stability, Sorption and Deposition of Silica Nanoparticles in Porous Media based on (X)DLVO and Filtration Theory

In this Chapter, the focus is on predicting the behavior of the engineered silica-based nanoparticle tracers and their dispersion stability by calculating the interaction potential by DLVO theory and predicting the particle retention risk using the filtration theory. Further, the impact of surface modifications is elucidated by applying the extended DLVO theory. Recommendations on future particle design are given to achieve a stable and reliable nanoparticle tracer.

This Chapter is under review at *Geothermics*.

CHAPTER 2

Fundamentals of nanoparticle-based tracers

Tracer tests in geoscientific applications, such as hydrogeology or geothermal engineering, aim to gain insight into subsurface reservoir conditions and flow paths (Käß 2004). Tracers are compounds naturally present or added to (ground)water that can be transported with the fluid flow (Chrysikopoulos 1993). They are transported by advection and/or diffusion and possibly undergo interaction with the environment, such as sorption, retention or degradation. The tracers are identifiable and measurable in fluid samples taken from caves, springs or wells and allow estimation of parameters such as reservoir geometry, interconnections, fluid pathways and flow directions but also fluid velocity, fluid residence time, hydraulic conductivity, dispersivity, porosity and fracture surface areas (Ayling and Rose 2006, Chrysikopoulos 1993, Davis et al. 2006, Käß 2004). Accurate knowledge about these subsurface conditions can help design sustainable geothermal power plants but also serves to protect the vulnerable drinking water resources in the shallower aquifers.

Although the first ever described tracer tests date back to the first century (Davis et al. 2006, Käß 2004), it was in the 19th century when awareness of the importance of fluid pathways in the underground emerged due to the spreading of waterborne diseases such as typhoid fever (Dole 1906). The first (semi)quantitative tracer test was performed by Knop (1878) and proved the connection between the Danube and the Aach in the karstic system of the Swabian Alps, Germany. To trace the fluid flow, shale oil, sodium chloride and sodium fluorescein (uranine) were injected into the Danube and detected about 60 hours later in the discharge of the karstic spring Aachtopf, thus proving their connection (Knop 1878). Encouraged by this success, tracer tests became increasingly popular (Dole 1906) and are nowadays one of the first choices for reservoir exploration (Käß 2004).

2.1 General overview of tracer technology

Various tracers exist, classified as natural or artificial (Käß 2004). Natural tracers such as radionuclides (e.g., ^{222}Rn, ^{226}Ra) or stable isotopes (e.g., ^{2}H, ^{18}O) are substances already present in the natural fluids and do neither change the properties of the fluids nor harm the ecosystem (Cozma et al. 2016). An exceptional natural tracer is the temperature, which impacts the viscosity and density of the fluids (Anderson 2005, Davis et al. 2006).

Artificial tracers such as dyes (fluorescent/not fluorescent), salts, anions, certain types of chemicals and particulate tracers are substances injected into the fluids that are (ideally) able to follow the fluid flow (Käß 2004). The first recorded tracer test by Knop (1878) relied on the usage of artificial tracers that are naturally absent or only contained to a small amount in the fluids. Particulate tracers like phages, spores and colloids are generally useful for mimicking the transport of pollutants and microorganisms such as bacteria or viruses but have limitations such as settlement, interaction with the matrix and degradation. Thus, they are used mostly only in high-flow regimes (Davis et al. 2006). Anions, such as Br^- and I^-, are less prone to adsorption or ion exchange with the reservoir minerals due to their negative charge, benefiting from the anion exclusion effect (Davis et al. 2006, Elimelech et al. 2000).

Geothermal reservoirs present challenging conditions for tracers. For example, the use of salts like NaCl as tracers is often impractical due to high background concentrations (Finster et al. 2015). Therefore, specialized tracers have emerged to withstand these harsh conditions. For example, tracers with high-temperature stability, such as (naphthalene) sulfonates, have been developed for use in geothermal environments (Rose et al. 1999, 2002). Recent innovations include thermoreactive tracers designed using molecular approaches Cao et al. (2020), as well as temperature-reactive tracers such as hydrolyzable compounds (e.g., acetates, esters, amides), that aid in predicting the temperature and assess thermal front propagation (Hawkins et al. 2021, Nottebohm et al. 2012, Schaffer et al. 2013). Further approaches to achieve a responsive behavior of the molecular tracers to environmental properties such as temperatures are reactive/adsorbing tracers (Rose and Clausen 2014). The concept of adsorbing tracers is that in conjunction with inert (conservative) tracers, they can help gather detailed information about reservoir surface area (Hawkins et al. 2018). Additionally, in recent years, DNA-based tracers have emerged as uniquely identifiable groundwater tracers (Foppen 2023, Zhang et al. 2016). However, DNA-based tracers are unsuitable as reliable geothermal tracers due to DNA degradation above 90 °C (Karni et al. 2013, Zhang and Huang 2022).

Despite these advances, conventional fluorescent dyes remain the most common tracers in geosciences due to their absence in natural environments and ease of detection (Käß 2004). Some fluorescent dye tracers are discussed below, highlighting their advantages and limitations and possible usage in the development of nanoparticle-based tracers.

Uranine: Uranine is by far the most applied fluorescent dye tracer and its first applications date back to the 19th century (Dole 1906, Knop 1878). Uranine is the sodium salt of fluorescein and is known for its bright green color, good water solubility, low detection limit and mostly conservative/inert behavior in groundwater tracing studies (Käß 2004). In the 1980s, applications of uranine as a tracer in geothermal reservoirs emerged (Chrysikopoulos 1993) as the dye is stable below 200 °C in the absence of natural oxygen Adams and Davis (1991). However, Behrens et al. (2006) found that uranine could still react at temperatures of 130-140°C even without atmospheric oxygen. While generally considered conservative, uranine's behavior may vary depending on specific reservoir conditions, mineralogy, and surface charges, potentially leading to anion exclusion or anion adsorption (Chrysikopoulos 1993, Korom and Seaman 2012). Additionally, uranine's fluorescence is sensitive to pH and salinity, with optimal detection above pH 8.7, where it exists in an anionic form (Käß 2004). In acidic environments, the uranine ion may become cationic resulting in low fluorescence quantum yield and high sorption affinity, making it unsuitable for such conditions (Klonis and Sawyer 1996, Magal et al. 2008, Smart and Laidlaw 1977, Weidner et al. 2011).

Sulforhodamine G Sulforhodamine G (or amidorhodamine G), similar to uranine, is an anionic dye expected to behave conservatively. Indeed, tracer tests performed with sulforhodamine G show low sorption affinity and high recovery (Müller et al. 2023, Ravbar et al. 2012). Despite its potential, it is not commonly used in geothermal applications. Thus, there exists only limited data about its temperature stability. Nonetheless, it is supposed to have lower temperature stability compared to uranine, based on the behavior of other rhodamine species (rhodamine WT, Rose et al. (2001)).

Rhodamine B Rhodamine B is a cationic/amphoteric dye that is no longer used due to its possible carcinogenic effect and strong sorption tendency caused by its amphoteric/cationic nature (Kasnavia et al. 1999). Compared to uranine, it shows lesser sensitivity toward UV irradiation and pH variations. Käß (2004) reported some successful tracer tests with rhodamine B but recommended limiting the usage to karstic environments where high flow rates are prevalent.

Rhodamine 6G Rhodamine 6G, also a cationic rhodamine dye, is prone to strong sorption and retention and additionally has an elevated toxicity (Kasnavia et al. 1999, Käß 2004). Despite these drawbacks, it is an excellent dye with high quantum yield, often used in microscopy and able to be incorporated into a silica matrix (Avnir et al. 1984, Käß 2004).

Ru(bpy)$_3^{2+}$ Tris(2,2'-bipyridyl)dicholororuthenium(II) (Ru(bpy)$_3^{2+}$) is another cationic dye that is not commonly used as a groundwater tracer. Nevertheless, it finds application in synthesis techniques producing fluorescently labeled silica nanoparticles, as reported by Bagwe et al. (2004).

Saf O Safranin O is a cationic azine dye and such as Ru(bpy)$_3^{2+}$ not commonly used as a groundwater tracer. It shows strong sorption toward silica and silicate minerals and can be

applied as fluorescent labeling agent for silica nanoparticles (Gimenez et al. 2015, Sieren et al. 2020).

2.2 Challenges and drawbacks of conventional tracers

The applicability of tracers to monitor subsurface conditions is highly dependent on prevalent fluid properties such as fluid temperature, pH values and salinity (Smart and Laidlaw 1977). There are several challenges tracers need to overcome:

- Sorption (Kasnavia et al. 1999)
- Degradation (Rose et al. 2001)
- Detection limit (Käß 2004)
- Stability of the measurement signal (Cao et al. 2017)

Sorption and retention of tracers due to interaction with the reservoir matrix are critical, particularly when tracers carry an opposite charge to the reservoir minerals (Kasnavia et al. 1999). As shown by DLVO theory (Section 2.4.6), oppositely charged species attract each other, resulting in adsorption. Since the surface charge (i.e., ζ-potential, Section 2.4.5) of most reservoir minerals is negative, positively charged tracers like rhodamine B or rhodamine 6G are often unsuitable (Kasnavia et al. 1999). Korom and Seaman (2012) emphasized the importance of understanding the reservoir's mineralogy and fluid geochemistry when selecting tracers, as surface charges may vary and concluded that even allegedly conservative tracers like uranine could be susceptible to sorption. Factors such as salinity and pH of the fluids also influence sorption, detection limits, and the stability of the measurement signal (Cao et al. 2017, Magal et al. 2008). For instance, high saline geothermal fluids impede the usage of artificial tracers such as alkali halides due to high background concentrations (Chrysikopoulos 1993) and high turbidity or natural fluorescence can further complicate detection (Käß 2004). Tracer degradation can be induced by UV irradiation, exposure to high temperatures and microbiological activity (Adams and Davis 1991, Käß 2004, Rose et al. 2002). Even uranine undergoes, similar to most organic molecules, temperature-induced degradation but also was reported to suffer microbiological-induced degradation in natural fluids (Käß 2004).

For tracers to be reliable, reproducible, and predictable, especially in geothermal environments, they should meet the following criteria:

1. Endure harsh conditions: Retain functionality and properties under harsh conditions like high temperatures, salinities, and pressures.

2. Long-term integrity: Maintain stability and integrity over extended periods (weeks to months).
3. Identification: Be distinguishable and identifiable even at low concentrations.
4. Favorable transport properties: Exhibit low sorption affinity and minimal interaction with the matrix and fluids.

Traditional fluorescent molecular tracers used in hydrogeology to study aquifers are often inadequate for geothermal research, and only a limited number possess the necessary properties. Therefore, developing new types of tracers is crucial for comprehensive reservoir characterization. The following Section evaluates the potential of nanoparticle tracers as candidates for this purpose.

2.3 Concept of nanoparticle tracers

Indeed, the first reported tracer tests in history were performed conducted using particulate tracers like chaff and sawdust (Davis et al. 2006, Käß 2004). At that time, particles as tracers had the incontrovertible argument of being visible and observable by the naked eye. Nowadays, particle tracers remain valuable for predicting bacterial transport, mimicking contaminant transportation by natural colloids and understanding the spread of micro- and nanoplastics in the environment as their transport and sorption behavior can deviate strongly from common molecular tracers (Corapcioglu and Jiang 1993, Flury and Qiu 2008, Pradel et al. 2023). Commonly used particle tracers in hydrogeology include spores, phages and nano-/microparticles (Käß 2004), with polystyrene/latex microparticles being particularly widespread due to their density, which is similar to that of natural water, reducing sensitivity to gravitational settling. Nevertheless, their use in geothermal reservoirs is limited by factors like thermal instability and the inability to adapt to specific conditions (Ren et al. 2023, Rieger 1996).

In recent years, efforts have been made to develop new particle tracers. For example, Rose et al. (2011) proposed quantum dots as modular tracers for geothermal reservoir exploration and Smitha et al. (2024) suggested using carbon quantum dots encapsulated in a silica matrix as a groundwater tracer. Others like Agenet et al. (2012) and Clemente et al. (2016) proposed using fluorescently labeled micro- and nanoparticles as potential tracer candidates. Alaskar (2013) studied the applicability of several nanomaterials, such as silica, silver, tin-bismuth and hematite nanoparticles, as potential tracer candidates. These studies highlight the need for novel tracers that can provide more detailed information about subsurface reservoir conditions, whether hydrological or geothermal.

Using custom-designed tracers that match the geochemical and hydromechanical conditions of a reservoir could yield more information than current tracers alone. For example, using

uniquely identifiable tracers with identical transport and sorption properties would allow for simultaneous multiple tracer tests, offering insights into geological structures and enabling injections at various points. Additionally, these tracers could help map karstic structures and record information such as temperature distribution in the reservoir.

While fluorescent dyes remain widely used due to their favorable properties (Käß 2004), their behaviors vary, particularly in challenging environments. Nanoparticle carriers with embedded dyes offer a solution by shielding dyes from environmental influences and allowing for tunable surface properties, making them a more flexible and reliable option for tracer tests.

2.4 Colloidal transport processes and physical forces

The transport processes of (nano)particles/colloids differ from the transport processes of solute molecules. In the following, these transport processes are explained, with a special focus on particle deposition mechanisms. Furthermore, the significance of particle-particle and particle-reservoir environment interactions are discussed.

2.4.1 Advection

Advective transport is caused by hydraulic gradients or external forces such as pumping. The colloids are transported without mixing in the fluid flow direction. The advective transport process can be mathematically described using the Darcy equation, which is a discrete solution of the Navier-Stokes-equation:

$$Q = -KA\frac{dh}{dx} \tag{2.1}$$

with Q (volumetric) flow rate in m^3/s, A area in m^2, K hydraulic conductivity in m/s and dh/dx hydraulic gradient.

Advective transport of colloids in geo-environments takes place in the pore space or fracture area. Therefore, the mean flow velocity can be used to describe the advective transport:

$$v_a = \frac{K}{n_e}\frac{dh}{dx} \tag{2.2}$$

with v_a mean flow rate in m/s and n_e effective porosity.

2.4.2 Diffusion

Diffusive transport results from the Brownian motion, a random temperature-driven movement of small particles (Elimelech et al. 1995). This movement eventually leads to the migration of the particles along concentration gradients, equalizing the distribution. Diffusion can be described by Fick's first law:

$$\vec{J} = -D\nabla c \tag{2.3}$$

with $\vec{J}$ diffusion flux vector, D diffusion coefficient/diffusivity and ∇c concentration gradient. The diffusion coefficient depends on the thermodynamic properties of the system (Atkins and de Paula 2006). For colloids, the diffusion coefficient is determined by the Stokes-Einstein equation:

$$D = \frac{k_B T}{6\pi r \eta} \tag{2.4}$$

with k_B Boltzmann constant (J/K), T absolute temperature (K), r particle radius (m) and η dynamic viscosity of the fluid (Pa s).

2.4.3 Dispersion

While diffusion describes the process of movement due to Brownian motion and concentration gradients, dispersion results from the inhomogeneities of the porous media. Formation of preferential flow paths along fractures or wider pore spaces leads to variability in the mean flow velocity of individual particles, resulting in a widening of the particle cloud in the flow direction (longitudinal dispersion) and perpendicular to the flow direction (transverse dispersion) (Käß 2004). A combination of dispersion and diffusion is given by the hydrodynamic dispersion coefficient:

$$D_h = \alpha v_a + D_m \tag{2.5}$$

with D_h hydrodynamic dispersion coefficient, α dispersion length, v_a mean flow velocity and D_m molecular diffusion coefficient (i.e., diffusion coefficient). Dispersion of solutes and colloids in porous media results in a parabolic velocity profile within pore spaces and fractures, described as Taylor dispersion (Taylor 1953). Unlike solutes, colloids can be

hindered from occupying the whole pore space due to size and charge exclusion effects leading to apparently faster transport of colloids (Kessler and Hunt 1994).

The relationship between advection and hydrodynamic dispersion is given by the Péclet number:

$$Pe = \frac{v_a x}{D_h} \tag{2.6}$$

with v_a mean flow velocity, x distance and D_h hydrodynamic dispersion coefficient. For Péclet numbers below 1, the transport process is driven by hydrodynamic dispersion, whereas above 1, advection dominates.

The three-dimensional transport process of solutes/particles in porous media can be described by the combination of advection and dispersion in the form of a differential equation (Käß 2004):

$$\frac{dc}{dt} = D_l \frac{d^2c}{dx^2} + D_t \frac{d^2c}{dy^2} + D_v \frac{d^2c}{dz^2} - v_a \frac{dc}{dx} \tag{2.7}$$

with $D_{l,t,v}$ longitudinal, transverse and vertical dispersion coefficients, respectively. The space is described by x, y and z coordinates, with x pointing in the flow direction and t being time.

2.4.4 Particle deposition mechanisms and filtration theory

Particle deposition in porous or fractured media can be attributed to four main mechanisms: inertia/impaction, interception, electrostatic attraction and diffusion (Han et al. 2021). A schematic representation is given in Figure 2.1. Inertia/impaction applies mostly to particles larger than 1 µm. Due to their size, these particles are unable to follow the streamlines, resulting in contact with the mineral grains/surfaces, as shown in Figure 2.1. Interception applies when the particles are small enough to be transported along streamlines but come in contact with mineral grains, thus resulting in deposition. Electrostatic attraction is described in detail by the DLVO theory (Section 2.4.6). In brief, when charged particles in a fluid come into contact with oppositely charged mineral surfaces, they adhere and are retained. Diffusion applies when the particles are small (typically below 1 µm). The Brownian motion can lead to particles escaping the streamlines, randomly moving through the fluid and possibly coming into contact with mineral grains/surfaces (Han et al. 2021).

In Figure 2.1, these processes are illustrated in a porous medium. Additionally, aggregation and sedimentation bridging and straining/sieving processes are displayed. Aggregation and

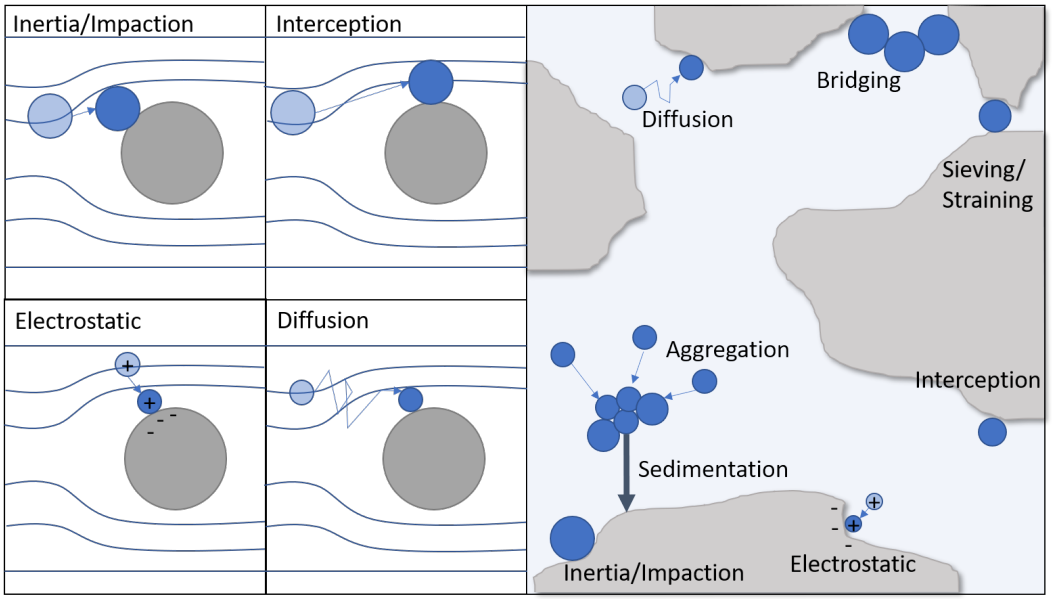

Figure 2.1: Particle retention mechanism in porous media (not true to scale). The four main mechanism are hereby inertia/impaction, interception, electrostatic attraction and diffusion (Han et al. 2021). On the right side, these processes are transferred to a porous media. Additionally, retention/particle filtration mechanism are bridging, sieving/straining (size exclusion), aggregation and sedimentation (Chen and Kibbey 2008).

sedimentation due to gravity can also result in impaction and is a function of the interaction between the particles. The DLVO theory can be used to determine if the particles are prone to aggregation (Section 2.4.6). Bridging describes the formation of a physical barrier by the collision of multiple particles resulting in the blocking of a pore throat. Sieving/straining describes size exclusion. If the particles are too large to enter a pore space, they can be trapped (Chen and Kibbey 2008).

The reversibility and irreversibility of these particle deposition mechanisms depend also on the fluid dynamics (McDowell et al. 1986). High flow rates could re-mobilize formerly trapped particles (e.g., trapped by inertia/impaction). Additionally, changing the fluid parameters, such as pH values, could also result in reversible deposition (e.g., when trapped by electrostatic attraction). To quantify these processes, the particle filtration theory can be applied to describe the transport of (nano)particles in (saturated) porous media. Here, the porous media is assumed to contain several individual single grains, the so-called single grain collectors and their interaction with particles can be calculated according to Tufenkji and Elimelech (2004). Calculating the single-grain collector contact efficiency (η_0), the attachment efficiency (α) and the single grain collector removal efficiency (η) gives a measure of particle retention in porous media. The single grain collector contact efficiency is determined by (Tufenkji and Elimelech 2004):

$$\eta_0 = 2.4A_S^{\frac{1}{3}}N_R^{-0.081}N_{Pe}^{-0.715}N_{vdW}^{0.052} + 0.55A_S N_R^{1.675}N_{Att}^{0.125} + 0.22N_R^{-0.24}N_G^{1.11}N_{vdW}^{0.053} \tag{2.8}$$

Here, the first term corresponds to diffusion, the second to interception and the third to sedimentation due to gravitation (Auset and Keller 2006). Thus, the single grain collector contact efficiency accounts for various physical contributions such as interception, sedimentation and diffusion paired with hydrodynamic interactions and the attractive van der Waals force between particles and surfaces (Tufenkji and Elimelech 2004).

Definition of the parameters in equation 2.8 according to Tufenkji and Elimelech (2004):

$$N_R = \frac{d_p}{d_c} \quad \text{Aspect ratio} \tag{2.9}$$

$$N_{Pe} = \frac{U d_c}{D} \quad \text{Péclet number} \tag{2.10}$$

$$N_{vdW} = \frac{A_H}{k_B T} \quad \text{Van der Waals number} \tag{2.11}$$

$$N_{Att} = \frac{A_H}{12\pi\mu r_p^2 U} \quad \text{Attraction number} \tag{2.12}$$

$$N_G = \frac{r_p^2(\rho_p - \rho_f)g}{\mu U} \quad \text{Gravity number} \tag{2.13}$$

$$A_S = \frac{2(1-((1-f)^{\frac{1}{3}})^5)}{2-3(1-f)^{\frac{1}{3}}+3((1-f)^{\frac{1}{3}})^5-2((1-f)^{\frac{1}{3}})^6} \quad \text{Porosity dependent number} \tag{2.14}$$

with d_p and d_c particle and collector diameter and r particle radius. U is the fluid approach velocity, μ viscosity, g gravitation constant, f porosity and $\rho_{p,f}$ density of particle and fluid, respectively. Additionally, the following constants are used: A_H Hamaker constant (Section 2.4.6.1), k_B Boltzmann constant and g gravitational constant.

The single grain collector contact efficiency is usually overestimated. Therefore, Tufenkji and Elimelech (2004) suggested using the single grain collector removal efficiency (η), which is a product of single grain collector contact efficiency and attachment efficiency (α)

$$\eta = \alpha\eta_0 \tag{2.15}$$

Attachment efficiency is the probability of successful collisions between particles and collector grains resulting in attachment. Attachment efficiency can be calculated based on experimental data as:

$$\alpha = -\frac{2}{3}\frac{d_c}{(1-f)L\eta_0}\ln\left(\frac{C}{C_0}\right) \tag{2.16}$$

with L length of the filter bed (m), C/C_0 ratio of retrieved concentration to input concentration. If α reaches unity, the probability of successful attachment is 100%, which means each attachment results in the adhesion of the particles on the single grain collector. The calculations of the filtration theory do not account for the effect of unfavorable deposition conditions, i.e., if the particles and collectors repel each other. The force leading to repulsion is attributed to the surface charge of the particles/collectors and can be calculated by DLVO theory.

2.4.5 Zeta potential

Knowledge of the surface charge of a material is important to predict dispersion stability and interactions between different materials in fluids. Depending on the sign and magnitude of the surface charge (negative, neutral or positive), the materials/particles exhibit different characteristics, interactions and stabilities. Figure 2.2 shows a sketch of a negatively charged particle in an electrolyte solution. The negatively charged surface attracts positively charged counterions from the solution, collocated/bound in the Stern layer. The resulting charge of the particle (i.e., particle surface charge + charge of the Stern layer) leads to loose attraction of other oppositely charged ions from the solution, which are then present in the diffuse layer. The ions in this layer are not physically bound to the surface as in the Stern layer but are rather loosely attracted (Bhattacharjee 2016).

The surface charge can not be measured directly. Therefore, the ζ-potential is used as an approximation of the surface charge in suspension (Bhattacharjee 2016). It represents the charge at the shear/slipping plane and is always lower in absolute values than the surface charge. Like the surface charge, it can not be measured directly. However, the electrophoretic mobility can be measured and converted to ζ-potential and is defined as (Elimelech et al. 1995):

$$U_e = \frac{2}{3}\frac{\epsilon\zeta f(\kappa r)}{\eta} \tag{2.17}$$

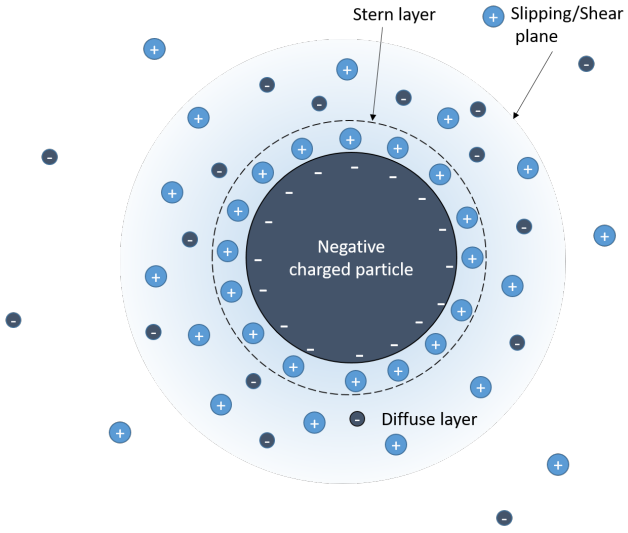

Figure 2.2: Schematic representation of the location of ζ-potential at the shear/slipping plane of a negative charged particle in a fluid.

with U_e electrophoretic mobility, $\epsilon = \epsilon_0\epsilon_r$ permittivity of free space (ϵ_0) and relative permittivity of solvent (ϵ_r) and η viscosity. The Henry equation f(κr) depends on κ, the inverse Debye length and r the particle radius. This equation can be re-formulated to calculate ζ-potentials based on electrophoretic mobility measurements (Elimelech et al. 1995, Pochapski et al. 2021):

$$\zeta = \frac{3}{2}\frac{\eta U_e}{\epsilon} \qquad \kappa r \ll 1 \tag{2.18}$$

$$\zeta = \frac{\eta U_e}{\epsilon} \qquad \kappa r \gg 1 \tag{2.19}$$

Equation 2.18 describes the Hückel approximation to the Henry equation, which is used in apolar solvents and when particle sizes are much smaller than the extent of their double layers (Debye length κ^{-1}). Equation 2.19 describes the Smoluchowski approximation used in polar solvents and when particle sizes are much larger than the extent of their double layers.

As the ζ-potential represents the charge on the shear plane of the particles and not directly the surface charge, one major implication is its strong dependence on the salinity and pH of the solution. One important information when interpreting ζ-potential data is the location of the isoelectric point (IEP). At this pH value, the ζ-potential is zero, meaning the surface charge of the particle and the charge of the attracted ions equal their charge. Below that point, ζ-potential is typically positive, whereas above that point, it is usually negative. Furthermore, the absolute value of ζ-potential can serve as an indication of agglomeration tendency or

colloidal stability, with the rule of thumb of above absolute values of 30 mV suspensions considered colloidal stable (Chakraborty and Panigrahi 2020, Salopek et al. 1992).

The ζ-potential can also be used to predict the critical coagulation concentration (CCC), i.e., the concentration of counterions needed to induce coagulation and aggregation of the particles (to overcome the repulsive charge). After Schulze (1882) and Hardy (1900), the CCC can be approximated for symmetrical electrolytes using:

$$CCC \propto z^{-6} A_H^{-2} tanh^4 \frac{ze\zeta}{4k_B T} \tag{2.20}$$

with z valence of the ion, e electron charge, A_H Hamaker constant, k_B Boltzmann constant and T absolute temperature. For high ζ-potentials, the CCC is rather proportional to z^{-2} than to z^{-6} and this proportionality of the ion valence to the CCC is known as the Schulze-Hardy rule.

The prevalent ζ-potential of particles and minerals in natural environments results from the interplay of various intrinsic and external parameters, like the surface charge, the pH-value and salinity of the solution, but also the valence of the ions present. Determining ζ-potentials of minerals and rocks in complex solutions, for example, in geothermal environments, is difficult. Existing literature data is complex and often incomplete in reporting ζ-potential with pH value and salinity (Walker and Glover 2018). In Figure 2.3, a selected fraction of literature data is compiled and presented in a ternary pH-salinity-ζ-potential diagram. ζ-potentials show a great variability in sign, magnitude and dependency on salinity for the selected minerals and rocks. Generally, most minerals show negative ζ-potentials with increasing negative values at increasing pH values. Higher salinities seem to lower the absolute ζ-potential, which is in accordance with experimental data (Franks 2002) and DLVO theory (Derjaguin and Landau 1941, Verwey and Overebeek 1948). Not presented here is the impact of higher valent ionic species. As indicated by the Schulze-Hardy rule, the higher valence of the counterions affects the ζ-potential to a greater extent than monovalent ones. There are indications of neutralization and overcharging of the surface in the presence of divalent and higher valent ions (Pianegonda et al. 2005).

Further, ζ-potentials show a dependence on temperature, with absolute ζ-potential increasing with increasing temperature. Tosha et al. (2003) proposed a formula to estimate the temperature effect on ζ-potentials:

$$\frac{\zeta(T)}{\zeta(T_0)} = 1 + 0.0171 \cdot (T - T_0) \tag{2.21}$$

with T temperature in °C. The formula shows a good fit for salinities below 0.001 M but deviates strongly from experimental data with increasing salinity.

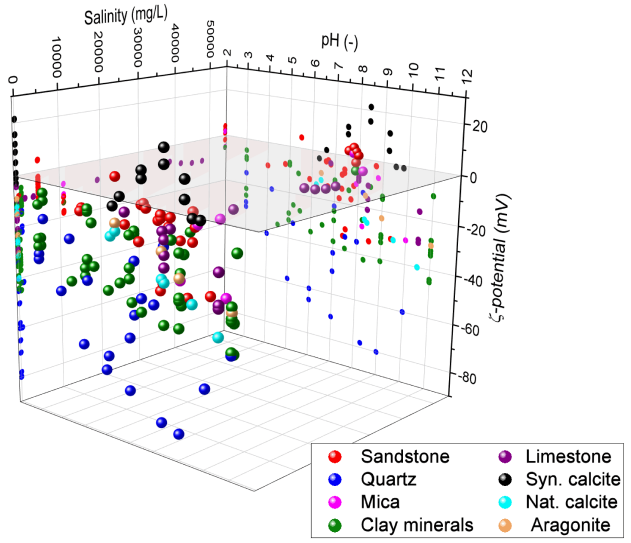

Figure 2.3: ζ-potentials of various silicate minerals, calcite, limestone and sandstone plotted against salinity and pH and projections on the salinity-ζ-potential plane as well as on the pH-ζ-potential plane. Sandstone and silicates Dong et al. (2014), Elimelech et al. (2000), Kaya and Yukselen-Aksoy (2011), Nasralla and Nasr-El-Din (2012), Rodriguez and Araujo (2006), Shehata and Nasr-El-Din (2015), limestone and carbonates Alroudhan et al. (2016), Sondi et al. (2009), Vdović (2001).

In summary, it should be noted that although ζ-potentials bear great potential in predicting colloidal stability and interactions of different species, they are dependent on a large number of variables leaving such predictions with a certain degree of inaccuracy.

2.4.6 DLVO theory

The Derjaguin-Landau-Verwey-Overbeek (DLVO) theory describes the forces between two particles or particle-surface in a fluid medium at the nanometer scale. The theory was formulated by Derjaguin and Landau (1941) and Verwey and Overebeek (1948) to determine the stability of colloidal suspensions, i.e., to assess whether the particles tend to aggregate or stay dispersed. The theory is usually applied for static conditions, i.e., only no-flow regimes are covered. The impact of transport properties on colloids is described in Section 2.4.4 and Chapter 7.

The DLVO theory sums up the attractive London-van der Waals force (V_{LvdW}) and the (repulsive) force originating from the electric double layer (V_{EDL}) to calculate the total interaction energy (V_t):

$$V_t = V_{LvdW} + V_{EDL} \tag{2.22}$$

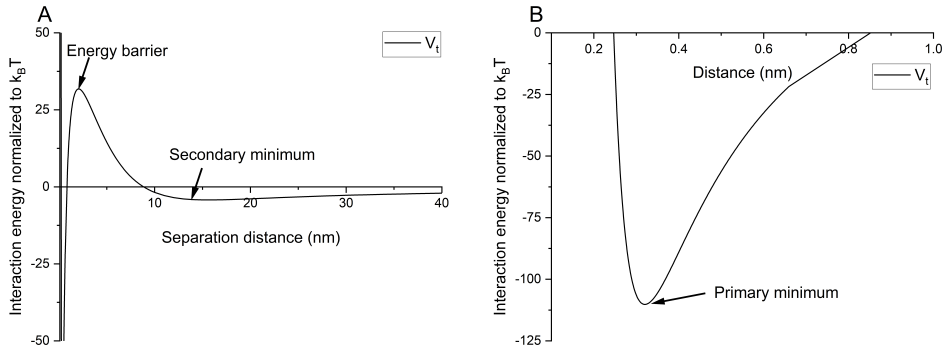

Figure 2.4: DLVO interaction profile normalized to k_BT over separation distance between particle-particle or particle-surface. In B, a zoom on the region between 0 and 1 nm distance is shown to emphasize the primary minimum.

DLVO total interaction energy (V_t) is usually normalized to the Boltzmann constant times the absolute temperature (k_BT) and is plotted over the separation distance of the two interacting particles/surfaces. In Figure 2.4, an exemplary DLVO interaction profile is shown. Three different characteristics can be observed:

- An (in)finitely deep primary minimum
- An energy barrier (maximum)
- A secondary minimum

All three properties can occur individually or together. If only an (in)finitely deep primary minimum is present, the particle dispersion is unstable and the particles will aggregate. If an (in)finitely deep primary minimum is present but also an energy barrier has formed, the particles need to overcome the energy barrier before they aggregate, i.e., coagulation is less likely and depends on the height of the energy barrier. If further a secondary minimum is present, aggregation of particles can occur in this secondary minimum. However, as the secondary minimum is usually shallow, the aggregation is not strong and the particles are re-dispersible by applying an external force.

2.4.6.1 London-van der Waals force

The van der Waals force is an attractive force and a fundamental interaction between all atoms and molecules. It is counted to the weak forces and describes the interactions between atoms and molecules. It can further be divided into three different kinds of interactions: the Keesom-interaction (permanent dipoles), the Debye interactions (permanent dipole-induced dipole) and dispersion interactions (fluctuating induced dipoles) (Elimelech et al. 1995).

The London-van der Waals force is a dispersion interaction defining the attraction between particles and molecules and is usually short-ranged up to several nanometers.

After Gregory (1981), unretarded LvdW interactions are applicable when the distance is less than the particle size. For unretarded equal particles, the following formula applies:

$$V_{LvdW} = -\frac{A_H r}{12h} \tag{2.23}$$

with A_H Hamaker constant of particle-particle or particle-surface interacting in a medium in J/(Vm), r radius of particles in m, h separation distance (in m).

Unretarded particle-surface LvdW interaction can be described as follows after Elimelech et al. (1995):

$$V_{LvdW} = -\frac{A_H}{6}[\frac{r}{h} + \frac{r}{h+2r} + \ln(\frac{h}{h+2r})] \tag{2.24}$$

Retarded interaction approach should be used for larger particles, i.e., particles larger than 1 µm and can be calculated with the Schenkel and Kitchener (1960) approximation:

$$V_{LvdW} = -\frac{A_H}{6h}\frac{r_1 r_2}{(r_1+r_2)}(1+\frac{14h}{\lambda})^{-1} \qquad \text{Particle-Particle} \tag{2.25}$$

$$V_{LvdW} = -\frac{A_H r}{6h}(\frac{1}{1+14h/\lambda}) \qquad \text{Particle-Surface} \tag{2.26}$$

with λ, the characteristic wavelength of the medium, usually assumed to be 100 nm.

Hamaker constant

The Hamaker constant is a material and medium-related constant for interaction between particles and particle-surface acting through a medium (water, vacuum, etc.). The constant was investigated by Hamaker (1937), who used an integration approach to sum up intermolecular forces acting between molecules in a particle with molecules in another particle (or surfaces). Typical values for Hamaker constants range from 10^{-21} to 10^{-19} Joule and are highly dependent on material and medium properties (Bergström 1997). For example, having two particles 1 and 3 interacting through a medium 2, the Hamaker constant for interaction can be calculated by:

$$A_{132} = A_{12} + A_{33} - A_{13} - A_{23} \tag{2.27}$$

Hamaker constants are typically positive, especially for two identical particles interacting in a medium. Nevertheless, Hamaker constants are occasionally found to be negative, for example, in the system carbon-water-teflon (Visser 1981). Negative Hamaker constants result in negative van der Waals force, thus causing repulsion instead of attraction.

One calculation approach for determining Hamaker constants is using the optical properties of the dispersion (Gregory 1970):

$$A_{12} = \frac{27}{32} \frac{\hbar \omega_1 \omega_2}{\omega_1 + \omega_2} \frac{(\epsilon_1 - 1)(\epsilon_2 - 1)}{(\epsilon_1 + 2)(\epsilon_2 + 2)} \tag{2.28}$$

with $\hbar$ being the reduced Planck constant (Planck constant divided by 2π), ω being the characteristic dispersion frequency and ϵ the dielectric constant ($\epsilon_0 \epsilon_r$).

2.4.6.2 Electric double layer force

A double layer forms when a charged particle/surface is placed in a fluid solution (Section 2.4.5). The force emanating from the formation of this double layer is called electric double layer force (or EDL force). It strongly depends on the surface potential of the charged objects and the ionic strength of the medium (Muneer et al. 2020). Depending on these parameters, the EDL force can be very short-ranged and weak or can act up to several tenth nanometers and possibly exceed the attractive London-van der Waals force (leading to the formation of an energy barrier, as shown in Figure 2.4). For calculations of EDL force, the surface potential is usually exchanged by its approximation: the ζ-potential. EDL force can be calculated after Hogg et al. (1966) as:

$$V_{EDL} = \pi \epsilon_r \epsilon_0 \cdot \frac{r_1 r_2}{r_1 + r_2} \cdot [2\zeta_1 \zeta_2 \cdot \ln(\frac{1 + e^{-\kappa h}}{1 - e^{-\kappa h}}) + (\zeta_1^2 + \zeta_2^2) \cdot \ln(1 - e^{-2\kappa h})] \tag{2.29}$$

$$V_{EDL} = \frac{\epsilon r \zeta^2}{2} \ln(1 + e^{-\kappa h}) \tag{2.30}$$

where ϵ_r and ϵ_0 are the relative permittivity of solvent and absolute permittivity of vacuum, respectively. ϵ in the simplified formula for equal particles (Equation 2.30) is the product of ϵ_r and ϵ_0. $r_{1,2}$ are the radii of the interacting particles. The term $\frac{r_1 r_2}{r_1 + r_2}$ reduces to r_1 if particle-surface interactions are calculated due to the assumption of an infinite size of the surface in comparison to the particle. $\zeta_{1,2}$ are ζ-potentials of interacting particles or

particle-surface. κ is the inverse of the Debye length, which describes the extent of the double layer force (with 1 Debye length, meaning 1/e initial force is present) and is highly dependent on the salinity of the medium. It can be calculated as

$$\kappa^{-1} = \frac{1}{\sqrt{(8\pi\lambda_B N_A 10^{-24} I)}} \tag{2.31}$$

with λ_B Bjerrum length (typically 0.71 nm), N_A Avogrado constant and I molar ionic strength. A more simplified equation for calculating Debye length (in nm) is

$$\kappa^{-1} = \frac{0.304}{\sqrt{I}} \tag{2.32}$$

From Equation 2.29, it can be deduced that EDL force is attractive or repulsive. The force is attractive if the interacting objects are of opposite charge and repulsive if they have the same sign.

2.4.7 Extended DLVO theory (XDLVO)

The classical DLVO theory is a simple approach to obtain a (semiquantitive) prediction of the stability of colloidal dispersion (Ninham 1999). Yet, there are certain cases where the experimental results strongly deviate from theoretical predictions, i.e., the theory does not accurately reflect reality (Adamzyck and Weroński 1999, Missana and Adell 2000). This discrepancy could be explained by the simplifications and assumptions considered in the formulation of DLVO theory, such as smoothness of the surfaces, independence and additivity of EDL and LvdW forces or disregard of contact angles (Adamzyck and Weroński 1999, Ninham 1999). On the other hand, these deviations could originate from the occurrence of forces not included in the DLVO theory, such as Born, steric and hydration force (Elimelech et al. 1995). The extended DLVO theory (XDLVO theory) was therefore established, accounting for the impact of additional (non-DLVO) forces (Christenson 1988).

Considering non-DLVO forces, the overall interaction energy can be determined by summing up DLVO forces and XDLVO forces:

$$V_t = V_{DLVO} + V_{XDLVO} \tag{2.33}$$

with XDLVO forces being, for example, Born force, steric force, hydration force and acid-base force. In the following sections, the most significant non-DLVO forces are briefly described.

2.4.7.1 Born repulsive force

Born force originates from overlapping electron orbitals (Elimelech et al. 1995). Born force is occasionally considered in DLVO calculations to determine the depth of the primary minimum. Although the force is short-ranged (below 0.5 nm), its effect on the overall interaction energy (V_t) is tremendous as it exceeds the attractive London-van der Waals force.

An approximation of Born force has been formulated applying the Lennard-Jones m-n potential (Fitts 1966):

$$V_{LJ} = \epsilon_E \frac{n}{m-n} (\frac{n}{m})^{\frac{m}{n-m}} [(\frac{\sigma_c}{h})^n - (\frac{\sigma_c}{h})^m] \tag{2.34}$$

with ϵ_E depth of the primary minimum, h separation distance and σ_c collision diameter. Using convenient assumptions of m=6 and n=12 reduces the formula to:

$$V_{LJ6-12} = \epsilon_E \cdot 4[(\frac{\sigma_c}{h})^{12} - (\frac{\sigma_c}{h})^6] \tag{2.35}$$

Ruckenstein and Prieve (1976) applied an integration approach on the Lennard-Jones m-n formula and obtained the simplified equation:

$$V_B = \frac{A_H r_p \sigma^6}{1260 h^7} \tag{2.36}$$

with A_H Hamaker constant, r_p particle radius, σ Born collision diameter typically 0.5 nm, h separation distance particle-surface.

For convenience, in the following calculations in Chapter 6 and Chapter 7, Born force is counted to DLVO force and added accordingly in the calculations of the interaction energy. This decision was made to enable the evaluation of primary minimum depth and facilitate interpretation of interaction energy curves.

2.4.7.2 Steric force

Steric repulsion originates from grafted polymers, ligands or ionic/nonionic surfactants on the surface of nanoparticles (Napper and Netschey 1971, Zhulina et al. 1990). Steric force counts to the non-DLVO forces and can act attractive or repulsive. If only low amounts of polymer/ligands are grafted to the surface, they rather induce aggregation and colloid formation due to polymer bridging than improve the stability. Healy and La Mer (1964)

determined the critical surface coverage to be half of the available particle surface: lesser surface coverage promotes polymer bridging. Surface coverage above half of the available surface can give rise to a repulsive force that enhances the stability of the dispersion and is known as steric stabilization, which is particularly useful for stabilization of emulsions (Napper 1977).

Steric force can be calculated as a sum of osmotic and elastic forces contribution:

$$V_S = V_O + V_e \tag{2.37}$$

Adding steric force to the calculation of total interaction energy yields:

$$V_t = V_{LvdW} + V_{EDL} + V_B + V_S \tag{2.38}$$

It is assumed that the steric layer impacts neither EDL force nor Debye length, although it should be noted that depending on the type of adsorbed polymer, indeed, the ζ-potential can vary, leading to increasing or decreasing EDL force.

Osmotic force Overlapping steric layers increase the osmotic pressure between particles/surfaces and contribute to the steric force. Calculations are usually made as piece-wise functions and depend on interparticle distance (h) and the length/thickness of the polymer/ligand layer (L). According to Vincent et al. (1986), Worthen et al. (2016) and Tran and Richmond (2021), three different regions can be identified and calculated:

$$V_O = 0 \qquad \text{if } 2L \leq h \tag{2.39}$$

$$V_O = \frac{4\pi r}{\nu_1}\Phi_p^2(\frac{1}{2} - \chi)(L - \frac{h}{2})^2 \qquad \text{if } L \leq h < 2L \tag{2.40}$$

$$V_O = \frac{4\pi r}{v_1}\Phi_p^2(\frac{1}{2} - \chi)L^2(\frac{h}{2L} - \frac{1}{4} - \ln(\frac{h}{L})) \qquad \text{if } h < 2L \tag{2.41}$$

with r particle radius, ν_1 volume of the solvent molecule, Φ being volume fraction of the polymer/ligand, L length of ligand/polymer, χ Flory-Huggins interaction parameter. χ describes the compatibility between the polymer/ligand and solvent, with χ <0.5 being compatible, i.e., raising a repulsive steric barrier and χ >0.5 being incompatible, i.e., no steric barrier is formed.

Elastic force The other contribution to the steric force is the elastic repulsive force that arises when a polymer/ligand is compressed below the interparticle distance (Napper 1977,

Worthen et al. 2016). Similar to the osmotic pressure, it is described by piece-wise functions depending on the interparticle distance (h) and length/thickness of the polymer/ligand layer. Elastic force is calculated according to Vincent et al. (1986) and Worthen et al. (2016) with:

$$V_e = 0 \qquad \text{if L}\leq\text{h} \quad (2.42)$$

$$V_e = \frac{2\pi r}{M_W}\Phi_p L^2 \rho_p [\frac{h}{L}\ln(\frac{h}{L}(\frac{3-h/L}{2})^2) - 6\ln(\frac{3-h/L}{2}) + 3(1+\frac{h}{L})] \qquad \text{if L}>\text{h} \quad (2.43)$$

with r particle radius, M_W molecular weight of polymer/ligand, Φ volume fraction polymer/ligand and ρ_p density of polymer/ligand.

2.4.7.3 Other forces

Hydration force Hydration force is a repulsive force originating from water molecule layers on the hydrated surfaces. This force was found by Pashley and Israelachvili (1984) in aqueous solutions with ionic strengths above 10^{-3} M and is typically only short-ranged (1.5-4 nm). It increases with the degree of hydration of oppositely charged ions in solution (for example, anionic particle: $Li^+ \approx Na^+ > K^+ > Cs^+$). In addition to the hydration force, Gregory (1988) identified an oscillatory force below 1.5 nm distance, possibly arising from the water layer with a periodicity of approximately 1 water molecule (i.e., approx. 0.25 nm). This force was only found in water.

Hydrophobic force Hydrophobic force can be surprisingly long-ranged (several tenth to hundred nanometers) and is an attractive force acting between hydrophobic surfaces in water (Elimelech et al. 1995). This attraction force is stronger than the London-van der Waals force and longer ranged (Israelachvili and Pashley 1982). Hydrophobic force is still subject to active research and not entirely understood (Agmo Hernández 2023). Though, the force is important for understanding the hydrocarbon interaction in aqueous environments or for particles having adsorbed surfactants with hydrophobic tails (Elimelech et al. 1995).

Magnetic force The impact of magnetic force on dispersion stability can be observed even without applying an external magnetic field and is attributed to the alignment of the magnetic spin of ferri- and ferromagnetic materials (Hotze et al. 2010). Phenrat et al. (2007) identified magnetic force as the root cause for the rapid aggregation behavior of iron-based nanoparticles that was not expected from DLVO calculations.

CHAPTER 3

Silica as natural and engineered geomaterial

As emphasized in Chapter 2 the concept of nanoparticles tracers requires design of a nanoparticle-based tracer carrier for transportation of fluorescent dyes. In this chapter, silica is introduced as such a carrier material. Its properties and behavior are elucidated as well as strategies presented to achieve modular and adaptable tracer carriers. Understanding the behavior of (natural) silica aids in understanding the behavior of engineered silica-based nanoparticle tracers in geological environments.

3.1 Origin and behavior of silica in natural fluids

Silicon dioxide (SiO_2, herein referred to as silica) is the main component of most rock-forming minerals, present as silicates or quartz (Krauskopf 1956). Through weathering processes, silica becomes part of the (thermal) water cycle (Dietzel 2000, Wu and Zhou 2024). The silica concentration in fluids is derived from equilibration processes between the fluids and reservoir minerals. It is driven by the maturity of the fluids and geochemical parameters such as temperature, pH and salinity (Alexander et al. 1954, Greenberg and Price 1957, Iler 1979) and equilibrium is usually established when the quartz solubility is reached (Henley 1983, Rimstidt and Barnes 1980). Silica concentrations in natural fluids vary widely, ranging from a few milligrams per liter in shallow groundwater to several hundred milligrams per liter in mature geothermal fluids and strongly depend on the temperature (Figure 3.1, Fournier and Rowe (1966)). This relationship between silica concentration and temperature is often used to estimate underground temperature through silica-based geothermometry (Fournier and Rowe 1966, Nitschke et al. 2017).

Natural ascent or the extraction of geothermal fluids, along with the subsequent pressure relief and temperature decrease, leads to the supersaturation of the waters with quartz and possibly amorphous silica (Henley 1983), as illustrated in Figure 3.1. Despite the strong supersaturation, quartz precipitates are rarely observed, as their crystalline structure results from a slow growth rate (Brown 2011). This contrasts with the rapid formation of the non-crystalline structure of amorphous silica. Although the saturation concentration of amorphous silica is higher than of other silica polymorphs such as chalcedony, amorphous silica precipitation, with its fast kinetics, is one of the limiting factors in the efficiency of geothermal power plants (Gunnarsson and Arnórsson 2003, Kristmannsdóttir 1989).

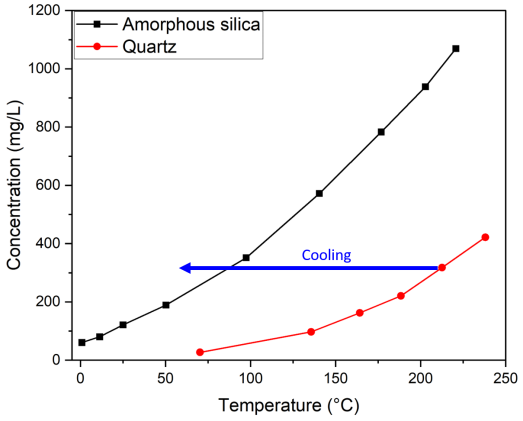

Figure 3.1: Amorphous silica and quartz equilibrium concentration in dependence of temperature. Data taken from Fournier and Rowe (1966). The cooling path illustrates the risk of amorphous silica scaling in geothermal power plants.

3.1.1 Geochemical equilibrium

The state of minerals in aqueous environments can be main attributed to two factors: mineral solubility and saturation index. Both values indicate whether the mineral will remain intact or dissolve as well as to what extent.

The solubility of a component A_aB_b can be determined by the chemical dissociation constant pK:

$$A_aB_b \rightleftharpoons aA^{b+} + bB^{a-} \tag{3.1}$$

$$K = \frac{\{A\}^a\{B\}^b}{\{A_aB_b\}} \tag{3.2}$$

$$pK = -logK \tag{3.3}$$

with curly brackets denoting activity. The saturation index (SI) is calculated using the dissociation constant and the ion activity product:

$$SI = \log \frac{IAP}{K} \tag{3.4}$$

$$SI = 0 \qquad \text{Solution in equilibrium} \tag{3.5}$$

$$SI > 0 \qquad \text{Solution supersaturated} \tag{3.6}$$

$$SI < 0 \qquad \text{Solution undersaturated} \tag{3.7}$$

If a solution is in equilibrium, the mineral or component remains intact and does not dissolve. If undersaturated, the mineral will dissolve until equilibrium is reached, and if supersaturated, it will precipitate until equilibrium is restored. Various factors, such as temperature, pressure, pH, mixing with immature fluids, changes in Eh, and even bacterial activity, can influence solubility and saturation (Nitschke et al. 2014, Robertson 1982).

Silica exists in several polymorphs, including the crystalline phases quartz, tridymite, cristobalite, and the amorphous phases chalcedony and amorphous silica (Washburn and Navias 1922). Quartz, the most abundant crystalline form of SiO_2 in nature, has the lowest solubility among these polymorphs (at 25°C 6 mg/L in comparison to 105-120 mg/L of amorphous silica, Drees et al. (1989), Morey et al. (1962), Okamoto et al. (1957)). While one might expect all natural waters to be in equilibrium with quartz, as suggested by saturation index theory, this is not always the case. Fluids are occasionally found instead to be in equilibrium with chalcedony (Azaroual et al. 1997, Gíslason et al. 1993, Nitschke et al. 2017).

Over the centuries, significant efforts have been made to understand the solubility and dissolution processes of quartz and other silica polymorphs. For example, Molengraf (1888) found a dissolution process for natural quartz attributed to etching phenomena induced by alkali-carbonates, which was an important extension of knowledge at that time. Roy (1945) clarified that silica dissolved in water forms a true solution, countering previous assumptions of colloidal dispersion (Kahlenberg and Lincoln 1898). Lunge and Millberg (1897) suspected that increasing surface area, such as by milling, increases the solubility of quartz. Differences in reported solubilities have been largely attributed to impurities (Lucas and Dolan 1939). However, Holt and King (1955) speculated that monolayers of silicic acid on silica surfaces are the root cause of increased solubility, a theory supported by van Lier et al. (1960), who further found that less than 0.1 M NaCl increases both dissolution rate and solubility. Iler (1979) proposed that adsorbed silicic acid layers on silica surfaces may desorb and re-adsorb, affecting the "apparent" solubility, and estimated that given enough time, true quartz solubility would be reached.

Despite these advances, the dissolution process and solubility of quartz and silica polymorphs remain incompletely understood. Blum et al. (1990) found quartz dissolution to be independent

of dislocation density. Williams and Crear (1985) proposed a formation mechanism for quartz and silica based on nucleation theory, with growth driven by the polymerization/condensation of silicic acid monomers (Volmer and Weber 1925). This theory, also used in modern approaches, explains quartz and silica dissolution and stability. For instance, Dove et al. (2008) attributed the different dissolution behavior to the surficial silanol and siloxane groups and proposed a dissolution mechanism-driven removal of Q2-silica species in the absence of salts and removal of Q3-species in the presence of salts. Q2 and Q3 describe one silica tetrahedron, with the numbers of bound oxygen atoms are 2 and 3, respectively (Gratz and Bird 1993). Crundwell (2017) further refined this theory by adding the effect of surface charge vacancies and the effect of ζ-potential differences.

3.1.2 Silica species distribution

Figure 3.2 shows a simplified silica species distribution in water at 25°C over a pH range of pH 8 to 13. Silica reacts with water to form silicic acid (H_4SiO_4) due to nucleophilic attack of the silanol (Si-OH) bonds (Cypryk and Apeloig 2002). In acidic and neutral fluids, the predominant silicic acid species is H_4SiO_4. From the equilibrium reaction of silica and silicic acid (Equation 3.8), it can be deduced that the concentration of silicic acid depends on the silica solubility (Dove et al. 2008). As pH values increase, H_4SiO_4 dissociates to $H_3SiO_4^-$ (Eq. 3.9) and further to $H_2SiO_4^{2-}$ (Brown 2011). These reactions shift the equilibrium of silica and silicic acid toward silicic acid and are the root cause for the increasing silica solubility with increasing pH value (Dove et al. 2008, Eikenberg 1990, Milne et al. 2014). Alexander et al. (1954) determined the equilibrium points of H_4SiO_4 and $H_3SiO_4^-$ and $H_3SiO_4^-$ and $H_2SiO_4^{2-}$ at pH 9.8 and pH 12.8, respectively.

The silica species distribution in water can be described according to Iler (1979):

$$SiO_2 + 2H_2O \rightleftharpoons H_4SiO_4 \tag{3.8}$$

$$H_4SiO_4 + OH^- \rightleftharpoons H_3SiO_4^- + H_2O \tag{3.9}$$

$$H_3SiO_4^- + OH^- \rightleftharpoons H_2SiO_4^{2-} + H_2O \tag{3.10}$$

3.1.3 Governing parameters of solubility

Several factors affect the solubility of silica, including temperature, pH values and salinity of the fluids. As described in Section 3.1.2, alkaline pH values catalyze the dissociation of silica significantly, thus increasing the solubility. By contrast, acidic or neutral pH values only show a minor impact (Alexander et al. 1954, Krauskopf 1956). Increasing temperatures also lead to higher solubility, as shown in Figure 3.1.

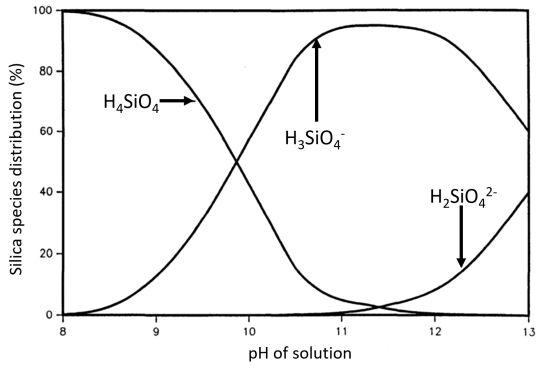

Figure 3.2: Simplified silica species distribution in dependence on pH values. Figure adapted from Eikenberg (1990).

The effect of different salts on the solubility of silica depends also on their concentration (Greenberg and Price 1957), with high concentrations exerting a stronger influence on solubility (Chen and Marshall 1982, Marshall 1980a). The impact of cations on solubility can be described by the so-called salt effect, which can be differentiated into the salting-out and salting-in effect (Marshall 1980b). The salting-out effect leads to a reduction in solubility with increasing concentration of the salt in solution whereas the salting-in effect has the opposite impact (Chen and Marshall 1982, Marshall and Warakomski 1980). Most salts lead to a salting-out effect (Chen and Marshall 1982) that is reduced with increasing temperature except for Na_2SO_4 and $MgSO_4$, which show a salting-in effect (Marshall and Chen 1982). Generally, cations have a more substantial impact on solubility than anions (Chan 1989). Furthermore, a correlation between the ionic charge and the decrease in solubility can be identified with higher-valent cations reducing solubility more strongly (Marshall and Warakomski 1980), likely due to a decrease in ζ-potential (Section 2.4.5). This change in surface charge diminishes the repulsive forces between particles, increasing polymerization, agglomeration, and precipitation of silica, thus reducing its solubility (Iler 1979).

3.1.4 Polymerization and formation of colloids

Silica can be categorized into three subgroups: soluble silica, polymeric silica and colloidal silica (Iler 1979). Soluble silica, i.e., the monomeric silicic acid, consists of one Si-atom surrounded by four tetrahedrally ordered hydroxyl groups (Figure 3.3A). Oligomers or polymeric silica are the dimers, trimers and higher polymerized forms of monomeric silicic acid formed by condensation reactions (Figure 3.3B-D, Iler (1979)). Particles with diameters greater than 5 nm are defined as colloidal silica (Iler 1979). As described in Section 3.1.2, monomeric silicic acid is the initial species formed when silica dissolves in water. To undergo polymerization, colloid formation and scaling formation three steps are necessary: nucleation, particle growth and agglomeration (Icopini et al. 2005).

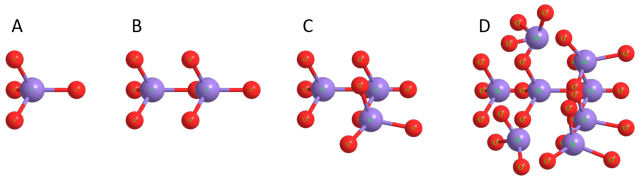

Figure 3.3: Schematic representation of homogeneous nucleation of monomeric silicic acid (A) to dimer (B), trimer (C) and polymeric species (D).

Nucleation begins when a solution becomes saturated with monomeric silicic acid. The rate of nucleation depends on silica concentration, temperature, pH, and salinity (Brown 2011). Higher temperatures, neutral pH, and high salinity increase the rate (Crear et al. 1981, Fleming and Crear 1982, Iler 1979, Kley et al. 2017). Nucleation can be homogeneous (condensation of monomers) or heterogeneous (induced by other ions or surfaces) (Brown 2011, Lunevich 2019, Volmer and Weber 1925). In alkaline solutions, OH^- concentrations catalyze condensation, while in highly acidic environments ($pH < 2$), H^+ concentrations drive the process (Wilhelm and Kind 2015).

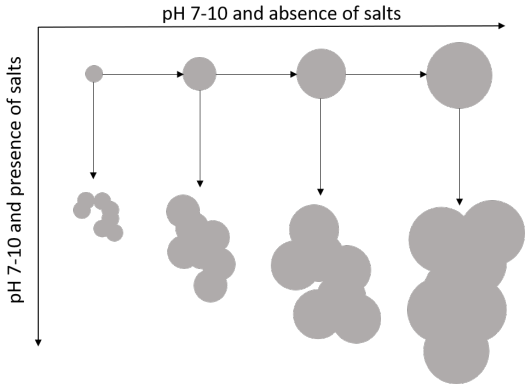

Figure 3.4: Silica nanoparticle growth mechanism according to Iler (1979). In neutral to moderate alkaline solutions without salts, the particles can grow up to a few 100 nm, whereas in the presence of salts, the particles aggregate and form gel networks.

As polymeric species form, monomeric silicic acid concentration decreases until equilibrium is reached, marking the start of the polymerization phase (Fleming 1986, Kley et al. 2017). In alkaline solutions without salts, particles can grow up to a few 100 nm due to repulsion between the negatively charged particle surfaces. In this phase, the so-called Ostwald ripening can take place (Scott et al. 2024). Ostwald ripening describes the dissolution of smaller particles for the benefit of the larger ones to form a mono-disperse colloidal suspension (Crear et al. 1981). The stability of these suspensions can be determined by the Derjaguin-Landau-Verwey-Overbeek theory (DLVO theory) (Derjaguin and Landau 1941, Verwey and Overebeek 1948, Yotsumoto and Yoon 1993). This theory is described in detail in Section 2.4.6. In brief, the theory states that forces between colloidal particles are either repulsive or attractive. If the attractive force dominates, it destabilizes the colloidal suspensions, whereas

if the repulsive force dominates, the colloidal suspension is stable. Unstable suspensions tend toward coagulation, aggregation and precipitation of the colloids. In stable suspensions, on the other hand, the repulsive forces dominate, which is the case mostly when no salts are present and pH ranges between pH 7 and pH 10 (Figure 3.4). Therefore, changing the chemical composition, pH value or temperature of the suspension can lead to destabilization of the suspension/dispersion.

Aggregation, the final phase of polymerization, involves the formation of a gel or coagulation and flocculation of colloidal suspensions (Baxter and Bryant 1952, Iler and Dalton 1956). Gels form through siloxane bonds (Si-O-Si) and exhibit high viscosity and constant volume (Nordström et al. 2011). Coagulation and flocculation lead to precipitation (Bergna 1994).

3.1.5 Silica scaling formation and mitigation

As discussed in Section 3.1, silica is a common component of natural fluids, posing a high risk of scaling in geothermal operations due to possible supersaturation regarding amorphous silica. Silica scaling is supposed to be one of the main obstacles in geothermal power plant operation (Gunnarsson and Arnórsson 2005). Though the mechanisms of its growth are not fully understood. Tamura et al. (2019) observed silica nanoparticles growing in geothermal fluids within minutes, reaching sizes up to 7 nm, while van den Heuvel et al. (2018) identified both homogeneous and heterogeneous nucleation in geothermal plants, with µm-sized particles formed through homogeneous nucleation and scaling occurring on surfaces like pipe walls. Mitigation of the problematic silica scaling is a complex task. Generally, two different methods can be distinguished: inhibition and precipitation techniques (Phillips et al. 1980). A strategy to selectively remove silica from geothermal fluids to minimize the risk of silica scaling by controlled precipitation is presented in a study by Spitzmüller et al. (2021) and can be found in Supplementary A.

Inhibition techniques

Inhibition refers to the prevention of scale formation by disrupting crystal growth. Common inhibitors including chelating agents like ethylenediaminetetraacetic acid (EDTA) and so-called threshold-scale inhibitors, which prevent coagulation and aggregation (Chapter 6, Mpelwa and Tang (2019)). However, these methods are mostly ineffective against silica scaling due to its amorphous nature (Spitzmüller et al. 2021).

An effective method for inhibiting silica scaling is pH modification. Lowering the pH of the fluid slows silica polymerization, thereby preventing scale formation (Finster et al. 2015). This technique has been successfully implemented in geothermal power plants in the USA and Iceland (Gallup 2011, Sigfusson and Gunnarsson 2011). Nevertheless, the method has significant drawbacks, including high acid demand (and costs), increased corrosion risk, and

the potential formation of other scales. Another approach involves raising the pH to alkaline levels, which shifts the silica species to negatively charged forms, increasing repulsive forces between silica monomers and preventing nucleation. Yet, this method is impractical due to the presence of cations, which can lead to co-precipitation of minerals like metal carbonates (Kashpura and Potapov 2000).

Forced precipitation techniques

Forced precipitation techniques follow a different approach compared to inhibition techniques: silica is removed from the solution through the formation of precipitates. Unlike inhibition techniques, where precipitation is unwanted and must be prevented, the focus here is on achieving a selective process that enables fast and effective silica removal from the fluids, ideally without affecting other elements in the solution. A variety of methods have been tested over the past decades, including seed-induced precipitation, lime precipitation, caustic precipitation, the addition of metal salts, electrocoagulation, and ultrafiltration (Spitzmüller et al. 2021).

Seed-induced precipitation involves adding silica seeds as nucleation sites to trigger silica scale formation. This method has several advantages, such as the re-usability of seeds, which reduces costs, the ability to produce seeds from geothermal brine, and high selectivity towards silica, minimizing the risk of co-precipitation (Sugita et al. 1999). Nonetheless, the major limitation of this method is that it cannot reduce the silica concentration in solution below saturation; it is only applicable when the initial solution is oversaturated with amorphous silica (Spitzmüller et al. 2021). As shown in 3.1.4, the processes of polymerization and colloid formation are also influenced by pH value and temperature. Sugita et al. (1999) and Kato et al. (2003) found that the optimal pH range is between 7-8, and elevated temperatures accelerate particle growth kinetics. However, higher temperatures also increase silica solubility, which in turn reduces removal efficiency via silica seeding. While the method offers some benefits, it is not viable for all geothermal environments. Nevertheless, successful examples of silica seeding have been demonstrated by Setiawan et al. (2019) and Sugita et al. (2000).

Lime and caustic precipitation methods aim to induce silica precipitation by increasing the pH of the solution, promoting the formation of calcium-silicate-hydrate phases (Iler 1975, Maraghechi et al. 2016, Rothbaum and Anderton 1975). At pH levels above 10, the dominant silicic acid species is the deprotonated anion $H_3SiO_4^-$ which forms especially with divalent cations insoluble precipitates. which forms insoluble precipitates with divalent cations. For example, with sufficient calcium present and a molar calcium-to-silicon ratio above 1.25, silica reacts preferentially with calcium at pH levels above 10, forming calcium-silicate-hydrate (CSH) phases (Section A.1). Adsorption of calcium cations replaces a hydrogen ion in the silicic acid molecule, resulting in a net positive charge (Section 2.4.5), which facilitates further adsorption of negatively charged silicic acid molecules. This leads to the formation

of Si-O-Ca-O-Si structures (Iler 1975, Maraghechi et al. 2016). The resulting structures coagulate rapidly, leading to precipitation due to reduced repulsive forces (Section A.1). The critical calcium concentration depends on the surface area of the particles, with smaller particles requiring more calcium due to their greater specific surface area. Still, this process is also pH-dependent: as pH increases, the relative importance of surface area decreases (Iler 1975).

The lime/caustic precipitation method has been successfully tested in geothermal power plants (Kato et al. 2003, Rothbaum and Anderton 1975, Sheikholeslami and Bright 2002, Ueda et al. 2003). It has been shown that allowing the fluids to age and induce polymerization improves the method's effectiveness (Ueda et al. 2003, Vitolo and Cialdella 1994). Spitzmüller et al. (2021) demonstrated with synthetic and real geothermal fluids that calcium chloride, calcium oxide, and caustic soda effectively remove silica from the fluids. Key factors include the molar Si-to-Ca ratio and achieving pH values above 10. Additionally, they showed that monovalent ions are minimally incorporated into the precipitates, while divalent and trivalent cations display selectivity toward them.

In summary, silica scaling is a challenge in geothermal power plant operations. Nevertheless, methods exist to either inhibit silica scaling or remove silica from the solution. Both techniques have advantages and disadvantages, and their use depends on power plant operation (e.g., whether raw material extraction is intended). Due to the amorphous nature of the scales, it is often sufficient to maintain a temperature that results in undersaturation with respect to amorphous silica, even though quartz may be oversaturated. As will be shown in Chapter 4, the degree of silica oversaturation depends on factors such as initial temperature, silica concentration, pH, and salinity.

By applying a silica-based nanotracer, the silica concentration in the system could be slightly increased, potentially leading to localized oversaturation of quartz. However, because the silica nanoparticles are amorphous, they are more likely to dissolve under geothermal conditions than to cause scaling. Interestingly, if the fluids are cooled and the risk of amorphous silica scaling is increased, the particles could act as seeding material, thus reducing the silica concentration in the fluids to the saturation level and finally lowering the risk of silica scaling.

3.2 Engineered silica nanoparticles

Although the unconscious application of nanoparticles dates back to the 4th century with the famous example of the Lycurgus cup that changes color depending of light reflection or transmission (Bayda et al. 2020), the awareness of nanoparticles and nanoscience emerged in the 20th century. Silica nanoparticles were put into focus by the development of a synthesis procedure by Stöber et al. (1968), yielding highly reproducible monodisperse silica nanoparticles with size ranges from 50 nm to 2 µm. In the 90s of the last century, two different

classes of mesoporous silica nanoparticles were invented: the MCM type and the SBA type. The MCM type originates from inventors at the Mobil Oil Cooperation and is characterized by a hexagonal, well-ordered pore structure (Beck et al. 1992, Kresge et al. 1992). The SBA type originates from research at the University of Santa Barbara (USA) and is characterized by its highly ordered mesoporous structure, which exhibits larger pore diameters compared to the MCM type (Zhao et al. 1998). The difference originates from the usage of surfactants as pore spacers in the MCM type and block copolymers in the SBA-type.

Silica nanoparticles, both solid and mesoporous, have in common the extremely high surface area, the possibility of variation in sizes and shapes and further the control of porosity. Further, the possibility of surface functionalization and the advantageous properties of these nanomaterials opened diverse and vast application fields ranging from biosciences over material sciences to geosciences (Jeelani et al. 2020).

3.2.1 Application fields

3.2.1.1 Silica nanoparticles in life sciences

Only few applications of silica nanoparticles in life sciences existed until the early 2000s when the research group of Prof. Vallet-Regí created the first linkage of nanotechnology and medical application (Vallet-Regí et al. 2001). By incorporating ibuprofen in biocompatible mesoporous silica nanoparticles, they invented the vast application field of targeted drug release (Barandeh et al. 2012, Liberman et al. 2014, Maggini et al. 2016, Tonelli et al. 2020). As a result, engineered silica nanoparticles established over the last decade as tunable nanocarriers for water-insoluble drugs and chemotherapeutics and as soluble drug encapsulation enabling long-term release applications (Bharti et al. 2015, Bouchoucha et al. 2016, Kwon et al. 2013, Liong et al. 2008, Wang et al. 2015). The favorable properties of silica nanoparticles are furthermore highlighted by the easily functionalizable surface of the nanoparticles for targeted or stimuli-responsive drug release thus enabling the concept of personalized nanomedicine, the theranostic (Baeza and Vallet-Regí 2020, Song et al. 2017, Yamada et al. 2012, Zhao et al. 2010). This ease of functionalization opens the field of nanobiophotonics, as fluorophores can be incorporated into the particle's structure or covalently bound on the surface (Korzeniowska et al. 2013, Sola et al. 2021, Wang et al. 2006). Additionally, the small size of the nanoparticles offers the unique opportunity of targeted drug release and bioimaging in formerly inaccessible areas like inside the brain, as nanoparticles can cross the blood-brain barrier (Andersson et al. 2004). Finally, due to their presumed high biocompatibility, silica nanoparticles are the most promising nanocarrier and nanobiophotonic material (Xu et al. 2017).

3.2.1.2 Silica nanoparticles in geosciences

Silica nanoparticles in geosciences can be categorized as naturally occurring and engineered silica nanoparticles. Examples of silica nanoparticles originating from natural sources could be biogenic or geogenic (Iler 1979), for example, by the formation of diatoms or through weathering from minerals. Mori et al. (2019) and Tobler and Benning (2013) found silica nanoparticles forming naturally in geothermal fluids and Yang et al. (2019) developed a method to distinguish natural silica nanoparticles from engineered ones by their isotopic signature. Watanabe et al. (2021a) raised concern about silica nanoparticles negatively affecting permeability in geothermal applications. However, recent studies suggest that silica nanoparticles and nanofluids in general, could enhance the heat transfer coefficient, thus improving geothermal power plant efficiency (Cui et al. 2024, Jahanbin et al. 2022, Soltani et al. 2022). Engineered silica nanofluids also find application in enhanced oil recovery to stabilize emulsions, decrease the interfacial tension, alter rock wettability, increase sweep efficiency and assist in re-mobilizing oil (Chakraborty and Panigrahi 2020, Lau et al. 2017, Mahmud et al. 2021, Muneer et al. 2020). Gazem et al. (2024) show that silica nanoparticles combined with an anionic and a non-ionic surfactant increase the oil recovery by 16%, while Li et al. (2020) point out the necessity of surface modifications of silica nanoparticles for long-term dispersion stability.

Another promising approach to combining nanotechnology and geoscience is the development of silica-based nanoparticle tracers. Starting with Paunescu et al. (2013), who labeled silica nanoparticles with DNA, interest in the possibility of silica nanoparticle tracers for hydrogeology and geothermal exploration sparked (Foppen 2023). Most recently, Fan et al. (2024) reported the development and successful testing of DNA-labeled porous silica nanoparticles in a strongly acidic geothermal reservoir of pH 2. In the following, research of four different research groups on the development of silica-based nanoparticle tracers is presented.

ETH Zürich: At the Eidgenössische Technische Hochschule Zürich (ETH Zürich), the group of Prof. Saar investigated the applicability of DNA-labeled silica nanoparticles as hydrogeological tracers. Using the approach of Paunescu et al. (2013) (also from ETH), they showed the first-ever field tests in a shallow aquifer (Kong et al. 2018, Mikutis et al. 2018). The distance between the injection and production well was less than 3 m (Kong et al. 2018). They experienced faster and sharper breakthrough curves for the particle tracers compared to the conventional molecular tracer dyes uranine and sulforhodamine B (Mikutis et al. 2018). Kittilä et al. (2019) performed the first field flow test in fractured crystalline rock at the Grimsel underground laboratory test site (Switzerland). They showed that although the DNA-labeled silica nanotracers traveled faster compared to molecular dyes, their recovery was lower due to heterogeneities in the flow field, gravitational settling and size exclusion effects. Nevertheless, the possibility of unlimited different DNA signatures and their absence

in natural fluids bears an outstanding chance for the applicability of these types of tracers (Kittilä et al. 2019).

Stanford University: At Stanford University, the group of Prof. Horne investigated the applicability of DNA-labeled silica nanoparticles as temperature nanotracers. Their approach comprised DNA degradation induced by high temperatures to estimate the subsurface reservoir temperatures (Alaskar et al. 2015a). Further, they showed while DNA-labeled silica nanoparticles are transported successfully through sand-filled columns and fractures, the thermal stability of the particles was poor (Alaskar et al. 2015b, Zhang et al. 2016). Additionally, Alaskar et al. (2015b) elucidated the (micro)particle transport processes through fractured rocks and encountered the main retention mechanisms to be gravitational settlement, aggregation and straining. Thus, they suggested designing silica particles with lower densities or application only in high-flow regimes.

Delft: Researchers at Delft University investigated the applicability of DNA-labeled silica nanoparticles having a magnetic core as groundwater tracers (Chakraborty et al. 2023). By conducting batch column flow-through experiments to elucidate nanoparticle transport properties and retention mechanisms, they found the transport properties of these nanoparticle tracers to be affected by the salinity and valence of the ions. Especially the presence of divalent ions strongly reduces the recovery (Kianfar et al. 2023) as can be expected by the Schulze-Hardy rule. Further, they investigated the role of parameters, such as fluid chemistry, flow velocity and occurrence of natural organic matter on the dispersion stability and applicability of DNA-labeled paramagnetic silica nanoparticles (Abdelrady et al. 2024, Kianfar et al. 2022, Tang et al. 2023). Their conclusions were mixed. On the one hand, these types of tracers possess great opportunities as they are uniquely identifiable tracers augmenting the toolbox of available tracers in geosciences. On the other hand, certain limitations and challenges need to be addressed and overcome, such as poor transportability in low-flow regimes (Kianfar et al. 2022). However, they point out the possibility of surface modifications and, thus, the possibility of influencing the transport processes and retention mechanisms (Abdelrady et al. 2024).

KIT: From a synergy of the nanotechnology/applied physics and geothermal research divisions at Karlsruhe Institute of Technology under the leads of Prof. Kohl and Prof. Schimmel, fluorescently labeled temperature-responsive silica nanoparticles for geothermal exploration were developed and the function principle patented (Rudolph et al. 2020, Schimmel et al. 2022). The concept is different from the other techniques presented here as it does not rely on the degradation of DNA but rather on a dual-emission system in a three-layered core-shell-hull architecture. The first dye, embedded in the core, serves as a reference function, while the second dye encapsulated in a mesoporous shell and a thermo-responsive hull serve as the reporting function. This system is based on the functionality of the hull to be activated by exceeding a certain threshold temperature, thus releasing the encapsulated dye from the mesoporous hull and shifting the reporting-to-reference signal (Rudolph et al.

2020). Berson et al. (2024) showed the applicability of these tracer types in a flow-through system with quartz sand and Yan et al. (2024) forecasted the expected breakthrough curves and signals in geothermal applications by numerical modeling. As will be shown in this thesis, Spitzmüller et al. (2023b), Spitzmüller et al. (2024a) and Spitzmüller et al. (2024b) addressed the challenge of silica nanoparticle stability and integrity and propose a stable encapsulation mechanism that prevents dye leakage from a mesoporous silica nanocarrier while maintaining the nanoparticle integrity. Further, they show the opportunity for surface modifications and their impact on transport properties.

3.2.2 Synthesis routes

Generally, there are two methods for synthesizing silica nanoparticles: top-down and bottom-up (Bayda et al. 2020). Top-down methods describe methods where bigger particles are converted to nanosize by milling/crushing or also flame spray pyrolysis (Mueller et al. 2003). Synthesis results in irregularly shaped and rough particles that are mostly polydisperse. Bottom-up methods are chemical synthesis, where precursors are used to selectively grow nanoparticles to desired sizes. The advantages of this approach are selectivity, size control, sphericity and monodispersity. Additionally, the shape can be easily controlled. Most synthesis methods involve a precursor, a catalyst, and a reaction medium. For bottom-up silica synthesis, there are mainly two routes: the Stöber method and the microemulsion methods.

3.2.2.1 Stöber method

A sol-gel type synthesis of spherical, highly monodisperse silica nanoparticles was first proposed by Stöber et al. (1968). The method includes an alcoholic solvent, water, a catalyst (base or acid) and a silica precursor/alkoxide (most commonly tetraethyl orthosilicate TEOS/tetramethyl orthosilicate TMOS). The first step is the hydrolysis of the ethoxy/methoxy groups of the silica precursor. This process is catalyzed in acidic or basic environments (Harris et al. 1992). Hydrolysis converts the silica precursor to monomeric silicic acid (see also Chapter 3 and Equation 3.11). The second step of the synthesis process is condensation (Equation 3.12), in which monomeric silica transforms into solid silica nanoparticles. The fundamental processes of polymerization and colloid formation are described in Section 3.1.4.

The hydrolysis and condensation processes were described by van Blaaderen et al. (1992):

$$Si(OC_2H_5)_4 + 4H_2O \xrightarrow[alcohol]{base} Si(OH)_4 + 4C_2H_5OH \qquad \text{Hydrolysis} \qquad (3.11)$$

$$Si(OH)_4 \xrightarrow[alcohol]{base} SiO_2 + 2H_2O \qquad \text{Condensation} \qquad (3.12)$$

with alcohol being monohydric alcohols such as methanol, ethanol, propanol or butanol and base being sodium or ammonium hydroxide. During the synthesis, the choice of alcohol does not significantly affect the nanoparticles' shape and uniformity but can impact their size (Harris et al. 1992). Lower molecular weight alcohols result in smaller particles.

It is worth noting that, despite its widespread application, the exact mechanisms behind nucleation during this synthesis are not fully understood. Two main explanation approaches exist: the critical supersaturation approach and the continuous nucleation approach (Bogush and Zukoski 1991, LaMer and Dinegar 1950). According to the critical supersaturation approach, the formation of colloids only occurs when the solution is supersaturated with silica monomers (LaMer and Dinegar 1950). As explained in Section 3.1.4, homogeneous nucleation of monomeric silicic acid is catalyzed by either OH^- or H^+ ions and consists of condensation reactions (Equation 3.12). The critical supersaturation approach implies that nucleation is stopped as soon as the monomeric silicic acid concentration is below the saturation concentration. Hence, the formation of new particles is prevented and only the already existing particles can grow/coagulate further. This would mean there is a limited amount of particles that can be formed. In the continuous nucleation approach, on the other hand, it is assumed that nucleation can take place continuously and growth of particles is governed by the aggregation of multiple nuclei (Bogush and Zukoski 1991).

3.2.2.2 (Reversed) Microemulsion

The synthesis route via a (reversed) microemulsion system is a variant of the classical Stöber process with the main advantage of having a controlled growth leading to highly monodisperse silica nanoparticles (Figure 3.6). A microemulsion describes micro-droplets of an apolar phase in a polar phase or vice versa. A typical example of such a system is milk with milk fat as apolar (oily) phase and water. In a reversed microemulsion, the microdroplets are water in an oily phase. The synthesis of silica nanoparticles is performed within these water droplets (Figure 3.5). This confined space thus leads to a size-controllable growth of monodisperse nanoparticles. For stabilization of the microdroplets, surfactants and co-surfactants are used (Figure 3.5). A typical method uses cyclohexane as apolar/oily phase and hexanol and triton X-100 as co-surfactants. Similar to the Stöber process, a silica-precursor and a catalyst are needed. The silica precursors TEOS/TMOS concentrate in the water droplets due to the polar nature of the molecules. Due to hydrolysis, the precursor is transformed into monomeric silica, which reacts in a homogeneous nucleation process to form silica colloids (Section

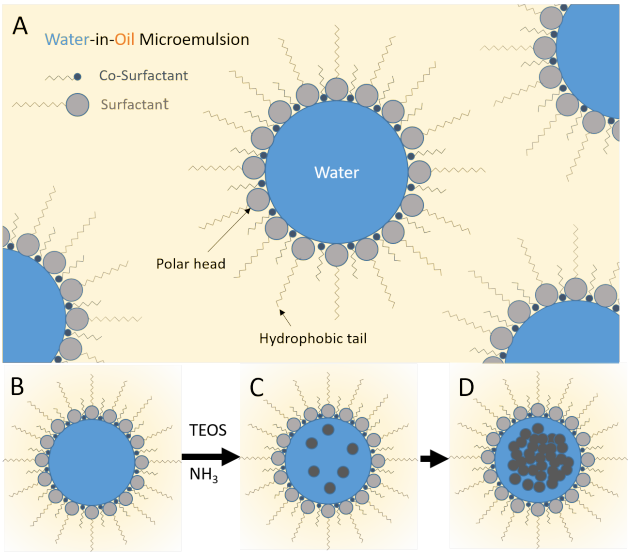

Figure 3.5: Schematic representation of water-in-oil microemulsion method. In A the formation of a microdroplet is shown: Co-surfactant and surfactants assemble to form water-droplets in oil. In B-D nucleation and growth of silica nanoparticles within microdroplets is shown.

3.1.4). As described before, the condensation process can be catalyzed in acidic or alkaline environments. Usually, ammonia is used as a catalyst and the synthesis is performed in an alkaline environment. The size of the microdroplets can be modified and is a complex function of the ratio of surfactant-water-catalyst (Chang and Fogler 1996).

The main advantage of this method is the high monodispersity of the silica colloids. Drawbacks are the limited size range, which is restricted by the confined space of the micro-droplets and the relatively low synthesis yield.

3.2.2.3 Modified Stöber synthesis - Mesoporous silica nanoparticles

Multiple pathways exist to produce mesoporous silica nanoparticles (Wu et al. 2013). The most common is using a modified Stöber synthesis to produce mesoporous silica nanoparticles by adding a template as a "placeholder" for the pores. Usually, CTAB is used as a template that self-assembles to liquid crystal meso-phases as soon as the critical micellar concentration is exceeded (Kresge et al. 1992). These hexagonal ordered structures are overgrown by silica (Beck et al. 1992). Finally, the template can be removed by either acid-catalyzed hydrothermal removal or calcination (heat treatment to remove organic compounds) (Wu et al. 2013). In the acid-catalyzed hydrothermal removal method, the template is removed under reflux in methanol. Calcination means that the organic template is burned at high temperatures (above 500 °C), leaving free space in the silica colloid, leading to a mesoporous structure and restructuring the silanol (Si-OH) to siloxane bonds (Si-O-Si). Both methods can produce mesoporous nanoparticles with highly ordered pore networks and pore sizes

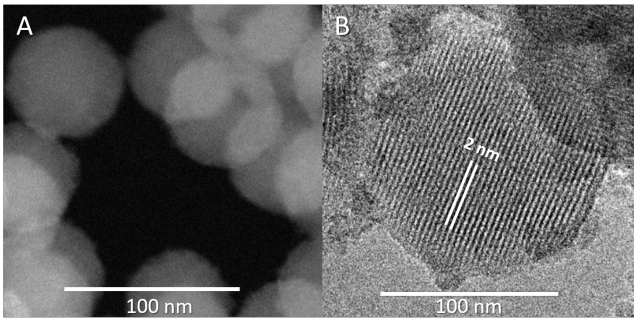

Figure 3.6: (S)TEM imaging of solid silica nanoparticles (A) and mesoporous silica nanoparticles (B) with pore size of approx. 2 nm. Solid silica nanoparticles were synthesized using a reversed microemulsion synthesis leading to highly monodisperse particles with sizes of approx. 45 nm. Mesoporous silica nanoparticles were synthesized with CTAB as template and show a hexagonal shape with highly ordered pore size distribution.

typically ranging from 2 to 4 nm (Figure 3.6B). Mesoporous nanoparticles offer the possibility of loading the pores and using them as carriers for different materials.

3.2.2.4 Fluorescent labeling of silica nanoparticles

To improve the detectability of silica nanoparticles, they can be labeled by fluorescent dyes. There are four different cases to distinguish (Figure 3.7):

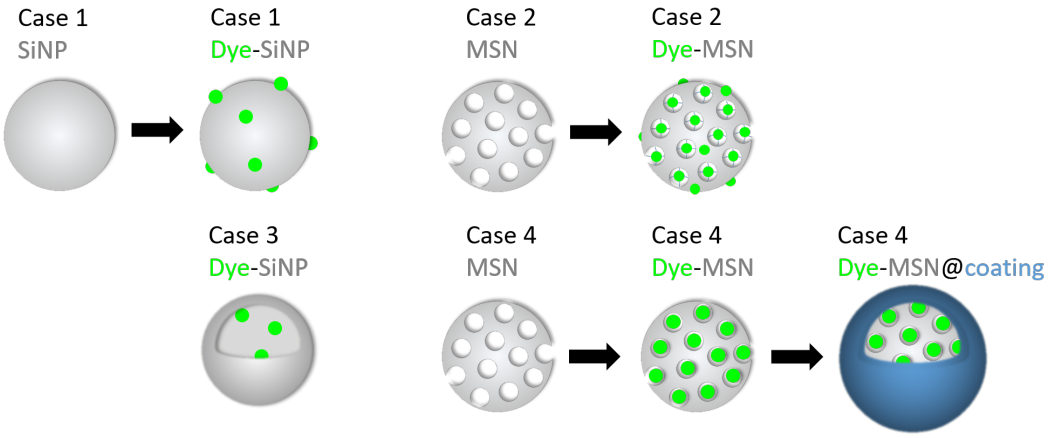

Figure 3.7: Fluorescent labeling of solid and mesoporous silica nanoparticles. Case 1 Solid particle + chemical bonding. Case 2: Mesoporous particle + chemical bonding. Case 3: Solid particle + physical entrapment. Case 4: Mesoporous silica nanoparticle + physical entrapment.

Case 1: Solid particle - (Surface) chemical bonding Fluorescent dye molecules are covalently bound to the surface of solid silica nanoparticles. This method is frequently used, but it limits the modifiability of the nanoparticle surface and exposes the dye molecules to

the surroundings. Consequently, also the surface properties like charges result from dye properties and are not controllable.

Case 2: Mesoporous particle - Chemical bonding The chemical bonding of dye molecules on or inside mesoporous silica nanoparticles is similar to that on solid particles, but it may still allow for surface modifications.

Case 3: Solid particle - Physical entrapment Fluorescent dyes are physically trapped within solid silica nanoparticles during the synthesis (Auger et al. 2011, Bagwe et al. 2004). Yet, this method has limitations, such as a restricted number of dyes that can be incorporated and potential leaching and instability of the silica structure due to defect sites in the silica network as a result of dye molecules hindering the silica condensation. This approach is followed to synthesize the silica nanoparticles studied in Section 3.3 and Chapter 4.

Case 4: Mesoporous particle - Physical entrapment For mesoporous particles, the physical entrapment of fluorescent dyes requires dye loading and a stable pore-blocking strategies. The advantage is that the silica nanoparticle can be pre-treated at elevated temperatures before loading the dye to have a denser siloxane network to enhance their stability and be less soluble in water. Due to the modularity of the pore sizes, various fluorescent dyes could be employed.

This approach is pursued in biomedical sciences. The need for a pore-blocking agent also enables stimuli-responsive reactions and the release of the entrapped molecules for targeted delivery. For the application in geo-environments, a stable and robust coating is needed that ideally also prevents the dissolution of the silica nanoparticle carrier. A synthetic approach for such a stable coating is presented in Chapter 5 and tested in Chapter 6.

In Figure 3.8, high-angle annular dark-field images (HAADF) and elemental mapping performed with a STEM are shown. In the upper row, synthesis was performed according to case 3 (Figure 3.7) with physical/structural entrapment of dye inside a solid silica nanoparticle. The presence of the dye is indicated by nitrogen accumulation (FITC, $C_{21}H_{11}NO_5S$). In the lower row, synthesis was performed following case 4 (Figure 3.7) with physical entrapment of the dye inside a mesoporous silica nanoparticle. In this case, the presence of the dye is indicated by sodium accumulation (Sulforhodamine G, $C_{25}H_{25}N_2NaO_7S_2$).

3.2.3 Modification of surface properties

Unlike molecules, nanoparticles offer the opportunity for surface modifications. Surface modifications describe the process of either chemically binding or physically adsorbing molecules to the surface of the particles. The molecules could be passive or functional, i.e.,

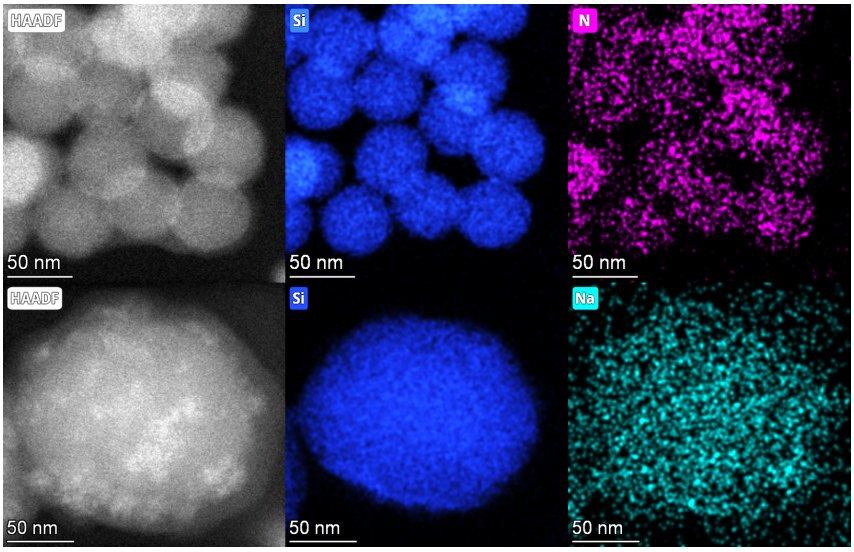

Figure 3.8: High-angle annular dark-field imaging (HAADF) and elemental mapping of silica nanoparticle with physically trapped dye (depicted by the presence of nitrogen, upper row, corresponding to case 3 in Figure 3.7) and mesoporous silica nanoparticle with physically trapped dye within the pores (depicted by the presence of sodium, lower row, corresponding to case 4 in Figure 3.7).

reacting to external stimuli such as temperature, pH or magnetic fields. For example, having a metal oxide coating is a passive surface modification, whereas temperature-responsive paraffin coating is a functional surface modification.

The surface properties of silica nanoparticles play an important role when determining the interactions of the particles with the surrounding environment. By modifying the surface, the ζ-potential and, hence, DLVO interactions are affected. Therefore, the advantage is that it is possible to control the particle-surface interactions and improve the performance of silica nanoparticle tracers by surface modifications. There are two main methods on how to employ surface modification/coating: Either by physisorption or by chemisorption.

3.2.3.1 Physisorption

Physisorption describes an adsorption process where surfactants/ligands are attracted to the surface of silica nanoparticles by relatively weak London-van der Waals interactions. Contrarily to chemisorption, the adsorption is easily reversible as no new chemical/covalent bonds are formed during this process. Physisorption is a weak attraction of oppositely charged surfactants/ligands to a (charged) surface with activation energies of about 4-10 kJ/mol (Ismail et al. 2020). For example, non-ionic, cationic or anionic surfactants can modify the surface properties. Cationic surfactants such as CTAB could be used to alter silica nanoparticle surfaces, as shown by Ma et al. (2010). They found that CTAB-physisorption results in the neutralization of ζ-potential, which in turn affects the particle-surface interactions (Section

2.4.6). An example of an anionic surfactant is SDS (Qiao et al. 2016). Due to its anionic structure, it effectively lowers the ζ-potential of the nanoparticles (Chapter 6). Triton X-100 is an example of a non-ionic surfactant (Yusuf et al. 2013) and sulfobetaine SB3-14 is an example of a zwitterionic surfactant (Chapter 6).

In summary, physisorption is an easy-to-employ and fast process that can impact the ζ-potential of silica nanoparticles, affecting their interaction with the surroundings. Indeed, they are used to increase the stability of the colloidal suspensions (Loosli and Stoll 2017). There is no need for complex chemical modification steps, which is an advantage compared to chemisorption processes. However, surfactants attached through physisorption processes are not stable and possibly not able to withstand harsher conditions such as geothermal environments.

3.2.3.2 Chemisorption

Chemisorption describes a type of adsorption where chemical bonds are formed and the surface modification is less likely to be reversible compared to physisorption processes. New chemical bonds are formed between the surfactant/ligand/polymer and the nanoparticles that could be covalent, ionic or metallic bonds. As the bond-dissociation energy and the activation energy are elevated (for example, approx. 60 kJ/mol, Li and Yuan (2014)), this means that compared to physisorption, chemisorbed surface modifications are more stable.

Chemisorption results mostly in (self-assembled) monolayers and requires compatible surface and surfactants that can react with each other. Therefore, the first step is the modification/preparation of the silica nanoparticle surface. This could be done during synthesis or post-synthesis (von Baeckmann et al. 2018). Usually, a linking agent is bound to the surface that can react with the selected surfactant. The most common linking agents are shown in Table 3.1. Possible coupling connections are amine-NHS, amine-epoxy, amine-isocyanate, thiol-carboxylate and thiol-maleimide. Silanol (Si-OH) groups on the surface can also serve as linking points for silanes such as octadecyltrimethoxysilane (C18, Chapter 4). Employing surface modifications can improve the biocompatibility of silica nanoparticles (Farooq et al. 2018) but also can impact the particle-surface interactions due to the influence on the ζ-potential and Hamaker constant (Section 2.4.6.1 and Chapter 7).

Chemisorption can alter the surface properties of the nanoparticles. For example, in Chapter 6, a surface modification is conducted to render the hydrophilic character of the nanoparticles to be hydrophobic by coating with a hydrophobic silane. Contrarily, hydrophilicity can also be increased upon coating with hydrophilic polymers such as polyethylene glycol (PEG, Chapter 5).

In summary, surface modification based on chemisorption is a powerful tool that can significantly impact the interactions of particles with the environment and could be beneficial

for developing silica nanoparticle tracers. It should be noted that surface modification is a tool that does not apply to molecular tracers such as uranine and is a significant advantage of nanoparticle tracers (Chapter 6).

Table 3.1: Linking agents for silica nanoparticle surface modifications.

Name	Functional group	Reference
Epoxy	C-O-C	von Baeckmann et al. (2021)
Isocyanate	-CHN	Lin and Zhou (2017)
Primary Amine	$-NH_2$	Bagwe et al. (2006), Mahtabani et al. (2020)
Silanol	-OH	Park et al. (2010)
Thiol	-SH	von Baeckmann et al. (2018)

3.2.3.3 Functionalization

Surface modifications of silica nanoparticles can be functional, i.e., they react/respond to specific external stimuli/triggers such as temperature, pH and UV irradiation (Table 3.2). Surface functionalization is beneficial in (bio)medical applications where targeted release is desired (Thi et al. 2019).

Table 3.2: Overview of selected triggerable surface functionalizations and examples of materials.

Functionalization	Example material	Reference
Temperature-responsive	Polymers, paraffin	Rudolph et al. (2020), Thi et al. (2019)
pH-responsive	Carboxylic acid	Thi et al. (2019), Zhao et al. (2010)
Light-responsive	Nitrobenzyl, thymine	Agasti et al. (2009), Thi et al. (2019)
Magnetic-responsive	Ferric oxide nanoparticles	Baeza et al. (2012)
Redox-responsive	Disulfide bonds (glutathione)	Thi et al. (2019)

Temperature-responsive functionalization reacts when a specific temperature threshold is exceeded. For example, Rudolph et al. (2020) synthesized temperature-responsive silica nanoparticles with a three-layer architecture consisting of a dense silica core, a mesoporous silica shell and a paraffin hull as triggerable moiety with threshold temperatures in the range of 50-90°C (see also Section 3.3). They showed that upon surpassing the threshold temperature, the encapsulated payload is released from the mesoporous silica shell. Below the threshold temperature, the paraffin acts as a pore-blocking agent and prevents premature leakage.

Besides paraffin, polymers can also be employed as temperature-responsive surface functionalization. The most common type of polymer is poly(N-isopropyl acrylamide) (PNIPAM) (Thi et al. 2019). For example, You et al. (2008) used PNIPAM to synthesize a polymer-nanoparticle composite that released the payload when temperatures fall below 32-34 °C, i.e., above that temperature, the polymer acts as a stable pore blocker, whereas below, the encapsulated payload is released. The process is reversible, i.e., upon increasing the temperature, the polymers can close the pores again.

Light-responsive functionalization reacts upon irradiation, mostly UV light (Thi et al. 2019). The light response emanates from the photosensitive nature of the used material, such as nitrobenzyl, thymine or certain derivatives of coumarine. Exposure to UV light leads to photodegradation and breaking of the bonds, resulting in a release of the encapsulated payload Park et al. (2009). This process is irreversible.

pH-responsive surface functionalization can be acquired by using carboxylic acid (Thi et al. 2019). Using pH as a trigger is especially beneficial in biomedical sciences, such as targeted drug release due to slightly more acidic pH levels in the vicinity of tumors (Murugadoss et al. 2017). For geoscientific applications, pH-triggerable nanoparticles could be a promising approach, for example, for targeted inhibition of scaling formation (see also A.1).

Other surface functionalization could be triggerable by, for example, magnetic fields, ultrasound, enzymatic activity, redox-potential and reactive oxygen species (ROS) (Thi et al. 2019). Additionally, combinations of different triggers are possible (e.g., temperature and pH).

3.3 Nanoparticle-based tracing techniques in geothermal reservoirs: Advances, challenges and prospects

This Section is published in *Proceedings 48th Workshop on Geothermal Reservoir Engineering, Stanford University* (2023) under the number SGP-TR-224. `https://pangea.stanford.edu/ERE/pdf/IGAstandard/SGW/2023/Spitzmueller.pdf`

Laura Spitzmüller, Fabian Nitschke, Annika Maercks, Jonathan Berson, Bastian Rudolph, Thomas Schimmel, Thomas Kohl (2023): Nanoparticle-based tracing techniques in geothermal reservoirs: Advances, challenges and prospects. *Proceedings 48th Workshop on Geothermal Reservoir Engineering*.

Abstract

Accurate knowledge of reservoir geometry and flow paths are critical parameters for successful geothermal operations. They are essential for evaluating the long-term behavior and sustainability of geothermal reservoirs. Conventional hydraulic testing and tracer tests are often inconclusive or provide limited information due to complex and challenging reservoir conditions (multiple well systems, complex reservoir geometry, and fracture network, etc.). Recently, a new class of tracer techniques has emerged in order to overcome the major drawbacks of molecular tracers: nanoparticle-based tracers. The main advantages of nanoparticle tracers compared to molecular tracers are their tunable properties and modular structure. Functional and smart nanoparticle tracers such as the threshold-triggered temperature nanotracer enabled the simultaneous evaluation of multiple reservoir conditions (flow paths, temperature distribution, etc.) and created an entirely new field of research. As new areas of research often require detailed insights into fundamental processes, there are still open questions about the interactions between particles, fluids, and rock minerals and their performance in complex geothermal environments. As an example, the application of embedded or surface-bound tracing features (e.g., fluorescent molecules, DNA, etc.) within or on a silica matrix prevents the tracing function from being affected by the environment (e.g., pH changes, salinity effects, redox sensitivity). Although silica has low hydro(thermal) stability and loses its protective function at high temperatures or long-term applications, nanoscience offers a comprehensive set of tools to design and protect the silica matrix. Another advantage is the possibility of surface modifications, which can help to achieve minimum sorption and retention by adapting the ζ-potential of the nanoparticles. In this study, we address recent advances in increasing long-term stability, improving hydrothermal stability of silica nanoparticles, sorption control. Furthermore, we present strategies for the development and functionalization of nanoparticle-based tracers.

3.3.1 Introduction

Successful development and operation of geothermal power plants require detailed characterization of subsurface reservoir properties, such as its geometry and flow paths. Their exploration is conducted so far with well-established tracer techniques that usually rely on molecular dyes such as uranine or eosin. However, molecular dyes can be greatly affected by the fluids pH, temperature and the rock properties of the underground (Maier et al. 2015). This can lead to thermal degradation and mineral surface adsorption and in extreme cases to complete retention of molecular tracers and impedes effective multi-well tests using multiple tracers as each molecule possesses different sorption characteristics. Thus, there is the requirement for new approaches to overcome the drawbacks of the molecular dyes and utilize the additional functionalities a particle-based approach would provide. Unlike molecules, nanoparticles facilitate the design of a much more complex and reactive system.

Particularly silica nanoparticles have proved to combine many favorable properties. They are comparatively easy to synthesize in a wide range of sizes. They can be built up modularly, while the particles properties and functionalities are tunable. The control of porosity enables the control of surface area. Basic research has been conducted on the application of silica nanoparticles as tracers in hydrology for aquifer and reservoir assessment (Vitorge et al. 2014). Further developments led to advanced temperature-sensitive silica nanoparticles as tracers in controlled environments for geothermal reservoir characterization (Puddu et al. 2016, Rudolph et al. 2020). Indeed, nanoparticle-based approaches to geothermal applications have so far been limited in the scope of their application. For example, DNA-embedded silica nanoparticle tracers could only be successfully employed at test sites with low temperature groundwater and distances of only a few meters between the injection and the extraction points (Kittilä et al. 2019, Kong et al. 2018, Mikutis et al. 2018). While some studies aim at temperature detection functionality (Puddu et al. 2016), other experiments at elevated temperatures contradict the viability of the application, where a simple experimental setup with Milli-Q water, quartz sand and temperatures of 150 °C resulted in high sorption rates and degradation of the nanoparticles (Zhang et al. 2016). The shortcomings in laboratory studies and application failures of the technology are always attributed to the lack of understanding of the fundamental geochemical interaction processes at the interfaces of the particle to the fluid and the reservoir rock mineral.

Within this study, we first present a new type of silica nanoparticle tracer that enables simultaneous flow path and temperature detection. The proof of concept is given by laboratory-scale flow through experiments where the nanoparticle tracer proofed to be as effective as uranine and shows better transportation properties than eosin. We also address the problem of silica (in)stability in aqueous environments and examine the impact on our particle system and evaluate sorption processes. We further provide stabilization and sorption control methods and proof their applicability and effectivity.

3.3.2 Nanoparticle tracers

The nanoparticle tracers are built in a 3-layer architecture to enable simultaneous flow path detection and temperature sensing. The fluorescent core (Fig. 3.9a) is designed to remain stable throughout the tracer test procedure and serves as a reference function to detect tracer retrieval. The second layer, a mesoporous shell doped with a second fluorophore, serves as the (temperature) reporting unit (Fig. 3.9c), while the third layer, the shell, is responsible for the temperature-triggered activation of the nanotracers (Fig. 3.9d). The nanotracer structuring process described here is modular, i.e., the sizes, materials, dyes, and temperature-dependent shell can be changed.

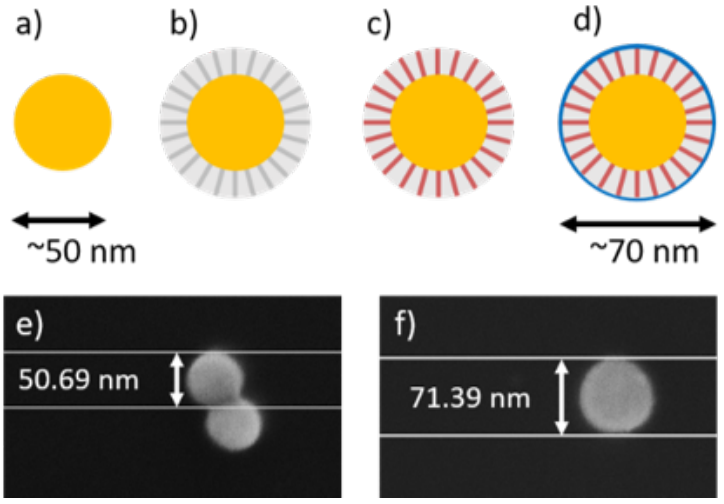

Figure 3.9: Schematic structure of the nanoparticle tracer synthesis (a-d) and respective SEM-images (e-f) of state a) and d). At first, the core incorporating a fluorophore is synthesized (a). Then, a mesoporous shell is grown on the core using CTAB micelles as template (b). Further, the micelles are removed and the pores are filled with a second fluorophore (c). To enable a temperature-triggered release of the second dye, the pores are sealed with a temperature-sensitive pore blocker (d). e) and f) show the size comparison of the core (e) and the functionalized nanotracer (f).

3.3.2.1 Synthesis

To synthesize the core, a reversed micro-emulsion synthesis with simultaneous incorporation of a fluorescent dye is performed (Fig. 3.9a). First, 15 mL cyclohexane (VWR Chemicals AnalaR Normapur), 3.44 mL n-hexanol (VWR GPR Rectapur, 98 %) and 3.44 mL Triton X-100 (Sigma Aldrich, analysis grade) are mixed and stirred until the solution is clear. Then, 0.96 mL of a 20 mM aqueous Tris(2,2-bipyridyl)dichlororuthenium(II) hexahydrate ($Ru(bpy)_3^{2+}$, Acros organics, 98 %) solution and 0.2 mL tetraethyl orthosilicate (TEOS, Sigma Aldrich, 99 %) are added to the mixture. After 20 minutes of stirring, 0.12 mL ammonium hydroxide solution (Merck, 28-30 %) is added. The solution is further stirred for 24 hours before adding 28 mL acetone (VWR Chemicals, 99.8 %) to break the micro-emulsion. The nanoparticles are collected by centrifugation (5 minutes at 16k·g) and subsequently washed with acetone, twice with ethanol (VWR Chemical, 99.9 %) and deionized water. In a second step, the mesoporous shell is formed in a sol-gel process with silica-precursor TEOS and CTAB-micelles as template (Fig. 3.9b, grey shell with dark grey radial pores). First, an aqueous 0.2 M cetyltrimethylammonium bromide (CTAB, Merck, 97 %) solution is prepared and kept for 24 hours under constant stirring. The core-nanoparticles (Fig. 3.9a) are dispersed using a sonotrode (Hielscher Ultrasond) in 6 mL Millipore water and added to 60 mL of the CTAB-solution under constant stirring for 30 minutes. The particles are then collected by centrifugation and re-dispersed in 60 mL Millipore water using a sonication bath and a vortex. 0.6 mL of an aqueous 0.1 M sodium hydroxide (NaOH, Sigma Aldrich) solution is added to the mixture. To grow the silica shell (light grey shell in Fig. 3.9b), 3 times

180 µL of 20 % v/v TEOS in methanol (VWR Chemicals, 99.9 %) are added dropwise over 30 minutes, i.e. 180 µL every 10 minutes). After 48 hours stirring the nanoparticles are re-collected by centrifugation (10 minutes 16k·g), followed by three washing-centrifugation cycles, two using water and the last with methanol. The particles now have a fluorescent core and a mesoporous shell, which is depicted in Fig. 3.9b. To remove the CTAB micelles from the pores and subsequently fill them with a second fluorophore (Fig. 3.9c), the particles are in a next step re-suspended in methanol. The extraction of the CTAB micelles is performed under reflux at 70 °C. At first, the particles are added to a mixture of 120 mL methanol, 2.48 mL H_2O and 1.24 mL hydrochloric acid (HCl, Fluka, 36.5-38 %) and heated to 70 °C under constant stirring. The mixture is refluxed for 24 hours. The particles are then re-collected by centrifugation and washed two times with methanol and one time with ethanol. In a next step, the particles are dried under vacuum and weighed. 2.9 mg Safranin O (Acros organics, 95 %) is added per 10 mg of nanoparticles. The particles and the dye are then stored under nitrogen atmosphere for at least 2 hours. Then, 0.5 mL dry acetonitrile (Merck, 99.5 %) is added per 10 mg of nanoparticles. The solution is stirred under nitrogen atmosphere for 16 hours. The stirring of dye and particles in dry acetonitrile enables the adsorption of the dye molecules inside the pores of the nanoparticles (Fig. 3.9c). Finally, the solution is taken out from the nitrogen atmosphere and exhibited to the ambient atmosphere. 75 µL n-Octadecyltrimethoxysilane (abcr GmbH, 95 %) is added per 10 mg of nanoparticles to enable the adsorption of the protective hull. The solution is stirred for 16 hours, the particles are then collected by centrifugation and washed with acetonitrile and hexane (VWR Chemicals, 99 %), followed by vacuum drying. The dried particles are re-suspended in 40 mL hexane and 75 mg of the desired paraffin is added as temperature-responsive hull. E.g., tetracosane (Sigma Aldrich, 99 %, T_t 50 °C), dotriacontane (Sigma Aldrich, 97 %, T_t 70 °C) and tetratetracontane (Sigma Aldrich, 99 %, T_t 90 °C) were used successfully as capping agents. The mixture of nanoparticles in hexane with added paraffin is sonicated for 15 minutes and stirred for 15 minutes, followed by collecting the particles via centrifugation and dried in vacuum. The paraffin-coated nanoparticles (Fig. 3.9d) are re-suspended in water with 10 mg mL^{-1} sodium dodecyl sulfate (SDS) and washed until the supernatant is clear. The temperature-responsive nanotracers are then ready for usage. SEM images of the different synthesis steps are depicted in Fig. 3.9e and Fig. 3.9f and show the initial core with a size of about 50 nm and the final nanoparticle tracer with a size of about 70 nm.

3.3.2.2 Function principle

The working principle of the temperature-triggered nanoparticle tracers is shown in Fig. 3.10a-c. The nanotracers were coated with paraffin during synthesis, which enables their threshold-triggered activation. Paraffins have a certain threshold temperatures (T_t) above which the paraffin begins to melt and, in our case, releases the pristine surfaces to the surrounding medium. Due to the irreversible loss of the protective function of the shell,

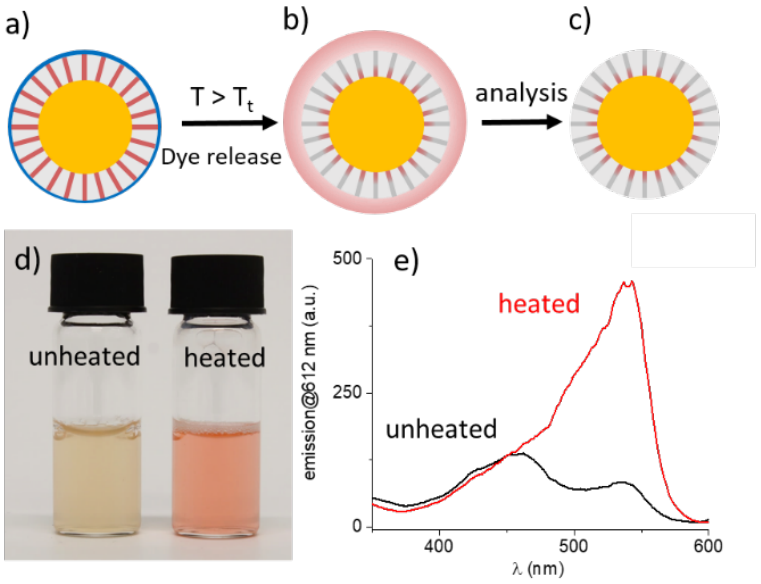

Figure 3.10: Function principle of the temperature-triggered nanoparticle tracers. A) to c) show the reaction of the nanoparticle tracers to elevated temperatures. At first, the particles are coated with a temperature triggered hull (a) which prevents the dye in the shell to leak. When the temperature threshold (T_t) of the hull is exceeded, the hull breaks and subsequently the dye in the shell is released (b). Thus, the reacted nanotracers (c) finally only contain the dye incorporated in the core. The difference between unheated, i.e. not reacted and heated, i.e. reacted nanoparticle tracers can be distinguished optically (d) and/or can be identified using fluorescence spectroscopy (e).

the dye safranin O is released from the mesoporous shell (Fig. 3.10b). Finally, the reacted particles contain only the $Ru(bpy)_3^{2+}$ dye, while the unreacted particles contain both the $Ru(bpy)_3^{2+}$ and safranin O dyes. The difference between the unheated, i.e., unreacted and the heated, i.e., reacted, particles can be observed optically (Fig. 3.10d) based on the color change and/or analytically with a fluorescence spectroscope (Fig. 3.10e). Since $Ru(bpy)_3^{2+}$ and safranin O both emit at the same wavelength (612 nm), they can be measured simultaneously, which facilitates the analysis of the state of the particles (reacted/unreacted).

3.3.2.3 Proof of concept

To demonstrate the applicability of the nanoparticle tracers, flow tests were carried out at ambient temperature with a 1 m long packed column (inner diameter 53 mm) with coarse quartz sand (1.0 - 1.6 mm diameter). The column is coated with epoxy and quartz sand to prevent the formation of channels along the wall surfaces. The outlets are sealed with sintered glass (mesh size 160 – 250 µm). To allow a continuous flow-through analysis cycle, the outlet of the column is connected via a tube to a flow-through quartz cuvette in a fluorescence spectrometer. A constant flow of 4 mL s^{-1} is maintained by placing a column filled with water 0.87 m (hydraulic gradient) above the inlet of the sand-filled column, which

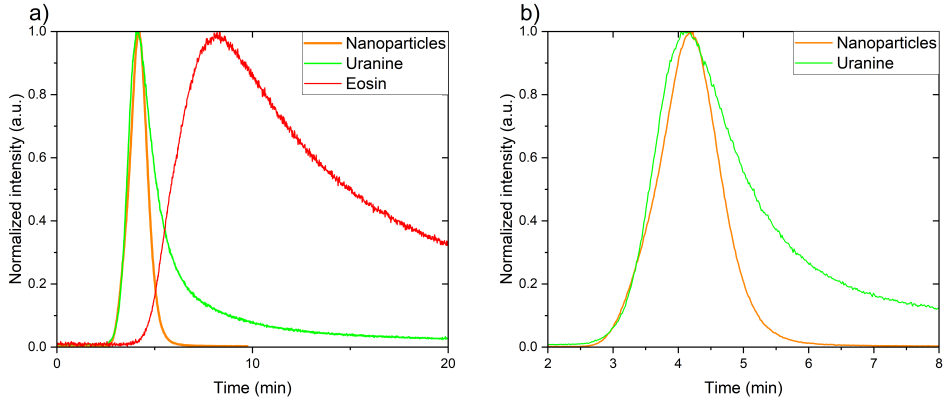

Figure 3.11: Breakthrough curves of tracers through a 1m packed column with coarse quartz sand. A) shows the normalized breakthrough curves of the nanoparticle tracers, uranine and eosin. In b) a magnification of the breakthrough curves of nanoparticles and uranine is shown.

Table 3.3: Results of the flow through experiments with different tracers. T_{min}, T_{max}, v_{max} and v_{max} are directly derived from the breakthrough curves, the retrieval rate is calculated using the input concentration, the cumulated output concentration and the flow rate.

Tracer	T_{min} (s)	T_{peak} (s)	v_{max} (10^{-3}m/s)	v_{peak} (10^{-3}m/s)	Retrieval rate (%)
Nanoparticles	171	264.6	5.8	3.8	78.5
Uranine	155.4	250.5	6.4	4.0	96.8
Eosin	250.2	494.4	4.0	2.0	8.2

is automatically refilled. The effective porosity of the sand-filled column can be estimated at 28 % (Stephens et al. 1998). The hydraulic conductivity (K) can be calculated using Darcy's law and is $2.08 \cdot 10^{-3}$ m/s, flow velocity (u) is $6.5 \cdot 10^{-3}$ m/s, permeability (k) is $2.13 \cdot^{-10}$ m^2, and the diffusion coefficient is $6.12 \cdot 10^{-12}$ m^2/s.

The tracers are injected with a syringe through a septum 16 cm upstream from the inlet of the sand-packed column. The performance of the nanoparticle tracers is compared with conventional molecular tracers, namely uranine and eosin. The breakthrough curves are shown in Figure 3.11a. All three tracers tested are retrieved and detected by fluorescence spectroscopy. However, they show significantly different behavior. While the nanoparticle tracer and uranine have almost the same T_{min}, eosin is significantly retarded. In addition, the T_{peak} of eosin is later than the T_{peak} of uranine and the nanoparticles, and the tailing of eosin is more pronounced (no baseline was reached within 60 minutes). Uranine and the nanoparticles behave almost ideally, with sharp peaks and low tailing. A magnification of the breakthrough curves between 2 and 8 minutes after injection of the tracers is shown in Figure 3.11b. It can be noted that although T_{min} of uranine is slightly smaller than T_{min} of the nanoparticles, the nanoparticles have a sharper breakthrough curve and lesser tailing.

This could be an indication of the lower diffusion of the nanoparticles, which experience size exclusion effects and tend to stay in the main streamlines. The retrieval rates are calculated using intensity-to-concentration calibration curves, flow velocity, and the input concentration. The retrieval of the nanoparticles is about ten times higher than the retrieval of eosin (Table 3.3), still not reaches the retrieval rate of uranine. These results indicate possible sorption phenomena or retention of the nanotracers and raises the question of the effect of particle-mineral surface interactions.

3.3.3 Application related challenges and advances

3.3.3.1 Hydrothermal (in)stability

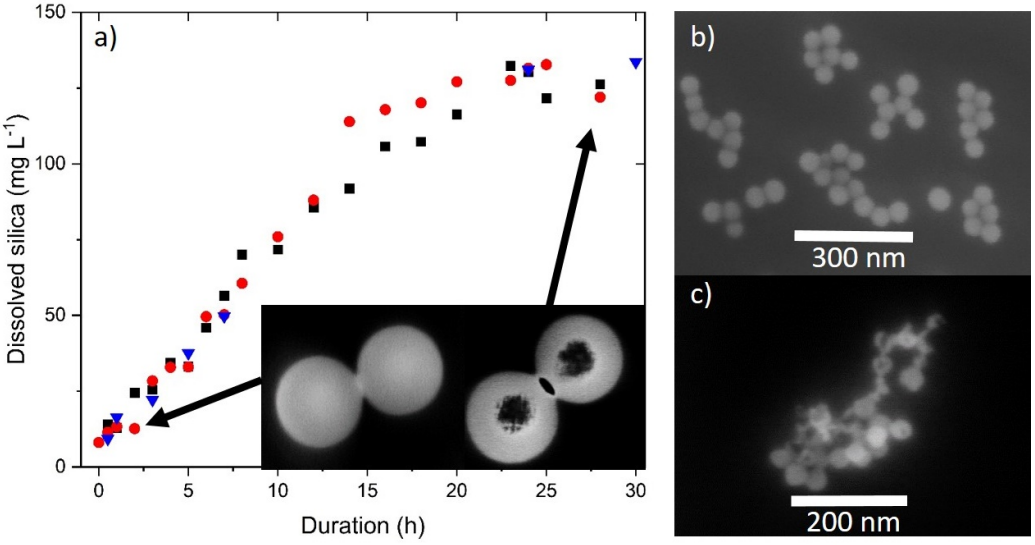

Figure 3.12: Dissolution of the silica nanoparticles in water over time at room temperature. A) On the y-axis the concentration of dissolved silica is shown. The saturation of (amorphous) silica at ambient conditions is in the range of 90 mg/L to 150 mg/L (Iler 1979). Inset of SEM images showing the undisturbed nanoparticles (SEM image left) and dissolution/disintegration of the particles (SEM image right) before and after 28 hours exposure to aqueous solution. B) SEM image of the undisturbed nanoparticles. C) SEM image of partly dissolved and disintegrated nanoparticles after 1 day in aqueous solution.

A few challenges must be overcome before the nanoparticle tracers can be applied successfully. The main challenge is the hydrothermal (in)stability of the silica nanoparticles themselves. Both the core and the shell are composed of silica and therefore dissolve in aqueous solutions due to the nucleophilic attack of the surface silanol groups (Si-OH) (Cypryk and Apeloig 2002). The dissolution is particularly problematic for the core, as the core must stay stable to be detected after passing through a reservoir to provide the information about successful

retrieval of the particles. The dissolution behavior of amorphous silica in water has been extensively studied (Alexander et al. 1954, Crundwell 2017, Iler 1979); however, the behavior of artificial silica nanoparticles is not yet fully understood. There is contradicting literature on the (in)stability of such nanoparticles in aqueous media (including biomedical/pharmaceutical applications), which may also be due to experimental conditions (Alaskar et al. 2015a, Jafari et al. 2019, Mikutis et al. 2018, Möller and Bein 2019). For example, particle concentration, temperature, pH, degree of condensation of the network, surface modification, and choice of analytical methods (e.g., aquatic analysis vs. dynamic light scattering) all play an important role in correctly determining the dissolution rate and can lead to incorrect conclusions. Figure 3.12a shows the result of a dissolution experiment with 1 mg mL^{-1} silica nanoparticles without surface modifications at room temperature and without fixing pH. The dissolution is monitored by UV-VIS measurement of the solution using the molybdenum blue method. This method explicitly analyzes only the dissolved silica (monomers, subordinated dimers) in solution and does not react with the particles or the surface of the particles (Iler 1979). Dissolution of the silica nanoparticles begins immediately after contact with the aqueous solution and progresses until equilibrium is reached (Fig. 3.12a). This equilibrium is the saturation concentration of the silica and depends on several factors, such as the temperature, pH, and salinity of the solution. The effect of dissolution can be carefully analyzed using SEM/TEM devices. Figure 3.12b and c show SEM images of pristine, undisturbed silica nanoparticles (Fig. 3.12b) to partly dissolved silica nanoparticles (Fig. 3.12c). A comprehensive study on the dissolution behavior of silica nanoparticles in different aqueous media with special attention to the impact of different factors (e.g. particle concentration, availability of silica, pH, etc.) can be found in Spitzmüller et al. (2023b).

3.3.3.2 Stability improvement strategies

To prevent the nanotracers from dissolution and degradation, we tested several surface modifications to improve the stability of the silica network. An overview of the most effective strategies is displayed in Figure 3.13a by monitoring the dissolution of silica over a 4-week exposure of 1 mg mL^{-1} nanoparticles to aqueous media. As expected, the untreated particles (Fig. 3.13a black square) suffer immediate dissolution and equilibrate as soon as the silica saturation concentration in solution is reached. Chemical surface modification strategies such as silanization (octadecyltrimethoxysilane, Fig. 3.13a light blue hexagon) and paraffin coating (dotriacontane, Fig. 3.13a olive square) proofed to lower the nanoparticle dissolution and seem to equilibrate at silica concentrations below 50 mg L^{-1} within 4 weeks at room temperature. Another approach on stabilizing is the coating with a metal oxide, in our case, titania (Fig. 3.13a pink triangle). The titania hull has a similarly stabilizing effect on the nanoparticles as silanization and paraffin coating. The by far most effective method stabilizing silica nanoparticles turned out to be calcination (Fig. 3.13a, red dot, blue triangle). Due to condensation processes at high temperatures, the silica network is stronger linked and can

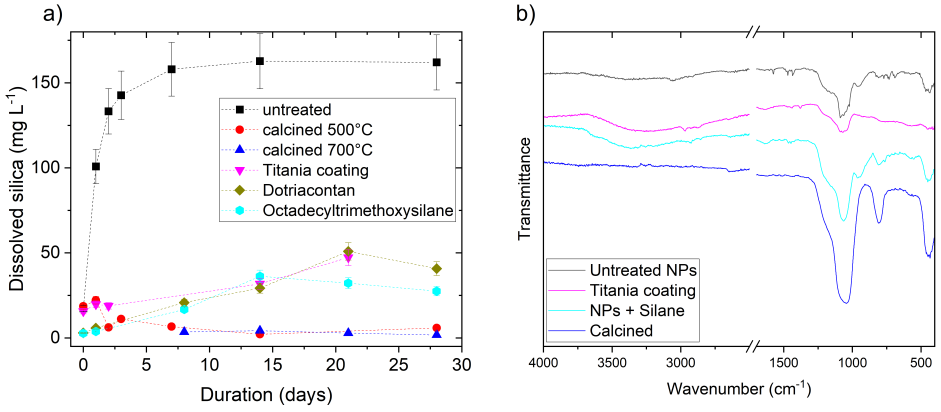

Figure 3.13: A) Impact on the dissolution behavior of silica nanoparticles by testing different stability improvement strategies over 4 weeks. The untreated nanoparticles show the expected behavior, an immediate dissolution and reaches the silica saturation concentration, whereas the treated particles show only minor dissolution and seem to equilibrate far below saturation. B) shows the FT-IR ATR spectra of untreated particles and surface modified particles.

resist the nucleophilic attack of the water. The success of the surface modifications is proofed via FT-IR ATR spectroscopy (Fourier-Transform Infrared Spectroscopy Attenuated Total Reflectance, Fig. 3.13b). FT-IR ATR spectroscopy is commonly used to identify chemical bonds based on their unique bending and stretching vibrational characteristics in the infrared wavelength region. Important wavenumbers for silica nanoparticles are 1100 – 1000 cm^{-1} for asymmetric Si-O-Si (siloxane) stretching, 802 cm^{-1} for symmetric siloxane wagging, 455 cm^{-1} for siloxane bending vibration, and 970 cm^{-1} for Si-OH (silanol) stretching (Socrates 2001, Widjornako et al. 2014). Other important information can be identified in the region of 3700 – 3200 cm^{-1}, vibrations can be assigned to stretching of adsorbed OH molecules (Widjornako et al. 2014). Silanized samples further exhibit CH_3 stretching in the region of 3000 – 2800 cm^{-1}, asymmetric C-H bending at 1450 cm^{-1} and symmetric C-H bending at 1400 cm^{-1} (Zeitler and Brown 1957). The titania coated samples should show additionally very strong Ti-O-Si vibration at 919 cm^{-1} (Zeitler and Brown 1957) which could not be identified in the samples. The calcined sample shows a prominent silanol (Si-OH) vibration vanishing (wavenumber 970 cm^{-1}) and only exhibit strong siloxane (Si-O-Si) vibrations. Furthermore, the broad OH peak present in non-calcined samples disappears. In conclusion, the silica network is stabilized due to the higher degree of condensation and the resulting lesser affection by nucleophilic attack of water (Cypryk and Apeloig 2002). Although from literature it can be expected that the surface rehydroxylates (Warring et al. 2016, Zhuravlev 2000), i.e. the effect of calcination is reversible, we did not experience such a rehydroxylation within 4 weeks, as there was no loss of functionality of the surface improvement strategy. Nevertheless, the negative side effect of calcination is the loss of fluorescence of the organic fluorophore (dye) which cannot withstand high temperatures (500 – 700 °C).

3.3.3.3 Sorption

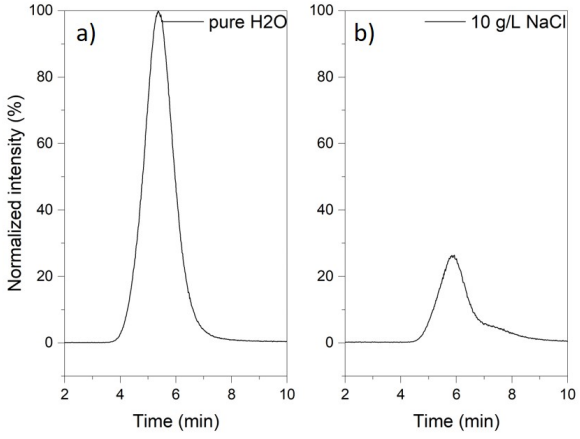

Figure 3.14: Breakthrough curves of nanoparticle tracers in flow through tests in coarse quartz sand using pure water (Millipore) and a 10 g L^{-1} NaCl solution. The curves are normalized on the breakthrough curve in pure water. The retention of the particles increases by about 70 % when salt is present in solution.

Sorption is a ubiquitous problem when conducting tracer experiments (Kasnavia et al. 1999). In hydrology, it is usually advisable to use tracers that have favorable sorption properties, for example, uranine, eosin, sodium naphthionate, etc. (Flury and Wai 2003). However, in geothermal reservoir exploration, two factors may be drastically different from hydrologic aquifer tests: temperature and salinity of the fluids (Chrysikopoulos 1993). Preliminary sorption tests at 80 °C using eosin showed sorption of about 55 % on coarse quartz sand in distilled water and 4 M NaCl solution, while using a natural clayey sediment under the same conditions increased sorption to 67 % and 100 % in distilled water and 4 M NaCl solution, respectively. These results are consistent with room temperature sorption tests of eosin performed by Magal et al. (2008). Corresponding tests for sorption of nanoparticle tracers at high temperatures are in preparation.

We evaluate our nanoparticle tracer in terms of flow performance at higher salinity. Figure 3.14 shows the intensities of the breakthrough curves normalized to the breakthrough curve in pure water (Fig. 3.14a). The addition of 10 g NaCl per liter lowers the breakthrough curve to about one-third, indicating strong retention and sorption within the sand-filled column due to the presence of dissolved salts. This behavior is consistent with the data of Liu et al. (1995). The affinity of the nanoparticles to adhere to quartz grains in electrolyte solutions can be explained by surface charges (Liu et al. 2020). Initially, the nanoparticle tracers have a negative ζ-potential ($\approx$ -34 mV), as do the quartz grains. In the absence of cationic ions in the solution, sorption is unlikely, whereas in the presence of a cationic ion (in this case sodium),

the ions can affect the electrostatic interactions between particles and matrix, promoting adsorption, adhesion and retention (Buoyer et al. 2001, Franks 2002, Pianegonda et al. 2005).

3.3.3.4 Sorption control

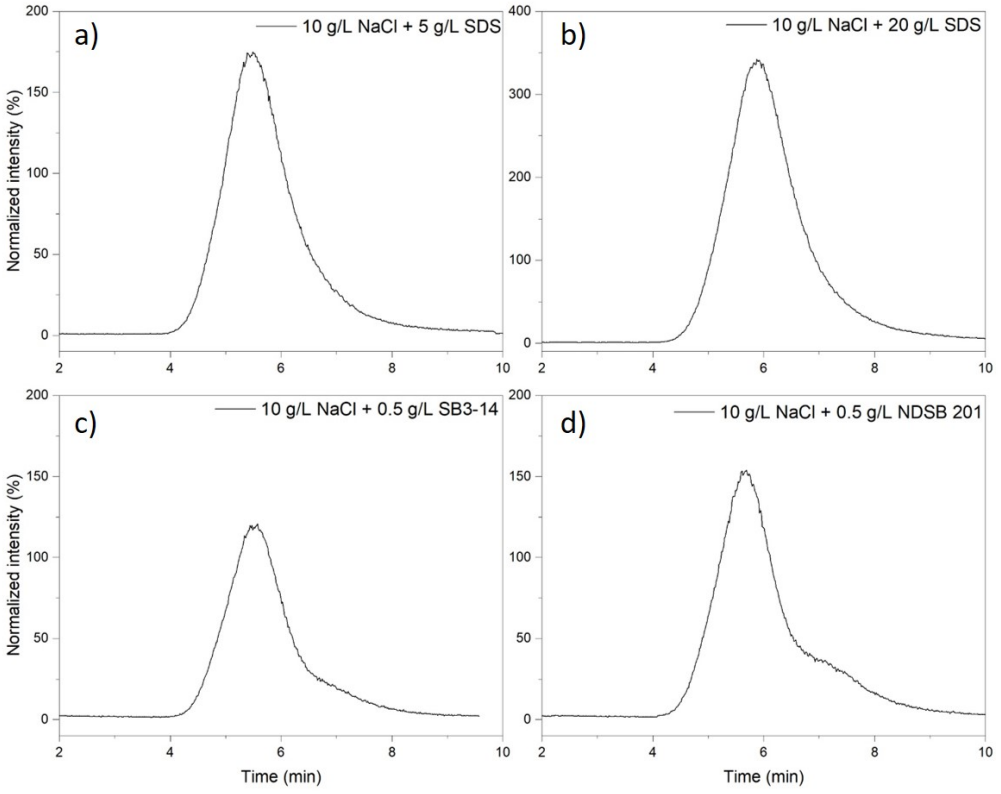

Figure 3.15: Breakthrough curves of nanoparticle tracers in 10 g L^{-1} NaCl solution with addition of various surfactants. The intensity is normalized on the breakthrough curve of nanoparticle tracers in 10 g L^{-1} NaCl solution. Please note the y-axis change in b).

Consequently, one approach to controlling the sorption of our nanoparticles would be to modify the ζ-potential of the particles so that they are either nearly neutral or have the opposite charge to the sand grains. Surfactants, especially anionic and cationic are known to affect effectively the surface charge of silica nanoparticles (Ahualli et al. 2011). To test the performance of such modification methods, four different additives were tested by monitoring the change in the nanotracer breakthrough curves. Sodium dodecyl sulfate (SDS), an anionic surfactant, cetyltrimethylammonium bromide (CTAB), a cationic surfactant and two zwitterionic surfactants SB3-14 (sulfobetaine 3-14, N-tetradecyl-N,N-dimethyl-3-ammonio-1-propanesulfonate) and NDSB 201 (pyridinium propylsulfonate-(1)) were chosen. While the addition of the cationic surfactant CTAB did not improve tracer breakthrough and

also negatively affected the protective function of the hull, the addition of 5 g L^{-1} SDS to the 10 g L^{-1} NaCl fluid increased the recovery of nanoparticle tracers to 175 % (Fig. 3.15a), assuming that the recovery in NaCl solution is 100 % (Fig. 3.14b). The addition of 20 g L^{-1} SDS further increased the recovery to 353 % (Fig. 3.15b). The zwitterionic surfactants increased the retrieval to 115 % (SB3-14, Fig. 3.15c) and 162 % (NDSB 201, Fig. 3.15d). Although the zwitterionic surfactants appear to have lower efficacy in controlling sorption, they are dosed about ten times lower than the anionic surfactant. From an economic point of view, the use of SDS is most advisable.

3.3.4 Conclusions and prospects

We presented the development and proof-of-concept of a novel type of nanoparticles-based tracers for simultaneous flow path and temperature detection in geothermal reservoirs. The $\approx$70 nm-sized nanotracers are designed by a three-layered architecture, namely a fluorescent core, a fluorescently doped mesoporous shell and a protective, temperature-triggered hull. This concept has the advantage of being modular and accurately detecting temperature due to the sharp threshold of the temperature-triggered hull. We evaluated the performance comparing the breakthrough curves of nanotracers through a quartz-sand filled flow-through column to breakthrough curves of uranine and eosin. We further identified the hydrothermal instability and the sorption on reservoir medium to be the most critical issues when applying nanotracers as tracers for geothermal reservoirs. To overcome these challenges, we provide and proof the effectiveness of a variety of stabilization methods (chemical surface modifications, strengthening the silica network, etc.) and control sorption rate through addition of surfactants. Further approaches would be adapting the structuring process of the nanotracers amplifying their application field and monitoring the ζ-potential and surface interactions of particles, reservoir fluids and different reservoir rocks.

CHAPTER 4

Dissolution Control and Stability Improvement of Silica Nanoparticles in Aqueous Media

This Chapter is published in Journal of Nanoparticle Research
https://doi.org/10.1007/s11051-023-05688-4

Spitzmüller, L., Nitschke, F., Rudolph, B., Berson, J., Schimmel, T., Kohl, T. (2023): Dissolution Control and Stability Improvement of Silica Nanoparticles in Aqueous Media. *J. Nanopart. Res.* 25, 40.

In this Chapter, the importance of rational particle design is highlighted. Silica nanoparticles are widely assumed to be stable and inert. This study shows that dissolution processes can not be neglected when applying engineered nanoparticles to geoscientific environments and bridges the gap between established applications in life sciences and geoscience applications of silica nanoparticles. The main findings are:

- Dissolution depends on many factors, such as temperature, pH, salinity, ion valence and the availability of silica.
- SiNP dissolution behavior resembles amorphous silica
- Effective stabilization methods are either modifications of surface properties or the restructuring of chemical bonds by heat treatments.

Abstract

Silica nanoparticles have become an important tool in material sciences, nanomedicine, biotechnology and pharmaceutics, with recent suggested applications also in environmental sciences. In life and environmental sciences, the application field is usually aqueous media, however the crucial issue of silica nanoparticle dissolution behavior and rate in the target medium is often neglected, overlooked or taken for granted. Silica nanoparticles are not stable in aqueous solutions until equilibrium silica concentrations are reached. While for life science applications, the degradability of silica nanoparticles is prerequisite for biocompatibility, this characteristic impedes the successful application of silica nanoparticles as environmental tracer, where long-term stability is needed. In this study, the impact of external (temperature, pH-values, salinity, availability of silica) and internal (degree of condensation, size, porosity) parameters on the stability of ∼45 nm sized silica nanoparticles is characterized. Results show that external factors such as elevated temperature and alkaline pH-values accelerate the dissolution, acidic pH, high salinities and high initial silica concentrations exhibit a contrary effect. Consequently, in applications, where external parameters can not be controlled (e.g. *in vivo*, subsurface reservoirs) dissolution control and stability improvement of silica nanoparticles can be achieved by various means, such as adding a protective layer or by condensation of the silanol bonds through calcination.

4.1 Introduction

Over the last decades, silica nanoparticles gained worldwide importance and attention Jeelani et al. (2020). The well-established industrial applications, e.g., application in material sciences, have in common that the silica nanoparticles are applied in/to dry environments, where silica nanoparticles are considered inert and stable (Scientific Committee on Consumer Safety 2019). Over the last decade, engineered silica nanoparticles have been developed for biomedical purposes, e.g., serving as tunable nanocarriers for water-insoluble drugs, chemotherapeutics and as soluble drug encapsulation facilitating long-term release applications (Andersson et al. 2004, Bharti et al. 2015, Bouchoucha et al. 2016, Cheng et al. 2010, Kwon et al. 2013, Liong et al. 2008, Maggini et al. 2016, Song et al. 2017, Tonelli et al. 2020, Tourne-Peteilh et al. 2011, van Rijt et al. 2015, Wang et al. 2015). The favorable properties of silica nanoparticles were furthermore highlighted by the easily functionable surface e.g. for targeted or stimuli-responsive drug release (Bouchoucha et al. 2016, Song et al. 2017, Yamada et al. 2012, Zhao et al. 2015,1), and in the field of nanobiophotonics (Gubala et al. 2020, Korzeniowska et al. 2013, Liong et al. 2008, Ow et al. 2005, Sola et al. 2021, Wang et al. 2006). Additionally, the small size of the nanoparticles offers the unique opportunity of reaching formerly inaccessible areas, e.g. across the blood-brain barrier (Andersson et al. 2004, Barandeh et al. 2012, Korzeniowska et al. 2013). The usage of nanoparticles as imaging sensors in life sciences

inspired research towards similar applications in the environmental sciences. In particular, hydrology and geothermal production are often facing the challenge of an exploitation from inaccessible reservoirs. However, a sustainable management of a reservoir and the long-term optimized commercial production requires a comprehensive knowledge about the structures and flow paths and their hydraulic behavior. For such analysis, well-established tracing techniques usually use fluorescent molecular dyes such as sodium fluorescein or eosin (Käß 2004). However, molecular dyes can be greatly affected by fluids pH and temperature and have a low photostability (Kasnavia et al. 1999, Magal et al. 2008, Zhu et al. 2005). In addition, the rock properties of the underground can lead to adsorption and in extreme cases to complete retention of molecular tracers and impede the characterization of the reservoir. Thus, there is the requirement for new approaches to overcome the drawbacks of the molecular dyes. Basic research has been conducted on the application of silica nanoparticles as tracers in hydrology for aquifer and reservoir assessment (Alaskar et al. 2015a, Clemente et al. 2016, Kong et al. 2018, Liao et al. 2018, Mikutis et al. 2018, Paunescu et al. 2013). Further developments led to advanced temperature-sensitive silica nanoparticles as tracers for geothermal reservoir characterization (Alaskar et al. 2015a, Rudolph et al. 2020, Zhang et al. 2016).

For all application in aqueous environments (geothermal tracer, groundwater marker, bioimaging, drug delivery, theranostic), the stability of the silica nanoparticles is a key parameter. Two factors are therefore of utmost importance: the silica solubility (i.e. the maximum SiO_2 concentration to attain equilibrium at given geochemical conditions) and the silica dissolution rate. From the environmental sciences it is well known, that the stability of silica, silicates and other SiO_2-polymorphs depends mainly on the crystallinity of the silica network, with higher crystalline order being less soluble (Iler 1979). The dissolution process of silica in water can be described in simplified form:

$$SiO_2 + 2H_2O \rightleftharpoons H_4SiO_4 \tag{4.1}$$

with H_4SiO_4 the monomeric, silicic acid species. This reaction takes place until the equilibrium, the thermodynamically governed silica saturation concentration (SSC), is reached. From natural systems, it is also well known, that elevated temperatures augment the SSC and increase the silica dissolution kinetic (Fournier and Rowe 1966, Gunnarsson and Arnórsson 2000, Okamoto et al. 1957). Studies found the SiO_2 concentration at equilibrium with amorphous silica, referred to as silica saturation concentration (SSC), to be in the range of 90 mg L^{-1} to 170 mg L^{-1} at room temperature and increasing up to the range of 270 mg L^{-1} to 310 mg L^{-1} at 80 °C (Alexander et al. 1954, Eikenberg 1990, Fournier and Rowe 1966, Greenberg and Price 1957, Rimstidt and Barnes 1980). The broad variation can be explained by differences of the natural amorphous silica itself such as the degree of hydration, the presence of areas of higher degree of crystallinity, the amount of impurities and the particle

size (Iler 1979). However, in fact, the proportionality of silica concentration in natural groundwater and geothermal fluids and their temperature is a widely used tool to deduce the subsurface temperature from the composition of natural springs (Arnórsson 1975, Fournier and Rowe 1966, Morey et al. 1962, Nitschke et al. 2017). Temperature is therefore expected to have also a high impact on the dissolution of artificial silica nanoparticles. Other important factors that are affecting the solubility of natural silica are pH and salinity of the solution. Hence, they are assumed to affect the solubility of artificial silica nanoparticles as well.

Even though artificial silica nanoparticles are mainly of an amorphous structure, differences in the degree of condensation of the silica network deriving from the synthesis makes comparison with natural amorphous silica not expedient. In particular, tunable properties like size, shape, porosity, functionalization and the high surface area of the silica nanoparticles complicate the analysis of behavior of silica nanoparticles in aqueous environments. Thus, only sparse data on the (aqueous) stability of artificial silica nanoparticles exist (Yamamoto and Kuroda 2016). Additionally, although several studies on the safety of silica nanoparticles in biological media or *in vivo* (Bakshi 2017, Bhavsar et al. 2019, Chang et al. 2007, Chen et al. 2018, Corbalan et al. 2011,1, Jiang et al. 2016, Kersting et al. 2020, Lin et al. 2006, Mohammadpour et al. 2020,1, Park et al. 2011, Ye et al. 2010) and ecotoxicological assessments (Ale et al. 2021, Koch et al. 2021) exist, the data situation is complex and partly contradicting, as there is no standardized testing procedure. The main consent seems to be the dependency on many factors, e.g. on dosage, cell type, protein corona, surface functionalization, size and shape the particles (Bakshi 2017, Cauda et al. 2010, Cedervall et al. 2007, Chang et al. 2007, Croissant et al. 2020, Gubala et al. 2020, Huang et al. 2010, Park et al. 2011), and the nontoxicity and biocompatibility of the degradation product silicic acid (Barandeh et al. 2012, Liberman et al. 2014). Therefore, the degradability of silica nanoparticles is a desired factor for most applications in life science. However, for long-term drug release, a slow, controlled and well-characterized drug release would be beneficial, as degradation of the carrier's matrix would lead to premature release of the incorporated drugs (Lin et al. 2012). Furthermore, the degradability of silica nanoparticles is up to now the major obstacle for hydrology and geothermal applications, where high (thermal) and long-term stability is crucial. Therefore, accurate knowledge of the degradation process by identifying factors affecting the dissolution rate and the solubility of silica is of utmost importance for both, life and environmental science applications (Croissant and Brinker 2018, Lindén 2018, Quignard et al. 2017). No fundamental studies have been performed on the individual effect of temperature, salinity, pH, particle concentration and initial silica concentration on the stability of artificial silica nanoparticles. This study aims to bridge the gap and obtain detailed knowledge of the behavior of artificial silica nanoparticles in aqueous environments by first performing a sensitivity study on the impact of various parameters on the stability of silica nanoparticles in aqueous media and second, the development and evaluation of surface modifications strategies for silica nanoparticles stability enhancement. For this study, nonporous, fluorescent ∼45 nm silica nanoparticles were chosen to represent a possible tracer for environmental sciences

(Rudolph et al. 2020) and simultaneously represent a possible usage in bioimaging (He et al. 2008). Especially for the application in environmental sciences, the fluorescence is beneficial for monitoring of tracer breakthrough and return curves. Within this study, we examine the individual effects of temperatures up to 80 °C, pH-values ranging from pH 3 to pH 11, salinity of mono- and divalent ions up to concentrations of 4 mol L^{-1}, physiological buffer solution PBS (phosphate-buffered saline) at 37 °C, silica nanoparticle concentrations up to 1 mg mL^{-1} and initial silica concentrations up to 250 mg L^{-1} on the stability of non-porous silica nanoparticles in aqueous solution over an application-relevant period of time and characterize the dissolution kinetics. Additionally, the stability of selected mesoporous silica particles was tested under physiological/biomedical relevant conditions. Finally, although several approaches exist modifying the surface of silica nanoparticles; either by adding a protective layer on the surface, organic functionalization or even by calcination of the particles (Cauda et al. 2010, Croissant et al. 2017, Liberman et al. 2014, Lin et al. 2011, Mahon et al. 2012, Möller and Bein 2019, Paris et al. 2017), their impact on the SSC and dissolution kinetic is yet not monitored sufficiently. We therefore tested and compared several approaches; chemical surface modifications including silanization (octadecyltrimethoxysilane and 1,2-Bis(trimethoxysilyl)decane), grafting of paraffin (dotriacontane) and metal oxide coating as well as calcination (300 °C, 500 °C and 700 °C).

4.2 Materials and Methods

4.2.1 Synthesis

Reversed microemulsion (fluorescent nanoparticles) The particle synthesis starts with a mixture of cyclohexane (VWR Chemicals AnalaR Normapur, 15 mL), n-Hexanol (VWR GPR Rectapur, Assay $<$ 98 %, 3.6 mL) and Triton X 100 (Sigma-Aldrich for analysis, 3.44 mL) magnetically stirred in a round bottom flask. After 1 min reaction time, Tris(2,2-bipyridyl)dichlororuthenium(II) hexahydrate ($Ru(bpy)_3^{2+}$, Acros organics, 98 %, 0.96 mL 20 mM) and tetraethylorthosilicate (TEOS, Sigma-Aldrich, 99.0 %, 0.2 mL) are added. After 20 min of continued stirring, ammonium hydroxide solution (Merck, 28–30 %, 0.12 mL) is added. After 24 h continued stirring, acetone (VWR Chemicals AnalaR Normapur, 28 mL) is added to break down the microemulsion. The solution is then collected, centrifuged at 4400 g (6000 rpm, Hermle Z206A) and undergoes 4 washing-centrifugation cycles using acetone, ethanol, ethanol + water (80:20), and water. A 5^{th} cycle (ethanol) can be added optionally to facilitate vacuum drying of the particles. When needed, a sonotrode (IUP200St, Hielscher Ultrasonics) or a sonication bath (Bandelin Sonorex) was applied to resuspend the pellets. The fluorescent particles show sizes of 44 ± 3 nm and an average ζ-potential of -37.2 ± 2.3 mV.

Stöber synthesis (non-fluorescent nanoparticles) Stöber synthesis following Stöber et al. (1968). Ethanol (26 mL) were mixed with H_2O (1.6 mL) and ammonium hydroxide (3 mL). After thoroughly stirring, tetraethylorthosilicate (3 mL) is added and the solution is stirred for 2 hours at 60 °C The solution is then collected and centrifuged at 4400 g (6000 rpm) and undergoes 3 washing cycles with ethanol and water.

4.2.2 Surface modifications

1,2-Bis(Trimethoxysilyl)decane: The coating of the fluorescent nanoparticles with 1,2-Bis-(trimethoxysilyl)decane (Gelest Inc.) was performed following the procedure of Arkles et al. (2014). Acetonitrile (Merck, 99.5 %) was used as solvent. 1,2-Bis(trimethoxysilyl)decane (1 wt%) was added to the solution and stirred for at least 20 hours. The nanoparticles are collected via centrifugation and dried in vacuum.

Octadecyltrimethoxysilane: Starting from the fluorescent nanoparticle synthesis, the NPs are dried and weighted. Dry acetonitrile (Merck, 99.5 %) and n-Octadecyltrimethoxysilane (ABCR GmbH, 95 %, 0.375 mL) per 50 mg particles is added. After stirring the solution for at least 12 hours, the nanoparticles are collected by centrifugation. One washing cycle with acetonitrile and one with hexane (Carl Roth, 99%) is performed. Then the particles are dried in vacuum. No surfactants were used to resuspend the particles in water for the stability experiments.

Dotriacontane: Starting from the capping with n-Octadecyltrimethoxysilane, the dried particles are resuspended in hexane (40 mL) per 50 mg particles and dotriacontane (Sigma Aldrich, 97%, 375 mg) per 50 mg particles are added. The solution is sonicated for 15 minutes, followed by a 15-minutes stirring cycle. The particles are collected by centrifugation and dried in vacuum. No surfactants were used to resuspend the particles in water for the stability experiments.

Titania coating: The coating with titania was performed following Joo et al. (2012). 50 mg fluorescent nanoparticles are dispersed in ethanol (20 mL) and stirred at 500 rpm. hydroxylpropyl cellulose (Acros Organics, 0.1 mg) and H_2O (0.1 mL) were added. Tetrabutyl orthotitanate (1 mL, TBOT, Sigma Aldrich, synthesis grade) was mixed with ethanol (4 mL) and added with a syringe pump with 0.5 mL min^{-1}. The solution was heated up in an oil bath to 85 °C. After 100 minutes, the nanoparticles are collected by centrifugation.

Calcination: The calcination of the non-fluorescent nanoparticles was performed using a quartz cuvette and an oven at the temperatures desired. The particles are heated for 24 hours and used afterwards as retrieved.

4.2.3 Experimental procedure

For the stability experiments, 1 mg mL^{-1} silica nanoparticle concentration and deionized water (18 MΩ) was used unless otherwise noted. First, the particles were dispersed in the aqueous media using a sonication bath. The experiments were performed under static conditions without disturbance of the dispersions by sonication or stirring. The duration of the experiments is displayed directly in the Figures, either as timescale on the x-axis, or if sampled at a specific time point, on the y-axis. Samples were taken according the following procedure: 50 µL of solution are diluted 1/100 with deionized water. The dissolution experiments were monitored by determination of the amount of dissolved silica in solution. For determination, the silico-molybdenum blue method (Iler 1979) was performed. After a reaction time of 10 minutes, the sample was measured with the UV-VIS.

Temperature experiments: Temperature experiments were performed in round glass bottom flasks heated in a silicon oil bath at the desired temperatures. To minimize evaporation, the experiments were performed under reflux. Contamination by dissolution of silica from the glass flasks was excluded as the blank silica concentration did not increase over one week at 80 °C and was negligible.

pH experiments: pH buffer solutions are produced as follows: pH 3 (potassium hydrogen phthalate [Sigma Aldrich] – hydrochloric acid [Honeywell Fluka]), pH 4 (potassium hydrogen phthalate – hydrochloric acid), pH 5 (potassium hydrogen phthalate – sodium hydroxide [Merck Emsure]), pH 6 (sodium citrate tribasic dihydrate [Sigma Aldrich] – citric acid [Sigma Aldrich]) pH 7 (Tris [Carl Roth, $\geq$ 99.9%] – hydrochloric acid), pH 8 (Tris – hydrochloric acid), pH 9 (glycine [VWR life science, proteomics grade] – sodium hydroxide), pH 10 (glycine – sodium hydroxide), pH 11 (bicarbonate [Sigma Aldrich] – sodium hydroxide). Experiments were performed at room temperature using centrifuge tubes to avoid silica contamination from glass vessels especially at high pH-values.

Salinity experiments: Calcium chloride (VWR technical), sodium chloride (VWR GPR Rectapur), potassium chloride (VWR GPR Rectapur) were used as purchased. The particles were suspended in the salt solutions. The experiments were performed at room temperature using centrifuge tubes.

Phosphate-buffered saline experiments: For the experiments using a simulated physiological solution, PBS (VWR life science, biotechnology grade) was used. PBS is a buffer solution composed of 137 mM NaCl, 2.7 mM KCl and 12 mM phosphate. The pH is fixed at 7.4. Different amounts of nanoparticles (nonporous, fluorescent ∼44 nm), mesoporous nanoparticles (MSN, Sigma Aldrich Silica mesoporous, 0.5 µm particle size, pore size 2 nm) and mesoporous microparticles (SBA-15, Sigma Aldrich, Silica mesoporous SBA-15 $<$150 µm particle size, pore size 6 nm, hexagonal pore morphology) are added to the PBS solution and heated in a water bath to 37 °C.

Availability of silica experiments: The solutions with variable amount of initial silica were prepared following the procedure of Spitzmüller et al. (2021). Silica (Merck, extra pure) and deionized water were mixed in a HDPE vessel and the pH was adjusted by addition of sodium hydroxide to pH 12. The solution was stirred overnight at 70 °C in an oven. Afterwards, the solution was cooled down to room temperature and the pH was readjusted to pH 7 by addition of hydrochloric acid. The solutions were used immediately after pH adjustment to avoid polymerization and ageing especially in oversaturated solutions.

4.2.4 Analytical devices

Spectrophotometric analysis: For the determination of the dissolved silica concentration (mainly Q^0, subordinate Q^1 and Q^2) the molybdenum blue method is used. The Q^0 species reacts with the Silicate (Silicic Acid) Test from Merck Supelco forming the blue silicomolybdic acid. For measurement of the silica concentration by photometry, an UV-VIS Perkin-Elmer Lambda 9 spectrometer is used (λ=810nm). Samples are diluted using deionized water to assure being in linear range of the Lambert-Beer-Law. 1 mg mL^{-1} SiO_2 standard (Carl Roth) was diluted 1/100 and measured repeatedly as reference for the calibration line. The deviations represent the error of the measurements and are depicted as error bars in the Figures in Results and Discussion. Reactions of the method with the colloidal species (Q^n) can be excluded as a test series with particles in solution, filtered (0.2 µm acetate filter) and supernatant (centrifugation 6000 rpm/4400 g, 30 min) did not exhibit a significant difference of the silica concentration measured.

SEM: For the SEM images, a Zeiss Leo 1530 was used. The aperture size was set to 30 µm. The EHT was with 1 kV to 2 kV relatively low. These low voltages are necessary due to the sample preparation. The nanoparticles were diluted with ethanol and one drop was put on a p-doted silicon wafer. The wafer was placed on top of an adhesive carbon-tab. With this procedure, the coating with carbon or gold was avoided. However, as the conductivity was low, only low voltages are used to not charge the samples. The working distance was usually around 1.5 to 2.5 mm.

FT-IR-ATR: For the FT-IR-ATR analysis, the Nicolet iS50 was used. The wavenumbers were between 400 cm^{-1} and 4000 cm^{-1}. 20 repetitions were performed. The samples were measured in dry conditions after vacuum drying or calcination.

4.3 Results and Discussion

For the following experiments, nonporous, fluorescent silica nanoparticles were synthesized using the reversed microemulsion method. Fluorescent particles were chosen to represent the nanoparticles used for most of the environmental applications and for bioimaging, which

require such a tracing function. The particles exhibit a spherical shape, with sizes of 44 ± 3 nm and an average ζ-potential of -37.2 $\pm$ 2.3 mV. For the stability experiments performed in this study, 1 mg mL^{-1} silica nanoparticle concentration and deionized water (18 MΩ) was used unless otherwise noted. In the course of the experiments, the pH values of the non-buffered solutions ranged between pH 7 and pH 6.2, which is due to the formation of silicic acid. The pH value decreases with increasing amount of dissolved silica. However, this pH range is not expected to additionally affect effectively the dissolution process of silica nanoparticles. For further details to the experimental procedure and the methods used, see the Materials and Methods section.

4.3.1 Effect of temperature

To monitor the impact of temperature on particle dissolution, the evolution of silica concentration in solution over a 28-h period at 20 °C (room temperature, RT), 40 °C, 60 °C, and 80 °C was measured (Fig. 4.1). Highlighted in colored areas in Fig. 4.1 are the silica saturation concentration (SSC) ranges at the respective temperatures derived from literature data and depending on the type of silica (Alexander et al. 1954, Eikenberg 1990, Fournier and Rowe 1966, Greenberg and Price 1957, Rimstidt and Barnes 1980). SEM-images of the silica nanoparticles after immersion for 24 h at RT and 80 °C (Fig. 4.9) show significant particle disintegration and dissolution at elevated temperatures. Since the initial particle concentration was 1 mg mL^{-1} and therefore above the SSC (i.e., $c(Si)_{particles} > c(Si)_{SSC}$, also defined as excess silica concentration — ESC) for all temperatures, the particles do not need to be completely dissolved to form an equilibrated solution, i.e., to reach the SSC. However, if the amount of silica nanoparticles is too high, all particles would exhibit only minimal dissolution and therefore only minimal size changes. In this case, monitoring the change of the particle size as an indicator of (thermal) stability using DLS or SEM can lead to less reliable results, as the changes may be below detection limit. This might explain the contradicting statements on thermal (in)stability in (Alaskar et al. 2015a, Mikutis et al. 2018), although the tests of contradicting results were conducted using the exact same silica nanoparticles.

Kinetic and thermodynamic dissolution

Figure 4.1 shows furthermore the kinetic and thermodynamic properties of the silica nanoparticle dissolution. Higher temperatures increase both the SSC and the dissolution rate. At RT, the saturation concentration is reached within 28 h, whereas at 80 °C, the dissolution rate increases and the SSC is reached within 2 h (Fig. 4.1). With the experimental data, the following formula could be established to describe mathematically the dissolution behavior of silica nanoparticles in dependence of temperature:

$$c = SSC \cdot (1 - e^{-kt}) \tag{4.2}$$

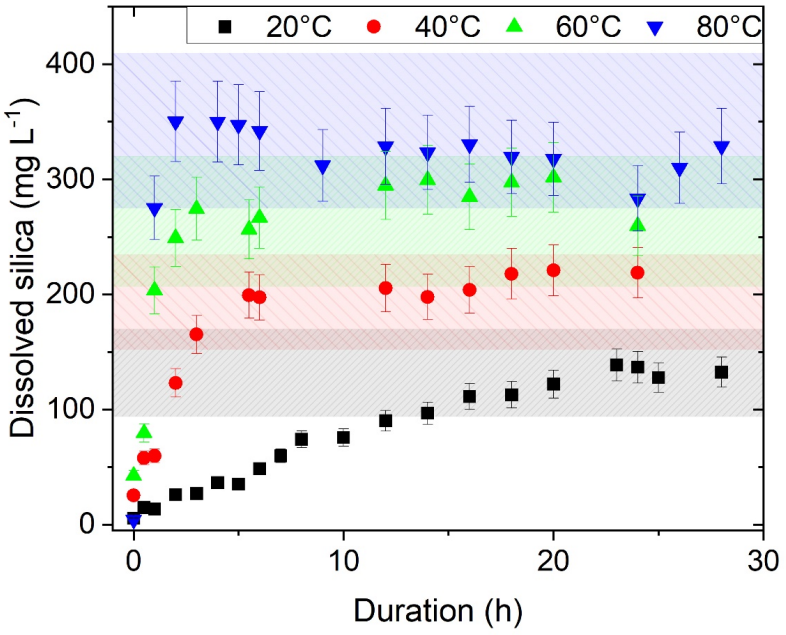

Figure 4.1: Time and temperature dependent dissolution of 1 mg mL^{-1} silica nanoparticles in deionized water over a 28-h time period at various temperatures. Highlighted in colored areas the saturation concentration ranges at the respective temperatures (black 20 °C/RT, red 40 °C, green 60 °C, blue 80 °C). Higher temperatures increase both, the silica saturation concentration (SSC) and the dissolution rate. The error bars are determined by the deviations of standard solutions to the calibration line.

with c the silica concentration in mg L^{-1}, SSC the (thermodynamic) silica saturation concentration in mg L^{-1}, k the (kinetic) temperature-dependent dissolution constant in h^{-1}, and t the time in hours. The relation between temperature and dissolution constant can be determined by a linear regression (Fig. 4.2b) and can be expressed as:

$$ln(k) = 2.32 \cdot ln(T) - 9.58 \tag{4.3}$$

with T in °C. Equation 4.4 can be then reformulated to:

$$k = e^{2.32\ln(T)-9.58} \tag{4.4}$$

The SSC shows a linear temperature dependence up to 80 °C and can be expressed as:

$$SSC = 2.89 \cdot T + 99.62 \tag{4.5}$$

For predicting the dissolution behavior of silica nanoparticles at a given temperature between 20 and 80 °C in deionized water, Eqs. 4.5 and 4.6 are used to determine the temperature-dependent factors k and SSC. Subsequently, the dissolution behavior can be modeled applying

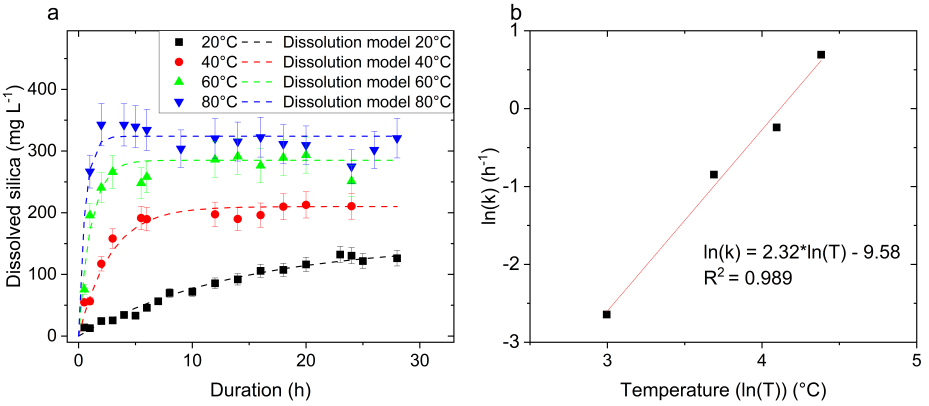

Figure 4.2: a Theoretical dissolution models deduced from of the data points by applying Eqs. 4.6, 4.5, and 4.3 at the respective temperatures. **b** Correlation of the dissolution constant k and the temperature plotted on a double logarithmic scale.

Eq. 4.3. This was done for 20 °C, 40 °C, 60 °C, and 80 °C and the resulting curves are displayed in Fig. 4.2a (lines) in direct comparison with the experimental data (symbols). The dissolution rate is further obtained by derivation of Eq. 4.2:

$$dc/dt = SSC \cdot k \cdot e^{-kt} \tag{4.6}$$

and depends on the SSC, the dissolution constant k, and the time t. The SSC is a critical value, as it represents the solubility limit of silica and does not only depend on the temperature but also on the crystallinity of the silica nanoparticles, the pH value, and the salinity of the solution. We further expect the dissolution constant k to be dependent on these factors and in addition, on the surface area of the nanoparticles and the initial silica concentration in solution. Figure 4.2a exhibits the quantification of the kinetics and solubility dependence on temperature by applying Eqs. 4.3, 4.5, and 4.6. The exponential dependence of the dissolution kinetic of the silica nanoparticles is in agreement with kinetic data of amorphous silica obtained by Rimstidt and Barnes (1980). The temperature-dependent formulations of the dissolution behavior found here only serve as an exemplary conduct and are not generally applicable for all types of silica nanoparticles, as the factors SSC and k depend also on other factors such as the particle surface area and need to be individually determined for each case where predictions of silica nanoparticle dissolution are desired. We therefore waive further modeling of the data in this study as it would not lead to a general applicable equation.

4.3.2 Effect of pH

Apart from the temperature, the pH value of the aqueous solution strongly affects the silica nanoparticle dissolution. Natural waters vary considerably in pH values and range mostly from pH 3 to pH 10 (Gunnarsson and Arnórsson 2003, Hájek et al. 2021, Suzuki et al.

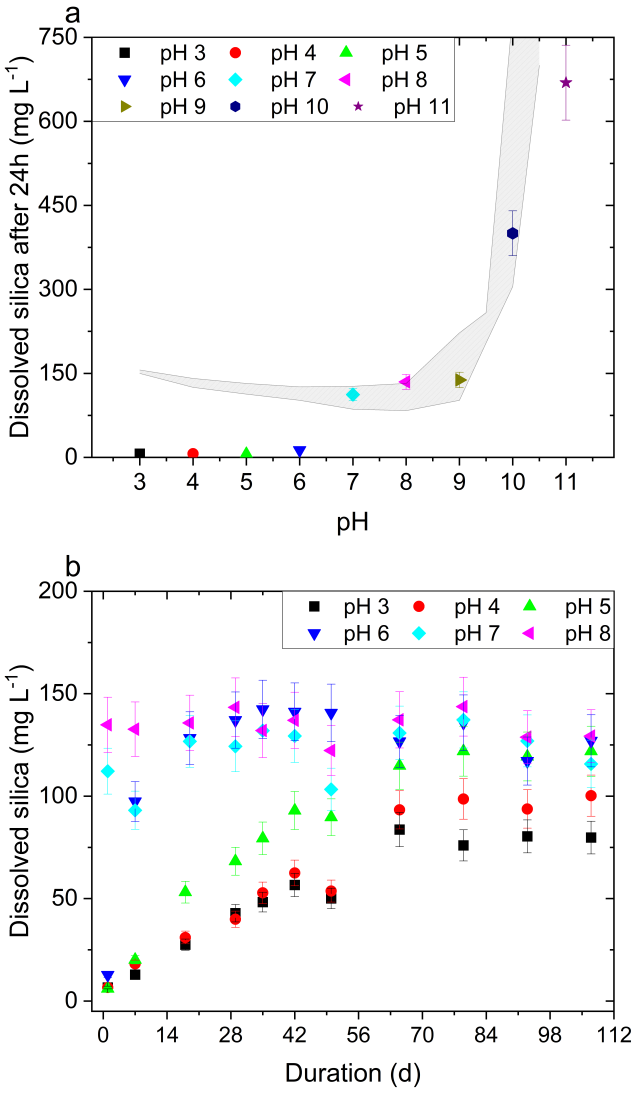

Figure 4.3: Impact of pH value on SSC and silica dissolution at room temperature. pH buffer solutions serve to maintain the pH and are not affected by dissolution of silica nanoparticles.**a** Dissolved silica after 24 h. The gray area represents the SSC at the respective pH values and is derived from literature data (Alexander et al. 1954, Iler 1979, Krauskopf 1956, Okamoto et al. 1957). After 24 h, the SSC was not reached under acidic conditions. The SSC does not significantly differ between acidic and neutral conditions but show a drastic increase with increasing alkalinity. **b** Equilibrium was not reached with 24 h under acidic conditions, since acidic conditions slow down the dissolution kinetics drastically. The dissolution was therefore monitored over 107 days and is compared to the constant behavior under neutral pH values. The error bars are determined by the deviations of standard solutions to the calibration line.

2017), which also covers almost the range of pH-values in human bodies (Proksch 2018). Additionally, it should be pointed out that while tissues exhibit under physiological conditions a fixed pH of 7.4, the pH in the environment of tumors and infectious bacterial often drops to acidic pH ranges (Murugadoss et al. 2017, Tannock and Rotin 1989). Hence, the relevance of pH value on the dissolution and degradation processes is a pivotal aspect for biomedical applications. Figure 3 shows the dissolved silica concentration in different pH buffer solutions after 24 h (Fig. 4.3a) and over a time interval of 107 days (Fig. 4.3b).

Acidic pH

Under acidic conditions, the concentration of the dissolved silica is low after 24 h (Fig. 4.3a) and increases constantly with time (Fig. 4.3b). This slow dissolution kinetic can help explain the different saturation concentrations reported in literature for acidic pH conditions (Alexander et al. 1954, Iler 1979, Krauskopf 1956, Vogelsberger et al. 1992). While the lowest silica solubility is expected at neutral pH values (Iler 1979), Fig. 4.3a shows that the lowest silica concentration after 24 h is observed under acidic conditions as the dissolution rate is slowed down. Furthermore, the polymerization and depolymerization rate is proportional to the availability of H^+ species at pH values between 3 and 7 (Goto 1956, Iler 1979, Okamoto et al. 1957).

Neutral pH

The pH 6 sample shows the transition from acidic and neutral pH values. The dissolved silica concentration after 24 h in pH 6 buffer solution (Fig. 4.3a) is lower than at neutral pH after the similar time period, but increasing faster over time than the dissolved silica concentration in acidic pH samples (Fig. 4.3). In contrast, neutral to slightly alkaline buffer solutions (pH 7 to pH 9) stay constant over time and show a SSC of about 150 mg L^{-1}. The dissolution is fast and the equilibrium is reached in less than 24 h.

Alkaline pH

Alkaline pH values show the highest dissolved silica concentration after 24 h (Fig. 4.3a) and a sharp increase of the SSC (gray area in Fig. 4.3a) in contrast to the acidic and neutral pH value SSC. This can be explained by the silica species distribution. At acidic and neutral pH levels, the H_4SiO_4 species is the predominant silica species whereas at alkaline pH above pH 9.8, the $H_3SiO_4^-$ becomes predominant and leads to an increase of the silica equilibrium concentration (Iler 1979). Furthermore, alkaline pH values catalyze the formation of deprotonated silica species through the availability of OH^- ions and enhance silica solubility (Alexander et al. 1954, Dove et al. 2008, Eikenberg 1990, Goto 1956, Greenberg and Price 1957, Krauskopf 1956).

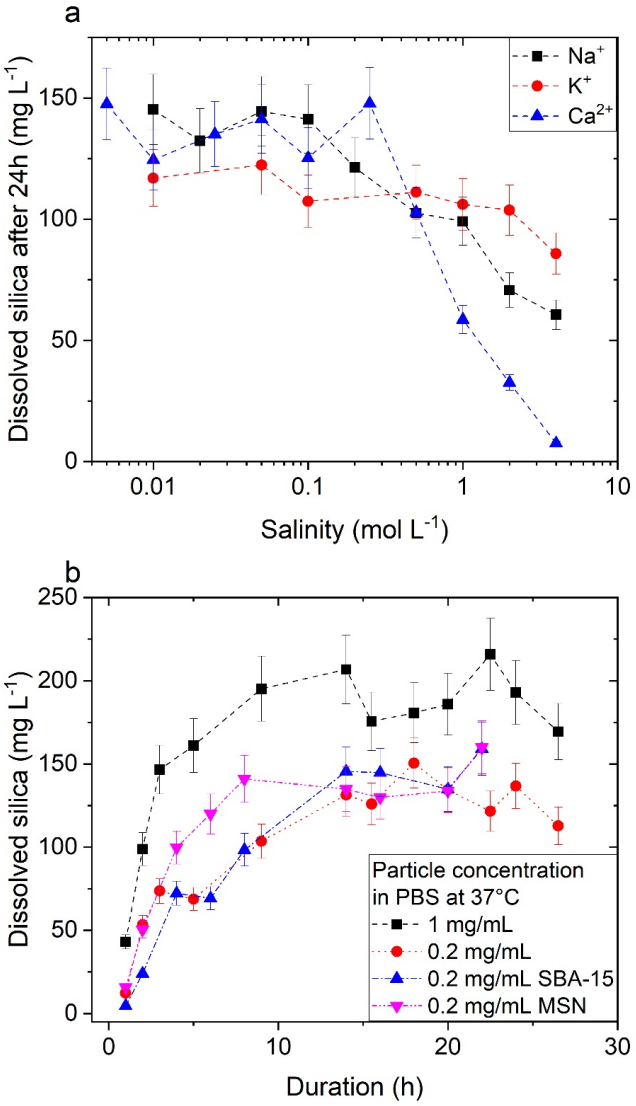

Figure 4.4: Dissolution of silica in complex solutions. **a** Dissolved silica in electrolyte solutions at room temperature after 24 h. Higher salinities lower the SSC. Divalent ions have greater effect than monovalent. **b** Evolution of dissolved silica concentration over time in phosphate-buffered saline (PBS) at 37 °C. The nanoparticle concentrations are varied to be comparable with biological applications. Unless otherwise noted, nonporous nanoparticles are used. For details regarding the silica particles used, see Materials and methods. The error bars are determined by the deviations of standard solutions to the calibration line.

4.3.3 Stability in complex solutions

The salinity of natural waters and biological media can vary considerably (Halperin et al. 2010, Khlebovich 2015). Natural waters can have a broad range of salinity, from freshwater to seawater with about 35 g L^{-1} salt (Durack et al. 2013, Neupane and Wendt 2017). Geothermal fluids can range up to 150 g L^{-1} salt concentration and in extreme cases to even higher than the Dead Sea's 330 g L^{-1} salt concentration (Finster et al. 2015, Neupane and Wendt 2017). First, the impact of sodium, potassium, and calcium is studied independently to identify the influence of each cation. Then, the effects were combined by testing the stability of silica nanoparticles in biological relevant media at 37 °C mimicking human body environment.

Ion valence

Figure 4.4a displays the dissolved silica concentration in NaCl-, KCl-, and $CaCl_2$-solutions over a 24-h time period at room temperature. Low salinities up to 0.5 mol L^{-1} exhibit only a negligible effect on the overall solubility of silica, whereas salinities above 1 mol L^{-1} decrease the solubility drastically (-58% for Na^+, -26% for K^+, -96% for Ca^{2+}). This behavior can be explained with the "salting-out" effect (Marshall and Warakomski 1980). The impact on the solubility can be ordered as follows $K^+ < Na^+ << Ca^{2+}$ for salt concentrations above 1 mol L^{-1}. The impact of monovalent ions is further ordered by the reverse order of the ionic radii and follows the Hofmeister series (Parsons et al. 2010). This order can be explained by the hydration number of the cation. An increase of the hydration number leads to a decreasing silica solubility (Marshall and Warakomski 1980, Stokes and Robinson 1948). Highly saline solutions, especially those containing high concentrations of divalent cations, seem to stabilize the silica nanoparticles against dissolution by reducing the water's activity coefficient and consequently lowering the silica solubility. Further studies on ζ-potential evolution at different salinities should be performed. Literature data indicate the formation of a shielding layer of cations at the diffusive double layer affecting the ζ-potential (Franks 2002, Franks et al. 1999, Parsons et al. 2010, Pianegonda et al. 2005, Tikhonov 2007), thus affecting the dissolution process.

Physiological buffer

Although the salinity in biological systems is much lower than in natural waters, salinity effects can still be present when using, e.g., phosphate-buffered saline (PBS, cations Na and K) or simulated body fluids (SBF, cations mainly Na, subordinate K, Ca, and Mg) (Braun et al. 2016, He et al. 2008, Khlebovich 2015, Lin et al. 2011). Figure 4.4b shows the dissolution behavior of silica in simplified physiological media using PBS at 37 °C. The nonporous silica nanoparticle concentration was varied to be comparable with the experiments reported in Fig. 4.1 (1 mg mL^{-1}) and in biological applications (0.2 mg mL^{-1}). Furthermore, the stability of mesoporous silica SBA-15 (<150 µm, pore size 6 nm, purchased from Sigma-Aldrich, assay 99.9%), and MSN (500 nm, pore size 2 nm, purchased from Sigma-Aldrich, assay 99.9%) was tested as well. The SSC observed in the experiments is about 150–200 mg L^{-1}

and corresponds to the toxic silica nanoparticle concentration of above 200 mg L^{-1} identified in literature (Chen et al. 2018, Kersting et al. 2020, Mohammadpour et al. 2019, Sun et al. 2021). If the SSC is reached, further silica nanoparticle dissolution is prevented as long as no silica is removed from the system, e.g., by excretion or digestion. The dose-dependent toxicity of silica nanoparticles may be greatly affected by the availability of silica and the SSC. Solutions having an excess silica concentration (ESC) can be assumed to be more toxic, as the particles cannot be completely dissolved due to the saturation limit of silica in solution. Therefore, for, e.g., design of toxicity studies, detailed knowledge of the SSC of the particles used as well as the dissolution kinetics are crucial factors. The faster dissolution of the MSN (pink downward pointing triangle) in comparison to the nonporous silica nanoparticles of the same concentration (red dot) is in accordance with Braun et al. (2016). They concluded that mesoporous particles are less stable due to large pore volumes, low wall thickness, and crystallization defects in the silica structure. However, although our silica nanoparticles are nonporous and about 3500 times smaller than the SBA-15 particles, the dissolution rate of 0.2 mg mL^{-1} silica nanoparticles (red dot) and SBA-15 (blue triangle) is similar. Surprisingly, the silica nanoparticles with a concentration of 1 mg mL^{-1} (black square) show the highest dissolution rate and the highest dissolved silica concentration, raising the question of the impact of the availability of silica.

4.3.4 Availability of silica

The availability of silica can be either defined as silica dissolved from the nanoparticles or as silica initially present in form of silica in solution. While silica available from particle dissolution is represented in several studies in a simplified form as different particle concentrations or dosages (Croissant and Brinker 2018, Croissant et al. 2017, He et al. 2008, Liberman et al. 2014, Murugadoss et al. 2017), the dissolved silica in solution is disregarded. However, especially for multiple exposure studies in biomedical applications, the dissolved silica concentration should be considered when the time interval is too short for clearance and complete excretion of the silica nanoparticles and their degradation products (He et al. 2008, Liu et al. 2011). Furthermore, silica is ubiquitous in natural waters from weathering of and/or lixiviation from Si-bearing minerals (Iler 1979). The availability of silica is an important factor, as the dissolution kinetic is affected by the distance to the saturation level (see Eq. 4.3).

Particle dosage/concentration

To order systematically the effects of particle concentration/dosage, three different cases must be distinguished. In case 1, the particle concentration is below the SSC, which means full dissolution of the particles would result in an undersaturated solution (i.e., $c(Si)_{particles} < c(Si)_{SSC}$). In case 2, the particle concentration is equal to the SSC, which means that dissolving all particles would result in an equilibrium solution (i.e., $c(Si)_{particles}$

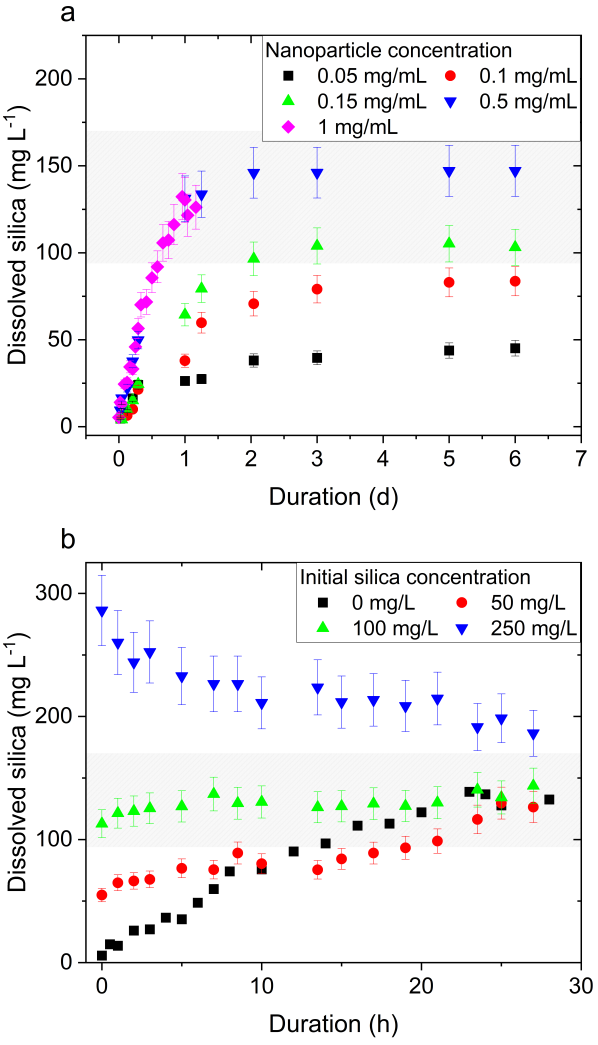

Figure 4.5: Effect of silica availability on dissolution of silica nanoparticles in deionized water at room temperature over time. **a** Impact of silica nanoparticle concentration on the dissolution. Gray area represents the SSC. Undersaturated solutions can not reach the SSC due to limited availability of silica. Dissolution speed depends on the particle concentration. **b** Effect of initial silica concentration in solution. The silica nanoparticle concentration was 1 mg mL^{-1} and consequently oversaturated for all trials. The higher the initial silica concentration in solution, the lower the dissolution speed. In initially oversaturated solutions (250 mg L^{-1}), silica starts precipitating and therefore the concentration decreases over time. The error bars are determined by the deviations of standard solutions to the calibration line.

$\approx c(Si)_{SSC}$). Finally, in case 3, the particle concentration is higher than the SSC, which means that equilibrium between particles and solution occurs with remaining particles (i.e., $c(Si)_{particles} > c(Si)_{SSC}$). All three different cases are shown in Fig. 4.5a. The gray area represents the SSC. For case 1 (i.e., $c(Si)_{particles} < c(Si)_{SSC}$), particle concentrations of 0.05 mg mL^{-1} and 0.1 mg mL^{-1} are tested (red dot, black square in Fig. 4.5a). Both experiments show the lowest dissolution rates, as expected due to lowest surface area available for dissolution (Croissant et al. 2017, Kumar et al. 2014, Yamada et al. 2012). The solutions do not reach SSC and consequently are not in equilibrium. For case 2 (i.e., $c(Si)_{particles} \approx c(Si)_{SSC}$), silica nanoparticle concentration of 0.15 mg mL^{-1} (green triangle, Fig. 4.5a) is used. As expected, the solution reaches the SSC range and leads to an apparent equilibrium state. For case 3 (i.e., $c(Si)_{particles} > c(Si)_{SSC}$), the dissolution behavior of silica nanoparticles is tested at concentrations of 0.5 mg mL^{-1} and 1 mg mL^{-1} (pink diamond, blue triangle pointing down, Fig. 4.5a). Solutions with silica nanoparticles concentrations above the SSC have an ESC and exhibit the highest dissolution rates which is what can be expected due to large surface area available for dissolution (He et al. 2010). The equilibrium at the SSC is reached within 4 h. Further, 0.5 mg mL^{-1} and 1 mg mL^{-1} show similar behavior, leading to the tentative conclusion that the ESC may not be the driving factor for dissolution rates, but the amount of surface area available for dissolution. In accordance, Rimer et al. (2007) and Diedrich et al. (2012) found that the dissolution rate neither depends on number density nor directly on particle radius of nanoparticles. The ESC is therefore not expected to affect the dissolution rate but since a higher surface area is available for dissolution, consequently, the SSC is reached faster.

Initial silica concentration

Another important yet overlooked factor for particle stability is the initial silica concentration in solution (Fig. 4.5b). As expected, the dissolution rate is highest if starting far from equilibrium (0 mg L^{-1}). The higher the initial silica concentration in solution, the slower the dissolution of the particles takes place, which is what can be expected. In supersaturated solutions, the mechanism is reversed. Thus, instead of dissolving the particles, the particles act as nuclei and remove dissolved silica from water. This process seems to be rather slow, since equilibrium was not reached within the period of the experiments. However, data from Fleming (1986) indicate the presence of a so-called pseudo-equilibrium point, which is at about 200 mg L^{-1} at room temperature. At this point, the monomeric silica concentration in solution seems to be pseudo-equilibrated and further polymerization and consequently precipitation rate is drastically decreased. Probably, this may explain the resulting high dissolved silica concentration in solution for the experiment with supersaturated solution (blue downward pointing triangle, Fig. 4.5). In SEM images, formation of new $\sim$ 8 nm size particles as well as regrown particles are visible (Fig. 4.9). This phenomenon is known from geothermal systems where high silica concentrations are characteristic and oversaturation is a common technical problem. Silica removal from geothermal fluids using silica particles as seeding material has been identified previously as element-selective and reduces the fouling

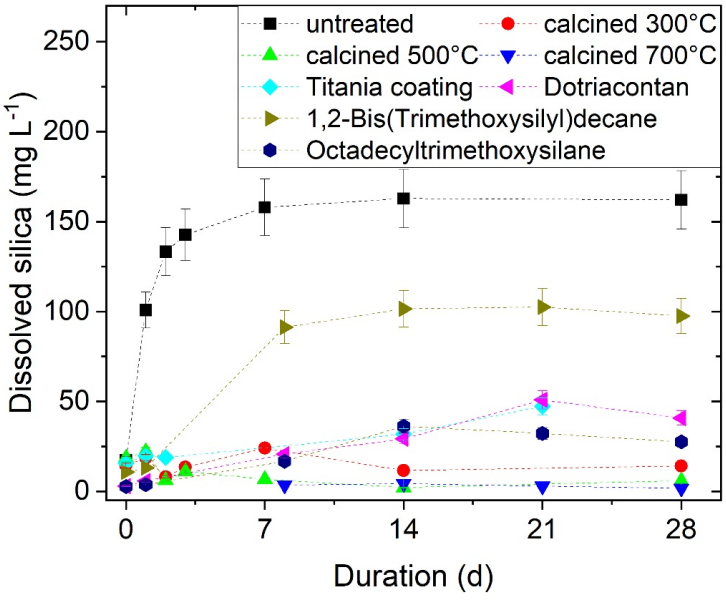

Figure 4.6: Stability enhancement treatments and their effect on dissolution of silica nanoparticles (1 mg mL^{-1}) at room temperature. Untreated particles exhibit fast dissolution, whereas the surface modified particles remain more stable over at least 4 weeks. The most effective stabilizing method is calcination at 300 °C, 500 °C, and 700 °C. Coating of the particles with titania, dotriacontane, and octadecyltrimethoxysilane also decreases the silica solubility effectively but not as effective as calcination. 1,2-Bis(trimethoxysilyl)decane shows the lowest impact on the stability of the nanoparticles, but the dissolved silica concentration is still lower than that of untreated nanoparticles after 4 weeks.

potential (Setiawan et al. 2019, Spitzmüller et al. 2021, Sugita et al. 2003). The formation of silica nanoparticles under geothermal conditions, i.e., in hot, supersaturated solutions, is studied by Tobler and Benning (2013) and under in situ conditions by Tamura et al. (2019). They conclude that particle growth is induced by temperature or pH drop during geothermal production. The final size of the particles observed was about 5 nm. However, the silica removal displayed in Fig. 4.5b was induced solely by addition of silica nanoparticles as the similar reference fluid does not exhibit a significant decrease of silica concentration over a 20-day time period; the added silica nanoparticles act therefore unequivocally as nuclei to the aqueous silica.

4.3.5 Surface treatment

Chemical coating

For chemical surface modifications, grafting of (alkoxy)silanes and paraffin as well as a coating with the metal oxide titania were chosen to represent the broad spectrum of modification

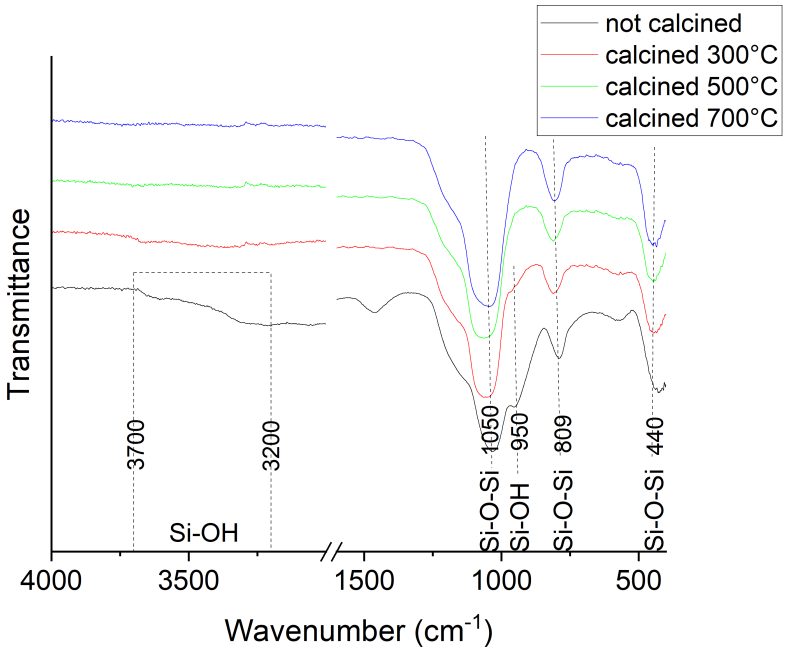

Figure 4.7: FT-IR ATR spectra of silica nanoparticles. The untreated particles (not calcined) have both silanol (Si–OH) and siloxane (Si–O-Si) bonds, whereas with increasing calcination temperature, the siloxane bonds become dominant and the silanol bonds disappear.

methods. For paraffin coating, dotriacontan was grafted on the octadecytrimethoxysilane-coated particles; for silanization, two different silanes were used: the dipodal 1,2-Bis(trimethoxysilyl)decane and octadecytrimethoxysilane. Of these chemical surface protection methods, octadecyltrimethoxysilane is the most effective protection layer, leading to a dissolved silica concentration of about 30 mg L^{-1} after 28 days (dotriacontan: 40 mg L^{-1}, titania coating: 47 mg L^{-1}, 1,2-Bis (trimethoxysilyl)decane: 97 mg L^{-1}). In comparison, untreated particles have a saturation concentration of about 150 mg L^{-1}.

Calcination

As expected, calcination of the particles turned out to be the most effective protective procedure (Fig. 4.6). However, calcination may hinder the synthesis of fluorescent silica nanoparticles, as elevated temperatures can negatively affect the functionality of guest molecules such as organic dyes. Therefore, calcination was performed on non-porous, non-fluorescent silica nanoparticles (Stöber-type) and are compared to the same type of non-calcined particles. The particles in the experiments were calcined at 300 °C, 500 °C, and 700 °C for 24 h. The concentrations after 28 days are 14 mg L^{-1} (calcined 300 °C), 6 mg L^{-1} (calcined 500 °C), and 2 mg L^{-1} (calcined 700 °C) and are below the expected SSC for untreated particles by a factor of 11, 25, and 75, respectively. An explanation for the effective stabilizing behavior of calcination can be given by the FT-IR ATR spectra of calcined and non-calcined silica particles (Fig. 4.7). The comparison of the non-calcined silica particles and calcined ones at 300 °C,

500 °C, and 700 °C clearly shows the disappearance of Si–OH bonds (band at 950 cm^{-1} and a broad shoulder at 3700–3200 cm^{-1} Socrates (2001)) with increasing temperatures. The silanol groups on the surface of silica are the point of attack for dissolution of silica nanoparticles (Cypryk and Apeloig 2002, Iler 1979, Stöber 1967), and the calcination condenses these silanol groups into more stable siloxane bonds. Rehydroxylation of the surface is expected especially if the silica is exposed to aqueous media (Warring et al. 2016, Zhuravlev 2000). However, the rehydroxylation rate appears to be low as no significant increase of the solubility of the calcined particles was observed over 28 days. In contradiction to previous studies where for effective silanol removal temperatures of at least 500–550 °C are required (Yan et al. 2014a), our data indicate stabilization already from 300 °C.

4.4 Conclusion

Many research areas regard silica nanoparticles as stable and inert in a simplistic way, but the stability of silica nanoparticles is in fact highly dependent on the system parameters and the time scale. Especially long-term stability is a crucial characteristic for e.g. environmental or slow-drug release applications. The main factors affecting the silica saturation concentration (SSC) and dissolution kinetics are temperature, pH-value and salinity. In addition, other factors may also play a role such as the shape, size, porosity and morphology of the nanoparticles.

For biomedical applications, the impact of pH on degradation and dissolution kinetic should be carefully examined since the pH in human environment change considerably (e.g. gastric juice, vicinity of tumors). Furthermore, drug release from surface modified mesoporous silica nanoparticles exhibits areas of plain silica surfaces to the aqueous environment, thus promoting the particle dissolution. Especially for biological applications, the impact of surface modifications, protein corona and ligand instability on the dissolution behavior, the SSC and the residence time could help gaining more control over the biodegradation process of silica nanoparticles *in vivo*. For some applications like hydrological applications or long-term drug release, improved stability of silica may be desired. Enhancing the stability could be reached by surface modifications or calcination of the particles. Especially calcination increases the stability drastically due to condensation of silanol bonds into more stable siloxane bonds. However, calcinating may not be suitable for all applications (e.g. bioimaging, environmental tracing techniques), especially those where guest molecules are embedded in the nanoparticles during the silica condensation stage of the particle synthesis.

Acknowledgments

Thanks to the reviewers and the editors for their constructive suggestions that helped us to improve the manuscript substantially. This study is part of the subtopic “Geoenergy“ in the

program “MTET—Materials and Technologies for the Energy Transition“ of the Helmholtz Association.

4.5 Supplementary

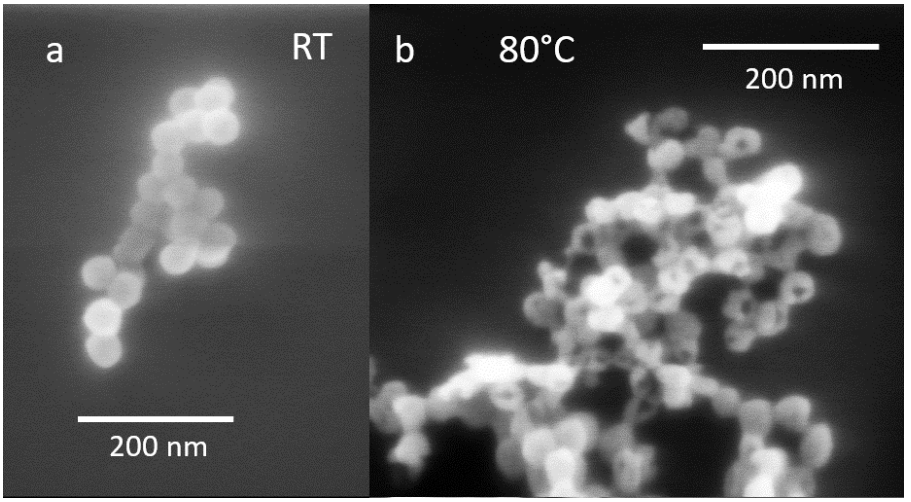

Figure 4.8: Particle disintegration and dissolution effect on silica nanoparticles after 1 day at room temperature (a) and at 80 °C (b). Even at higher temperatures, there still remain some particles unaffected. This can be explained by the high concentration of silica nanoparticles. Particles remain stable when the SSC of the solution was reached.

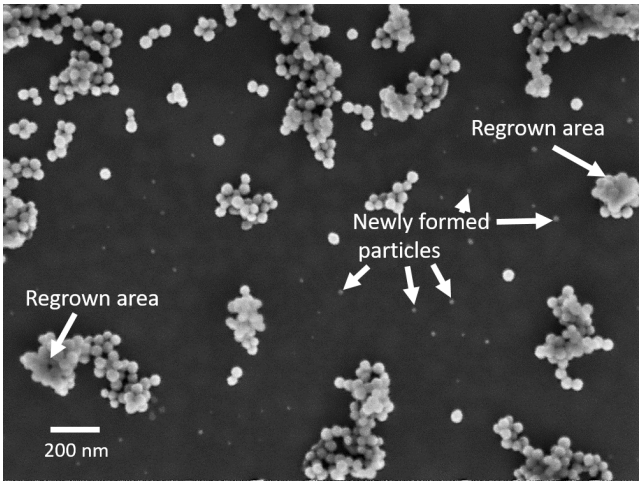

Figure 4.9: SEM image of the silica nanoparticles after 24 hours at room temperature in a 250 mg L^{-1} silica-solution (Section 4.3.4). Regrown particles as well as newly formed, ∼8 nm sized particles formed due to the oversaturation with silica. The nanoparticles act as nuclei for the aqueous silica in solution.

CHAPTER 5

Titania-Mediated Stabilization of Fluorescent Dye Encapsulation in Mesoporous Silica Nanoparticles

This Chapter is published in Nanoscale Advances
https://doi.org/10.1039/D4NA00242C

Spitzmüller, L., Berson, J., Nitschke, F., Kohl, T., Schimmel, T. (2024): Titania-Mediated Stabilization of Fluorescent Dye Encapsulation in Mesoporous Silica Nanoparticle. *Nanoscale Advances*, 6.

In this Chapter, a new and stable synthesis procedure is presented to overcome the stability problems of silica nanoparticles highlighted in Chapter 4. The major advancements are:

- Calcined mesoporous silica nanoparticles are used as host carrier for different fluorescent tracer molecules
- By growth of a protective titania shell, pores are blocked, hence leakage of the molecules and dissolution of the carrier are prevented

Abstract

Mesoporous silica nanoparticles hosting guest molecules are a versatile tool with applications in various fields such as life and environmental sciences. Current commonly applied pore blocking strategies are not universally applicable and are often not robust enough to withstand harsh ambient conditions (e.g. geothermal). In this work, a titania layer is utilized as a robust pore blocker, with a test-case where it is used for the encapsulation of fluorescent dyes. The layer is formed by hydrolysis process of a titania precursor in an adapted microemulsion system and demonstrates effective protection of both the dye payload and the silica core from disintegration under otherwise damaging external conditions. The produced dye-MSN@TiO_2 particles are characterized by means of electron microscopy, elemental mapping, ζ-potential, X-ray diffraction (XRD), nitrogen adsorption, Thermogravimetric analysis (TGA), fluorescence and absorbance spectroscopy and Fourier Transform Infrared Spectroscopy – Total Attenuated Reflectance (FT IR ATR). Finally, the performance of the titania-encapsulated MSNs is demonstrated in long-term aqueous stability and in flow-through experiments, where owing to improved dispersion encapsulated dye results in improved flow properties compared to free dye properties. This behavior exemplifies the potential advantage of carrier-borne marker molecules over free dye molecules in applications where accessibility or targeting are a factor, thus this encapsulation method increases the variety of fields of application.

5.1 Introduction

Mesoporous silica nanoparticles (MSN) emerged as versatile carriers for a wide variety of guest molecules, significantly advancing many research fields from nanomedicine, biotechnology, pharmaceutics and catalysis to environmental sciences including reservoir technology for renewable energies (Akhter et al. 2022, Jeelani et al. 2020, Nayl et al. 2022, Ren et al. 2023). Their well-defined pores with tunable sizes, large surface areas, and ease of functionalization make MSNs ideal for a variety of applications (Li et al. 2019). MSNs function as high-capacity carriers, useful for loading molecules and transporting them to specific locations or through preferred paths. Their intricate porous structure allows for the concentration and entrapment of a variety of molecules, ranging from therapeutic agents to diagnostic markers (Kim et al. 2008). The MSNs can be designed to carry their payload throughout their application or to release it at an opportune moment or location in response to a specific and predetermined external stimulus. Carrier MSNs can be directed to a desired location within biological or geological systems or across various mediums, leveraging the targeting capabilities conferred by surface modifications (Jafari et al. 2019, Paris et al. 2018, Rudolph et al. 2020). Such targeted transport is crucial in applications where the mere presence of concentrated molecules at a specific site can induce the desired effect, such as in imaging or

sensing (Manzano and Vallet-Regí 2020). In contrast, release MSNs is based on the ability to release the payloads at targeted locations, which is particularly advantageous for targeted drug delivery. This capability hinges on stimuli-responsive release mechanisms where the MSNs are engineered to respond to specific environmental triggers—such as pH changes, temperature fluctuations, or enzymatic activities prevalent at the target site (de la Torre et al. 2014, Gimenez et al. 2015, Li et al. 2019, Natarajan and Selvaraj 2014). The controlled release ensures that the therapeutic agents exert their action precisely where needed, minimizing systemic distribution and associated side effects. This precision in payload release from MSNs underscores a significant advancement in nanomedicine, offering a more targeted and effective therapeutic strategy (Mendiratta et al. 2019).

Whether the MSN system is designed to release its payload or retain it throughout the process, efficient encapsulation is essential. It has to prevent leakage of the loaded molecules, protect them from premature degradation due to prevalent conditions outside of the host nanoparticle but also ensures their controlled release at the target site (Braun et al. 2016). The process of encapsulation itself may be challenging, as the chemical modifications required to form the encapsulating layer may harm the stability and functionality of the payload.

The inherent instability of MSN in aqueous media is a double-edged sword in the realm of nanotechnology applications. In aqueous environments, unmodified silica nanoparticles tend to dissolve within hours (Croissant et al. 2017, Spitzmüller et al. 2023b). The silica dissolution and its rate depend on ambient factors such as temperature, pH-value and ionic strength of the solution, the presence of specific ions and chemicals as well as on properties of the silica itself such as degree of condensation, size and porosity (Braun et al. 2016, Croissant and Brinker 2018, Paris et al. 2017, Spitzmüller et al. 2023b).This instability can be advantageous in fields like biomedicine, where controlled dissolution can be harnessed for timed release of therapeutic agents or creating clearance pathways for excretion of the treatment and its metabolites (Lin et al. 2012, Manzano and Vallet-Regí 2020, Möller and Bein 2019). Conversely, it poses a challenge in applications requiring long-term structural integrity, such as in subsurface reservoir tracing (e.g. for hydrology, for oil and gas industry and as geothermal tracer), structural composites or as catalyst supports where premature dissolution would compromise functionality.

A strategic application of an encapsulation layer can slow the dissolution by restricting access of water molecules to the silica surface, thereby modulating the release kinetics of encapsulated substances (Mahon et al. 2012). A non-porous layer can provide an even more significant barrier, potentially halting the dissolution altogether (Cauda et al. 2010). Such encapsulation not only extends the range of environments in which silica nanoparticles can be utilized but also has the potential to fine-tune their dissolution kinetics for specific applications, enhancing their versatility and performance across various scientific and industrial fields (Spitzmüller et al. 2023b).

In this work, we present an approach that utilizes a titania (TiO_2) layer to encapsulate molecules within MSNs. Titania is robust and stable and exhibits low solubility in water under a wide range of pH values, properties which make it ideal for applications where (aqueous) long-term stability and/or endurance under harsh ambient conditions is needed (e.g. imaging, environmental tracing) (Bultreys et al. 2022, Schmidt and Vogelsberger 2009). By forming a protective titania layer over the encapsulated molecules, it is possible to enhance the stability and prevent leakage of the payload.

Titania can be applied to coat silica nanoparticles by either chemical or physical deposition techniques. Many different synthetic routes exist, using hydrothermal and/or microemulsion synthesis with various titania precursors (Guo and Dong 1999, Hanprasopwattana et al. 1996, Karkare 2014, Pineda-Aguilar et al. 2018), in either alkaline or acidic environments or as delayed co-condensation reaction with silica forming a silica-titania mixed layer. Other deposition methods include vapor deposition (Farooq et al. 2018) of a titania layer or nanoparticles or producing aerosols (Balboa et al. 1987). The synthesis parameters greatly affect the subsequent thickness, porosity, uniformity and crystalline structure of the formed layer, which in turn has a significant influence on the performance of the titania in terms of light transparency and scattering and stability. For the functionality of the particles in imaging and as fluorescent hydrological or geothermal tracers it is however pivotal to minimize the suppression of the optical signal of the encapsulated molecules, i.e. the titania needs to be sufficiently transparent in the range of visible light. Additionally, the titania coating is supposed to act as pore blocking agent and stabilization of the silica carrier against dissolution effects.

Moreover, for long-term applications (for example “geoimaging”, tracer technology in groundwater and reservoir exploration) it is crucial having a carrier that is not prone to degradation and additionally having ideally a pore blocking agent that prevents leaching of the loaded dye while also ensuring the integrity of the carrier. While titania has already been utilized as a thin film or coating layer for e.g. increasing biocompatibility by altering the surface of drug loaded MSN (Farooq et al. 2018), the robust and stable nature of titania has not been exploited for payload encapsulation applications.

The presented synthesis is applicable to encapsulate a wide variety of guest fluorescent dyes and the titania acts as an effective pore blocking agent for the tested mesoporous silica nanoparticles carriers. The dye-MSN@TiO_2 particles are characterized by electron microscopy, fluorescence and absorbance spectroscopy, infrared spectroscopy, x-ray spectroscopy and ζ-potentiometry. Successful encapsulation in proved by long-term stability experiments and flow-through experiments. Additionally, effect of titania-coating is compared to commonly applied hydrophobic and hydrophilic pore blockers.

5.2 Experimental

5.2.1 Synthesis

5.2.1.1 Materials

The following chemicals were used without further purification: Cetrimonium bromide (CTAB, Alfa Aesar 98%), tetraethyl orthosilicate (TEOS, Sigma Aldrich 99%), tetrabutyl orthotitanate (TBOT, Sigma Aldrich, synthesis grade), (3-mercaptopropyl)trimethoxysilane (MPTS, BLD pharm 95%), PEG-maleimide (BLD pharm 97% av. purity), n-octadecyltrimethoxysilane (C18, ABCR GmbH, 95%), dotriacontane ("paraffin" Sigma Aldrich, 97%), sodium dodecyl sulfate (Sigma Aldrich $\geq$99%), potassium chloride (KCl, VWR GPR Rectapur >99%), sodium chloride (NaCl VWR GPR Rectapur $\geq$99%) phosphate-buffered saline (PBS, VWR life science, biotechnology grade, pH 7.4), Millipore water (>18MΩ), ammonia (NH_4OH, Merck, 28-30%), ethanol (VWR Chemicals, AnalaR Normapur $\geq$99.8%), acetone (VWR Chemicals, AnalaR Normapur, $\geq$99.8%) dry acetonitrile (Merck, 99.5%), cyclohexane (VWR Chemicals, AnalaR Normapur $\geq$99.5%), n-Hexanol (VWR GPR Rectapur $\geq$98%), Triton X-100 (Sigma Aldrich for analysis), sulfuric acid (H_2SO_4, Merck Supelco 98%), absolute toluene (VWR Chemicals, AnalaR Normapur $\geq$99.5%), hexane (Carl Roth, 99%), hydrochloric acid (HCl, Honeywell Fluka 36.5-38%), sodium hydroxide (NaOH, Merck Emsure $\geq$99%), nitrogen (<10ppm O_2). The following dyes were used without further purification: coumarin 307 (C307, Radiant Dyes Chemie), sodium fluorescein (fluo, Sigma Aldrich), rhodamine 6G (R6G, Sigma Aldrich for fluorescence), rhodamine B (RhB, Sigma Aldrich for fluorescence), sulforhodamine G (SG, Sigma Aldrich 60% dye content), tris(2,2-bipyridyl)dichlororuthenium(II) hexahydrate ($Ru(bpy)_3^{2+}$, Acros organics, 98%) and rhodamine 800 (R800, Sigma Aldrich).

5.2.1.2 Synthesis of carrier

The mesoporous carriers are synthesized according to Huang et al. (2010). Briefly, 109 mg cetrimonium bromide (CTAB) is mixed with 54 mL Millipore water and 1.194 mL ammonia (NH_4OH) added. After stirring for 1 hour, 0.465 mL tetraethyl orthosilicate (TEOS) is added dropwise, followed by 5 hours at high stirring rate. Finally, the particles undergo several wash-centrifugation cycles with water and ethanol and are dried in vacuum. The template (CTAB) is removed via calcination at 550°C at a heating rate of 1°C/min over 6 hours.

5.2.1.3 Encapsulation of dyes

Encapsulation of dyes was performed in slightly altered version of Rudolph et al. (2020). 4 mg dye per 10 mg particles were added to the calcined particles, and stored overnight in a glovebox under nitrogen atmosphere. Then, 0.5 mL dry acetonitrile per 10 mg particles is added and the particle dispersion is stirred overnight in glovebox.

5.2.2 Surface modifications

5.2.2.1 Coating with titania

The particles are taken out of glovebox and retrieved by centrifugation. After washing with hexane, the particles are dried in vacuum, weighted (usually 50 mg) and redispersed in 4.8 mL Millipore water using a sonotrode. Titania coating was performed using a reverse water-in-oil microemulsion method adapted from Fu and Qutubuddin (2001). Briefly, 15 mL cyclohexane was mixed with 3.6 mL 1-hexanol and 3.44 mL TritonX-100. After stirring for 1 minute, the particle dispersion is added followed by dropwise addition of 307 µL TBOT. After further stirring for 20 minutes, 60.9 µL H_2SO_4 (98%) is added to the microemulsion and stirred for 48 hours. The microemulsion is broken by addition of excess amount of acetone, followed by washing-centrifugation cycles with acetone, ethanol, ethanol-water, and water.

5.2.2.2 Pore blocker

Two different type of pore blockers were chosen; a hydrophilic polymer (poly(ethylene) glycol, PEG), and a hydrophobic paraffin.

PEG: The particles are removed from the glovebox and retrieved by centrifugation. After washing with hexane, the particles are dried in vacuum. PEGylation was performed adapting von Baeckmann et al. (2018). Briefly, the dried particles are mixed with absolute toluene and heated under inert atmosphere to 100 °C while stirring moderately. After 3 hours, thiol-functionalization was performed by adding 12 mM (3-mercaptopropyl)trimethoxysilane (MPTS) per gram particles and stirred further for 4 hours under inert atmosphere at 100 °C. After, the particles are retrieved by centrifugation and dried in vacuum. For PEGylation, PEG-maleimide was used. The thiol-maleimide click chemistry reaction was performed as described by von Baeckmann et al. (2018). Briefly, 75 mg of thiol-functionalized nanoparticles are suspended in 5 ml Millipore water and stirred vigorously overnight. After, 0.5 mL phosphate buffered saline (PBS) is added to the solution, followed by 75 mg PEG-maleimide. The solution is stirred overnight at ambient temperature. Finally, the particles are retrieved by centrifugation and washed at least three times with water until supernatant remains clear. After drying in vacuum, the particles are ready to use.

Paraffin: After dye encapsulation, particles dispersed in acetonitrile are removed from the nitrogen atmosphere in the glovebox and 75 µL n-octadecyltrimethoxysilane (C18) per 10 mg particles is added. The solution is stirred overnight under ambient conditions. The particles undergo several washing-centrifugation cycles with acetonitrile and hexane and are eventually dried. For paraffin coating, dried particles are redispersed in 8 mL hexane and 75 mg dotriacontante is added per 10 mg particles. The solution is sonicated for 15 minutes, followed by stirring for 15 minutes. The particles are retrieved by centrifugation followed by washing-centrifugation cycles with a mixture of SDS-water and water until supernatant is clear.

5.2.3 Analytical devices

Samples were characterized using SEM, TEM, nitrogen absorption (BET surface measurement), TGA, FT-IR ATR, XRD, ζ-potentiometry, fluorescence and absorbance spectroscopy.

Scanning Electron Microscopy (SEM): A Zeiss Leo 1530 was used to analyze size, shape and size distribution of the nanoparticles. Operated in InLens and SE2 mode.

(Scanning) Transmission Electron Microscopy ((S)TEM) and elemental mapping: (S)TEM and elemental mapping was performed using a ThermoFischer Themis 300 probe-corrected (S)TEM with 300kV.

Brunauer-Emmett-Teller (BET) surface measurement: For BET measurements, the samples were degassed at 90°C overnight in vacuum and surface area was determined by nitrogen adsorption with a Quantachrome Nova 4000e.

Thermogravimetric Analysis (TGA): TGA measurements were performed with a STA 409PC Netzsch under atmospheric conditions with a heating rate of 10°C/min up to 600°C. The results were normalized to the relevant weight loss percentage expected for the respective dye (Qiu et al. 2015).

Fourier Transform Infrared Spectroscopy – Attenuated Total Reflectance (FT-IR ATR): FT-IR ATR analysis was performed using a Nicolet iS50 with wavenumbers from 4000 to 400 cm^{-1}. Measurements were repeated twenty times. Samples were measured in dry conditions.

X-Ray Diffraction (XRD): The powder x-ray (XRD) data of the samples were collected using a PANalytical X'Pert Pro x-ray diffractometer with Cu Kα radiation. The angle range between 5 and 80° (2Θ) was recorded over 2 hours at room temperature with a step size of 0.01°s^{-1}.

ζ **potentiometry**: ζ-potentials were retrieved measuring electrophoretic potential with a Malvern Zetasizer NanoZS using a folded capillary cell. Analyses were performed in 10 mM KCl solutions at pH 1.8, 4.4, 6.6, 8.5 and 9.5m at 25°C. pH-values were adapted by addition

of HCl or NaOH. Measured electrophoretic potential of the particles was automatically converted to ζ-potential values using Smoluchowski approximation. Generally, ζ-potential represents net electrical charge in the shear plane and are result of surface charge of particles, attached oppositely charged ions in the Stern layer and diffuse double layer. Therefore, ζ-potential can serve as approximation to surface charge of particles. However, they are strongly dependent on temperature, ionic strength, and pH.

Fluorescence and absorbance spectroscopy: Fluorescence was measured using a Cary Eclipse spectrofluorometer, UV-Vis absorbance was measured with an UV-VIS Perkin Elmer Lambda 9 spectrometer. For both analyses, cuvettes with an optical path length of 1 cm were used. Photodegradation of fluorescence was tested by exposing the samples in sealed quartz cuvettes to UV-light (lamp specification 400 W, MHL570). Reduction in fluorescence due to lower quantum yield of loaded dye molecules and adsorption and scattering of the particle matrix was determined by fluorescence spectroscopy comparing free dye and encapsulated molecules. The concentration of the dye solution used for this comparison was determined according to the calculated amount of loaded dye per particle, based on the results of the TGA analysis.

Flow-through experiments: A 25 cm glass column, with 0.8 cm inner diameter was filled with washed and dried (105 °C) coarse quartz sand (size 1.0-1.6 mm) and saturated with deionized water using a peristaltic pump. Flow rate was measured 5x over 30 sec to be 40 mL/min. The glass column was connected to a 3.3x1.0x1.0 cm^3 quartz flow-through cuvette. Fluorescence was measured automatically with a frequency of 1 Hz giving a continuously measured breakthrough curve of dye, dye-MSN and dye-MSN@TiO_2. Dye and particle concentration were measured in advance to obtain a calibration line to convert fluorescence intensity into concentration. With the concentration and flow-through velocity, retrieval rates and vice-versa retention of dye and particles can be calculated.

5.3 Results and discussion

5.3.1 Synthesis of dye-doped mesoporous silica nanoparticles

Mesoporous silica nanoparticle carrier was produced using modified Stöber synthesis with CTAB-micelles as the sacrificial organic template (Huang et al. 2010). Resulting carrier size was determined to be 142 $\pm$ 24 nm (Figure 5.1A,C), with mean pore sizes of 2.7 nm (Figure 5.1C), a BET surface area of 868 m^2/g and ζ-potential in 10 mM KCl at pH 6.6 of -18.8 mV $\pm$ 4.2 mV. To ensure long-term hydrothermal stability, the carrier was calcined. Spitzmüller et al. (2023b) showed that calcination is able to re-order silanol bonds to siloxane bonds on the silica surface, thus increasing hydrothermal stability. Fluorophore-doping was adapted from Rudolph et al. (2020) and resulting dye concentration inside the MSN carrier was determined

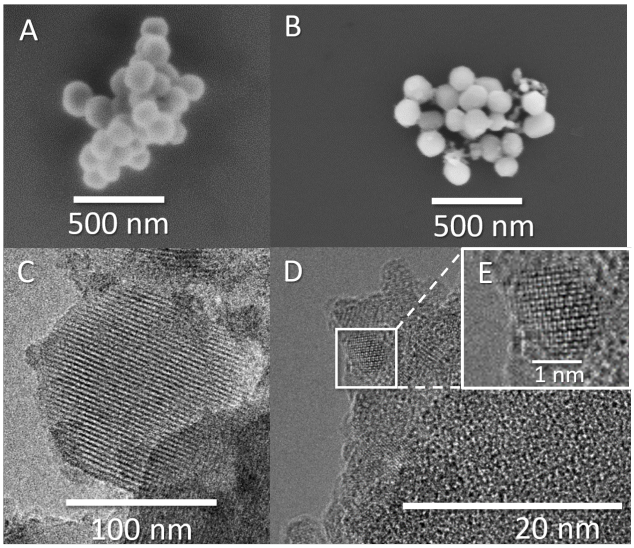

Figure 5.1: SEM and TEM images of MSN and dye-MSN@TiO_2 particles. (A) and (B): SEM image of pristine MSN (A) and dye-MSN@TiO_2 (B). (C) Shows pore structure of MSN, (D) shows interface of MSN and titania layer. Inset picture (E) shows crystal lattice of titania in the shell. Titania crystallites show sizes of 3–4 nm.

to be approx. 19 mg/g using TGA, comparable to previously reported MSN loading capacities of 5-70 mg/g (Hirayama et al. 2021, Mozafarinia et al. 2021). In this study, we deliberately used fluorophores that were contained in the pores but were not covalently bound to the silica matrix, both in order to show the generality of the encapsulation method and to be able to demonstrate adequate pore blocking functionality. Since fluorophore molecules were not chemically bound to the MSN matrix, sonication or dissolution in water would remove unbound fluorophore by diffusion unless this is prevented by a stable and leakage proof coating.

5.3.2 Titania coating of mesoporous carrier

Titania coating was performed adapting a reversed microemulsion synthesis (water-in-oil, W/O) from Fu and Qutubuddin (2001). Firstly, dye-impregnated mesoporous silica nanoparticles were well dispersed in water using a sonotrode. The amount of required water was derived using the ratio between water-surfactant and microemulsion droplet size (Arriagada and Osseo-Assare 1999, Richard et al. 2017). Even though the silica condensation reaction was performed with alkaline catalysis, acidic conditions were chosen for the growth of the titania layer, as this was found to be the most controlled and selective process, yielding highly reproducible results. Concentrated sulfuric acid was used to acidify the water phase of the emulsion due to its low water content, so that addition of the acid would have negligible influence on the size of the water-in-oil droplets. The titania precursor that was chosen

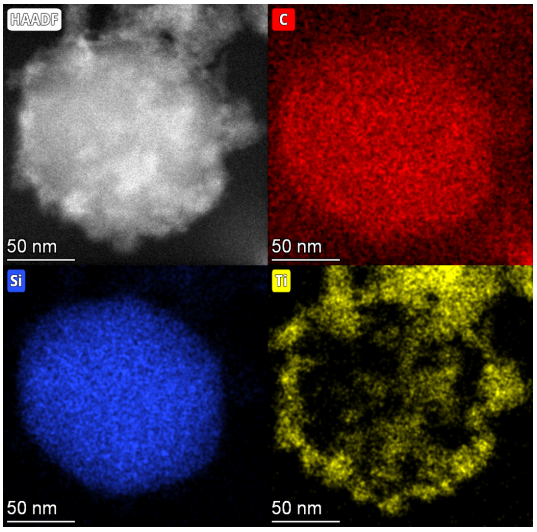

Figure 5.2: STEM image of dye-MSN@TiO_2 (top left) and the corresponding elemental mapping. Carbon (top right, carbon signal emanates from the R800 dye inside the particle with a slight background signal from the carbon tape), silicon (bottom left) and titanium (bottom right).

was tetrabutyl orthotitanate (TBOT), which likewise ensure high reproducibility of the hydrolysis products. The usage of a strong acid gives two major implications. First, the silica nanoparticles are prevented from degradation due to acidic environment (Spitzmüller et al. 2023b), which implies that the network remains intact during synthesis process. Second, some fluorophores are sensitive to acidic pH such as sodium fluorescein. We therefore advise to protect these fluorophores by growing a silica shell using the microemulsion method as described in Rudolph et al. (2020) prior of growing a titania shell in order to prevent fluorescence loss. By addition of a protective silica shell, the fluorophore inside the pores is shielded against the acid and maintains its fluorescence. However, solely using a silica shell does not sufficiently stabilize the particles against disintegration and still a protective titania layer is required. As example, we performed a fluo-MSN@SiO_2@TiO_2 synthesis (Supplementary Figure 5.7) yielding stable, protected fluorescent particles. Other dyes such as rhodamines do not require this additional step (Jorge et al. 2013), and we therefore focused on using dyes which are not sensitive to acidic environments. Resulting dye-MSN@TiO_2 particles show sizes of 151 $\pm$ 38 nm (determined by SEM, Figure 5.1B,D). The BET surface area is reduced from 868 m^2/g to 469 m^2/g, both values being in agreement with open and capped MSN, respectively (Cauda et al. 2011, Farooq et al. 2018, Li and Kim 2005).

5.3.3 (S)TEM and elemental mapping/Electron microscopy

STEM analysis of the MSN revealed ordered hexagonal pore shape with sizes of 2-3 nm (Figure 5.1C) which is in agreement with previous observations (Huang et al. 2010). The titania layer thickness is measured to be 7.1 nm $\pm$ 4.3 nm (n=36) and shows a mixture of

amorphous titania and anatase nanocrystallites with 3-4 nm average size (Figure 5.1D). Figure 4.1E shows a zoom on a titania crystallite in the titania layer with a clearly discernable crystal lattice. Elemental mapping further confirmed the presence of a silica core and a titania shell (Figure 5.2) with atomic fractions of 67.91 $\pm$ 3.6% oxygen, 27.31 $\pm$ 3.82% silicon and 4.78 $\pm$ 0.81% titanium. The presence of dye inside the MSN is indicated by carbon accumulation (Figure 5.2, corresponding to the presence of the R800 dye, $C_{26}H_{26}ClN_3O_5$ inside the pores).

5.3.4 Zeta potential

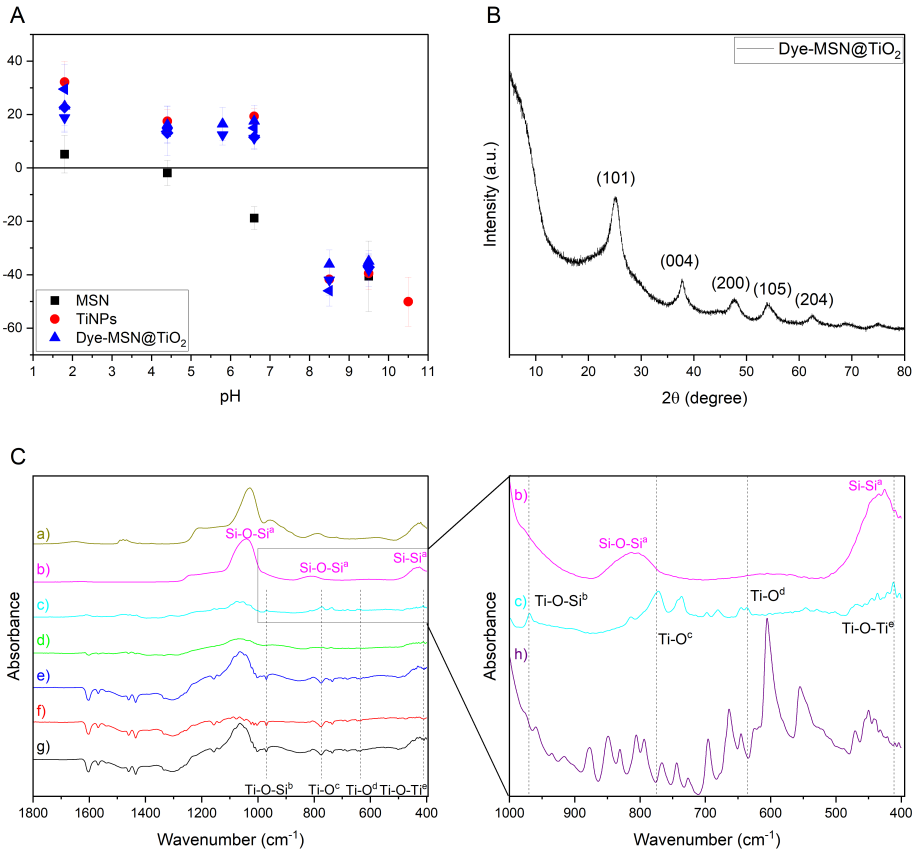

Figure 5.3: Overview of characterization methods. (A) ζ-potential evolution over pH for MSN (black squares), titania nanoparticles (red dots) and various dye-MSN@TiO_2 (blue symbols). (B) Representative XRD pattern of Dye-MSN@TiO_2. Peaks can be assigned to anatase, a polymorph of titania. (C) ATR absorbance spectra of CTAB-MSN (a), calcined MSN (b), SG-MSN@TiO_2 (c), fluo-MSN@SiO_2@TiO_2 (d), R800-MSN@TiO_2 (e), RhB-MSN@TiO_2 (f), R6G-MSN@TiO_2 (g). Zoom-in on the 1000-400 cm^{-1} region marked with a grey box in (C). Comparison of pristine, calcined MSN (b) to SG-MSN@TiO_2 (c) and spectra of SG-dye (h). Literature sources for peak assignment [a] Socrates (2001), [b] Zu et al. (2015), [c] Islam et al. (2023), [d] Hema et al. (2013), [e]. Pérez et al. (2020)

ζ-potential evolution over pH-range for pristine MSN (black square), pure titania (red dot) nanoparticles and various dye-MSN@TiO_2 (blue symbols) is displayed in Figure 5.3A. Pristine MSN carrier and pure titania particles show an isoelectric point (IEP) between 1.8 and 4.4 and 6.6 and 8.5 respectively, which is in agreement with data from similar nanoparticle systems (Balboa et al. 1987, EL Mekkawi and Abdel Mottaleb 2005, Franks 2002, Wilhelm and Stephan 2006). The dye-MSN@TiO_2 nanoparticles consist of both silica and titania. Consequently, one could expect the ζ-potential to be in range between these two "end-points" (Hsu et al. 1992, Ryu et al. 2003). In fact, ζ-potential variations are decent indicators in assessing titania-coating efficiency on silica nanoparticles (Wilhelm and Stephan 2006). Wilhelm and Stephan (2006) observed a slight shift of IEP from 6.7 for pure titania to 5.7-6.7 for titania-coated silica nanoparticles and only minor differences in absolute ζ-potential. For our dye-MSN@TiO_2, ζ-potential evolution and IEP also resembles titania more than pristine MSN. Hence, two major implications can be drawn: the coating of MSN with titania was successful and the coating layer further effectively shields the core (MSN and dye) as there is also no significant difference between the measured potential of different incorporated dyes, regardless of their charge (anionic, cationic).

5.3.5 XRD

XRD was used to analyze the titania properties. A representative XRD pattern is shown in Figure 5.3B. The broadness of the peaks is either a sign of amorphous nature of the samples or of small crystallite size, which can be expected from sol-gel process without subsequent heat treatment (Lebedev et al. 2016, Pineda-Aguilar et al. 2018, Yanagisawa and Ovenstone 1999, Zhang et al. 2001). The peaks at 25.1°, 37.8°, 47.8°, 54°, 62.6° can be assigned to the (101), (004), (200), (105), and (204) planes of anatase (TiO_2 polymorph), respectively (Wang et al. 2013a). Amorphous silica diffraction peak is in the 2Θ range between 23° and 25° (Yan et al. 2005), possibly leading to the broadening of the anatase diffraction peak at 25.1°. Crystallite size of anatase particles can be estimated to be 3-4 nm using Scherrer equation which is confirmed by TEM data (Figure 5.1E). Anatase has a band gap of 3.2 eV, i.e. is transparent for visible light (Luttrell et al. 2014, Ullattil and Periyat 2017). As result, titania is applicable as coating layer for the fluorophore-doped mesoporous silica nanocarriers as long as the excitation-emission wavelengths of the loaded fluorophores lay outside of the UV-range.

5.3.6 FT-IR ATR

Figure 5.3C shows FT-IR ATR absorbance spectra of MSN and various dye-MSN@TiO_2. Successful template removal through calcination is proven (CTAB-MSN (a) to calcined MSN (b)). Additionally, the disappearance of Si-OH bonds at 950 cm^{-1} indicate higher hydrothermal

stability of the synthesized silica nanoparticles due to a higher degree of condensation (Spitzmüller et al. 2023b). Figure 5.3C c to g show ATR spectra of SG-MSN@TiO_2, Fluo-MSN@SiO_2@TiO_2, R800-MSN@TiO_2, RhB-MSN@TiO_2 and R6G-MSN@TiO_2. The spectra reveal the characteristic Si-O stretching, bending and rocking vibrations at 1100 cm^{-1}-1000 cm^{-1}, 811 cm^{-1} and 430 cm^{-1}, respectively (San Andrés et al. 2000). Any additional peak originate either from the dye or to the titania. As shown in zoom-in on Figure 5.3C, absorbance spectra of dye-MSN@TiO_2 are mostly a superimposition of the silica carrier (a) and the spectra of the dye (h). Consequently, non-assigned peaks must originate either from titania coating process chemicals, from titania bonds or from interaction of titania and silica. Generally, the spectra intensity is lowered which can be attributed to the presence of titania (Vuluga et al. 2008). Studies show Si-O-Ti bonds in the region of 960-910 cm^{-1}, Ti-O stretching and Ti-O-Ti bending vibrations at around 770 cm^{-1}, sym. Ti-O-Ti stretching at 411 cm^{-1} and deformation vibration of Ti-O-Ti in the area 1200-1000 cm^{-1} (Islam et al. 2023, Kumar et al. 2014, Li et al. 2005, Murashkevich et al. 2008, Teamsinsungvon et al. 2022, Zeitler and Brown 1957). The peak observed at 960 cm^{-1} in all dye-MSN@TiO_2 might therefore indicate Si-O-Ti but could be also be assigned to Si-OH bonds. However, since there is no peak at the MSN carrier (Figure 5.3C) the appearance of the bond might indicate Si-O-Ti bonds rather than Si-OH bonds. This assumption can be based on data from Zhuravlev (2000) that showed slow rehydroxylation (i.e. Si-OH bonds) of calcined silica surfaces (i.e. Si-O-Si bonds) under ambient conditions. Furthermore, the peaks at 770 cm^{-1}, 635 cm^{-1} and 411 cm^{-1} can be ascribed to Ti-O stretching and Ti-O-Ti bending, Ti-O vibrations and sym. Ti-O-Ti stretching (Hema et al. 2013, Kumar et al. 2014, Murashkevich et al. 2008, Zeitler and Brown 1957). In summary, the ATR spectra of the dye-MSN@TiO_2 particles show silica-related, dye-related, titania-related vibrations as well as additionally silica-titania bonds, supporting the observation that dye-encapsulation by titania coating was successful.

5.3.7 Fluorescence and absorbance spectroscopy and UV-sensitivity

Figure 5.4 compares fluorescence emission spectra of various dyes (C307, RhB and Rubpy, spectra of additional dyes are shown in Figure 5.7) and corresponding spectra of the dyes encapsulated in the MSN@TiO_2 system. The spectral shifts seen upon encapsulation of the dye molecules can be explained by influence of the chemical surrounding (Jorge et al. 2013), i.e. replacing the water solvent with the silica-titania matrix or can be attributed to rigid framework of the carrier reducing rotational freedom of incorporated dyes (Avnir et al. 1984). In both cases, the shifts indicate the successful encapsulation of the dyes (Auger et al. 2011). Corresponding to the peak shifts in fluorescence spectroscopy, shifts could also be observed in UV-Vis absorbance spectra (Supplementary Figure 5.8). Strongest peak shifts were found for R800-MSN@TiO_2 and fluo-MSN@SiO_2@TiO_2 (Figure 5.8A,B). While the absorbance spectra of free rhodamine 800 dye shows both, monomer (at 689 nm) and dimer (at 629 nm),

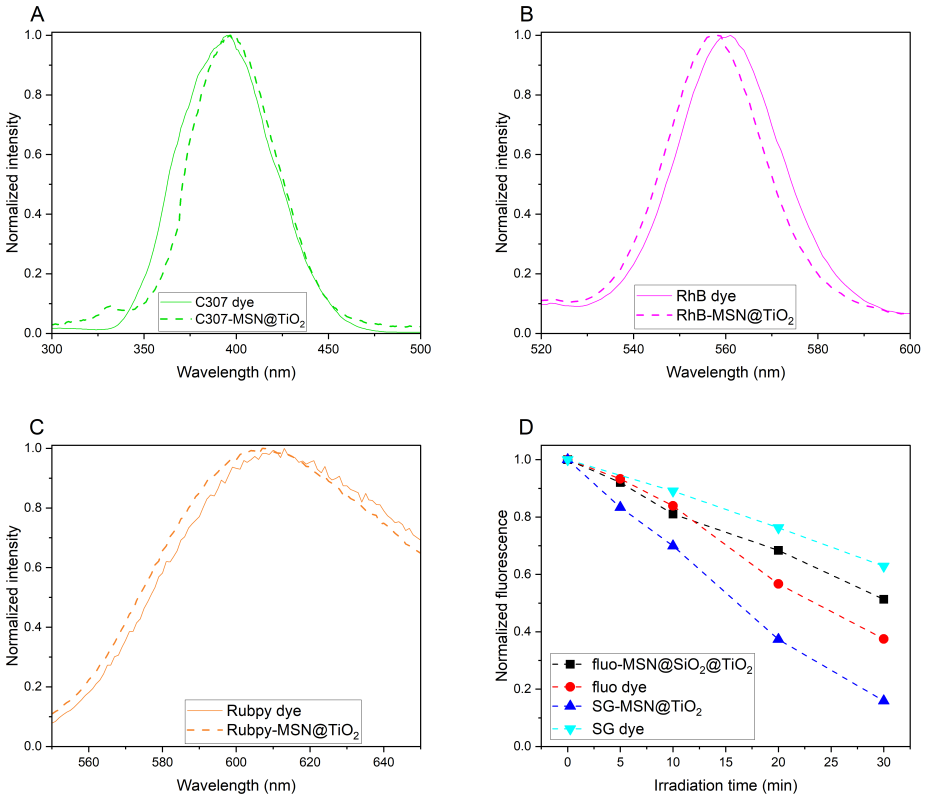

Figure 5.4: Normalized fluorescence intensity of coumarin 307 and C307-MSN@TiO_2 (A), rhodamine B and RhB-MSN@TiO_2 (B) and tris(bipyridine)ruthenium(II) chloride ("Rubpy") and Rubpy-MSN@TiO_2 (C). Normalized fluorescence and fluorescence loss over irradiation time under UV-light is shown for sodium fluorescein and SG (D).

upon encapsulation a single peak is shifted to 618 nm, likely as a result of dimerization of the encapsulated dye molecules (Sekigushi et al. 2006). For sodium fluorescein dye, absorbance peaks can be assigned to dianionic and monoanionic forms, while upon encapsulation only the dianionic absorbance peak with a minor shift is visible. This can be explained by the synthesis procedure: dianions preferentially form in basic environments while the occurrence of other forms increases with decreasing pH values (Klonis and Sawyer 1996). Based on the TGA results, an estimation of the loss of fluorescence intensity due to phenomena such as dye dimerization or absorption and scattering by the different particle layers can be performed. Comparison of the fluorescence intensity of a 10^{-2} mg/mL RhB-MSN@TiO_2 and a free RhB solution with a concentration corresponding to the amount of encapsulated dye ($1.9\ 10^{-4}$ mg/mL) shows 10% fluorescence intensity for the encapsulated dye. Reduction in fluorescence signal originate from lower quantum yield of the encapsulated dye as well as absorption and scattering by the nanoparticle matrix. However, it should be noted that even with the reduction in fluorescence signal, the concentration of dye molecules in a confined

space inside the particles results in a strong fluorescence signal. Achieving comparable signal intensities with free dye molecules in a large volume system such as a geological reservoir would require a very large amount of dye.

Sodium fluorescein is highly pH-sensitive and an additional silica shell between dye-MSN and titania layer was necessary to avoid contact of the acid used in titania layer synthesis and the encapsulated dye. This additional silica shell has proven to have further advantages as it helps reducing titania-mediated photocatalytically-induced degradation of the encapsulated dyes. The additional silica layer acts as a separation from the anatase crystallites, which are known to accelerate photodegradation under UV-light (Haghighatzadeh et al. 2017, Hu et al. 2013). Accelerated photodegradation was indeed observed for particles without the silica separation layer, such as SG-MSN@TiO_2 (Figure 5.4D). In contrast, in the case of fluo-MSN@SiO_2@TiO_2 and free sodium fluorescein, the encapsulated sodium fluorescein dye photodegradation is slowed.

5.3.8 Stability, sorption and flow-through experiments

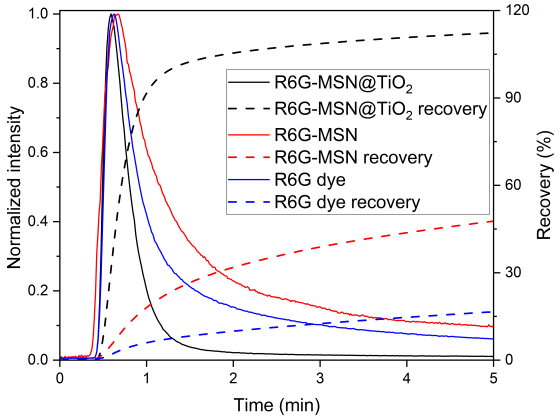

Figure 5.5: Flow-through quartz sand filled 25 cm column. Dye R6G is known to adsorb on quartz while R6G-MSN@TiO_2 can penetrate through column. As reference for pore blocking ability of titania in R6G-MSN@TiO_2, R6G-MSN are used without any coating.

Leaching tests were conducted to assess the possible payload leak due to imperfections in the titania encapsulation layer monitoring the fluorescence signal of the dye-loaded MSNs. Fluorescence intensity changes over 48 hours in Millipore water by average 4.77% $\pm$ 2.57% (n=5), in 0.01 M NaCl by average 4.96% $\pm$ 2.95% (n=10) and in 0.1 M NaCl by average 2.82% $\pm$ 1.71% (n=8) Supplementary Table 5.1) while monomeric silica concentration in solution (measured with photometry) remains in the solubility range of quartz (<10 mg/L at room temperature). These results underline the stability of the encapsulation method in

order to prevent leakage of the dye and dissolution and disintegration of the silica carrier. In contrast, if the coating would not have been protective, stronger deviations in fluorescence intensity (as measured for free dyes in 0.01 M NaCl, Table 5.1 in Supplementary) and increased monomeric silica concentrations due to carrier dissolution/disintegration could be expected (Spitzmüller et al. 2023b). Flow-through experiments were conducted to further assess the encapsulation stability of the titania layer by comparing the transport properties of free dye, dye in MSN without encapsulation and encapsulated dye. Hereby, a cationic dye was chosen, as retention is expected to be high. Figure 5.5 shows a comparison of the breakthrough curves of R6G dye, R6G-MSN and R6G-MSN@TiO_2. R6G as a cationic dye is expected to adsorb on the negatively charged surface of the sand grains and indeed only 16.4% are retrieved within 5 minutes. Contrary, when dye is encapsulated inside MSN carrier coated with a protective titania layer the cationic dye is effectively shielded from its surrounding (as also corroborated by the ζ-potential measurements) and the adsorption depends on the outer titania layer. Consequently, sorption is dramatically reduced and the retrieval of R6G-MSN@TiO_2 is nearly 7-fold that of the free R6G dye, with full recovery within 5 minutes. Furthermore, R6G-MSN@TiO_2 show a shorter retention time and less pronounced tailing compared to dye breakthrough curve, which implies lesser dispersion and diffusion of the particles and proofs stable encapsulation of the dye. The stability of the encapsulation method is further highlighted by comparison with R6G-MSN without titania coating (Figure 5.5): While the recovery is higher for dye-MSN than for free dye, the long tailing observed indicates flow of free dye molecules and is hence a strong sign of leakage.

5.3.9 Comparison to other pore blockers

When a guest molecule is hosted inside a nanoparticle, the change in chemical environment and sterical effects lead to changes in guest molecule properties. In the case of loaded fluorescent molecules, this often manifests in shifts in the fluorescent emission wavelength. The addition of an encapsulation layer further changes the chemical environment and therefore causes an additional shift. The effect of titania coating is compared here to commonly used encapsulation strategies such as PEG or paraffin pore blocking. The thickness of the titania shell is with 7.1 nm comparable to the thicknesses of the organic modifications (5-15 nm (Aznar et al. 2011, von Baeckmann et al. 2018)). PEGylated MSN show hydrophilic surfaces while paraffin coated MSN are hydrophobic. Fluorescence spectra R6G-dye, R6G-MSN@TiO_2, R6G-MSN-SH-PEG, and R6G-MSN-C18-paraffin is shown in Figure 5.6. It can be seen that PEG and paraffin induce a bathochromic peak shift while titania induces a hypsochromic one. The shift can also be seen by the naked eye, as is shown in the inset picture in Figure 5.6A. In terms of ζ-potential, the titania coating leads to positive ζ-potentials at pH 6.6 in 10mM KCl while PEG- and paraffin-coated particles still show negative ζ-potentials under same conditions. Having positive ζ-potential bearing particles can favor for example their cellular uptake (Paris et al. 2018).

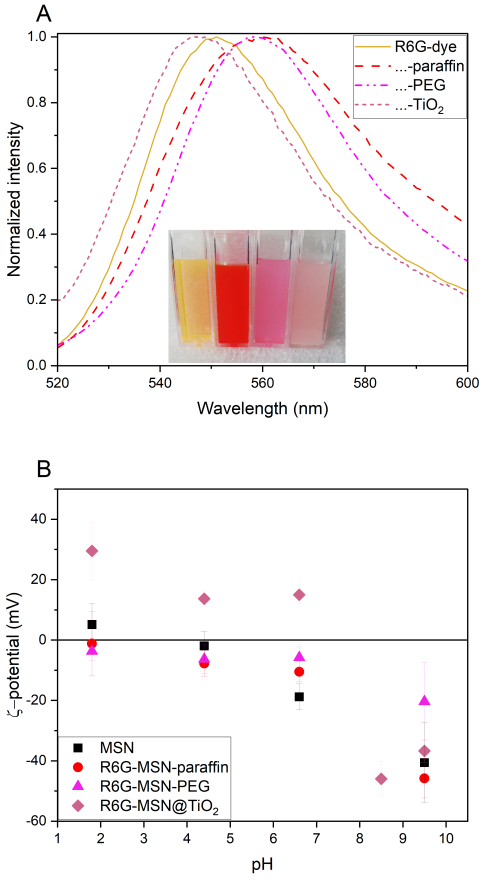

Figure 5.6: Fluorescence spectra (A) and ζ-potential (B) of hydrophilic, hydrophobic and metal oxide coating of mesoporous silica nanoparticles doped with rhodamine 6G dye. (A) Normalized fluorescence emission spectra for excitation wavelength at 480 nm. Bathochromic peak shift for PEG and paraffin coating 7 nm and 8 nm, respectively. Hypsochromic peak shift for titania coating 4 nm. Inset picture from left to right R6G-dye, R6G-MSN-C18-paraffin, R6G-MSN-SH-PEG and R6G-MSN@TiO_2. (B) ζ-potential of R6G-MSN@coating in comparison with carrier (MSN) over pH.

5.4 Conclusion

The here presented titania-mediated encapsulation method for fluorophores inside silica nanocarriers enables synthesis of highly stable and robust fluorescent nanoparticles. The synthesis chosen for this purpose utilized a reverse (water-in-oil) microemulsion environment, adapted for the size of the carriers, which facilitated selective titania growth in separate droplets while avoiding merging of particles. The synthesis has proven to be highly reproducible, which is another known advantage of using microemulsions (Wolf and Feldmann 2016), and was found to be applicable for a wide range of payloads. Capping the 140 nm-sized MSN, the

synthesized titania layer has a thickness of about 7.1 ± 4.3 nm, which XRD shows consist of a mixture of amorphous titania and anatase. Bonding of the titania layer to the silica surface is confirmed by formation of Ti-O-Si bonds as can be learned from FT IR spectroscopy. Leaching tests and flow-through experiments further show that the payload is effectively encapsulated. The band gap of anatase with 3.2 eV prohibits usage of UV-fluorophore, but does not impact visible light fluorophores. Moreover, the ability of titania to absorb and scatter UV-light can be a challenge if encapsulated fluorophores are prone to photodegradation (such as sodium fluorescein). A prevention strategy could be the addition of a silica shell between dye-MSN and titania layer that reduces photodegradation under UV-light, which can be of particular interest in hydrology applications.

It should be noted that while the titania layer provides a robust coating to endure harsh ambient conditions, it comes with the drawback that its robustness does not enable a stimuli-responsive degradation, rendering the system impractical for release applications.

Just like as in the case of silica, titania also presents a high density of hydroxyl groups on its surface, making it facile for a wide array of surface modification of particles (Hajareh Haghighi et al. 2023). Additionally, recent studies suggest that titania coating improve the biocompatibility of nanoparticle carriers (Farooq et al. 2018), i.e. using titania as pore blocker could be useful in biological and biomedical applications. This allows the here presented particles to be of particular interest as bio- and geoimaging tracers as they can be applied regardless of ambient conditions due to the stable and robust nature of the titania coating layer.

Acknowledgments

This study is part of the subtopic “Geoenergy” in the program “MTET—Materials and Technologies for the Energy Transition” of the Helmholtz Association. The authors gratefully acknowledge Mr. Arsenii Mokrov for his assistance with the XRD measurements. The authors gratefully acknowledge Dr. Elisabeth Eiche and Rebekka Reich from KIT Institute of Applied Geosciences – Geochemistry and Economic Geology for assistance with TGA measurements and Dr. Günter Beuchle and Julia Podszuweit from KIT Institute for Technical Chemistry for BET measurements. (S)TEM imaging and elemental mapping was carried out with the support of the Karlsruhe Nano Micro Facility (KNMFi, www.knmf.kit.edu), a Helmholtz Research Infrastructure at Karlsruhe Institute of Technology (KIT, www.kit.edu), under Proposal 2024-032-031995.

5.5 Supplementary Material

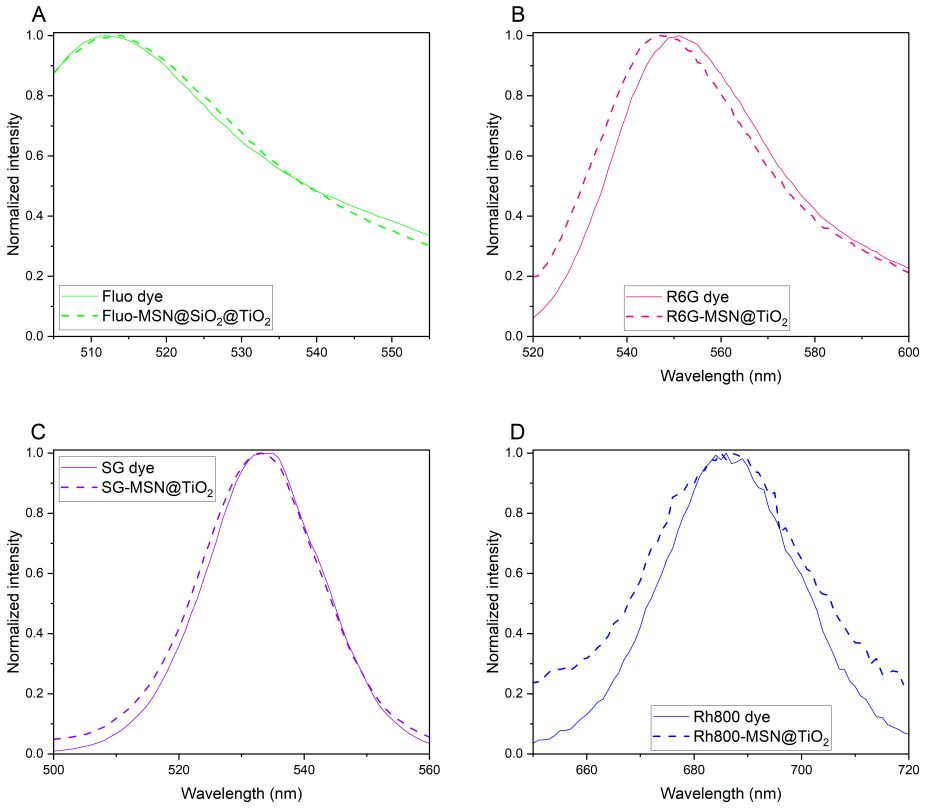

Figure 5.7: Fluorescence emission spectra for sodium fluorescein/uranine/Fluo and Fluo-MSN@SiO_2@TiO_2 (A), synchroscan spectrum (lambda 20) for rhodamine 6G and R6G-MSN@TiO_2 (B), synchroscan spectrum (lambda 20) sulforhodamine G and SG-MSN@TiO_2 (C) and synchroscan spectrum (lambda 23) for rhodamine 800 and Rh800-MSN@TiO_2 (D).

Table 5.1: Stability of fluorescence intensity of dye-MSN@TiO_2 and dye in different solutions over time.

Sample	Solution	Fluorescence intensity at time 0	Fluorescence intensity after 48 hours	Difference (%)
Rubpy-MSN@TiO_2	Millipore water	217.97	209.86	3.7
Rh800-MSN@TiO_2	Millipore water	458.74	483.85	5.5
R6G-MSN@TiO_2	Millipore water	130.41	135.93	4.2

Sample	Solution	Fluorescence intensity at time 0	Fluorescence intensity after 48 hours	Difference (%)
RhB-MSN@TiO_2	Millipore water	287.67	284.02	1.3
SG-MSN@TiO_2	Millipore water	126.94	139.71	9.1
R6G-MSN@TiO_2	0.01M NaCl	243.89	238.86	2.1
R6G-MSN@TiO_2	0.01M NaCl	274.07	281.09	2.6
R6G-MSN@TiO_2	0.01M NaCl	271.22	284.77	5.0
RhB-MSN@TiO_2	0.01M NaCl	514.55	558.97	8.6
RhB-MSN@TiO_2	0.01M NaCl	521.07	522.12	0.2
RhB-MSN@TiO_2	0.01M NaCl	272.58	256.37	5.9
RhB-MSN@TiO_2	0.01M NaCl	657.08	724.38	10.2
SG-MSN@TiO_2	0.01M NaCl	639.12	667.36	4.4
SG-MSN@TiO_2	0.01M NaCl	420.96	434.96	3.3
SG-MSN@TiO_2	0.01M NaCl	533.25	571.53	7.2
R6G-MSN@TiO_2	0.1M NaCl	276.33	283.04	2.4
R6G-MSN@TiO_2	0.1M NaCl	313.24	319.64	2.0
R6G-MSN@TiO_2	0.1M NaCl	311.01	314.86	1.2
RhB-MSN@TiO_2	0.1M NaCl	551.30	573.99	5.4
RhB-MSN@TiO_2	0.1M NaCl	488.26	508.33	5.5
SG-MSN@TiO_2	0.1M NaCl	714.82	709.33	0.8
SG-MSN@TiO_2	0.1M NaCl	742.28	769.30	3.6
SG-MSN@TiO_2	0.1M NaCl	723.21	734.68	1.5
R6G dye	0.01M NaCl	439.12	272.52	37.9
R6G dye	0.01M NaCl	451.18	271.23	39.9
RhB dye	0.01M NaCl	430.30	357.39	16.9

Sample	Solution	Fluorescence intensity at time 0	Fluorescence intensity after 48 hours	Difference (%)
RhB dye	0.01M NaCl	396.75	246.17	38.0
RhB dye	0.01M NaCl	409.32	250.28	38.9
SG dye	0.01M NaCl	448.98	467.17	4.1
SG dye	0.01M NaCl	499.32	522.26	4.6
SG dye	0.01M NaCl	434.10	463.33	6.7
R6G dye	0.1M NaCl	612.83	646.30	5.5
R6G dye	0.1M NaCl	773.09	680.35	12.0
RhB dye	0.1M NaCl	691.79	694.53	0.4
RhB dye	0.1M NaCl	571.79	576.54	0.9
SG dye	0.1M NaCl	203.70	208.70	2.5
SG dye	0.1M NaCl	211.22	213.33	1.0

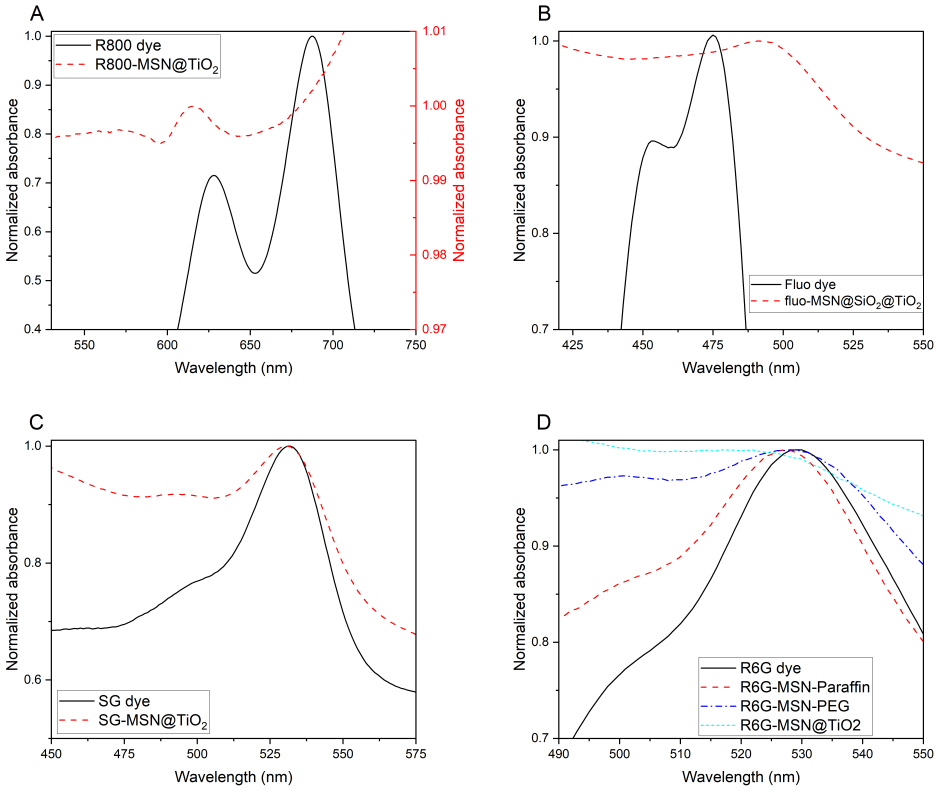

Figure 5.8: Absorbance spectra: R800: Peak dye 629 nm (dimer) and 689 nm (monomer), R800-MSN@TiO_2 617 nm (dimer). Fluorescein peak from mono- and dianionic forms, peak shift fluo-MSN@SiO_2@TiO_2 corresponds to dianionic form. SG and SG-MSN@TiO_2, R6G and R6G-MSN@TiO_2 show only minor peak shifts.

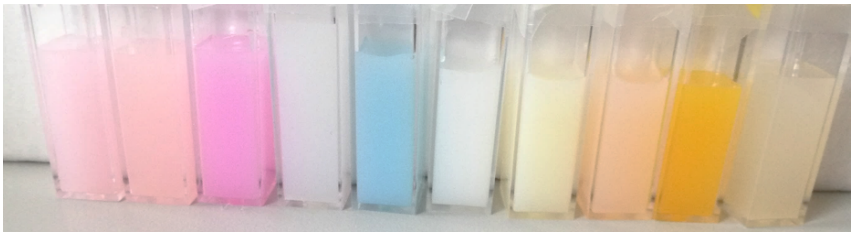

Figure 5.9: Photograph of dye-MSN@TiO_2. From left to right: R6G-MSN@TiO_2, SG-MSN@TiO_2,RhB-MSN@TiO_2, C307-MSN@TiO_2, NBA-MSN@TiO_2, 1,3,6-naphthalene sulfonate NTS-MSN@TiO_2 (UV-Tracer, therefore no color visible and no fluorescence detected), Fluo-MSN@SiO_2@TiO_2, Rubpy-MSN@TiO_2, Rubpy@SiNPs@SiO_2, Fluo-MSN@TiO_2.

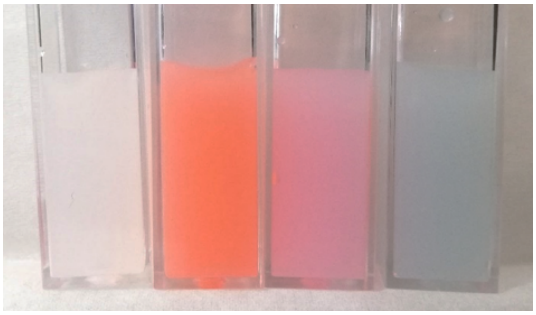

Figure 5.10: Photograph of pure titania particles, SG-MSN@TiO_2, R6G-MSN@TiO_2, R800-MSN@TiO_2 (from left to right).

CHAPTER 6

Temperature stability and enhanced transport properties by surface modifications of silica nanoparticle tracers for geo-reservoir exploration

This Chapter is published in Scientific Reports
https://doi.org/10.1038/s41598-024-70132-z

Spitzmüller, L., Berson, J., Schimmel, T., Kohl, T., Nitschke, F. (2024): Temperature stability and enhanced transport properties by surface modifications of silica nanoparticle tracers for geo-reservoir exploration. *Scientific Reports*, 14.

In this Chapter, the proof-of-concept of applicability of the dye-MSN@TiO_2 tracer nanoparticles developed as described in Chapter 5 is given. The major findings and implications are:

- Protection of embedded dyes is achieved
- Surface modifications can further reduce sorption affinity
- Hydrodynamic forces are more important for transportability than particle-mineral surface interactions (DLVO theory)

Abstract

Tracer tests are an important tool for characterizing and monitoring subsurface reservoir properties. However, they are limited both because of the tracer molecules constraining factors such as irreversible adsorption, retention, and degradations, i.e. interaction processes of fluorophore molecule with surrounding media resulting in a large variation in transport properties. Elaborate tests utilizing more than one tracer to distinguish time or location of injection are complex and interpretation is ambiguous because each tracer interacts differently. In this study, we present an approach to increase tracer stability and enhance the transport uniformity of different tracers, thus making tests utilizing multiple tracers simpler and more feasible. We present this concept of tracer multiplicity by encapsulating an anionic, cationic or amphoteric fluorophore inside mesoporous silica nanoparticle carriers coated with a protective titania layer. Upon encapsulation, increased thermal resistance and drastically lowered sorption affinity towards quartz sand was detected in batch and flow-through experiments. An additional advantage of the presented nanoparticle tracers over molecular tracers is their modularity, which is demonstrated by surface modifications and application of additives that greatly reduce sorption and increase recovery rates in the flow experiments. With the here presented concept of tracer multiplicity, we introduce a new approach for colloidal tracer design that has the potential to expand and enhance measurable parameters, measurement accuracy and simplicity of analysis.

6.1 Introduction

The application of molecular fluorescent dyes as tracers is a standard method in hydro- and geosciences to study underground conditions, e.g. fluid pathways, flow direction, flow velocity and interconnections (Davis et al. 2006, Leibundgut 1974, Ren et al. 2023). However, their applicability is highly dependent on prevalent fluid properties such as pH-values, fluid temperature and salinity (Smart and Laidlaw 1977). In fact, the ideal circumstances for fluorescent molecular tracers to behave conservatively are narrowly constrained, that only the sodium salt of fluorescein (uranine) behaves nearly conservative, though only at shallow groundwater aquifer conditions (Behrens et al. 2006, Käß 2004). This makes uranine the most used groundwater tracer (Gerke et al. 2013). Other commonly employed tracers in hydrology are xanthene group dyes, namely eosin Y, sulforhodamine G and rhodamine WT, as well as sodium naphthionate. Cationic xanthene dyes such as rhodamine B and rhodamine 6G are i.a. scarcely used due to their inherent high sorption affinity (Kasnavia et al. 1999). For geothermal exploration purposes, prevalent geochemical conditions are harsher than in groundwater, with high salinities promoting sorption (Magal et al. 2008), high temperatures degrading the fluorescent molecules (Rose et al. 2001) and a wider range of pH-values affecting fluorescence intensity (Cao et al. 2017). While photobleaching becomes irrelevant in

subsurface, the low temperature stability of most organic dyes limits their applicability (Rose et al. 2002). For example, uranine decays above 200°C in absence of dissolved oxygen (Adams and Davis 1991), sorption affinity increases under acidic conditions (Kasnavia et al. 1999) due to conversion of anionic forms to other prototropic forms of the molecule (Klonis and Sawyer 1996) and fluorescence is quenched at high salinity (Magal et al. 2008). Rose et al. (2001) established therefore the naphthalene sulfonates that can withstand high temperatures (Rose et al. 2002) as a new class of tracers to overcome the hurdles of geothermal systems. These ultraviolet tracers (UV-tracer) require sophisticated analysis tools such as HPLC augmenting the analytical cost and effort. Additionally, naphthalene sulfonates tend to isomerize, which has to be taken into consideration during analysis. Moreover, as well as the need to ensure high temperature stability of the tracers to avoid them decaying in the reservoirs, leading to long-term permanence in the produced fluids getting reinjected and hence affect analysis of future tracer tests (Kristjánsson et al. 2016, Rose et al. 2002). Other approaches developing new tracers for geothermal include reactive or temperature responsive molecular tracers (Hawkins et al. 2021). Furthermore, within the last years, particle tracers such as quantum dots (Rose et al. 2011), nanocrystals (Brauser et al. 2013), DNA-encapsulated nanoparticles (Kittilä et al. 2019, Mikutis et al. 2018) and temperature-responsive fluorescent nanoparticles (Alaskar et al. 2015a, Rudolph et al. 2020) emerged. This linkage of nanotechnology and geosciences offers new opportunities and possibilities. Nanoparticles tend to stay in main streamlines, having lesser diffusivity and consequently showing faster breakthrough (Suzuki et al. 2020). Recently, the capabilities of DNA-labeled silica nanoparticles and silica encapsulated superparamagnetic DNA tracers were demonstrated in small-scale field applications mainly in groundwater (Chakraborty et al. 2023, Kianfar et al. 2022, Kong et al. 2018). While usage of DNA offers the opportunity of virtually unlimited amount of uniquely identifiable tracers, they are not designed for geothermal applications due to inherent temperature instability of DNA (Zhang and Huang 2022) and solubility of silica (Iler 1979). In fact, no silica-based nanoparticle tracer can be successfully applied in aqueous environments unless silica is sufficiently protected against disintegration and dissolution (Spitzmüller et al. 2023b). However, since/because the possibilities/advantages of (silica) nanoparticles tracers outweigh the drawbacks, it is worth developing strategies to overcome these challenges.

In this work we present an approach on a laboratory scale for a nanoparticle carrier that enhances protection of its payload from surrounding conditions and improves uniformity of transport-determining properties between different tracers.

6.1.1 Concept of nanoparticle tracer and tracer multiplicity

With a limited range of reservoir conditions where tracers are applicable and a narrow variety of tracers that can be used simultaneously (Kasnavia et al. 1999, Smart and Laidlaw

1977) augmenting the toolbox of possible fluorescent tracers is needed to make tracer tests more widely applicable and more significant, both for hydrological or geothermal reservoirs. By combining nanotechnology-based approaches with geoscientific research questions, we propose fluorescent dye-encapsulated nanoparticle tracer that fulfills important prerequisites, which are essential for any tracer system that is intended for application in subsurface environments:

- Long-term integrity: Ability to withstand harsh conditions (temperatures, salinities, pH, ...) while maintaining functionality
- Identification: The tracers should be clearly distinguishable, easily analyzable e.g. by fluorescence spectroscopy and possibly enable real-time detection
- Favorable transport properties: Tunable retention and/or rock-fluid-tracer interactions

By encapsulating fluorescent dye molecules inside a silica-based nanoparticle carrier, we aim to protect the dye from environmental influences assuring long-term integrity. Consequently, the fluorescence of the dye should not be affected by fluid properties such as pH or salinity. Furthermore, interactions of dye with the surrounding will be limited due to shielding by the carrier; hence, properties of the dye are no longer the decisive factor for transport properties and sorption affinity. This concept of tracer multiplicity enables the possibility of using various uniquely identifiable tracers (by color/fluorescence absorbance/excitation-emission spectra) that have identical transport behavior and sorption properties. An additional advantage of using a particle carrier for transportation of molecular dyes is the modifiable surface of the particle. Whereas transport properties and sorption affinity of molecular tracers are entirely dependent on properties of the molecules themselves such as their charge, which cannot be changed without losing functionality of the molecules, the surface and chemical composition of the nanoparticle carriers can be easily modified to optimize tracer performance. By modifying nanoparticle carrier parameters such as surface charge, surface hydrophilicity and surface roughness, the transport properties can be adapted and controlled without influencing the dye properties.

The herein introduced fluorescent nanoparticle tracers present a feasible approach to tracer multiplicity. In brief, different molecular fluorescent dyes are encapsulated in mesoporous silica nanoparticle carrier capped with an impermeable titania layer. Synthesis and chemical and structural characterization of these nanoparticle tracers is described in a previous study (Spitzmüller et al. 2024a). This study focuses on testing and application of these type of tracers. As investigated in a previous study, pristine silica nanoparticles are not suitable for applications in aqueous environments, as silica nanoparticles are mainly amorphous and consequently soluble in water (Spitzmüller et al. 2023b). However, because silica nanoparticles are a versatile tool, having a highly reproducible synthesis, controllable sizes and porosities, they are still an ideal carrier venue. For applications in aqueous environments

long-term (hydro)thermal stability can be achieved by modifying the silica network and/or modifying the surface. Therefore, in the study herein, we base our approach on thermally stable fluorescent nanoparticle tracers (dye-MSN@TiO_2). The usage of a metal oxide layer overcomes most issues of classical capping agents such as polyethylene glycol (PEG) or other coatings widely used for nanoparticles in biomedical science applications (Croissant et al. 2017, Gimenez et al. 2015, Jeelani et al. 2020) mostly used as reversible pore blockers that can be rendered permeable when triggered with a pH-/temperature-/radiation-stimuli in biological systems but are not robust enough to withstand the more extreme geothermal conditions. In order to maintain particle tracer integrity at high temperatures, calcined mesoporous silica nanoparticle carriers are used to reduce hydrolysis-induced degradation and solubility (Fournier and Rowe 1977, Spitzmüller et al. 2023b). Addition of a titania layer further increases the (hydro-)thermal stability due to extremely low solubility in water ($\approx 10^{-9}$ mol/L) (Schmidt and Vogelsberger 2009). A detailed description of synthesis and characterization of the dye-MSN@TiO_2 nanoparticle tracers can be found in Spitzmüller et al. (2024a). Three different dyes, the anionic sulforhodamine G (SG, excitation-emission wavelength 532 nm-550 nm), the amphoteric rhodamine B (RhB, excitation-emission wavelength 546 nm – 567 nm) and the cationic rhodamine 6G (R6G, excitation-emission wavelength 480 nm – 548 nm) are chosen as model dyes for this proof-of-concept investigation as they are comparable but differ in a broad value range in terms of charge and sorption affinity.

This work focuses on examining a laboratory-scale proof-of-concept of the applicability of these nanoparticle tracers. The study consists of three parts: particle characterization, assessment of sorption behavior and particle surface modification. First, we show successful encapsulation and protection of the dye by measuring ζ-potential evolution over a pH-range from pH 1.8 to pH 10.5. By comparing these results to literature data of pristine mesoporous silica nanoparticles and titania nanoparticles, the impact of each individual part (MSN core, dye, titania shell) on the ζ-potential of the dye-MSN@TiO_2 nanoparticle tracers can be identified. These measurements are used for evaluation of colloidal stability using DLVO force calculations. To evaluate further the protective effect of the encapsulation method, the performance of the particles and the molecular dyes was compared under prolonged exposure to high temperatures (160 °C) in moderately saline fluids (0.1 M NaCl). The fluorescence loss due to high temperatures of the molecular dyes is compared to fluorescence loss of the encapsulated dyes.

The shielding efficiency is further assessed by sorption batch and flow-through column experiments. Hereby, sorption affinity of dyes-MSN@TiO_2 tracer particles towards quartz sand in 0.01 M NaCl, 0.1 M NaCl and 1 M NaCl solutions and tap-water was compared to the sorption affinity of their respective dyes in the batch experiments. Additionally, flow-through experiments were conducted to examine the effect of particle transport properties and non-static conditions on sorption and retention of the dyes and the encapsulated dyes in 0.01 M NaCl solution.

Finally, we highlight the advantages of tracer particles over molecular tracers, namely the modularity of the particle's surfaces. By addition of surfactants as well as by chemically modifying the surface, we show the possibilities of the presented concept of nanoparticle tracers. We examined a zwitterionic surfactant (ZI), an anionic surfactant (SDS) and a chelating agent (EDTA) as additives to the fluid matrix and tested their ability to reduce sorption affinity of the nanoparticles towards the quartz sand surfaces. The anionic surfactant SDS serves to stabilize the colloidal suspension and keeps the particles separate (Loosli and Stoll 2017) while EDTA is commonly used to inhibit scaling formation in geothermal brines and are therefore selected as suitable additives (Cobos and Søgaard 2022). Contrarily to solely adding additives, we also modified the nanoparticle tracers directly by bonding silanes to hydrophobize the surface of the nanoparticles. Having a hydrophobic tracer could be beneficial for example in applications where oil or oil residues might be present and could be of particular interest for oil and gas industry (Stricker et al. 2020). All these kind of modification strategies are a unique option for colloids and particles, hence expand the possible application range and scope for tracer tests.

6.2 Experimental

The nanoparticle tracers used in this study are 151 ± 38 nm with a of 142 ± 24 nm mesoporous silica core and a 7.1 ± 4.3 nm thick titania shell determined by SEM and TEM imaging (Spitzmüller et al. 2024a). The dye (R6G, SG or RhB) is located within the 2-3 nm-sized pores in the mesoporous silica. A sketch of the dye-MSN@TiO_2-nanoparticles and an elemental mapping image depicting silica and titania is given in Figure 6.1. In the supplementary information, the synthesis procedure is briefly described. A more comprehensive study of the whole synthesis process and characterization can be found in Spitzmüller et al. (2024a) with detailed structural analyses. Figure 6.9 (Supplementary file) shows FT-IR-ATR spectra with titania-related, silica-titania-related and dye-related vibration bands and representative SEM images of the particles.

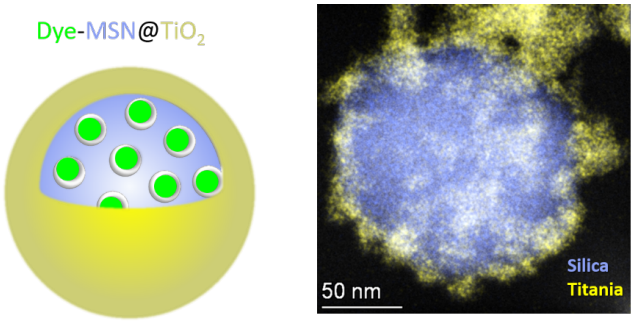

Figure 6.1: Sketch of the dye-MSN@TiO_2 nanotracer and elemental mapping image depicting silica and titania. The dye is located within the pores of the mesoporous silica nanoparticle. A titania shell is added as a stable pore blocker and protects the mesoporous silica carrier.

6.2.1 Analytical devices

SEM: A Zeiss Leo 1530 was used for SEM imaging with aperture 30 µm, EHT-voltage of 1 kV to 3 kV, and usually working distances of 1.5 mm to 3 mm. Samples were prepared following the latter procedure. First, a p-doted silicon wafer was placed on top of an adhesive carbon-tap. Then, nanoparticle suspension was diluted with ethanol and 5 µL were dropped to the silicon wafer and dried under nitrogen atmosphere. Because coating of the samples with carbon or gold was avoided, measurements were performed at low EHT voltages in order to not charge the samples. Images were taken in InLens or SE2 mode.

ζ-potentiometry: To measure ζ-potential of the nanoparticles a Malvern Zetasizer NanoZS and folded capillary cell were used. ζ-potential analyses were performed in 10 mM KCl solutions at 25 °C at pH 1.8, 4.4, 6.6, 8.5 and 9.5. pH was adjusted prior to measurement using HCl or NaOH. pH was measured using pH-meter VWR pH20. Electrophoretic mobility was measured and converted according to Smoluchowski approximation to ζ-potential. Measurement sets were repeated threefold with minimum 10 individual measurements within sets. ζ-potential represents the charge on the shear plane of the particles implying its strong dependence on salinity and pH of the solution. From literature experimental data (Franks 2002) and DLVO theory (Derjaguin and Landau 1941, Verwey and Overebeek 1948) a general decrease of the absolute ζ-potential can be expected with increasing salinity and especially in presence of divalent ions. There are indications of neutralization and even overcharging of the surface (Pianegonda et al. 2005). One important information when interpreting ζ-potential data is the location of the isoelectric point (iep). At this pH-value resulting ζ-potential is zero, meaning the surface charge of the particle and the charge of the ions in the Stern and diffuse double layer are equaling their charge. Below that point, ζ-potential is typically positive, whereas above that point it is usually negative. Furthermore, the absolute value of ζ-potential indicates agglomeration tendency or colloidal stability, with rule of thumb of above absolute values of 30 mV suspensions considered colloidal stable (Chakraborty and Panigrahi 2020, Salopek et al. 1992).

FT-IR-ATR: FT-IR ATR analysis was performed using a Nicolet iS50 with wavenumbers from 4000 to 400 cm^{-1}. Measurements were repeated twenty times. Samples were measured in dry conditions.

Fluorescence: Fluorescence was measured with a Cary Eclipse fluorescence spectrometer using 10 mm x 10 mm PMMA cuvettes for static conditions and quartz glass flow-through cuvette for monitoring breakthrough curves in flow-through experiments. Rhodamine 6G emission spectra were measured with excitation wavelength 480 nm, rhodamine B and sulforhodamine G were measured as synchroscans with Stoke shifts of 20 nm and 18 nm, respectively.

6.2.2 Sorption experiments

6.2.2.1 Fluid preparation

Sorption and temperature experiments were performed using stock solutions of NaCl in Millipore water ($\geq$ 18MΩ) with concentrations of 0.01 M (pH 6.9), 0.1 M (pH 6.7) and 1 M NaCl (pH 5.9). Tap water (pH 6.6) with ionic strength (IS) comparable to 0.01 M NaCl solution was used as retrieved (Table 6.1). No buffers were used to fix the pH as they would affect the overall ionic strength of the fluids. Instead, the fluids were equilibrated for 24 hours with the quartz-sand under ambient atmospheric conditions before pH was measured. Flow-through experiments were performed using 0.01 M NaCl fluid. This low salinity was chosen to be able to perform DLVO-calculations based on measured ζ-potentials that are standardly measured in 0.01 M NaCl or KCl solution. For temperature experiments, 0.1 M NaCl fluids were used.

6.2.2.2 Sorption experiments

Sorption experiments were performed in glass vials. Washed and dried quartz sand (grain diameter 1-1.6 mm, CAS number: 14808-60-7) was mixed with the fluid (tap water (TW), 0.01 M NaCl, 0.1 M NaCl, 1 M NaCl, Table 6.1) in a w/v-ratio of 1:2.5. The solutions are rotated 24h using a laboratory shaker (IKA rocker 3D) at a speed of 60 rpm to equilibrate the fluid with the quartz sand. After equilibration, molecular tracers are added to reach concentrations of 10^{-4} – 10^{-3} mg/mL (0.1-1 ppm), particle tracers are added to yield concentrations of 10^{-2} - $5{\cdot}10^{-2}$ mg/mL (10-50 ppm). For each experiment, an individual min. 4-point fluorescence calibration with the corresponding fluid was measured to correlate fluorescence intensity and concentration. The vials were shaken at 60 rpm while protected from photodegradation by wrapping with aluminum foil. Samples were measured after 1.5 h, 4 h, 24 h, 48 h and 168 h to monitor fluorescence of the fluid. To possibly identify and consider effects such as aggregation of nanoparticles and settling of aggregates as removal mechanism (i.e. resulting in lower concentration in the fluid although not induced by sorption) in the evaluation, the calibration points were re-measured at each time point when samples were measured. All experimental sets (dyes with each of the fluids and particles with each of the fluids) were triplicated and individually calibrated to calculate sorption percentage. Three different dyes were used: the anionic sulforhodamine/amidorhodamine G (SG), the amphoteric rhodamine B (RhB) and the cationic rhodamine 6G (R6G). Testing sorption affinity in batch experiments might overestimate sorption affinity due to high residence/contact time of the tracers and particles with the mineral surfaces and due to reversible adsorption (Sabatini and Austin 1991). However, testing the properties under least favorable conditions mimics the “worst-case-scenario” and benchmarks the highest sorption affinity.

Table 6.1: Composition of fluids used for sorption and temperature experiments. All concentrations are displayed in mg/L, ionic strength (IS) in mmol/L. pH was measured after 24 hours equilibration time of fluid with quartz sand at ambient conditions.

	Tap water[a]	0.01 M NaCl	0.1 M NaCl	1 M NaCl
Na^+	12.7	230	2 300	23 000
K^+	1.9	<0.004[b]	<0.04[b]	<0.4[b]
Ca^{2+}	115			
Mg^{2+}	11.1			
SiO_2	5.7			
Cl^-	25.8	355	3 550	35 500
HCO_3^-	333	[c]	[c]	[c]
SO_4^{2-}	49.2			
TDS[d]	558	585	5 850	58 500
IS	11	10	100	1000
pH[e]	6.6	6.9	6.7	5.9

[a] Composition according to Stadtwerke Karlsruhe 2022

[b] <15 mg $K_4(Fe(CN)_6)$ per kg NaCl as stated by VWR GPR Rectapur

[c] due to equilibration with atmospheric CO_2 HCO_3^- concentration always above 0

[d] as calculated

[e] as measured after 24 hours equilibration in quartz sand in glass vials

6.2.2.3 Calculation of K_d values

K_d-values (L/kg) are calculated after 48 h according to Bork et al. (2020)

$$K_d = \frac{(c_0 - c_{aq})V_0}{m_{sample}c_{aq}} \tag{6.1}$$

With c_0 (µg/L) initial concentration, c_{aq} (µg/L) concentration in fluid after 48 hours, V_0 (L) initial fluid volume, m_{sample} (kg) sample weight. K_d values express sorption affinity with higher values indicating faster and stronger sorption than lower values.

6.2.2.4 Flow-through experiments

To test the transport ability in flow-through setup, particles and dyes were circulated through a 25 cm PVC column (inner diameter 32 mm) packed tightly with washed and dried quartz sand (approx. 320 g, grain size 1-1.6 mm). To avoid preferential flow paths along the column wall, they were coated with a continuous layer of quartz sand. The inlet and outlet were covered with sinter glass plates (pore size 160-250 µm, VitraPOR Por. 0 ISO 4793-80, ROBU Glasfiltergeräte GmbH Germany). The liquid exiting the column was directed into a

quartz flow-through cuvette inside the fluorescence spectrometer, where measurements were performed with a frequency of 1 Hz. The produced fluid were not reinjected into the system. The column was connected to the measurement setup using Festo and silicon pipes of 10 mm and 3 mm diameter, respectively with constant flow rate of 0.27-0.28 mL/s maintained by a peristaltic pump (DüLabo PLP380). Flow direction was from bottom to top in order to avoid air bubbles inside the column. Particles and dyes were injected as one-pulse injection into the pipe upstream of the column inlet with a syringe through a septum. A sketch of the setup can be is shown in Figure 6.2. Concentration was calculated from the fluorescence intensity through intensity-concentration calibration curves. Dye and particles were mixed with 0.01 M NaCl solution to make 10^{-3} mg/mL and 10^{-1} mg/mL solutions, respectively. Flow velocity was kept constant and monitored for each measurement separately. To ensure comparability, the measured time was converted to volume and signals were normalized according to peak intensity. Breakthrough curves were analyzed according the cpeak-method (Małoszewski and Zuber 1985, Schudel et al. 2002) (Supplementary Information section 6.5.2.1).

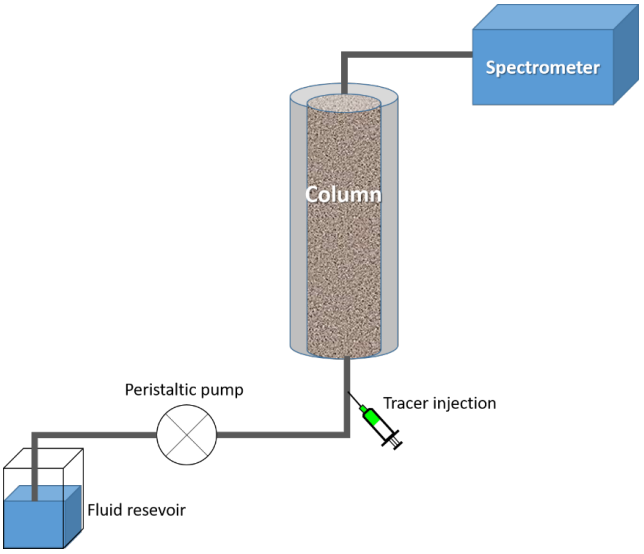

Figure 6.2: Sketch of the flow-through setup (not true to scale). The fluid used is 0.01 M NaCl solution which is flown through the system with 0.27-0.28 mL/s. A peristaltic pump is used to maintain the flow rate. The tracers are injected through a septum upstream of the column. The column is packed with quartz sand. Produced fluids are measured in a flow-through quartz cuvette in the spectrometer and are wasted afterwards (i.e. not reinjected).

6.2.3 Modification of surface properties

Surface modifications can be performed either by chemically bonding, coupling or grafting molecules like silanes or polymers or by weaker electrostatic interaction with surfactant materials such as sodium dodecyl sulfate (SDS) or cetrimonium bromide (CTAB) (Bagwe et al. 2006, Kango et al. 2013, Sperling and Parak 2010).

6.2.3.1 Sorption experiments with additives

The impact of different additives on sorption affinity of the particles was tested using the anionic surfactant sodium dodecyl sulfate (SDS), the zwitterionic surfactant SB3-14 (sulfobetaine 3-14, N-tetradecyl-N,N-dimethyl-3-ammonio-1-propanesulfonate, herein abbreviated as "ZI"), and the chelating agent ethylenediaminetetraacetic acid (EDTA). The effective concentration for each surfactant varies, with the concentration used in the herein described experiments being 0.1 mg/mL SDS, 0.1 mg/mL ZI and $5 \cdot 10^{-3}$ mg/mL EDTA. Sorption tests and calibration curves were performed as described in the previous section. For ζ-potential analyses, samples underwent two washing-centrifugation cycles with Millipore water to remove free additive molecules from the solution, i.e. ζ-potential differences indicate attachment of additives to nanoparticle surfaces.

6.2.3.2 Phase-separation experiments

The surface of dye-MSN@TiO_2 nanoparticle tracers is hydrophilic, i.e. the particles are easily dispersible in water. By chemically modifying the surface via silanization, the particles were altered hydrophobic, i.e. dispersible in apolar solvent. To demonstrate the effect of surface modifications, phase-separation experiments are conducted in a separation funnel with water being the polar and hexane being the apolar phase. Fluorescence was measured from each of the phases to determine the presence or lack thereof the nanoparticles. Furthermore, the silanization of the surface is proven by FT-IR ATR measurements.

6.2.4 Thermal degradation

Temperature stability of the dyes and dye-MSN@TiO_2 was examined at 160 °C for 120 hours in 0.1 M NaCl solution with air as head space. Pressure can be approximated to be 6-8 bar. Experiments were duplicated and individually calibrated. Calibration was repeated after 120 hours in order to identify aggregation and clumping effects (particles) or degradation in aqueous medium (dye). 20 mL of 10^{-4} mg/mL dye solution and 20 mL of 10^{-2} mg/mL particle-dispersion were placed in teflon liner inside stainless steel autoclaves and heated in an oven at 160 °C under static conditions. After 120 hours, the samples were cooled to room temperature before fluorescence was measured. It should be noted, that in geothermal environments, no dissolved oxygen is present.

6.3 Results and discussion

6.3.1 Nanoparticle tracer characterization

6.3.1.1 ζ-potential and DLVO theory

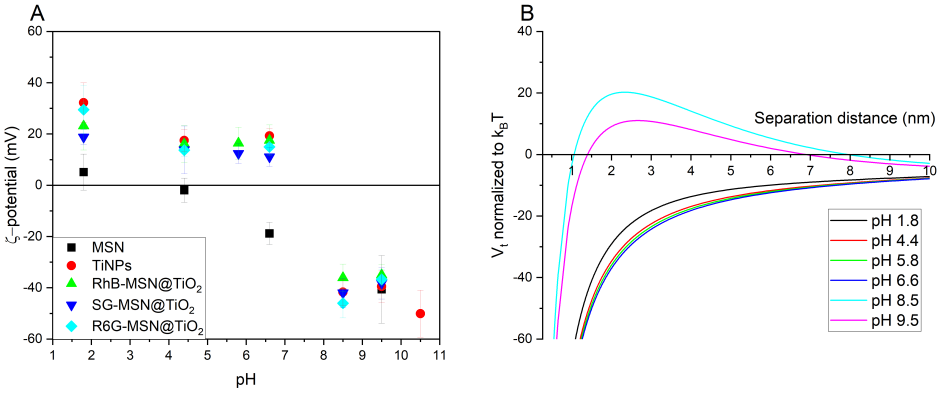

Figure 6.3: A: ζ-potential over pH in 10 mM KCl solution of pristine mesoporous silica nanoparticles (MSN), titania nanoparticles (TiNPs), and dyes encapsulated in mesoporous silica nanoparticles coated with a titania layer (dye-MSN@TiO_2). The nanoparticle tracers exhibit zeta potentials in the range of titania nanoparticles, indicating successful surface coating. RhB rhodamine B (amphoteric), SG sulforhodamine/amidorhodamine G (anionic), R6G rhodamine 6G (cationic). B: Particle-particle interaction energy according to DLVO theory at different pH for SG-MSN@TiO_2.

Figure 6.3 depicts ζ-potential evolution over pH-value for pristine MSN carrier, titania nanoparticles, and dye-MSN@TiO_2 tracer nanoparticles and compares impact of ζ-potential on surface interactions described by DLVO theory. The isoelectric point (iep) of MSN lays in the range between pH 1.8 and 4.4, in agreement with literature data (Franks 2002). The negative charge at neutral pH-values correlates to low sorption affinity of silica nanoparticles towards minerals with negatively-charged surfaces such as quartz. Contrarily, pure titania nanoparticles show their isoelectric point between pH 6.6 and 8.5, corresponding to iep 6.8 in literature (Chakraborty and Panigrahi 2020, EL Mekkawi and Abdel Mottaleb 2005, Wilhelm and Stephan 2006). Below pH 6.6 the ζ-potential is positive, possibly indicating stronger sorption tendency on negatively charged mineral grains. The ζ-potential of dye-MSN@TiO_2 nanoparticle tracers show comparable behavior to pure titania nanoparticles: their iep is located between pH 6.6 and 8.5 with slightly positive charges in neutral pH-range and highly negative ones in alkaline environment. This finding implies two indications: First, the synthesis did yield a continuous titania coating as intended, otherwise the silica core would have influenced the resulting ζ-potential. Second, the procedure effectively shields the dye from surrounding; the ζ-potentials are similar regardless of the type of incorporated dye

(anionic, cationic or amphoteric). In conclusion, the coating layer affects the ζ-potential more significantly than the mesoporous silica core and the encapsulated dye.

Calculation of DLVO interaction energy can be used to estimate the colloidal stability of the suspensions, i.e. whether the particles are prone to aggregation, flocculation and clumping. Figure 6.3B shows the sum curve of attractive van-der-Waals forces and repulsive electric double layer (EDL) forces calculated for SG-MSN@TiO_2 nanoparticles (Supplementary Information section 3). Hereby, positive values represent repulsive forces while negative values are attractive. In close proximity, the attractive van-der-Waals forces are predominant leading to a primary minimum, i.e. if the separation distance of the particles is below that value then the particles aggregate irreversibly (Hotze et al. 2010). EDL forces highly depend on the ionic strength of the solutions and the surface charge of the particles. From the force curves in Figure 6.3B it can be seen that alkaline pH-values stabilize colloidal suspensions due to higher absolute ζ-potential and hence higher repulsive force between the nanoparticles. Contrary, near neutral ζ-potentials are not sufficient to overcome the attractive van-der-Waals forces resulting in coagulation and flocculation. The energy barrier can be used to determine the rate of coagulation in dependence on the particle concentrations (Agmo Hernández 2023). For example, in a dispersion at pH 8.5 with 1 mg/mL particles, the system is a stable colloidal dispersion for approx. 6 500 years ($20k_BT$, Supplementary Information section 3.2.3).

ζ-potentials were measured in 0.01 M KCl solution at 25 °C. However, in geothermal environments, ionic strength usually exceeds 0.01 M and the temperature is higher. Studies with simulated and measured data of ζ-potential evolution of nanoparticles and reservoir minerals with increasing salinity (Erzuah et al. 2023, Franks 2002, Liu et al. 2019, Shehata and Nasr-El-Din 2015) generally show the following trend: increasing ionic strength reduces (i.e. neutralizes) the ζ-potential of both nanoparticles and reservoir minerals, thus decreasing the Debye length and absolute values of EDL forces (either attractive or repulsive). Liu et al. (2019) found 1 M NaCl solution to be ζ-potential neutralizing and high Ca^{2+}-concentrations even being able to reverse the ζ-potential of silica nanoparticles, thereby strongly affecting both the dispersion stability and the sorption affinity. Estimation of the Debye length yields approximately 3 nm in 0.01 M NaCl, 0.96 nm in 0.1 M NaCl and 0.3 nm in 1 M NaCl (Supplementary Information Section 3).

6.3.1.2 Temperature stability - Evaluation of protection and isolation of payload molecules by the encapsulating layer

The crucial point for tracer application in high-temperature environments is the fate/degradation of the organic fluorescent dye. Figure 6.4 shows fluorescence emission spectra of dye and dye-MSN@TiO_2 before and after heating for 120 h at 160 °C in 0.1 M NaCl solution. Fluorescence intensity decreased by 82.3 % and 94.9 % for SG-dye and R6G-dye, respectively. Under identical conditions, fluorescence loss of SG-MSN@TiO_2 is 8.4 % and

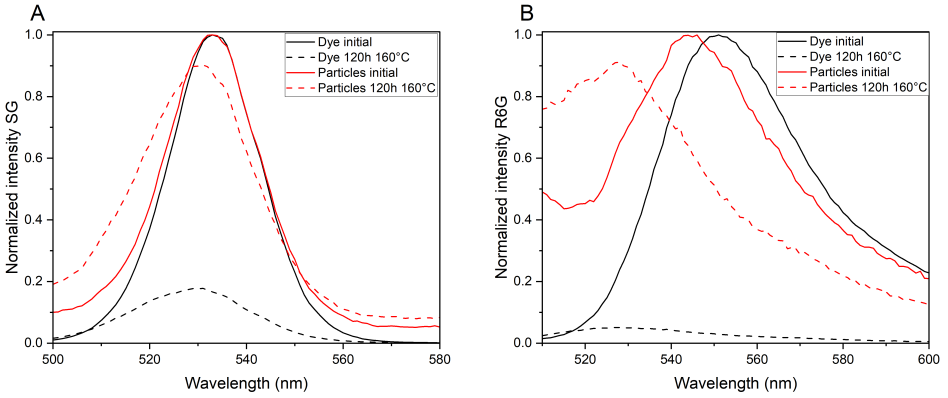

Figure 6.4: Normalized fluorescence emission spectra of SG and encapsulated dye SG-MSN@TiO_2 (A) and R6G and encapsulated dye R6G-MSN@TiO_2 (B). Spectra shows initial fluorescence intensities and fluorescence after 120 h at 160 °C in 0.1 M NaCl solution. Intensity loss of SG-dye fluorescence 82.3 % while for SG-MSN@TiO_2 fluorescence loss of 8.4 % (A). Intensity loss of R6G-dye 94.9 % and R6G-MSN@TiO_2 8.7 %, respectively (B).

for R6G-MSN@TiO_2 8.7 %. Hence, protection of the encapsulated molecules is achieved and fulfills one/two of the main prerequisites presented in the introduction for tracer: the long-term integrity under harsher conditions and the identification. Possible explanations for the protective effect could be reduction of degrees of freedom of the encapsulated dye, damping of the thermal energy by the carrier matrix or protection from oxygen. It is known that presence of oxygen accelerates the thermal decomposition of dyes (Adams and Davis 1991). It can therefore be assumed, that the nanoparticle carrier acts as a barrier and protects successfully the encapsulated dye. Further, it is an indication, that the particles stay intact, otherwise the fluorescence loss would be as observed for the free dyes. SEM images of the nanoparticles after heating can be found in Supplementary Figure 6.10.

The peak shift to shorter wavelength in both the spectra of the dye and the dye-MSN@TiO_2 after heating could be a sign of reduced conjugation of the chemical bonds of the fluorophore or could be due to interactions with the particle matrix (Auger et al. 2011, Avnir et al. 1984, Jorge et al. 2013). The peak shifts of 3-4 nm for SG and SG-MSN@TiO_2, 22 nm for R6G-dye and 16 nm for R6G-MSN@TiO_2 in the experiments were permanent, i.e. even after days at room temperature the peak shift was still present for heated dyes and dyes-MSN@TiO_2. Implications of these systematic peak shifts could affect interpretation of breakthrough curves and calculation of tracer recovery in geothermal tracer tests since fluorescence measurements are usually performed at fixed wavelengths of fixed Stoke shifts possibly underestimating the peak intensity. Therefore, the excitation and emission wavelengths of tracer dyes should be reassessed at conditions that simulate the thermal exposure endured during geothermal tracer tests, as the resulting shifts may considerably affect the test results.

6.3.2 Assessment of sorption affinity and transport properties

The aim of nanoparticle carriers is to protect the encapsulated dye from the surrounding, i.e. dye properties ideally should be independent of the sorption, retention and transport behavior of the nanoparticles. To examine the effect of encapsulation on the interaction of the tracer with the environment, sorption tests were performed comparing sorption affinity towards quartz sand of the dye and dye-MSN@TiO_2.

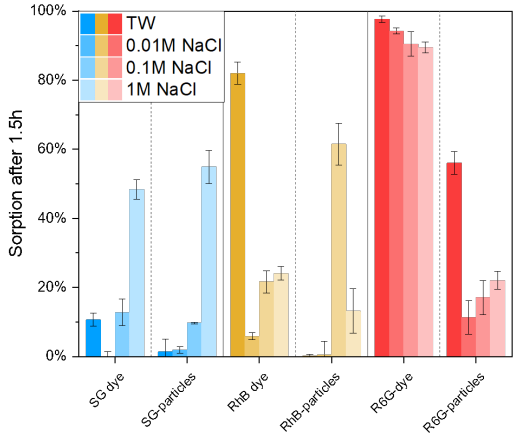

Figure 6.5: Comparison of sorption percentage in different salinities after 1.5 hours reaction time. Experiments were triplicated and individually calibrated. Bluish colors refer to SG = Sulforhodamine G (anionic dye), yellowish colors RhB = Rhodamine B (amphoteric dye), and reddish colors to R6G = Rhodamine 6G (cationic dye).

Table 6.2: Calculated K_d-values in L/kg after 48 hours interaction time of dye and dye-MSN@TiO_2 in different salinities.

	Tap water	0.01 M NaCl	0.1 M NaCl	1 M NaCl
SG dye	0.19 ± 0.10	0.11 ± 0.13	0.48 ± 0.11	4.99 ± 0.13
SG-MSN@TiO_2	0.21 ± 0.06	0.24 ± 0.1	0.65 ± 0.1	10.61 ± 1.89
RhB dye	18.21 ± 11.20	0.24 ± 0.03	0.99 ± 0.05	0.98 ± 0.15
RhB-MSN@TiO_2	0.42 ± 0.42	0.83 ± 0.32	16.28 ± 8.29	2.38 ± 0.43
R6G dye	227.41 ± 58.54	95.12 ± 32.00	347.73 ± 314.07	349.96 ± 219.50
R6G-MSN@TiO_2	6.75 ± 2.08	0.58 ± 0.19	1.73 ± 1.29	1.19 ± 0.16

6.3.2.1 Anionic dye - Sulforhodamine G

Whereas low sorption affinity of anionic SG-dye towards negatively charged quartz grains can be expected (Duy Thanh and Sprik 2015, Rodriguez and Araujo 2006), high salinities

are known to increase sorption affinity of molecular dyes as their solubility is decreased (Magal et al. 2008). As expected, experiments reveal strong sorption dependency on fluid's salinity, with highest sorption of 48 % after 1.5 h in 1 M NaCl solution (Figure 6.5). A dependency on ion valence can be assumed due to slightly increased sorption in tap water (calcium-carbonate system, Table 6.1) with K_d 0.19 L/kg compared to K_d 0.11 L/kg in 0.01 M NaCl solution (Table 6.2). Encapsulation of the anionic dye in nanoparticle carriers does not significantly reduce sorption affinity. In NaCl solutions SG-MSN@TiO_2 behave like SG-dye, presenting strong dependency on fluid's salinity. In 1 M NaCl sorption affinity is stronger for particles compared to dye molecules (55 % compared to 48 %). However, in complex fluid (tap water) this behavior is reversed (1 % for particles compared to 11 % for dye). One explanation for increasing sorption affinity of nanoparticles with increasing salinity can be found in the DLVO-theory. High salinities decrease the electric double layer (EDL) thickness and net charge, hence lowering repulsion forces between particles. Consequently, the particle dispersion tends to destabilize and forms aggregates (Samari-Kermani et al. 2021). However, high salinities also affect the surface charge of quartz, possibly resulting in lowered attractive forces.

6.3.2.2 Cationic dye - Rhodamine 6G

Cationic dyes are unfavorable tracers due to their strong sorption affinity toward negatively charged surfaces such as quartz. As expected, R6G-dye shows high sorption affinity, mostly independent of fluid properties with 90-100 % sorption (Figure 6.5) and K_d values of 95 L/kg to 350 L/kg (Table 6.2). In contrast, when encapsulated in the nanoparticle carrier, sorption is significantly lowered in NaCl solutions and is only slightly dependent of fluid ionic strength with 11 % sorption in 0.01 M NaCl solution and 22 % in 1 M NaCl solution (Figure 6.5). Highest sorption affinity with 56 % is observed in tap water (calcium-carbonate system, Table 6.1) which could hint a dependency on ionic valence. However, the overall enhanced sorption properties for R6G-MSN@TiO_2 under all tested conditions can be unequivocally ascribed to encapsulation and effective protection/shielding of the cationic dye.

6.3.2.3 Amphotheric dye - Rhodamine B

RhB-dye shows slight dependency on fluid salinity (6 % in 0.01 M NaCl to 24 % in 1 M NaCl) but stronger dependency on ion valence, i.e. highest sorption affinity in tap water with 82 % sorption (calcium-carbonate system) and K_d 18.2 L/kg. In comparison, for encapsulated RhB in nanocarriers K_d value is reduced significantly to 0.42 L/kg under the same conditions. However, RhB-MSN@TiO_2 show unexpected strong sorption affinity in 0.1 M NaCl (61 %), which could be neither attributed to increasing ionic strength, as sorption affinity in 1 M NaCl is significantly lower (13 %), nor to pH-value which was similar to pH of tap water. Consequently, this setup was chosen to assess the effect of additives on sorption affinity.

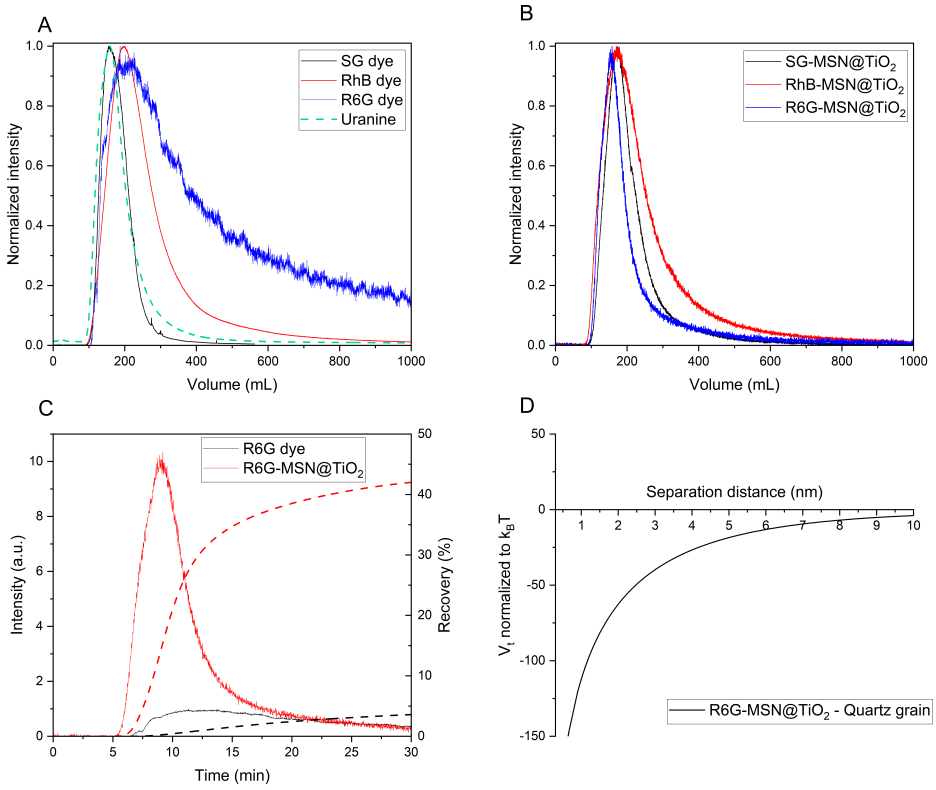

Figure 6.6: Breakthrough curves of dyes and particles through a 25 cm long column filled with quartz sand at room temperature in 0.01 M NaCl solution and DLVO interaction calculations. A and B compare breakthrough curves of dyes (with uranine being the "ideal" reference tracer) and dye-MSN@TiO_2 particles, respectively. Intensity is normalized to peak intensity and measured time is calculated to volume by multiplication with flow rate to balance slight differences in flow rates between the experiments. C shows breakthrough curves of R6G dye and R6G-MSN@TiO_2. Dashed lines represent recovery rate over time. D shows total DLVO interaction energy between R6G-MSN@TiO_2 and quartz grains in 0.01 M NaCl solution.

Additional to batch sorption experiments, laboratory scale flow-through experiments were performed to test the effect of previously assessed sorption behavior on transport properties. Figure 6.6 compares breakthrough curves of molecular dye tracers and dye-MSN@TiO_2 through a 25 cm column filled with quartz sand. As expected from batch experiments, the cationic dye R6G-dye shows sorption and retention (indicated by long tailing) while the breakthrough curve of the anionic SG-dye is nearly ideal (Figure 6.6A, uranine as comparison for ideal behavior). For the dyes-MSN@TiO_2 differences in breakthrough curves are less pronounced, indicating a more uniform transport behavior as compared to their respective dyes (Figure 6.6B). Furthermore, direct comparison of R6G-dye to R6G-MSN@TiO_2 highlights the advantages of particle tracers with faster arrival of particles and shorter peak time values (Figure 6.6C). This behavior can be attributed to flow properties of colloids where particles tend to stay in the main streamlines and hence experiencing reduced dispersion

(Chrysikopoulos and Katzourakis 2015). Furthermore, the difference becomes apparent when comparing the recovery: while only 3.5 % of the initial amount of R6G dye is retrieved, particle recovery is 42 %. Thus, upon encapsulation, recovery is increased by a factor of 12. Contrarily, from DVLO calculations, one can expect highly attractive conditions between dye-MSN@TiO_2 and quartz grain collectors, which should result in adsorption of the particles and high retention rates (Figure 6.6D). However, DLVO calculations omit hydrodynamic forces related to flow-through conditions such as drag and torque forces (Chequer et al. 2019, Torkzaban et al. 2007) and surface roughness of the collector grains (Abdelfatah et al. 2017). These factors, according to the relatively higher particle recovery rate, seem to have a more significant contribution in determining particle transportability. Additionally, another explanation for the high recovery could be related to the size difference of particles, quartz grains and pore throats. With a size ratio of particles-to-grain of 0.01 % below the threshold of 0.5 % retention of the particles due to straining is not expected (Göppert and Goldscheider 2019). However, it should be noted that other physicochemical filtering processes could still be relevant (Tufenkji and Elimelech 2004). Calculations of dispersivity, dispersion coefficient, and mean velocity show less dispersivity, less dispersion and higher mean velocity of particles compared to dyes (see also Supplementary information Table 6.4). Dispersivity ranges for particles between $4.55 \cdot 10^{-3}$ m to $1.32 \cdot 10^{-2}$ m, for dyes between $6.34 \cdot 10^{-3}$ m to $3.25 \cdot 10^{-2}$ m. Dispersion coefficient ranges for particles between $1.64 \cdot 10^{-2}$ cm^2/s and $4.28 \cdot 10^{-2}$ cm^2/s and for dyes between $2.93 \cdot 10^{-2}$ cm^2/s to $8.76 \cdot 10^{-2}$ cm^2/s. Mean velocity ranges for particles between $3.24 \cdot 10^{-4}$ m/s to $3.6 \cdot 10^{-4}$ m/s and for dyes between $2.7 \cdot 10^{-4}$ m/s to $3.55 \cdot 10^{-4}$ m/s.

6.3.3 Modification of surface properties

The sorption tests presented above were performed with the dye-MSN@TiO_2 tracer without any additives or surfactants. However, unlike molecular dyes nanoparticles offer the unique opportunity to modify their behavior via surface treatment. This can be achieved either by loose electrostatic attraction or by self-assembly of a covalently-bound monolayer to the nanoparticle surfaces.

6.3.3.1 Additives

To test the ability of tuning sorption affinity by simply modifying nanoparticle surface and net surface charge, the system 0.1 M NaCl solution + RhB-MSN@TiO_2 was chosen as this combination showed highest sorption values (Figure 6.5).

Zwitterion: The tested zwitterionic additive was least effective in lowering sorption affinity, but still sorption was reduced to 39 % and K_d valued of 1.62 after 48 hours which is lower than sorption and K_d of unmodified RhB-MSN@TiO_2 (84 % and 16.28, respectively). The ζ-potential at pH 6.6 of RhB-MSN@TiO_2 with ZI is 23.9 mV ± 3.2 mV and therefore

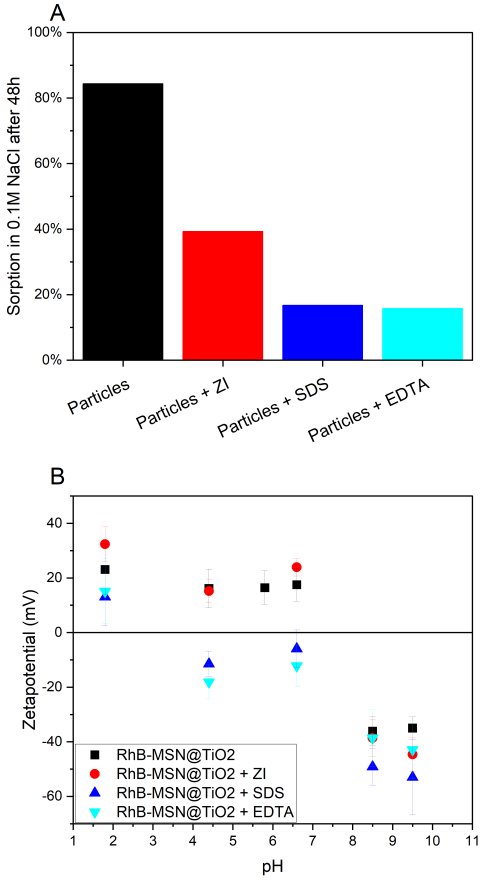

Figure 6.7: Impact of three different additives on sorption of RhB-MSN@TiO_2 in 0.1 M NaCl solution under batch reactor conditions. Tested additives zwitterion SB3-14 (ZI), sodium dodecyl sulfate (SDS) and ethylenediaminetetraacetic acid (EDTA) proved to be effective in lowering sorption affinity towards quartz. B: Impact of additives on ζ-potential of RhB-MSN@TiO_2. Addition of SDS and EDTA significantly reduce ζ-potential in acidic to near neutral pH ranges.

slightly more positive than without ZI (17.5 mV ± 6 mV) (Figure 6.7B). Zwitterions are not expected to affect ζ-potential because the molecule carrying positive and negative charges can exhibit both sides to particles and/or surrounding. However, attached molecules can affect interparticle forces (Agmo Hernández 2023) thus possibly increasing repulsive forces, and consequently lowered sorption affinity is observed.

SDS: Addition of SDS lowered the sorption affinity significantly; within 48 hours only 17 % of the particles were sorbed from the solution compared to 84 % sorption without addition of SDS (Figure 6.7A). K_d value is reduced to 0.5, which is also lower than K_d of free dye (0.99). Despite improving colloidal stability (Loosli and Stoll 2017), the anionic surfactants altered the ζ-potential; attachment of SDS molecules shifted the iep of the particles to more

acidic (between 1.8 and 4.4, Figure 6.7B). Furthermore, ζ-potential is significantly lowered compared to unmodified RhB-MSN@TiO_2, negative at pH 6.6 and resembles that of pure MSN (Figure 6.3). Both, the colloidal stability and sorption affinity are enhanced by addition of anionic surfactant. The observed lower sorption affinity can be attributed to increased repulsive forces between particle and particle as well as between the particles and the mineral surfaces.

EDTA: EDTA also effectively lowered sorption affinity (16 % and K_d 0.47 after 48 hours) and the ζ-potential of the particles. The impact of EDTA is similar to SDS. Iep was shifted into the acidic region similar as through addition of SDS. EDTA is known to adsorb on titania nanoparticles improving their colloidal stability (Borhan and Lee 2015, Li et al. 2005).

All additives successfully lowered the sorption affinity of the tested RhB-MSN@TiO_2 tracer nanoparticles. Possible explanations for this enhancement can be found in DLVO theory. On one hand, the repulsive electric double layer forces are affected by the change of the ζ-potential (Figure 6.7B) leading to higher colloidal stability and possibly to a reduction in the potential difference between particles and quartz surface. On the other hand, adsorption of surfactants can build up a steric barrier (Spitzmüller et al. 2023a) (XDLVO theory), drastically increasing the repulsive forces, and are able to compensate the attractive van der Waals forces at small distances (usually twice the length of the polymeric chain). Overall, the additives are effective in reducing sorption and coagulation. As preliminary flow-through experiments suggest, this surface modification strategy is also valid for flow-through setups (Spitzmüller et al. 2023a).

6.3.3.2 Surface modification

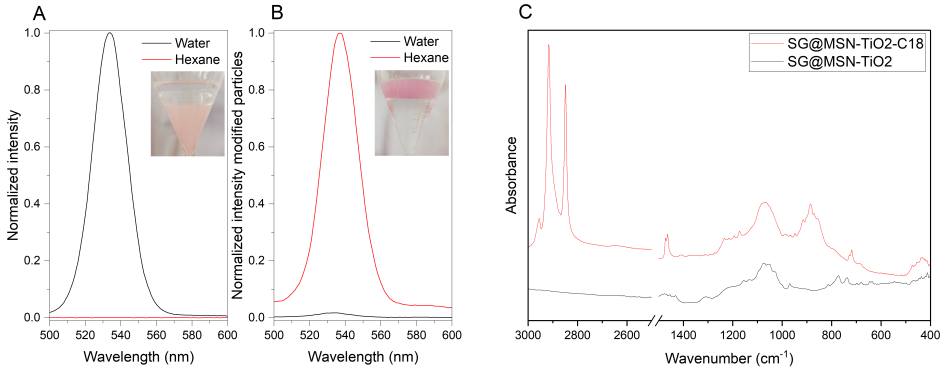

Figure 6.8: Normalized intensity of SG-MSN@TiO_2 in water and hexane (A) and normalized intensity of C18 modified SG-MSN-TiO_2 in water and hexane (B). Inset photographs in A and B show phase separation with bottom phase water and top phase hexane. C: ATR spectra of unmodified SG-MSN@TiO_2 and C18 modified SG-MSN@TiO_2 particles.

Whereas additives mostly change the effective charge of the nanoparticles, the hydrophilic/hydrophobic properties of the nanoparticle surface can also be modified. In order to alter the hydrophilic character of dye-MSN@TiO_2 particles to hydrophobic, we modified the surface by self-assembly of a hydrophobic silane monolayer (octadecyltrimethoxysilane, C18). To prove successful surface modification, non-modified particles and modified particles were dispersed in a water-hexane (oily phase) mixture. Consequently, hydrophilic (i.e. unmodified) particles were only dispersible in water, whereas hydrophobic (i.e. modified) particles were only dispersible in hexane. Figure 6.8A shows normalized fluorescence emission spectra of unmodified SG-MSN@TiO_2 and modified SG-MSN@TiO_2-C18 in water and hexane (Figure 6.8). The photographs show phase-separation of water-hexane with SG-MSN@TiO_2 (A) and SG-MSN@TiO_2-C18 (B) (bottom phase water, top phase hexane). Fluorescence spectra confirm that while having hydrophilic particles, no fluorescence in hexane could be detected. Changing surface properties to be hydrophobic shows opposite behavior with fluorescence in hexane and minor fluorescence in water, which proofs successful surface modification. Additionally, the ATR spectra (C) of modified SG-MSN@TiO_2-C18 reveals the presence of asymmetric and symmetric CH_2 stretching vibrations at 291 cm^{-1} and 2850 cm^{-1}, respectively as well as CH_3 asymmetric stretching vibration at 2950 cm^{-1} which can be assigned to the C18 monolayer.

6.4 Conclusions

Performing tracer tests to assess and characterize reservoirs and aquifers is an established method in geosciences. However, the variety of possible applicable tracers is limited due to constraints such as degradation, sorption and/or retention of the tracer molecules. There is a need for new kind of tracer types to overcome these issues. With a multidisciplinary approach combining nanoscience, chemistry and geoscience we present an approach to develop tracer technology and present a first proof-of-concept demonstration on a laboratory scale. The introduced concept of tracer multiplicity bears great promise for geothermal and hydro-geological exploration purposes owing to the broad variety of possible applicable and distinguishable tracers. By encapsulating dye inside a nanoparticle carrier, the dye is shielded from surrounding media and can remain unaffected by harsh environments. Since the properties of tracer dye become less decisive when encapsulated, properties of nanoparticle carriers will be decisive for transport and sorption within reservoirs. Moreover, utilizing complex systems such as nanoparticles entail the advantage of its modular architecture, which offers numerous modification possibilities. An advantage, which does not exist for molecular tracers: The outer surface of the nanoparticle can be easily modified to specifically adapt the tracers to each unique challenge a certain medium may pose through its distinct combination of mineralogy, fluid composition and flow parameters.

We proved that:

- Successful encapsulation and protections/shielding of different dyes inside a modular nanoparticle carrier is achievable.
- Encapsulation increases temperature resistance of organic dye molecules.
- Sorption affinity towards quartz sand can significantly be reduced for cationic dyes upon encapsulation.
- Encapsulated dyes show higher similarities in breakthrough curves compared to free dye. Despite the fact that DLVO calculations suggest higher sorption affinity for nanoparticles under static conditions, flow experiments have shown that transport is more dependent on hydrodynamic forces.
- By modifying surface properties of nanoparticles through addition of surfactants and hence altering ζ-potential the sorption affinity can lowered.

Furthermore, the presented type of nanoparticle tracer system satisfies the prerequisites for tracers of having long-term integrity, being identifiable and possessing favorable transport properties. The encapsulated dyes serve as uniquely identifiable entity while the silica nanocarrier and the titania shell act as shielding and protection against influences from the surrounding. The protective feature of the nanocapsule ensures long-term integrity and is prevented from dissolution by the stable titania layer. The favorable transport properties of nanoparticles can further be enhanced by surface modification strategies, the toolbox of nanoparticle engineering is vast and can help adapting particle properties to reservoir conditions.

This first proof-of-concept experiments on a laboratory scale have to be followed-up with implementation under increasingly more complex and realistic conditions, all the way to successful application in field experiments. Enabling simple and feasible tracer multiplicity tests could significantly extend the toolbox of tracers for geothermal and hydrological tracer tests, thereby enabling multi-well tracer tests or multi-tracer tests, thus increasing the scope of attainable information, simplifying analysis and reducing ambiguity in subsurface reservoir exploration tests.

Acknowledgments

This study is part of the subtopic “Geoenergy” in the program “MTET—Materials and Technologies for the Energy Transition” of the Helmholtz Association.

6.5 Supplementary Material

6.5.1 Synthesis

6.5.1.1 Chemicals

For synthesis the following chemicals were used: Millipore water (18 MΩ), ethanol (VWR Chemicals, AnalaR Normapur, $\geq$ 99.8 %), acetone (VWR Chemicals, AnalaR Normapur, $\geq$ 99.8 %), %), n-hexanol (VWR GPR Rectapur), cyclohexane (VWR Chemicals, AnalaR Normapur), hexane (Carl Roth, 99 %), dry acetonitrile (Merck, 99.5 %), Triton X-100 (Sigma Aldrich for analysis), ammonia (NH_4OH, Merck, 28-30 %), sodium hydroxide (NaOH, Merck Emsure pellets), hydrochloric acid (HCl, Honeywell Fluka 36.5-38 %), sulfuric acid (H_2SO_4, Merck Supelco 98 %), ethylenediaminetetraacetic acid (EDTA, Sigma Aldrich 99.4-100.6 %), tetrabutyl orthotitanate (TBOT, Sigma Aldrich, synthesis grade), tetraethyl orthosilicate (TEOS, Sigma Aldrich 99 %), n-octadecyltrimethoxysilane (C18, ABCR GmbH, 95 %), cetrimonium bromide (CTAB, Alfa Aesar, 98 %), N-tetradecyl-N,N-dimethyl-3-ammonio-1-propanesulfonate (SB3-14, "ZI", Sigma Aldrich, $\geq$ 98 %), sodium dodecyl sulfate (SDS, Sigma Aldrich 99 %), potassium chloride (KCl, VWR GPR Rectapur >99 %) and sodium chloride (NaCl, GPR Rectapur, $\geq$ 99 %). Additionally, the following dyes were used: rhodamine B (RhB, Sigma Aldrich for fluorescence), rhodamine 6G (R6G, Sigma Aldrich for fluorescence), sulforhodamine G (SG, Sigma Aldrich, dye content 60 %), uranine (Sigma Aldrich for fluorescence).

6.5.1.2 Synthesis of dye-MSN@TiO_2

Synthesis of the dye-MSN@TiO_2 is described in detail in Spitzmüller et al. (2024a). In brief: To synthesize the silica nanoparticle carrier cetrimonium bromide (CTAB 109 mg) is mixed with Millipore water (54 mL) and ammonia (NH_4OH 1.194 mL) and stirred for 1 hour. Tetraethyl orthosilicate (TEOS 0.465 mL) is added dropwise and the solutions is further stirred for 5 hours. The particles undergo several washing-centrifugation cycles with water and ethanol and are dried in vacuum. CTAB template is removed via calcination at 550°C with a heating rate of 1 °C/min over 6 hours. The fluorescent dye is encapsulated following a synthesis procedure of Rudolph et al. (2020) and Spitzmüller et al. (2024a). The dye is added to the particles (weight ratio 4:10) and stored overnight in a glovebox under inert nitrogen atmosphere. Then 2.5 mL dry acetonitrile per 50 mg particles is added and the particles are stirred overnight in the glovebox. The particles are retrieved by centrifugation, washed with hexane, dried in vacuum and redispersed in 4.8 mL Millipore water using a sonotrode to ensure a well dispersed solution. Titania coating was performed using a reverse water-in-oil microemulsion method as described in Spitzmüller et al. (2024a). Cyclohexane (15 mL) is mixed with n-hexanol (3.6 mL) and Triton X-100 (3.44 mL). After stirring for about 60 second,

the particle dispersion and tetrabutyl orthotitanate (TBOT 307 µL) are added dropwise. After 20 minutes of stirring, H_2SO_4 (60.9 µL) is added to the formed microemulsion and stirred overnight. The particles are retrieved by addition of excess amount of acetone, followed by washing-centrifugation cycles with acetone, ethanol, and water.

6.5.1.3 Surface modification with octadecyltrimethoxysilane

The titania-coated particles were silanized with octadecyltrimethoxysilane (C18) to render their surface hydrophobic analog to a procedure described in Spitzmüller et al. (2023b). Briefly, the titania-coated particles are dried and weighted. Per 50 mg particles, dry acetonitrile (2.5 mL) is used. The particles are redispersed in acetonitrile and n-octadecyltrimethoxysilane (0.375 mL) is added to the dispersion. After stirring for 12 hours, the coated nanoparticles are retrieved by centrifugation and washed twice with acetonitrile and hexane. Eventually, the particles are dried in vacuum.

6.5.2 Analysis

6.5.2.1 Sorption experiments - c_{peak}-method

Breakthrough curves were analyzed applying the c_{peak} method to calculate v_{mean}, dispersivity and dispersion coefficient (D) according to Małoszewski and Zuber (1985):

$$\frac{D}{vx} = \frac{(1-\varphi)^2}{4\sqrt{\varphi[\ln 2\varphi^{3/2} + 1.5(1-\varphi)][\varphi \cdot \ln 2\varphi^{3/2} + 1.5(1-\varphi)]}} \tag{6.2}$$

and

$$\alpha = \frac{D}{v} = \frac{D}{vx}x \tag{6.3}$$

Mean velocity is calculated:

$$v_{mean} = \frac{x}{t_0} \tag{6.4}$$

With:

$$t_0 = t_{peak}\sqrt{1 + (3\frac{D}{vx})^2 + 3\frac{D}{vx}} \tag{6.5}$$

6.5.2.2 DLVO theory - Calculations

DLVO theory and colloidal stability calculations were made following Agmo Hernández (2023), Muneer et al. (2020) and Worthen et al. (2016).

Van-der-Waals force The attractive van-der-Waals forces were calculated with:

$$V_{vdW} = -\frac{A_H r}{12h} \tag{6.6}$$

With A_H Hamaker constant, r particle radius (in m) and h separation distance (in m). The exact values for the calculations are displayed in Table 6.3.

Electric double layer force The EDL forces were calculated with:

$$V_{edl} = \pi\epsilon_r\epsilon_0 \cdot \frac{r_1 r_2}{r_1 + r_2} \cdot [2\zeta_1\zeta_2 \cdot \ln(\frac{1 + e^{-\kappa h}}{1 - e^{-\kappa h}}) + (\zeta_1^2 + \zeta_2^2) \cdot \ln(1 - e^{-2\kappa h})] \tag{6.7}$$

With ϵ_r relative permittivity of the medium and ϵ_0 absolute permittivity of vacuum, $r_{1,2}$ radii of the interacting particles (the term reduces to r_1 if interaction between particle and surfaces are calculated), $\zeta_{1,2}$ ζ-potentials of the interacting particles and h separation distance. Debye length κ^{-1} is calculated with:

$$\kappa^{-1} = \frac{1}{\sqrt{(8\pi\lambda_B N_A 10^{-24} I)}} \tag{6.8}$$

with λ_B Bjerrum length (in nm), N_A Avogadro constant, I ionic strength (mol/L).

Colloidal stability The colloidal stability is calculated with:

$$k_{coag} = k_0 e^{\frac{-v_{max}}{k_B T}} \tag{6.9}$$

with v_{max} being the height of the energy barrier taken from the total DLVO interaction curve (Figure 6.3B), k_B Boltzmann constant, T absolute temperature and k_0 expected particle collision frequency. K_0 can be calculated with:

$$k_0 = \frac{4 N_A k_B T}{3\eta} \tag{6.10}$$

With η viscosity of the medium. Finally, coagulation rate, i.e. colloidal stability is calculated with:

$$v_{coag} = k_{coag} C^2 \tag{6.11}$$

With C being the particle concentration in mol/L. Unit of v_{coag} is s^{-1}, i.e. to determine colloidal stability, v_{coag} is converted to yield the desired time (minutes, hours, months, years, etc.).

Table 6.3: Values used for DLVO calculations.

Parameter	Symbol	Value	Literature
Hamaker constant	A_H	$5.35 \cdot 10^{-20}$ (TiO_2-water-TiO_2), $6.9 \cdot 10^{-21}$ (TiO_2-water-silica)	Bergström (1997)
Particle radius	r	$75 \cdot 10^{-9}$	own data
Relative permittivity of water	ϵ_r	80.1	
Absolute permittivity of vacuum	ϵ_0	$8.85 \cdot 10^{-12}$	
ζ-potential	$\zeta_{1,2}$	variable, in V	own data
Debye length	κ^{-1}	depends on ionic strength	
Bjerrum length water	λ_B	0.71	
Boltzmann constant	k_B	$1.38065 \cdot 10^{-23}$	
Temperature	T	293.15	

6.5.3 Supplementary data

Table 6.4: ATR wavenumber identifications.

Wavenumber (cm^{-1})	Identification	Literature
1050/1040	Si-O-Si	Socrates (2001)
967	Ti-O-Si or Si-OH	Zu et al. (2015)
811	Si-O-Si (siloxane)	Socrates (2001)
770	Ti-O str. or Ti-O-Ti bend.	Islam et al. (2023)
430	Si-O	Socrates (2001)
420	sym. Ti-O-Ti str.	Pérez et al. (2020)

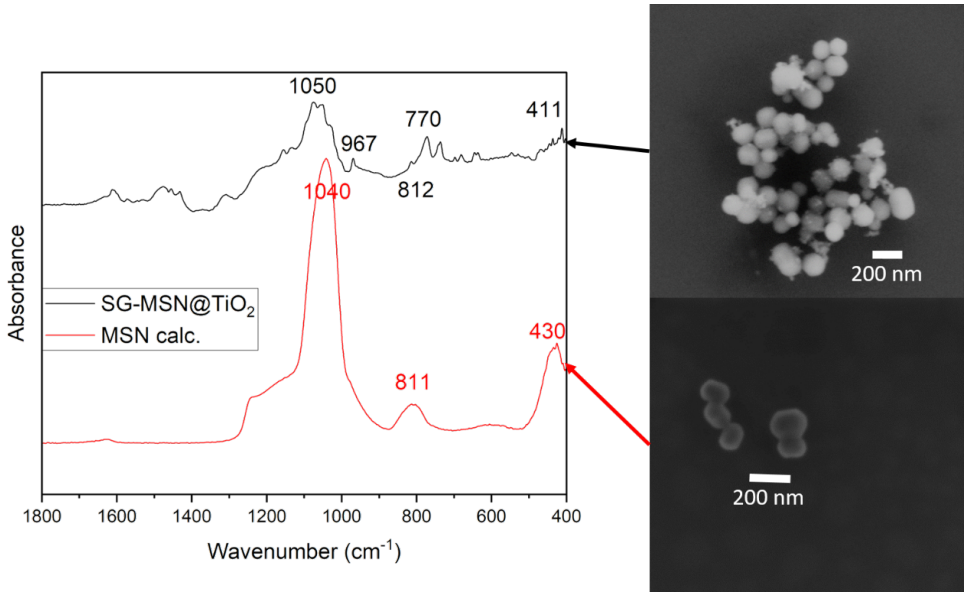

Figure 6.9: Representative ATR spectra and SEM images of dye-MSN@TiO_2 and pristine MSN carrier. Wavenumber identification in Table 6.4.

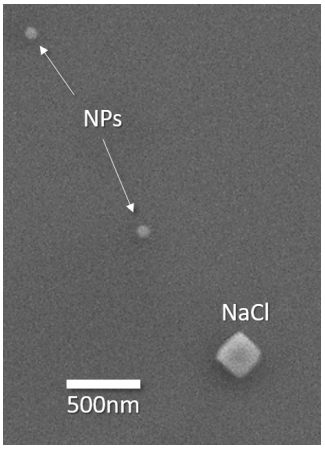

Figure 6.10: SEM image of the particles after the heated experiments. The occurrence of NaCl crystal is due to cooling of the 0.01 M NaCl fluid used in the experiments.

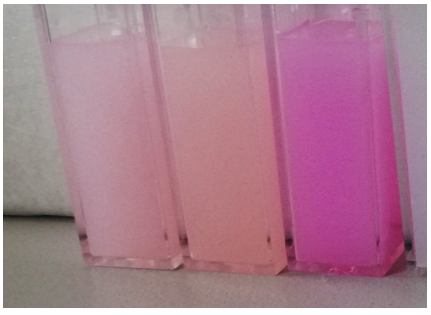

Figure 6.11: Photograph of the used particle tracers in this study. From left to right: R6G-MSN@TiO_2, SG-MSN@TiO_2, RhB-MSN@TiO_2.

Table 6.5: Calculated mean velocity (m/s), dispersivitiy (m) and dispersion coefficient (cm^2/s) from the flow-through experiments displayed in Fig. 6.6 main text.

	v_{mean}	Dispersivity (10^{-3}/m)	Dispersion coefficient (10^{-2} cm^{-2}/s)
SG-MSN@TiO_2	3.54	6.34	2.25
SG dye	3.55	8.25	2.93
RhB-MSN@TiO_2	3.24	13.22	4.28
RhB dye	3.39	10.34	3.5
R6G-MSN@TiO_2	3.6	4.55	1.64
R6G dye	2.7	32.49	8.76

CHAPTER 7

Design of silica nanoparticle tracers with optimized dispersion stability, sorption and deposition properties based on (X)DLVO and filtration theory

This Chapter is under review at *Geothermics*.

Spitzmüller, L., Berson, J., Schimmel, T., Kohl, T., Nitschke, F: Design of silica nanoparticle tracers with optimized dispersion stability, sorption and deposition properties based on (X)DLVO and filtration theory.

In this Chapter, the properties of nanoparticles are examined using DLVO, extended DLVO and filtration theories to provide recommendations on tracer design. The major findings are:

- Material-dependent Hamaker constant and ζ-potential are crucial parameters
- The smaller the particles the higher the impact of diffusion-dominated filtration
- Surface modifications are a powerful tool to improve nanoparticle performance

Abstract

Functional nanoparticles emerged as a potential new tracers for geoscientific applications, such as geothermal reservoir exploration. In this study, optimization strategies based on DLVO, extended DLVO (XDLVO) and filtration theory are presented. Our results show that nanoparticle material should have a low Hamaker constant, making metallic nanoparticles unfavorable. To ensure dispersion stability and minimize sorption on commonly negatively charged reservoir minerals, the nanoparticles should exhibit ζ-potentials below -30 mV. Decreasing the size of nanoparticles increases the diffusion-driven collisions with minerals grains and the probability of deposition while keeping the particle-to-grain size ratio below 0.008 prevents size exclusion effects. The impact of gravity on particle deposition is negligible for nanoparticles, making higher-density nanoparticle tracers viable. Experimental findings and XDLVO theory confirm the applicability of surface modifications to form a steric barrier that lowers attachment efficiencies while increasing colloidal dispersion stability. The impact of temperature cannot be assessed in a straightforward manner as it depends on multiple factors that can have contradicting effects. The presented study can serve as a guideline for the design of stable nanoparticle tracers with predictable transport properties in reservoirs. It shows that selecting appropriate materials, adapting ζ-potentials or employing effective surface modifications are key strategies to improve the performance of engineered nanoparticle tracers for geothermal exploration.

7.1 Introduction

In recent years, efforts to combine nanotechnology with geoscience emerged. Engineered silica nanoparticles currently find applications as nanofluids in enhanced oil recovery aiming to stabilize emulsions, decrease the interfacial tension, alter rock wettability, increase sweep efficiency and assist in re-mobilizing oil (Chakraborty and Panigrahi 2020, Gazem et al. 2024, Muneer et al. 2020). Further, the feasibility of functionalization of silica-based nanoparticles offers the possibility of applications as tracer also in challenging environments due to encapsulation of identifiable entities, such as DNA (Alaskar et al. 2015a, Chakraborty et al. 2023, Paunescu et al. 2013) or fluorescent molecules (Berson et al. 2024, Rudolph et al. 2020). The encapsulation process has two significant advantages. First, the shielding/protection of the encapsulated identification entity and second, unlike molecules, nanoparticles offer the possibility of surface modifications. Furthermore, this novel kind of tracers enables tracer multiplicity: using uniquely identifiable tracers with identical transport and sorption properties that allow simultaneous multiple tracer tests, offering insights into geological structures and enabling injections at different points (Spitzmüller et al. 2024b). Field applications of silica-based nanoparticle tracers were reported by Kong et al. (2018) and Mikutis et al. (2018) in shallow groundwater aquifers. Kittilä et al. (2019) tested the applicability of

these nanoparticle tracers in the underground laboratory Grimsel, Switzerland and Fan et al. (2024) recorded the successful tracer test using DNA-labeled silica nanoparticles in a strongly acidic (pH 2) geothermal reservoir site in Taiwan, conditions which are known to slow down dissolution (Spitzmüller et al. 2023b). For widespread applications in geological and geothermal reservoirs (elevated temperatures, wide pH ranges), however, stabilizing measures must be taken to increase the stability and ensure the integrity of silica-based nanoparticle tracers (Spitzmüller et al. 2024a). Further open question regarding applicability and transportability remain. In the study, theoretical, analytical calculations based on (X)DLVO and filtration theory are made to assess the dispersion stability, sorption tendency and deposition properties to elucidate the requisites for designing silica-based nanoparticle tracers with optimized behavior, such as low sorption affinity and high dispersion stability. This study aims to provide fundamental insight into how to use established colloid science based methods, such as the (X)DLVO theory paired with the filtration theory, which describes the behavior of colloids in (natural) porous media on the pore-scale to design and optimize nanoparticle tracers for geoscience applications, i.e. to elucidate the crucial factors for successful applications..

The classical DLVO theory is used to describe the stability of colloidal dispersion and was developed by Derjaguin and Landau (1941) and Verwey and Overebeek (1948). It sums up the contribution of the attractive London-van der Waals dispersion force and the force originating from the formation of an electric double layer on charged particle surfaces and allows to determine dispersion stability (Adamzyck and Weroński 1999, van Oss 2008). Accurate knowledge about colloidal dispersion stability, sorption tendency and assessment of risk of aggregation and particle deposition is crucial in many geoscientific applications, such as enhanced oil recovery using nanofluid (Chakraborty and Panigrahi 2020), environmental remediation processes (Klaine et al. 2009) and tracer tests (Tang et al. 2023). Evaluating the dispersion stability and sorption tendency toward reservoir minerals using DLVO theory is pivotal when aiming to transfer nanoscientific applications to geoscientific research questions (Jia et al. 2024).

Similar to molecular tracers conventionally used in geothermal science and hydrology to assess reservoir conditions and properties, such as extension and interconnection, particle tracer transport properties are determined by advection, diffusion, dispersion and sorption (Bradford et al. 2002). Therefore, in addition to dispersion stability, the impact of fluid dynamics on the transport properties and deposition of nanomaterials in geoscientific environments needs to be considered (Higgo et al. 1993, Liu et al. 2020, Ryan and Elimelech 1996). Tufenkji and Elimelech (2004) developed a novel solution for the convective-diffusion equation of the classical filtration theory that also considers nanoparticle-related factors, such as hydrodynamic interactions and van der Waals attraction. The equation consists of three parts: the contributions to the filtration process by diffusion, interception and gravity. Together, they represent the single grain collector contact efficiency, i.e., they give an overview of the probability of collision of a transported particle with the reservoir medium (treated

as individual single grains in Elimelech et al. (1995)). Pairing this theoretical value with measured or calculated attachment efficiencies, i.e., if sorption is reversible or irreversible, the single grain collector removal efficiency is determined. This value describes the overall tendency of particles to deposit within and be filtered by porous media (Elimelech et al. 1995).

Ideal nanoparticle tracer particles should exhibit minimal sorption and retention and a high dispersion stability, i.e., the repulsive forces in DLVO theory should exceed the attractive ones. However, these forces are partly dependent on extrinsic parameters, such as the salinity of fluids that cannot be adapted. Therefore, for the development of nanotracers, the focus should lay on the surface of the nanoparticles themselves. Here, the advantage of nanoparticles comes into focus: Their modularity enables modification of the surface. By modifying the surface properties of the particles, the ζ-potential can be altered and additional forces are created, such as steric force originating from surfactants/ligands/polymers bound to the surface. The impact of steric force is described by the extended DLVO (XDLVO) theory. Surfactants, such as for example the anionic sodium dodecyl sulfate (SDS) or the zwitterionic SB3-14, additionally increase the dispersion stability (Zareei et al. 2018) and polymer-coated nanoparticles proved to be less sorptive and more stable in high saline fluids compared to unmodified ones (Li et al. 2014). However, if the surfactant concentration is above the critical micelle concentration (CMC), the effect of steric stabilization could also be reversed due to depletion effects and free micelles, resulting in destabilization of the dispersion (Jódar-Reyes et al. 2006). Therefore, design calculations should also account for the importance of XDLVO theory.

As shown in Spitzmüller et al. (2024b), applying silica nanoparticle-based tracers as (hydro)geological tracers aims to augment the toolbox of available tracer candidates for geothermal and hydrogeological tracer tests. Therefore, the sorption tendency of these nanoparticle tracers and their deposition in reservoir media needs to be assessed and the governing deposition mechanisms elucidated (Liu et al. 2020). Additionally, to facilitate the design of suitable nanoparticle tracers, an understanding of the interaction processes between the particles and the reservoir is needed. In this study, we use DLVO, XDLVO and filtration theory to predict their behavior and identify parameters that can be adapted for design of enhanced nanoparticle-based tracers. First, we investigate the interaction between different tracer particle candidates based on DLVO theory to determine the governing factors required for dispersion stability. Once identified, the interactions of these tracer particles with typical reservoir minerals are further studied. In the next step, the filtration theory is applied to analyze the governing factors increasing the collision probability (i.e., the single grain collector contact efficiency) and to determine crucial points to consider in designing suitable tracers. The theory is examined with experimental results from flow-through tests and the advantage of surface modifiability is demonstrated. The positive effect of surface modifications is predicted by the extended DLVO (XDLVO) theory and is confirmed real-flow through experiments analyzed with filtration theory. Finally, the impact of temperature is assessed and discussed and recommendations on designing suitable nanoparticle-based

tracers for geo-reservoir applications are given based on findings from DLVO, XLDVO and filtration theory.

7.2 Methods

7.2.1 DLVO-theory

Dispersion stability of colloids in an aqueous media can be predicted based on DLVO theory (Agmo Hernández 2023). The DLVO theory (named after the investigators Derjaguin, Landau, Verwey and Overbeek) adds the attractive and repulsive forces acting on the nanometer scale mutually between particles. Attractive force is the London-van der Waals force (LvdW), while repulsive force is comprised of electric double layer force (EDL) and occasionally Born repulsive force. The resulting overall force acting on spherical particles or surfaces can be attractive (negative) or repulsive (positive). When the separation distance between the objects is below approx. 0.5 nm, the repulsive Born force dominates, which originates from overlapping atomic orbitals (Christenson 1988). Above that distance, whether the EDL or the LvdW force dominates depends on the magnitude of the EDL force. The DLVO is displayed as the resulting energy over the inter-particle distance. Its possible results are:

- A primary energy minimum
- A primary minimum and an energy barrier
- A primary minimum, an energy barrier and a secondary minimum

The depth of the primary minimum is an indication of the stability of aggregation. The deeper the primary minimum, the less likely is reversibility of aggregation. The height of the energy barrier, on the other hand, indicates the stability of the dispersion. This means, the higher the energy barrier is, the less likely is formation of aggregates and the more probable is a stable dispersion. The importance of the secondary minimum is related to its depth. The relationship is as follows: the deeper the minimum in the attractive region (i.e., values below 0), the more likely is (reversible) aggregation of particles in the secondary minimum (Elimelech et al. 1995).

DLVO forces are calculated according to Elimelech et al. (1995), Gregory (1981), Hogg et al. (1966), Muneer et al. (2020) and Ruckenstein and Prieve (1976):

$$V_{DLVO} = V_{LvdW} + V_{EDL} + V_B \tag{7.1}$$

$$V_{LvdW} = -\frac{A_H r}{12h} \tag{7.2}$$

$$V_{LvdW} = -\frac{A_H r}{6h} \tag{7.3}$$

$$V_{EDL} = \pi\epsilon_r\epsilon_0 \cdot \frac{r_1 r_2}{r_1 + r_2} \cdot [2\zeta_1\zeta_2 \cdot \ln(\frac{1 + e^{-\kappa h}}{1 - e^{-\kappa h}}) + (\zeta_1^2 + \zeta_2^2) \cdot \ln(1 - e^{-2\kappa h})] \tag{7.4}$$

$$V_B = \frac{A_H r \sigma^6}{1260h} \tag{7.5}$$

Equation 7.2 describes the non-retarded LvdW force between particles and Equation 7.3 between a particle and a surface. The Debye length can be calculated as:

$$\kappa^{-1} = \frac{1}{\sqrt{8\pi\lambda_b N_A 10^{-24} I}} \tag{7.6}$$

With A_H being the material-dependent Hamaker constant, r particle radius, h separation distance, ϵ_r and ϵ_0 relative permittivity of medium and absolute permittivity of vacuum, respectively, $\zeta_{1,2}$ ζ-potential of interacting particles/surfaces, σ Born collision diameter, N_A Avogadro constant, λ_B Bjerrum length of fluid and I molarity of the solvent (Table 7.2). ζ-potentials of silica and titania nanoparticle are taken from Spitzmüller et al. (2024b). Hamaker constants were used from literature data for the interaction of particle-particle and particle-surface in water. The constants used for the following calculations are displayed in Table 7.1.

7.2.2 Filtration theory

The single grain collector contact efficiency is calculated based on an approach by Tufenkji and Elimelech (2004) to assess the deposition of particles in porous media. Here, the porous media is assumed to consist of multiple so-called single grain collectors, which are defined as being spherical. Three different factors can be calculated: the single grain collector contact efficiency, the attachment efficiency and the single grain collector removal efficiency. They describe the probability of collision of particles with the single grain collector, the efficiency of (irreversible) attachment upon collision and the actual removal efficiency of the single grain collectors, respectively (Elimelech et al. 1995). The single grain collector contact efficiency (η_0) of particles in porous media can be described theoretically as the sum of three different mechanisms: diffusion (η_D), interception (η_I) and gravity (η_G). Single grain collector contact (η_0), removal (η) and attachment (α) efficiencies can be calculated following

Table 7.1: Hamaker constants used for calculations

Particle-particle (in water)	Hamaker constant A_H in 10^{-20}J	Reference
Silica-Silica	0.63	Bergström (1997)
Titania-Titania	5.65	Bergström (1997)
Polystyrene-Polystyrene	0.77	French et al. (2007)
Gold-Gold	12.6	Pinchuk and Jiang (2015)
Particle-surface (in water)	**Hamaker constant A_H in 10^{-20}J**	**Reference**
Silica-Silica	0.63	Bergström (1997)
Silica-Mica	1.16	Bergström (1997)
Silica-Calcite	0.69	Bergström (1997)
Silica-Alumina	1.83	Bergström (1997)
Titania-Silica	0.69	Bergström (1997)
Titania-Mica	1.83	Bergström (1997)
Titania-Alumina	3.11	Bergström (1997)

the numerical solutions of the convective-diffusion equation by Tufenkji and Elimelech (2004) that also includes the contribution of hydrodynamic interactions and van der Waals attraction:

$$\eta_0 = \eta_D + \eta_I + \eta_G \tag{7.7}$$

$$\eta_0 = 2.4 A_S^{\frac{1}{3}} N_R^{-0.081} N_{Pe}^{-0.715} N_{vdW}^{0.052} + 0.55 A_S N_R^{1.675} N_{Att}^{0.125} + 0.22 N_R^{-0.24} N_G^{1.11} N_{vdW}^{0.053} \tag{7.8}$$

$$\eta = \alpha \eta_0 \tag{7.9}$$

$$\alpha = -\frac{2}{3} \frac{d_c}{(1-f) L \eta_0} \ln\left(\frac{C}{C_0}\right) \tag{7.10}$$

with d_c collector grain size, f porosity, C/C_0 ratio of recovered particle concentration to initial concentration derived from flow-through experiments. Other parameters are:

$$N_R = \frac{d_p}{d_c} \quad \text{Aspect ratio} \quad (7.11)$$

$$N_{Pe} = \frac{U d_c}{D} \quad \text{Péclet number} \quad (7.12)$$

$$D = \frac{k_B T}{6\pi r \mu} \quad \text{Diffusion coefficient} \quad (7.13)$$

$$N_{vdW} = \frac{A_H}{k_B T} \quad \text{van der Waals number} \quad (7.14)$$

$$N_{Att} = \frac{A_H}{12\pi\mu r_p^2 U} \quad \text{Attraction number} \quad (7.15)$$

$$N_G = \frac{r_p^2(\rho_p - \rho_f)g}{\mu U} \quad \text{Gravity number} \quad (7.16)$$

$$A_S = \frac{2(1-((1-f)^{\frac{1}{3}})^5)}{2-3(1-f)^{\frac{1}{3}}+3((1-f)^{\frac{1}{3}})^5-2((1-f)^{\frac{1}{3}})^6} \quad \text{Porosity dependent number} \quad (7.17)$$

with d_c and d_p collector and particle size, respectively. U fluid velocity, k_B Boltzmann constant, T absolute temperature, r_p particle radius, μ viscosity, A_H Hamaker constant, ρ_p and ρ_f density of particle and fluid, respectively, g gravitational constant and f porosity. The porosity-dependent number is based on Happel's sphere-in-cell model (Elimelech et al. 1995). It should be noted that the calculations of the filtration theory do not consider the effect of a repulsive energy barrier between the single grain collector and the particle.

7.2.3 XDLVO theory

Nanoparticles offer the possibility of surface modifications, for example, by physi- or chemisorption of surfactants/ligands. Their presence impacts the interaction between particles and surfaces and particles with other particles. The stabilization effect of such surface modifications is usually described as steric stabilization and can be calculated by the addition of steric force to the DLVO forces:

$$V_t = V_{DLVO} + V_O + V_e \quad (7.18)$$

with osmotic and elastic forces calculated by piece-wise functions according to Tran and Richmond (2021), Vincent et al. (1986) and Worthen et al. (2016):

$$V_O = 0 \qquad \text{if } 2L \leq h \tag{7.19}$$

$$V_O = \frac{4\pi r}{\nu_1}\Phi_p^2(\frac{1}{2}-\chi)(L-\frac{h}{2})^2 \qquad \text{if } L \leq h < 2L \tag{7.20}$$

$$V_O = \frac{4\pi r}{v_1}\Phi_p^2(\frac{1}{2}-\chi)L^2(\frac{h}{2L}-\frac{1}{4}-\ln(\frac{h}{L})) \qquad \text{if } h < 2L \tag{7.21}$$

$$V_e = 0 \qquad \text{if } L \leq h \tag{7.22}$$

$$V_e = \frac{2\pi r}{M_W}\Phi_p L^2 \rho_p [\frac{h}{L}\ln(\frac{h}{L}(\frac{3-h/L}{2})^2) - 6\ln(\frac{3-h/L}{2}) + 3(1+\frac{h}{L})] \qquad \text{if } L > h \tag{7.23}$$

with r particle radius, ν_1 volume of one solvent molecule, h separation distance, Φ volume fraction of surfactant/ligand/polymer, L length of surfactant/ligand/polymer, M_W molecular weight of surfactant/ligand/polymer, ρ_p density of ligand and χ Flory-Huggins parameter. χ describes the compatibility of the surfactant and the solvent, with χ<0.5 being compatible and χ>0.5 incompatible.

7.3 Results and Discussion

In the following section, the crucial factors for the design of nanoparticle tracers are indicated and discussed. First, the focus is on maintaining a stable dispersion that prevents aggregation of particles and pore-clogging by aggregates in reservoirs. Then, the interaction of selected nanoparticle tracer candidates is assessed regarding their sorption tendency toward selected reservoir minerals. In the next step, the filtration theory is applied to analyze the governing factors that increase the collision probability and thus the nanoparticle tracer retention rate in porous media. The theory is compared with experimental results from flow-through tests and the advantage of surface modifiability of nanoparticles is demonstrated. The effect of surface modifications is predicted by the extended DLVO (XDLVO) theory and is confirmed by experimental flow-through tests analyzed with filtration theory. Finally, the impact of temperature is assessed and discussed in the framework of possible intended applications within geothermal reservoirs.

7.3.1 Dispersion stability - DLVO particle-particle interaction

Stable dispersions are pivotal for multiple applications, such as stable nanofluids for enhanced oil recovery (Muneer et al. 2020) or dispersed colloids for tracer tests (Berson et al. 2024) to prevent particle aggregations that could lead to pore-clogging. The dispersion stability can be assessed through calculation and interpretation of the total interaction energy (V_t) between two (spherical) particles. As shown before, V_t (Equation 7.1) is the sum of the contributions of the LvdW force (Equation 7.2), electric double layer (EDL) force (Equation 7.4) and Born force (Equation 7.5).

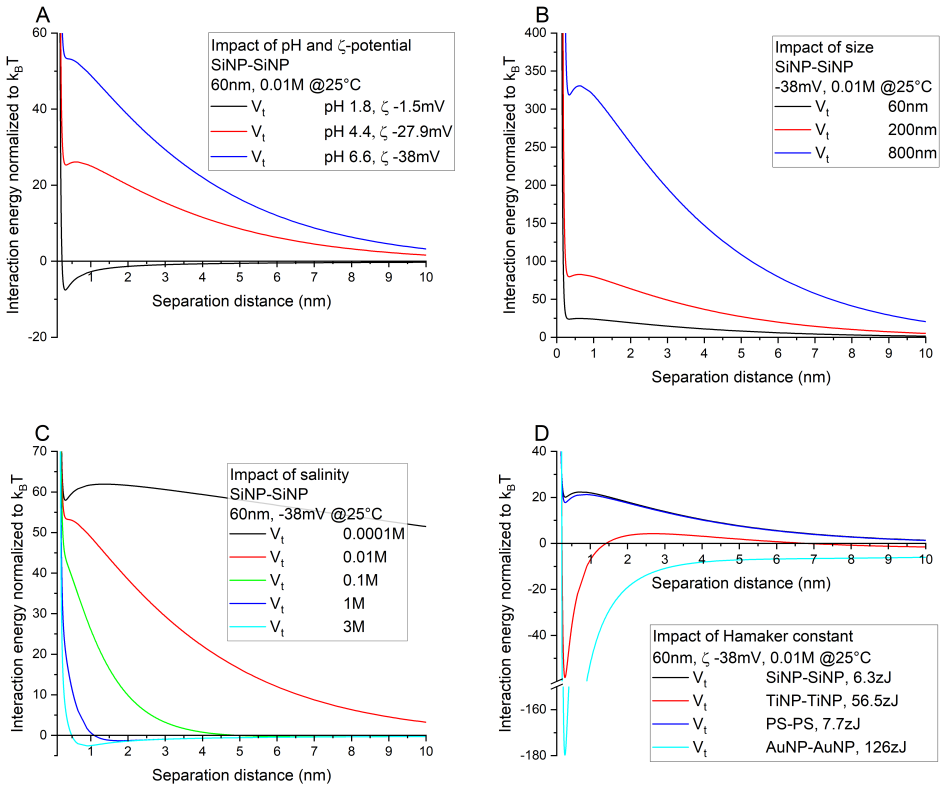

Figure 7.1: DLVO interaction calculation for particle-particle. Impact of ζ-potential (A), size (B), salinity (C) and Hamaker constant (D). Note the y-axis scaling break in D.

Figure 7.1 shows various DLVO interaction profiles and elucidates the impact of the parameters used for the calculations. Factors impacting the overall DLVO interaction are pH value and salinity of the solution, ζ-potential and size of the particles and the Hamaker constant of the particles. Generally, a rule of thumb when interpreting DLVO interaction curves is that the shallower the primary minimum, the less stable aggregation could occur. On the other hand,

the higher the energy barrier, the greater the dispersion stability is, i.e., the less likely the particles are to aggregate.

Figure 7.1A shows the impact of pH and the ζ-potential of the particles on 60 nm-sized silica nanoparticles in 0.01 M 1:1 electrolyte at 25°C. It can be seen that higher ζ-potentials lead to the formation of an energy barrier and hence, dispersion stability is increased. Lower pH values that lead to near-neutral ζ-potentials are located near the so-called isoelectric point (IEP), where the resulting surface charge of particles is net-neutral. It can be seen that the further away the pH of the IEP, the more stable the dispersion as the energy barrier increases with increasing pH values and hence increasing absolute ζ-potential. The ζ-potential/pH-values impact the EDL force directly (Equation 7.4). Figure 7.1B shows the impact of the size of the particle while maintaining pH/ζ-potential, salinity, material and temperature constant. It is noticeable that increasing the size of the particles also increases the energy barrier. Further, the size of particles could also affect the ζ-potential and increase the risk of gravitational settling, which is neglected in this calculation. The size of the particles affects all three forces (LvdW force, EDL force and Born force, Equations 7.2-7.5). The impact of salinity in a 1:1 electrolyte is shown in Figure 7.1C while maintaining pH/ζ-potential, size, material and temperature constant. Lower salinity leads to a higher energy barrier. This behavior is attributed to increased EDL force caused by the increase of the Debye length, which inversely depends on salinity. Contrarily, when salinity increases, the Debye length decreases. Hence, the EDL force range is short, which, in turn, results in attractive force overpowering repulsive force. Thus, the energy barrier is lowered or even an attractive primary minimum appears (as in Figure 7.1C 3M case) that lowers the dispersion stability drastically. Figure 7.1D points out the impact of nanoparticle material represented as a change in the Hamaker constant (individual interaction constant for materials within a medium, i.e., water, values see Table 7.1). All other factors are kept constant to elucidate the impact of the nanoparticle material: 60 nm-sized particles, pH/ζ-potential constant, 0.01 M 1:1 electrolyte and 25°C. Tested cases are silica, titania, polystyrene/latex and gold nanoparticles with A_H $6.3 \cdot 10^{-21}$ J, $5.65 \cdot 10^{-20}$ J, $7.7 \cdot 10^{-21}$ J and $1.26 \cdot 10^{-19}$ J, respectively. The Hamaker constant contributes to the Born repulsive force (Equation 7.5) and the LvdW attractive force (Equation 7.2). It can be seen that increasing values lead to the formation of a deep primary minimum, i.e., the LvdW force outweighs the repulsive EDL force. However, it should be remarked that nanoscale roughness can affect the Hamaker constant, leading to reduced attractive force and, hence, additionally stabilizing the particle dispersion (Valmacco et al. 2016).

In general, colloidal dispersions are stable when the resulting interaction energy based on DLVO theory is positive, i.e., repulsive. This is primarily the case when the particles have ζ-potentials of the same sign, when the fluid's salinity is low and when the material-dependent Hamaker constant is small. The resulting overall interaction energy is an interplay of many factors. Silica nanoparticles have sufficiently low Hamaker constants and form stable dispersions below 0.1 M salinity. The ζ-potential should be far from the IEP, i.e., pH values

should be significantly higher or lower. As a general recommendation, nanotracers should preferably be made out of silica or polystyrene but not (entirely) metallic.

However, it should be noted that these calculations represent isolated calculations with only one variable. However, in sizes, temperatures, pressure, material and salinity also impact ζ-potential and Hamaker constant values (e.g., Pinchuk and Jiang 2015). Therefore, the calculations presented here are simplified, but serve to obtain a first-order impression on dispersion stability.

7.3.2 Sorption tendency - DVLO particle-surface interaction

When nanoparticles are used as tracers in natural environments, their interaction with reservoir mineral surfaces is crucial in determining their overall performance, particularly their tendency for sorption and retention. The DLVO theory is applied to assess these interactions between silica and titania nanoparticles and four different mineral surfaces — silica, mica, calcite, and alumina — chosen for their significantly varying ζ-potentials. Mica has the most negative ζ-potential at -70 mV (Zaucha et al. 2011), followed by silica with a ζ-potential of -30 mV (Hartmann et al. 2018) and the most positive is alumina with +40 mV (Izrael-Živković et al. 2015). For calcite, the span of ζ-potential found in literature is vast. However, to represent an intermediate value, a ζ-potential of -5 mV is chosen from data by Al Mahrouqi et al. (2017). The ζ-potentials of silica and titania nanoparticles were measured with a ζ-sizer and are valid for 0.01 M 1:1 salt solutions at ambient temperatures (Spitzmüller et al. 2024b).

To calculate the attractive LvdW force, Hamaker constants are employed. The specific values used in calculations and their references are listed in Table 7.1. For the titania-water-calcite system, the Hamaker constant is assumed to be similar to that of the titania-water-mica system.

Figure 7.2 illustrates the DLVO interactions between the silica and titania nanoparticles and the surfaces. For silica nanoparticles, an energy barrier is observed in interactions with mica (A) and silica (B). The height of the energy barrier depends on the value of the ζ-potential with SiNP-mica owing the highest energy barrier. Interestingly, the interaction of silica nanoparticles with calcite (C) leads to the formation of a small and negative “energy barrier” at larger separation distances of about 5 nm. As expected, when interacting with alumina (D) no energy barrier forms due to the opposite charges between the negatively charged SiNPs and positively charged alumina surface, resulting in a deep primary minimum that indicates strong adsorption.

For positively charged titania nanoparticles, the behavior contrasts with silica nanoparticles. Deep primary minima and no energy barriers are observed in interactions with mica, silica, and calcite (A, B, C). However, in the interaction with the positively charged alumina surface

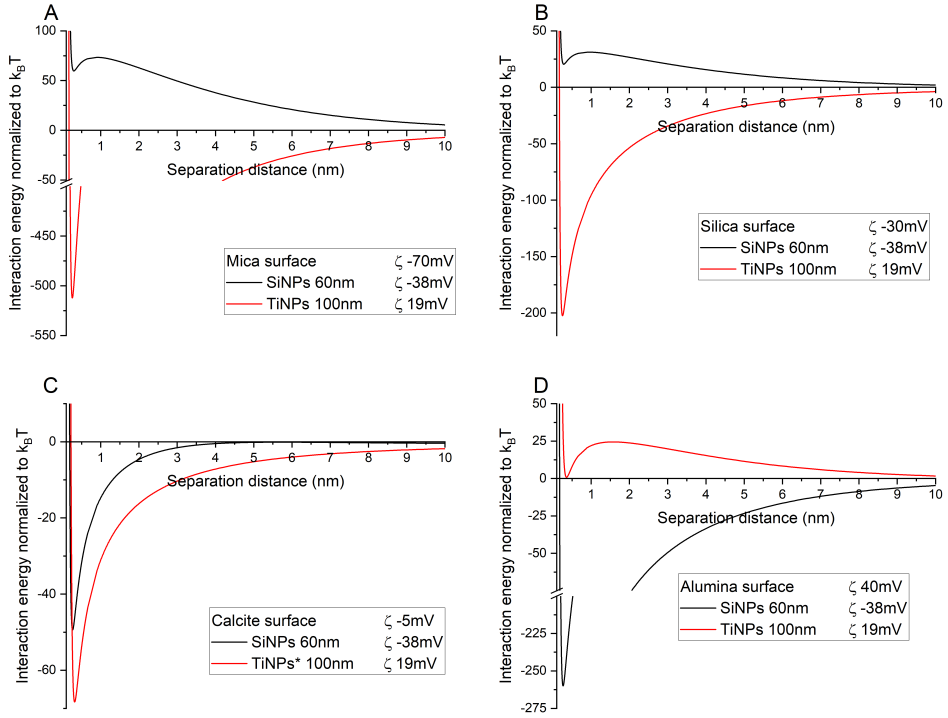

Figure 7.2: DLVO interaction calculations for particles-surfaces. * Hamaker constant for titania-water-mica used. Note the y-axis scaling break in A and D.

(D), an energy barrier appears. Compared to the interaction of SiNPs with mica and silica, the energy barrier is relatively small and the primary minimum is deeper. This behavior is attributed to the near-neutral ζ-potential of the TiNPs, which are below the threshold of ± 30 mV for stable dispersion and to the Hamaker constant of $3.11 \cdot 10^{-20}$ J, which is higher than for the other interactions. As shown before, higher Hamaker constants increase the LvdW force to exceed possibly the repulsive EDL force. Although having the same sign, attraction dominates between titania and the alumina surface at short separation distances.

In most cases, the silica nanoparticles are superior to the positively charged titania nanoparticles due to the predominantly negative charges of most natural minerals and reservoir rocks (Walker and Glover 2018). Therefore, having a nanoparticle tracer with negative charges is more likely to have less sorption tendency than a positively charged tracer. It should be noted, however, that the salinity of the fluids is of great importance for the dispersion stability and sorption tendency. Especially for geothermal environments where salinity can reach up to several hundred grams per liter (Sanjuan et al. 2016), maintaining a high surface potential is crucial. As the Debye length is affected by the salinity, the effect of the repulsive EDL force is rather low and might not suffice to overcome the London-van der Waals force. However, it is shown that especially polyvalent ions might have a greater impact on dispersion stability

than the level of salinity (Xie et al. 2016). For example, divalent ions, in general, increase the ionic strength, thus reducing the Debye length and, therefore, lowering the EDL forces (Muneer et al. 2020). Furthermore, divalent ions greatly influence the ζ-potential, as this value also depends on the ionic strength. Additionally, it should be noted here that the classical DLVO does not account for the impact of hydration of the ions (Ninham 1999). For example, cesium is experimentally proven to affect the interaction to a greater extent than sodium at the same concentration, although both are monovalent ions (Wang et al. 2013b). Their effect on dispersion stability can be best described by reversed or direct Hofmeister series (Ninham 1999).

In conclusion, negatively charged silica nanoparticles typically form energy barriers when interacting with the selected surfaces, reducing their sorption tendency. Positively charged titania nanoparticles generally do not form energy barriers, leading to a higher sorption tendency in most cases, unless the mineral surfaces are also positively charged.

7.3.3 Predictions of particle deposition based on filtration theory

Filtration theory can be used to assess the probability of particle deposition within a porous medium. The correlation-equation derived by Tufenkji and Elimelech (2004) accounts for the contribution of three different processes on the overall single grain collector contact efficiency (see Equation 7.8): Diffusion, interception and gravity (gravitational settlement). For calculation, the single grain collector size is kept constant at 1 mm and the density of the particles is assumed to be 1.6 g/cm^3 (a typical value for SiNPs Qiao et al. (2009), Silencieux et al. (2015)). The Hamaker constant is $6.9 \cdot 10^{-21}$ J (titania-water-silica interaction, considered as representative for dye-MSN@TiO_2 tracer particles). Porosity of the flow system is set to 35 % (Berson et al. 2024).

Figure 7.3 shows the contribution of each of the physical fluid dynamic parameters in dependence of flow velocity and particle size. To facilitate better categorization of the flow velocities: the mean flow velocities determined by tracer tests in the geothermal system Soultz-sous-Forêts (France) range between $3.7 \cdot 10^{-5}$ m/s (3.2 m/d) and $2.25 \cdot 10^{-3}$ m/s (194.4 m/d) (Radilla et al. 2012, Sanjuan et al. 2006). In Figure 7.3, η_0, as well as individual contributions of diffusion, interception and gravity, are shown in dependence of particle size. Reaching a probability of collision of unity means 100 % of particles will collide with the single grain collector. In Figure 7.3A-D, the impact of variation in fluid velocity is shown as well. Two main trends can be identified: Diffusion is the governing mechanism at decreasing particle size and a lower flow rate increases the probability of collision independent of particle size. The impact of gravity diminishes drastically with increasing fluid velocity and is more dependent on velocity than particle size, although increasing particle size increases gravitational settling. Interception depends rather on particle size than on fluid velocity. The lowest probability of collision is in all cases shown in Figure 7.3 in the lower range of

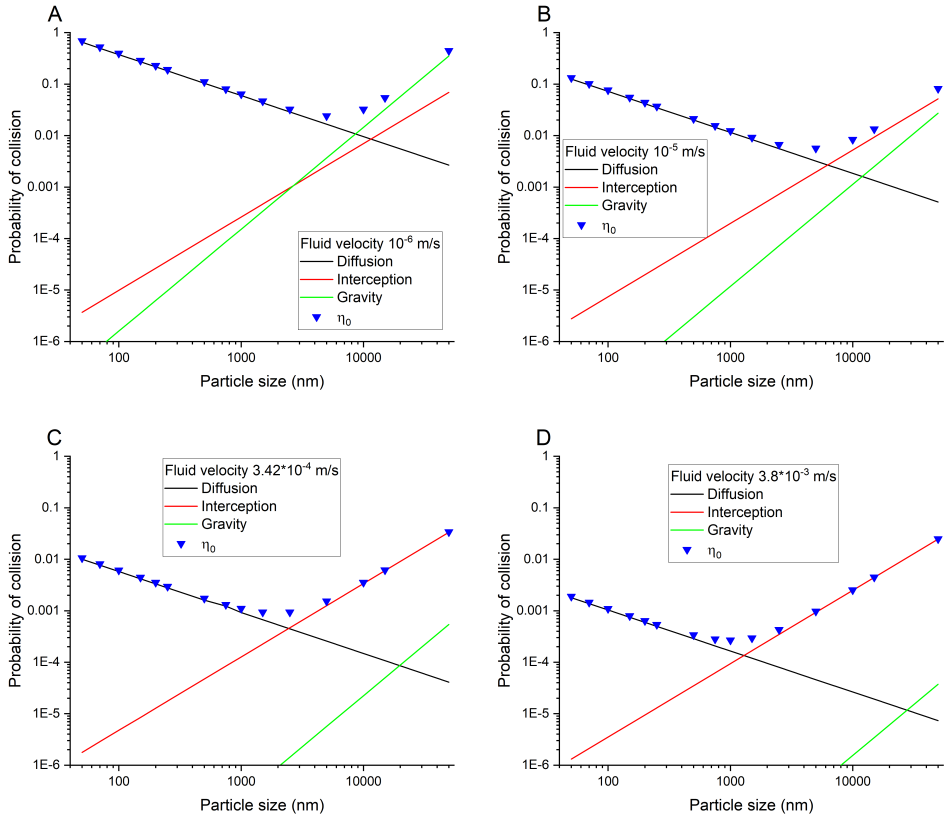

Figure 7.3: Factors contribution to the single grain collector contact efficiency η_0 in dependence of particle size. Collector size 1mm, density 1.6g/cm^3, A_H 6.9·10^{-21}J, porosity 35%.

µm-sized particles. The probability of collision increases drastically with decreasing particle size due to the contribution of diffusion-dominated collisions and increases with increasing particle size due to the contribution of interception and gravity.

Figure 7.4 demonstrates the impact of particle size and fluid velocity on the probability of collisions. The parameters are equal to those used for calculations displayed in Figure 7.3, but here, they are shown in dependence on fluid velocity. It can be seen that for particle sizes 50 nm and 500 nm, the single grain collector contact efficiency (η_0) is governed solely by diffusion, whereas for the 5000 nm (5 µm) particles, interception dominates at higher flow rates. In the case of 50000 nm (500 µm)-sized particles, the dominant mechanism at low flow rate is gravity and at flow rates above 10^{-5} m/s interception.

For calculations shown in Figure 7.3 and Figure 7.4, the size of the particle collector was kept constant at 1 mm, which is in the range of coarse sand. Figure 7.5 shows the impact of the collector grain size on the collision probability. Figure 7.5 shows the impact of

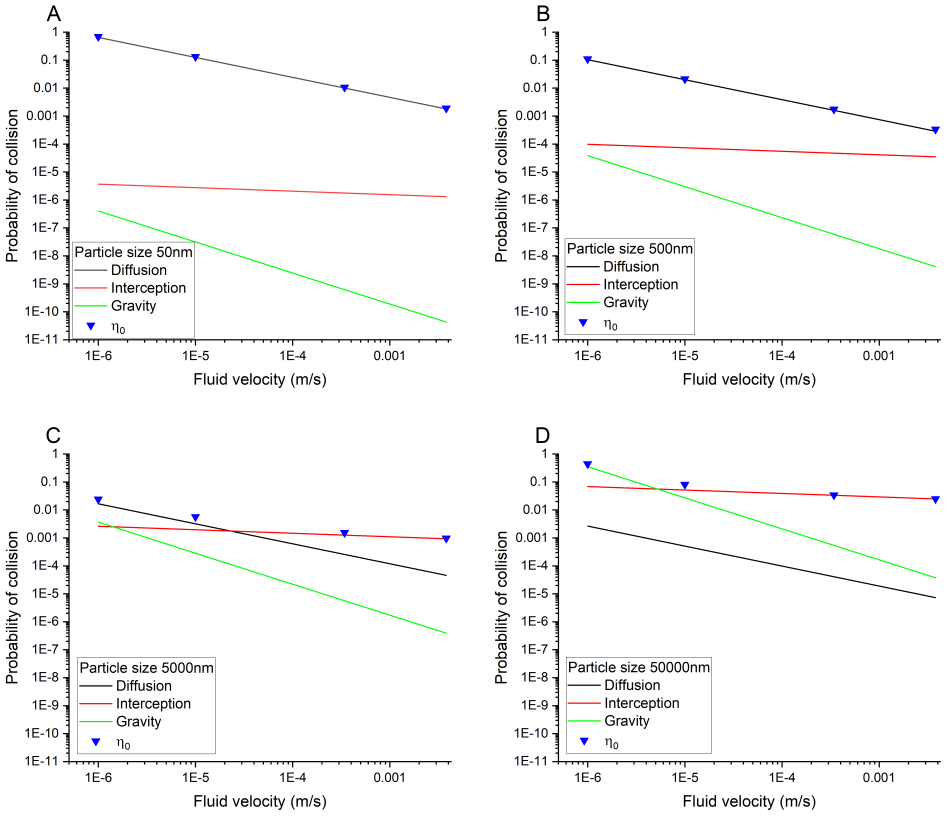

Figure 7.4: Factors contribution to single grain collector contact efficiency η_0 and overall probability of collision in dependence particle size and flow velocity. Collector size 1 mm, density particles 1.6 g/cm^3, A_H 6.9·10^{-21} J, porosity 35%.

varying collector size from 1 µm to 1000 µm (1 mm) for particle sizes of 150 nm (Figure 7.5A) and 1000 nm (Figure 7.5B) with a density of 1.6 g/cm^3, A_H 6.9·10^{-21} J at constant fluid velocity of 3.8·10^{-3} m/s. For 150 nm particles and collector sizes below 10 µm, the dominant mechanism for collision is interception. Above 10 µm, the dominant mechanism is diffusion, as was anticipated by calculations presented in Figure 7.3 and Figure 7.4. The unexpected dominance of interception at collector grain sizes below 10 µm can be explained by straining, i.e., size exclusion. According to Xu et al. (2006), the limit for straining to occur is at a particle-to-collector size ratio of above 0.008. In the case of 150 nm particles and 1 µm collector grain, this ratio is 0.15, which means that straining is likely to contribute to particle deposition/retention. It should be noted that equation 7.8 does not accomplish the impact of straining and η_0 values are inaccurate at these conditions (Bradford et al. 2002).

For 1000 nm (1 µm) particles, the behavior is principally similar to the 150 nm particles: at low particle-to-collector ratios, the dominant mechanism seems to be interception. Up to

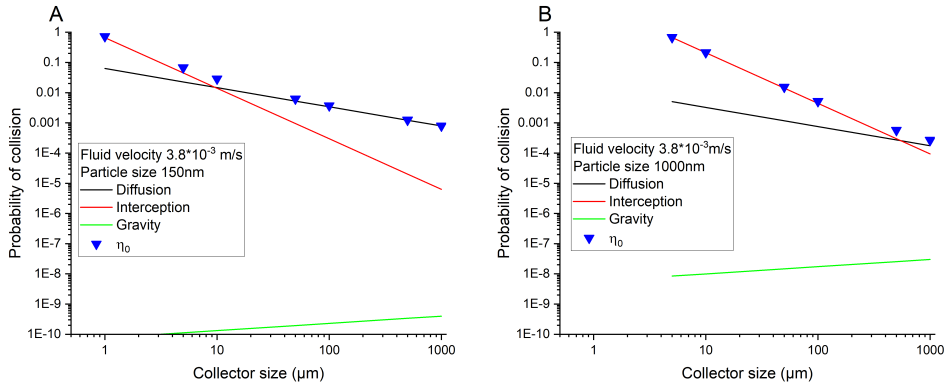

Figure 7.5: Impact of collector size on probability of collision. A) particle size 150 nm, B) particle size 1 µm. As size exclusion effects are not considered in equation 7.8, estimation of η_0 for particle/collector ratio above 0.008 is not sufficiently accurate (Auset and Keller 2006, Xu et al. 2006).

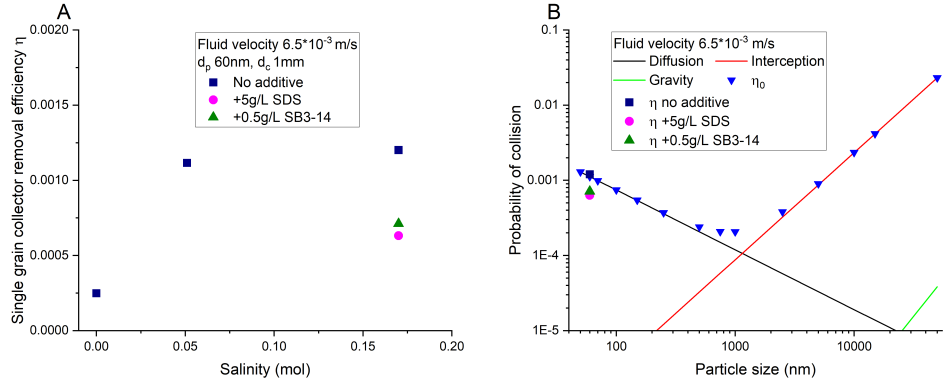

Figure 7.6: A) Single grain collector removal efficiency η in dependence of salinity. α calculated using data from flow-through experiments by Berson et al. (2024), Rudolph (2021) and Spitzmüller et al. (2023a). Impact of additives is shown by effectively lowering the removal efficiency. B) probability of collision and impact of diffusion, interception and gravity. η calculated according equation 7.9.

a collector size of approx. 500 µm (collector/particle 0.002) interception is the dominant mechanism above that diffusion dominates. Although the impact of gravity is increased, it is still orders of magnitudes lower than the impact of interception and diffusion.

η_0 is mostly overestimated. Consequently, for calculations of the actual single grain removal efficiency (η), η_0 is adapted by multiplication with a factor called the attachment efficiency α that is derived from experimental data. In Figure 7.6 calculated η values have been calculated by multiplication of η_0 with attachment efficiencies (α) determined by flow-through experiments (Berson et al. 2024, Rudolph 2021, Spitzmüller et al. 2023a). The particle size is 60 nm, collector size 1 mm, porosity 35%, the density of the particles is approx. 2 g/cm^3 and the Hamaker constant is $6.3 \cdot 10^{-21}$ J (Table 7.1).

In Figure 7.6A, the single grain collector contact efficiency (η) is shown as a function of salinity with increasing salinity resulting in increased collision probability. By adding the anionic surfactant SDS or the zwitterionic surfactant SB3-14, the attachment efficiency is lowered and hence η is lowered. In Figure 7.6B, these data points (at a salinity of 0.17M) are plotted in a collision probability diagram and compared to η_0 values and the three main removal mechanisms. It can be seen that the governing mechanism for particle deposition at the used particle size (60 nm) is diffusion. However, the η-values for the experiments are lower than the expected η_0 values (Figure 7.6B). That means the attachment efficiency (α) must therefore be lower than unity (less than 100%), which implies that not all collisions lead to attachment. Similar to these results, lower than predicted attachments were also lower than seen in several other studies (Elimelech et al. 1995, Elimelech and O'Melia 1990, Hull and Kitchener 1969, Marshall and Kitchener 1966). This discrepancy was attributed either to surface charge heterogeneity or to a repulsive double layer (and hence an energy barrier). In this experimental setup with SiNPs and quartz sand, DLVO theory predicts the formation of a repulsive barrier between silica and quartz sand. It should be noted that if the attractive forces described in the DLVO theory govern colloidal retention/filtration, the salinity of the fluids could play an important role. On the other hand, if filtration/retention of particles is rather caused by hydraulics, it is mostly independent of ionic strength (Carstens et al. 2019).

For the experiments with additives, the η is even lower, which indicates that the attachment efficiency is further decreased due to the presence of the additives (Tian et al. 2010). The anionic surfactant shows the highest impact on lowering the attachment efficiency and hence, the probability of collision. An explanation for the behavior cannot be found in the traditional DLVO theory as it does not account for steric factors. This requirement elaboration is augmented in the XDLVO theory.

7.3.4 The importance of XDLVO theory: Adding a steric barrier

As shown in Figure 7.6, adding surfactants that physisorb on the surface of the nanoparticles changes the attachment efficiency (and single grain collector removal efficiency). An explanation is given by the XDLVO theory: the surfactants form a steric barrier and increase the repulsive force, thus creating an energy barrier (Napper and Netschey 1971, Zhulina et al. 1990).

Here, calculations on the impact of such a steric barrier are made according to XDLVO theory for the zwitterionic SB3-14 surfactant on dye-MSN@TiO_2 nanotracers described in Chapters 5 and 6. Four different cases are chosen to determine the effect of the steric barrier: Particle-particle and particle-surface interactions, with three different surfaces - silica, alumina and mica. For the calculations, RhB-MSN@TiO_2 nanoparticles are used with a size of 150 nm with added 0.1 mg/mL of zwitterionic surfactant SB3-14 and a ζ-potential of +19 mV at pH 6.6 in 10 mM KCl at 25°C (Spitzmüller et al. 2024b). ζ-potentials for

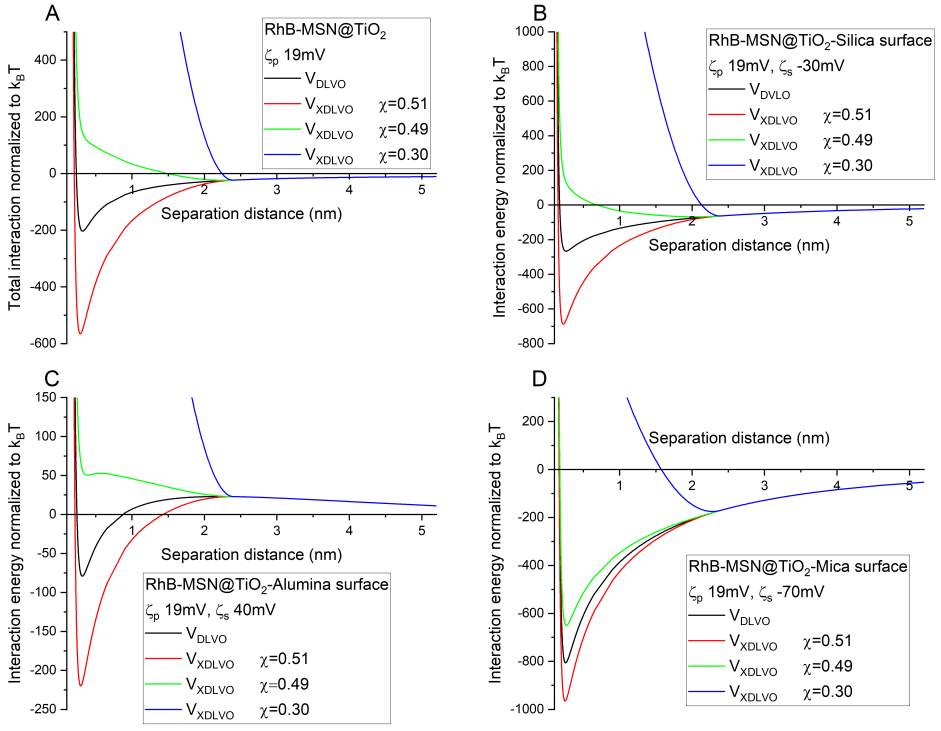

Figure 7.7: XDLVO forces calculations with varying Flory-Huggins χ parameter for particle-particle interaction (A) and particle-surface interaction (B).

the surfaces are -70 mV, -30 mV and +40 mV for mica, silica and alumina, respectively (Hartmann et al. 2018, Izrael-Živković et al. 2015, Zaucha et al. 2011). Hamaker constants for the interactions are chosen according to Table 7.1 for titania interactions.

Figure 7.7 shows the DLVO forces in black and the XDLVO forces in red, green and blue for varying Flory-Huggins χ-parameter. The χ-parameter indicates the compatibility of the surfactant with the surrounding media (water). Values below 0.5 indicate compatibility, with smaller values showing increasing compatibility and values above 0.5 indicate incompatibility (e.g., hydrophobic particles in water). In Figure 7.7 χ-parameters are therefore chosen to be highly compatible (χ=0.30), slightly compatible (χ=0.49) and slightly incompatible (χ=0.51). The effect of incompatible surfactants/surface coating (χ=0.51) is drastic: instead of forming an additional energy barrier, the depth of the primary minimum increases. As shown in Fig 7.7 for χ=0.51, the attraction between the particles and particles-surface is enhanced and no steric barrier is formed due to the incompatibility of the surface coating and the medium. On the other hand, with slightly compatible surfactants (χ=0.49), a steric barrier is formed and its effect is further increased at χ=0.30. Two significant conclusions can be drawn: The steric barrier function only acts up to twice the length of the polymer and increases with

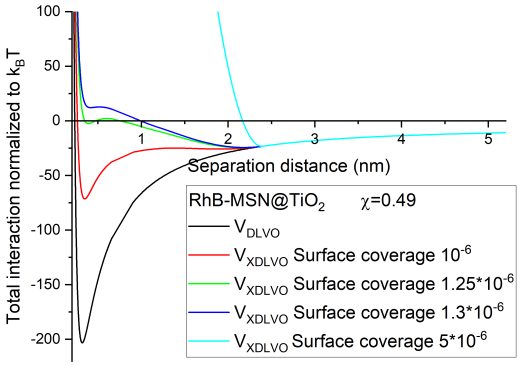

Figure 7.8: Impact of surface coverage on effectiveness of steric barrier calculated using XDLVO theory.

polymer-fluid compatibility. For example, in Figure 7.7D, the secondary minimum at approx. 2.5 nm is still existent and remains unaffected by the surface coating.

In this example, the surface coverage was set to be 10^{-6} mol/m^2 whereas in Figure 7.8, this value is varied up to $5{\cdot}10^{-6}$. An energy barrier starts forming in this set-up at a surface coverage of $1.25{\cdot}10^{-6}$ mol/m^2, even for a Flory-Huggins value of χ=0.49. Therefore, having adequate surface coverage further increases the stabilizing effect of the steric barrier. From literature data, it is anticipated that coverage of up to half of the available particle surface is ideal (Healy and La Mer 1964).

Finally, it should be noted that the calculations made here are only exemplary with several assumptions (e.g., surface coverage, molecular weight of the polymer, χ-parameter, listed in Table 7.2) and neither account for fluid salinities above 0.01 M nor temperatures above 25°C. Consequently, the ζ-potentials are assumptions or measurements but must be considered to have uncertainties. However, calculations based on XDLVO theory show the importance and effect of surface modifications on reducing particle-particle aggregation or particle-surface adsorption.

7.3.5 Impact of temperature

Temperature affects multiple parameters used in (X)DLVO and filtration theory calculations, namely ζ-potential/pH, Debye length κ^{-1} due to temperature dependence of the Bjerrum length λ_B, Hamaker constant A_H, relative permittivity ϵ_r, diffusion coefficient D, viscosity μ and fluid density ρ_f (Table 7.3). While the temperature dependence of most parameters is well determined, there is a lack in accurate datasets for the changes in the ζ-potential and the Hamaker constant values. While ζ-potential measurement at elevated temperatures is technically complicated, Tosha et al. (2003) established an empirical formula by experimental

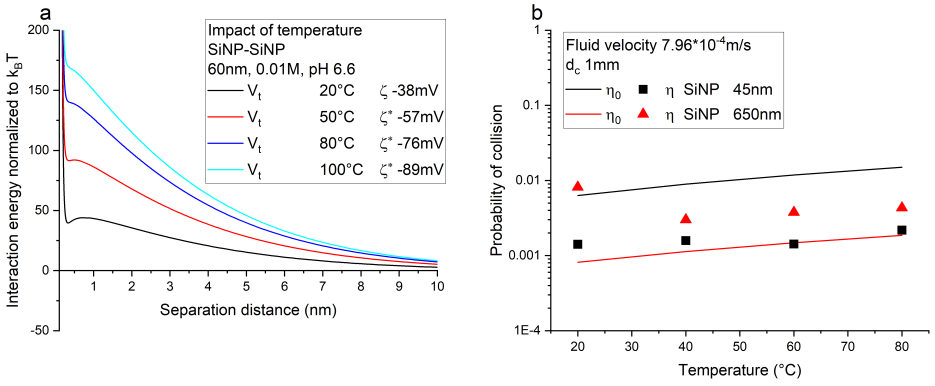

Figure 7.9: Impact of temperature on DLVO theory and collision probability. η calculated using α-values from unpublished flow-through experiments at elevated temperatures. * ζ-potential calculated according to the formula by Tosha et al. (2003).

results (Ishido and Mizutani 1981) to determine the temperature-dependent ζ-potential up to 150°C. While this formula only applies to salinities below 0.01 M, increased salinity cancels the temperature dependence of the ζ-potential (Al Mahrouqi et al. 2017). In the following calculations, the ionic strength is therefore fixed to 0.01 M 1:1 electrolyte. The other unknown temperature-dependent parameter is the Hamaker constant, which can be determined following the Lifshitz approach using the permittivity of the particles and the medium as well as the frequency. Jiang et al. (2016) showed that the Hamaker constant of metal nanoparticles is size- and temperature-dependent. Lefèvre and Jolivet (2009) reported a Hamaker constant change of by a factor of 2 up to temperatures of 350°C. Barton (2019) approximated the Hamaker constant change of silica to be 1.6 from 25°C to 100°C. While Lefèvre and Jolivet (2009) and Ghosh et al. (2006) estimated an increase in the Hamaker constant with increasing temperature, Barton (2019) and Yan et al. (2014b) predicted a decrease. We therefore assume in the following calculations that the Hamaker constant remains temperature-independent for the selected cases, which are below 100°C. Figure 7.9 shows the impact of temperature on DLVO forces and the single grain collector contact efficiency (η_0). Generally, increasing temperature increases the energy in the system, thus either increasing the risk of deposition due to increased probability of collisions (filtration theory) or decreasing the risk of deposition due to higher energy barriers (DLVO theory). In the case of DLVO forces, the energy barrier increases likely due to increased absolute ζ-potential (calculated according to Tosha et al. (2003)), although ϵ_r and κ^{-1} decrease. Simultaneously, the probability of collision increases with increasing temperature mainly driven by increased diffusion due to the temperature-dependence of the Brownian motion (Supplementary Figure 7.10). However, calculations of η using results from flow-through experiments show an inhomogeneous pattern with lower-than-predicted single grain collector removal efficiencies for 45 nm particles and higher-than-predicted values for 650 nm particles. Explanations for $\eta < \eta_0$ could be the presence of an energy barrier or particle detachment,

while for $\eta > \eta_0$, factors, such as particle aggregation, straining, sieving and bridging might play an important role. Comparable literature data on temperature dependence is scarce and often inhomogeneous. For example, Caldelas et al. (2011) found retention of 5 nm silica nanoparticles within porous media to increase by only 2% at 80°C, while Abdelfatah et al. (2017) calculated a reduced retention for the same setup. Therefore, to finally understand the impact of temperature more fully, additional tools like atomic force microscopy (AFM) should be employed (Wang et al. 2013b).

7.4 Conclusions and guidelines on nanoparticle tracer design

Although the presented calculations are not comprehensive due to inaccuracies in unknown, vague or estimated parameters, such as ζ-potential, Hamaker constants and Flory-Huggins χ-parameter, an overall trend can be observed. Guidelines based on these trends in (X)DLVO and filtration theory for nanoparticle tracer design are:

- Nanoparticle material should exhibit low Hamaker constant, i.e., preferably not metallic
- Nanoparticles with (strong) negative ζ-potential are less likely to be retained within the porous media due to mostly negatively charged reservoir minerals
- Particle sizes below 1 µm increase the probability of collision with mineral grains caused by increased diffusion
- Particle size needs to be adequate for the fluid velocity and the particle-to-grain size ratio should be below 0.008 to avoid size exclusion effects
- Impact of gravity on collision is mostly negligible for particle sizes below 1 µm. Therefore, a higher density of smaller nanoparticles is not detrimental
- Compatible surface modifications (i.e., $\chi < 0.5$) give rise to an additional repulsive force, stabilize colloidal dispersion due to steric stabilization and can lower attachment efficiencies
- The range of the steric force is limited to twice the length of the surfactant. Therefore, possibly multi-layer coatings could be more effective in reducing aggregation

Considering these recommendations, it could be possible to design a tracer that exhibits high colloidal stability and a reduced sorption tendency. Additionally, by applying surface modifications, there is a high potential to enhance the performance of these nanoparticle tracers and improve their transport properties. To create a more comprehensive base of knowledge, further investigations are needed to accurately identify the impact of geothermal conditions on parameters, such as ζ-potential and Hamaker constant.

7.5 Supplementary Material

Table 7.2: Parameters used for DLVO and XDLVO calculations.

Parameter	Symbol	Value
Relative permittivity of water	ϵ_r	80.1
Absolute permittivity of vacuum	ϵ_0	$8.85 \cdot 10^{-12}$ F/m
Bjerrum length of water	λ_B	0.71 m
Boltzmann constant	k_B	$1.38065 \cdot 10^{-23}$ J/K
Born separation distance	σ	$5 \cdot 10^{-10}$ m
Avogadro constant	N_A	$6.02214 \cdot 10^{23}$ mol^{-1}
Length of surfactant ZI	L	$1.2 \cdot 10^{-9}$ m
Bulk density of surfactant ZI	ρ_p	1
Molecular weight of ZI	M_W	329.5 g/mol

Table 7.3: Paramters used for calculation of temperature impact on DLVO and filtration theory.

Parameter	Symbol	20°C	40°C	50°C	60°C	80°C	100°C
Fluid density	ρ_f	1	0.9922		0.9832	0.97179	
Fluid viscosity	μ	0.001	0.0006539		0.0004656	0.003537	
ζ-potential	ζ	-0.038		-0.057494		-0.076988	-0.089984
Relative permittivity	ϵ_r	80.1		69.91		61.027	55.72

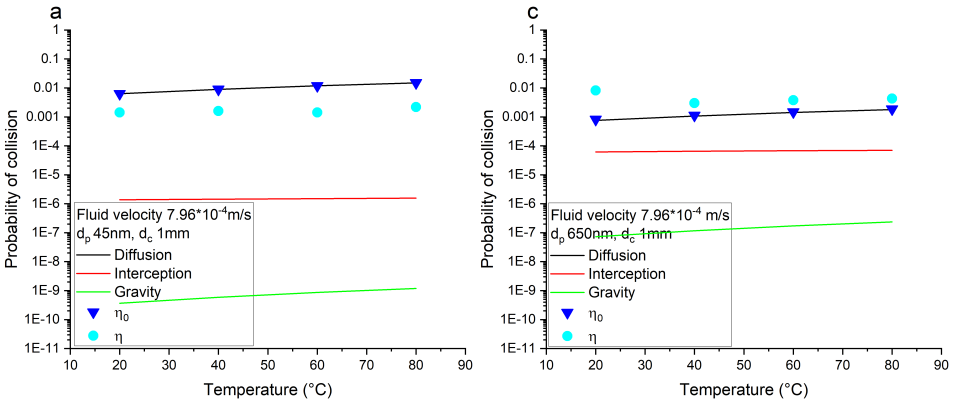

Figure 7.10: Contribution of diffusion, interception and gravity on η_0 of 45 nm and 650 nm silica nanoparticles. η calculated using α determined by flow-through experiments.

CHAPTER 8

Conclusions

The purpose of this thesis is to enhance the understanding of the behavior, interactions, and function of engineered nanoparticles in geo-environments, as well as to lay the foundation for the further development of nanoparticle-based tracers of optimal design. More precisely, fluorescent silica-based nanoparticle tracers with enhanced stability and functionality are developed, adapted and tested under geological-relevant conditions. Additionally, further improvements were performed by applying chemical surface modifications and the applicability as tracers were simulated and tested experimentally. The obtained results help gain insight in the complex interactions and behavior of nanoparticle-based tracer in geological environments.

First, a review of available molecular and particulate tracers was given and their limitations, such as low thermal stability and low resistance toward degrading environments, were explained. In the **first study** (Section 3.3), nanoparticle tracers based on silica were introduced and their advantages, disadvantages, challenges and perspectives were discussed. While the concept of nanoparticle tracers bears great potential, the main challenges in incorporating the particles into real environments that have been addressed in this thesis are:

1. Integrity: The solubility of silica and hence solubility of the silica-based nanoparticle tracers.
2. Functionality: Designing nanoparticles loaded with fluorescent markers that are protective and leakage-proof to maintain their intended functionality.
3. Transportability: The interaction of the nanoparticle tracer with the reservoir media may result in adsorption and retention that impacts tracer tests.
4. Stability: Ensuring that dispersion remains stable to prevent nanoparticle aggregation.

The integrity of the particles and the dispersions were addressed in the **second study** (Chapter 4). By evaluating the dissolution behavior of engineered silica nanoparticle-based tracers, the study identifies elevated temperatures, high pH values, low salinities, low initial silica concentration in the natural fluids and low degree of condensation of the nanoparticles as governing factors. Since external parameters such as temperature cannot be influenced, particles must be designed to withstand aggressive environments. Resistance can be attained by applying surface coatings, such as grafting silanes to the surface or by re-ordering the weak silanol (Si-OH) bonds on the surface of the silica nanoparticles to more stable siloxane bonds (Si-O-Si) through calcination. Heat treatment at 550 °C was particularly effective in lowering solubility and decreasing the dissolution rate. The treated nanoparticles were stable in water for over 4 weeks, whereas non-treated particles tended to dissolve within hours. Furthermore, calcined silica nanoparticles equilibrate with quartz solubility rather than amorphous silica solubility as the untreated nanoparticles do. This behavior is particularly beneficial for applications in geological environments, where fluids are typically in equilibrium with quartz, allowing the nanoparticles to remain stable and preserve their integrity. However, the procedure of calcination is not applicable for typical synthesis routes, where heat treatment at above 300 °C would cause thermal degradation of the embedded organic dyes or markers.

In a **third study** (Chapter 5), a new approach to synthesizing silica nanoparticles was pursued. Instead of physically embedding dyes in the silica structure, a mesoporous silica nanoparticle carrier was first synthesized, and then the dyes were loaded in a second step. This approach allowed the silica nanoparticle carrier to be stabilized by calcination before adding the organic dye molecules. However, as the dyes were placed in the mesopores and not bound to the surfaces, they can escape by diffusion processes from their location in the absence of a stable and effective pore blocker. Existing pore-blocking strategies mainly derive from biological and medical sciences, which have to function under much milder conditions and are therefore not necessarily applicable in geological environments. Therefore, a stable and robust surface coating/pore-blocking strategy is pivotal to maintaining the functionality of the nanoparticle tracers. This was accomplished by growing a protective titania shell that is able to block the pores preventing dye leakage but also serves as protection of the carrier itself, while the layer is thin enough to maintain a good fluorescence signal from the loaded dye molecules. This approach leads to the development of dye-MSN@TiO_2 nanoparticle tracers with a size of approx. 150 nm, pore sizes of 2-3 nm and a titania shell thickness of approx. 7 nm. The titania shell is composed of a mixture of anatase and amorphous titania crystals, which are bound to the silica surface by the formation of Si-O-Ti bonds. The procedure was repeated and a variety of different fluorescent dyes could be encapsulated. This procedure leaded to higher resistivity against UV irradiation, as shown in the example of uranine.

The transportability and applicability of these dye-MSN@TiO_2 nanoparticle tracers were tested in a **fourth study** (Chapter 6). The protective measure of the nanoparticle carrier was tested by exposure to hot fluids (160 °C) for 5 days under atmospheric conditions. While the free dyes degraded rapidly, possibly catalyzed by atmospheric oxygen, the encapsulated

dyes showed enhanced stability, highlighting the protective function of the nanocarrier. Further, particle transportability was tested in a flow-through setup and the sorption tendency towards quartz sand was evaluated in different fluid matrices. Three different model dyes were selected to represent the variety of anionic, cationic and amphoteric tracer dyes. In all experiments, the behavior of encapsulated dyes was compared to the behavior of free dyes. It was shown that, especially for cationic dyes, sorption was be significantly reduced upon encapsulation. Furthermore, in flow-through tests, the dye-MSN@TiO_2 nanoparticle tracers showed more uniform breakthrough curves and transport behavior compared to the free dyes, i.e., differences between nanoparticles with different payloads are much less than between the payloads themselves. The study also showed how surface modification of the nanoparticles can serve to significantly lower sorption tendency when additional negatively charged surfactants were physisorbed to the surface. In a further application of surface modification, the were rendered hydrophobic for preferential dispersion in non-polar solvents.

The stability of dispersions and probability of particle adsorption can be determined using the DLVO theory (named after the inventors Derjaguin, Landau, Verwey and Overbeek). In the **fifth study** (Chapter 7), DLVO theory and filtration theory were applied to predict the applicability of silica-based nanoparticles and the dye-MSN@TiO_2 nanoparticles as tracers by determining their interaction energy profiles with different reservoir minerals under various conditions. It was shown that highly negative surface potentials of the tracers are beneficial for establishing an energy barrier that prevents irreversible adsorption. Furthermore, low saline environments reduce sorption tendency in comparison to high salinities and due to the importance of the Hamaker constant on the attraction, it can be concluded that a silica-based nanoparticle system is advantageous as a tracer in comparison to a metal-based one. Nevertheless, as determined in the fourth study, although DLVO calculations predicted a high sorption affinity of the dye-MSN@TiO_2 nanoparticles, their recovery was high. This was attributed to the importance of fluid hydrodynamics. To assess this impact, the filtration theory was employed, elucidating the particle retention mechanisms in porous media. Diffusion was revealed to be the dominant factor for particle-mineral grain collisions, especially at low flow rates. Whether a collision results in an irreversible attachment depends on the DLVO interaction profile. By evaluating the collision efficiency (i.e., filtration efficiency) of silica-based nanoparticles, flow-through tests were used. It was demonstrated that the addition of surfactants that modify the nanoparticle surfaces by physisorption already lowers the retention of the nanoparticles significantly. By applying the extended DLVO theory (XDLVO) incorporating the effect of grafted surfactants, it was shown that the additives give rise to an additional repulsive force: the steric force. This force is particularly impactful and the cause for increased dispersion stability as well as for decreased sorption tendency due to the possible formation of an energy barrier. It can be concluded that placing polymers/surfactants on the surface of the nanoparticles increases the functionality and lowers the likelihood of particle adsorption. Finally, the effect of elevated temperatures on DLVO interactions and particle filtration was examined. Generally, higher temperatures can induce both, deepening

of a primary minimum and heightening of an energy barrier depending on which feature was present at room temperature. Diffusion of colloids is directly dependent on the temperature of the system, therefore increasing temperature results in an increase of the diffusion-dominated filtration process.

8.1 Advances in nanoparticle-based tracer technology

The major advances based on four research hypotheses are presented both in detail as explored in this thesis and in a more generalized form:

1. **Nanoparticle-based tracers can be designed to maintain particle integrity and functionality throughout a tracer test, especially in challenging environments.**

   In this thesis, I used silica as a source material for the nanoparticle carrier. Silica nanoparticles are simple to synthesize, offer a variety of surface modifications and the possibility of adjusting the porosity as well as permit the encapsulation of fluorescent dyes as tracing entities. The major drawback of silica is its solubility and instability in aqueous environments. To address this challenge, I tackled it from two sides: Improving the stability of the silica nanoparticles themselves by heat treatment and applying a stable and robust titania coating layer to prevent dissolution of the nanoparticles and hinder diffusion of the encapsulated dye molecules. With these approaches, it was possible to ensure the particle integrity and functionality also in challenging environments.

   In general: Nanoparticle-based tracers need to be designed stably and robustly to ensure applicability in harsh conditions as those encountered in geological environments (e.g., high salinities, high temperatures). Therefore, a viable approach must have a stable and robust nanoparticle carrier that secures the encapsulated marker payload (for example, a fluorescent dye molecule) and shields it from the environment. This approach promises a captivating advantage: the functionality of the payload is not affected by the environment, i.e., independent of environmental influences. The only decisive factor for transport, interactions and integrity is the surface of the carrier itself.

2. **Functionalization of nanoparticle tracers can ensure a straightforward and robust detectability function.**

   In this thesis, I proved that various fluorescent dye molecules, particularly those with relatively high quantum yields (e.g., rhodamines), were suitable for encapsulation in mesoporous silica nanoparticle carriers, enabling real-time monitoring through fluorescence spectroscopy. By encapsulation, the robustness of the measurement signal was maintained. For example, the dye rhodamine 6G retained only 5.1 % of its initial fluorescence intensity after being exposed to 160°C for 5 days, while the encapsulated

dye maintained 91.7 % under the same conditions. Additionally, encapsulated dyes showed reduced sorption tendencies and higher similarities in tracer breakthrough curves than free dyes. Therefore, the encapsulation process improves the robustness and functionality of the dyes by shielding them from the surroundings and hence, ensures detectability of the nanoparticle tracers.

In general: Recently developed novel tracer types, such as DNA-based tracers, require (extensive) laboratory investigations to obtain the desired information about tracer breakthroughs or the presence/absence of the tracers. By using fluorescent dye molecules, a rapid and on-site evaluation is enabled, simplifying the tracer test procedure and enabling real-time monitoring. Encapsulation in a nanoparticle carrier also ensures the long-term functionality of the dyes as they are protected from the surrounding environment.

3. **Nanoparticle tracer performance can be optimized in geological environments.**

   In this thesis, I found that silica nanoparticles typically exhibit negative ζ-potentials. However, coating them with titania can render their ζ-potentials more neutral or even positive. Additionally, due to their size of 150 nm, the nanoparticles have a limited transportation range because of their tendency to diffuse, which increases the probability of collisions with mineral grains, potentially leading to attachment. To enhance their performance in geological environments, I optimized the nanoparticles by adapting them to the environmental conditions. By applying surface modifications, such as physi- or chemisorption of surfactants and polymers, I reduced their sorption tendencies and collision probabilities, thereby improving their applicability as tracers.

   In general: Nanoparticle behavior in geological environments is an intricate research area with still a variety of open questions. The behavior can be best described as an interplay of physical forces acting at the nanometer scale (DLVO theory) and hydrodynamic forces (filtration theory) acting at the pore scale. Nanoparticles behave mostly conservatively when their surface charge (i.e., ζ-potential) is in the range of the reservoir mineral charges, i.e., when an energy barrier in the DLVO interaction profile exists. In most cases, the surface charge of reservoir minerals is negative. Thus, having a negatively charged tracer increases the chance of conservative behavior. Additionally, if the transport processes are dominated by high fluid velocities, the relative importance of DLVO forces and diffusion on the nanoparticles are reduced, leading the fewer possibilities of interactions and a more conservative behavior.

4. **Nanoparticles offer the opportunity of surface modifications to restrict interaction with the environment, resulting in minimized sorption and retention.**

   In this thesis, I performed surface modifications using physi- or chemisorption of anionic and zwitterionic surfactants, polymers and silanes. Anionic surfactants, particularly SDS, proved to be highly effective in lowering sorption affinity in both batch

sorption and flow-through experiments, with sorption dropping from 84 % without SDS to 17 % with it. DLVO and XDLVO calculations indicated that a steric barrier and the resulting increase in repulsive forces between the particles and the surface were the main factors behind the improved performance of surface-modified nanoparticles.

In general: There are several ways to control the interactions of the nanoparticles with the environment, with the addition of surface coatings to increase the repulsive forces being the most effective method. This procedure increases the dispersion (colloidal) stability and, if applied correctly, can give rise to an additional repulsive force that generates an energy barrier in the DLVO interaction profile, reducing the chance of irreversible adsorption of the particles.

Finally, as indicated in the motivation section, these tracers are a first step toward "smart" and functional nanoparticle-based tracer concepts. With the implications obtained from the studies in this thesis, a necessary step toward novel tracer methodology was performed. Additionally, by elucidating and assessing the particle interactions with the environments, conclusions can be transferred in other research areas, for example, for the understanding of colloid-assisted contaminant transport or nanoplastic behavior in the environment.

8.2 Outlook

The approach of using silica-based nanoparticles as tracers for exploration is captivating. Silica, as an abundant geomaterial, is a major constituent of most reservoir minerals and is present in all natural fluids, leading to an interesting inference. It might be possible to use silica from a natural source as a silica precursor in the synthesis. Indeed, there exist a few approaches using geothermal silica for synthesis, for example, as shown by Watanabe et al. (2021b). Removal of silica from geothermal fluids is particularly useful for both reducing the silica scaling risk and facilitating selective raw material extraction, as shown by Spitzmüller et al. (2021). A major hurdle in the synthesis of silica-based nanoparticle tracers from geothermal fluids is the disturbance by cations. As shown in Chapter 3, nanoparticles form at alkaline pH values in the absence of cations. Otherwise, the growth of colloids would result in the formation of a gel. However, as further shown, it is also possible to synthesize nanoparticles in acidic environments, especially below pH 2. Synthesis under acidic pH conditions might be a feasible approach for the production of silica nanoparticles from geothermal fluids. Further, due to the positive ζ-potential at low pH, incorporation of cations is hindered. Nevertheless, for synthesizing mesoporous silica nanoparticles in acidic environments other pore spacers than the cationic CTAB are required. A viable approach could be using an anionic sacrificial template such as SDS.

The predictions of dispersion stability, particle-particle and particle-surface interactions using DLVO theory hinge on accurate determination of the surface charge. As direct measurement

of surface charges is impossible, the calculations rely on ζ-potential measurements. As shown in Chapter 2, ζ-potentials are only a more or less close approximation of surface charge and depend on many factors, such as temperature and salinity of the fluids. Direct measurements of the force acting between particles/surfaces are needed to circumvent this auxiliary step. These measurements can be performed using sophisticated tools such as atomic force microscope (AFM). For example, Ishida and Craig (2019) measured the interaction force between different surfaces directly in liquid and Wu et al. (2024) assessed reservoir properties using high-temperature AFM. Accurately measuring the interacting forces between nanoparticle tracers and reservoir minerals, ideally under simulated reservoir conditions, is a huge step toward understanding transport behavior in geological environments.

Future developments of "smart" nanoparticle tracers should incorporate the usage of a variety of grafted polymers. As shown by XDLVO theory, grafting polymers on the surface of nanoparticles enhance the dispersion stability and reduce sorption tendency by the formation of an energy barrier in the interaction profile, preventing aggregation. Additionally, polymers can serve as a sensitive hull to enable gaining and recording additional information about subsurface conditions such as temperature distribution. Furthermore, the possibility of functionalization also unlocks a new approach to inhibit scaling. For example, using a mesoporous silica nanocarrier with encapsulated inhibitors covered by a triggerable polymer hull that can be activated by pH value changes could selectively and precisely prevent scaling formation.

Finally, it can be concluded that while there remain open questions about the interactions and applicability of silica-based nanoparticle tracers, the combination of nanoscience and geoscience significantly advances the research fields. The incorporation of nanoscience-based technologies allows the answering and formulation of novel geoscientific research questions. Moreover, ease of functionalization of nanoparticles expands the field of tracer technologies and extends the amount of obtainable information from tracer tests.

APPENDIX A

Appendix

A.1 Selective Silica Removal in Geothermal Fluids: Implications for Applications for Geothermal Power Plant Operation and Mineral Extraction

This section is published in Geothermics
https://doi.org/10.1016/j.geothermics.2021.102141

Spitzmüller, L., Goldberg, V., Held, S., Grimmer, J. C., Winter, D., Genovese, M., Koschikowski, J., Kohl, T. (2021): Selective Silica Removal in Geothermal Fluids: Implications for Applications for Geothermal Power Plant Operation and Mineral Extraction. *Geothermics* 95.

Abstract

Raw material extraction from geothermal fluids often comprises concentrating and cooling steps, which increases the risk of silica scaling formation. However, existing silica removal strategies do not consider the impact on raw material extraction. In this study, the applicability and element-selectivity of three silica removal techniques (seed-induced, lime and caustic precipitation) were tested in batch experiments using synthetic and natural geothermal fluid samples. Increasing the pH value to 10.5 and the Ca/Si ratio > 1.25 was found to mitigate silica scaling effectively via formation of calcium-silicate-hydrate phases (C-S-H phases). The developed silica removal process does not affect the raw materials and is therefore suitable for brine mining purposes.

A.1.1 Introduction

Geothermal fluids may attain high silica concentrations during fluid-rock interaction at high temperatures (Fournier and Rowe 1966, Henley 1983, Iler 1979). The fluids are thus assumed to be in equilibrium with silica under reservoir conditions. Cooling and fluid concentrating processes involved in geothermal power plant operation cause the saturation index (SI) of silica to increase to SI$\geq$0 and hence precipitation may commence. In flash-steam geothermal power plants with operational temperatures $\geq$200 °C concentration of the geothermal fluid occurs due to the steam-phase separation. The resulting increase of the silica concentration in the residual geothermal fluid may lead to scaling problems, depending on initial silica concentration and the fraction of steam-phase separation (e.g. Setiawan et al. 2019). In binary geothermal power plants, commonly operating at temperatures of 120 °C < T < 200 °C, cooling-induced silica oversaturation of the geothermal fluid may occur in the reinjection pipeline. Recently, geothermal fluids moved into focus as a new source for several raw materials such as Li (Bourcier et al. 2005). However, the concentration of the raw materials in geothermal fluids is relatively low compared to conventional deposits (Kesler et al. 2012, Schmidt 2017). Therefore, concentration of the fluids as a pre-treatment process may be required to increase the effectiveness of raw material extraction (Ryu et al. 2016). Thus geothermal fluids with relatively low ion-concentrations (Tassi et al. 2010) may become economically viable resources. However, power plant operations as well as raw material extraction processes increase the risk of silica scaling significantly.

Silica removal prior to cooling or enrichment of the geothermal fluid can therefore be crucial for both geothermal power plant operation and mineral extraction purpose. For economic, environmental and sustainability reasons silica precipitates should not contain environmentally harmful elements or substances as they must be either disposed or re-used as a product. Furthermore, the silica precipitates should not contain elements of economic interest, as they are the target of a later stage mineral extraction process. This concerns especially for Li, Zn, Cs, Rb, and trace elements like B, Ag, and Au (Bourcier et al. 2005, Finster et al. 2015, Maimoni 1982, Neupane and Wendt 2017). Moreover, highly pure silica and silicates are valuable raw materials themselves (Johnston et al. 2019, Lee et al. 2018, Mathieux et al. 2017). There are various approaches to extract silica from geothermal fluids (Bourcier et al. 2001,0,0, Finster et al. 2015, Lin et al. 2003,0, Mroczek et al. 2015), which are limited to low saline geothermal fluids. For highly saline geothermal fluids, there is a lack of information about commercial silica extraction.

This study is associated with the German-Chilean BrineMine project funded by the Federal Ministry of Education and Research (BMBF). The project aims to develop a system for sustainable raw material and drinking water production from thermal waters in Chile. The developed methods shall derive alternative mining concepts to the conventional mineral extraction as in the Salars of the Atacama Desert, which are associated with high environmental impact. Therefore, this study consists of two parts: The first part comprises lab experiments

with synthetic geothermal fluids inspired by the composition of the waters in the El Tatio geothermal field in northern Chile. The main focus is to develop a silica removal strategy that does not affect the raw materials, especially the lithium concentrations. In the second part we apply the developed processes on a natural, complex geothermal fluid from a thermal spring in Baden-Baden (e.g. Stober 2002), close to the Eastern Main Boundary Fault of the Upper Rhine Graben (Grimmer et al. 2017). The main focus is also on silica removal and conservation of Li concentrations in the geothermal fluid, whereas a minor focus is on the behavior of trace elements.

A.1.2 Materials and Methods

Table A.1: Overview of the most common silica removal techniques.

Method	Additive	Reference
Seed induced precipitation	Silica seeds	Setiawan et al. (2019), Sugita et al. (1999), Sugita et al. (2003)
Lime precipitation	$Ca(OH)_2$	Badruk and Matsunaga (2001), Borrmann and Johnston (2017), Borrmann et al. (2009), Kato et al. (2003), Putera et al. (2018), Rothbaum and Anderton (1975), Vitolo and Cialdella (1994)
Caustic precipitation	NaOH	Gallup et al. (2003)
Metal salt addition	Zn	Zeng et al. (2007)
	Al	Sugita et al. (1999), Yokoyama et al. (1989)
	Fe	Gallup et al. (2003), Renew and Hansen (2017)
	Mg	Lin et al. (2003), Morita et al. (2017)
	Cu	Gallup et al. (2003)

This study aims to develop a selective silica removal strategy to enable raw material extraction from geothermal fluids. Therefore, different silica scaling mitigation techniques were tested using synthetic and natural geothermal fluid samples to identify the most effective silica removal process. A special focus is on their impact on raw materials and trace elements.

A.1.2.1 Review of silica scale mitigation techniques

Generally, scaling mitigation techniques are distinguished into inhibition and precipitation methods. The use of synthetic inhibitors for silica scaling mitigation has turned out to be ineffective due to the amorphous structure of the silica scales (Gallup 2002, Gallup and Barcelon 2005, Milne et al. 2014, Neofotistou and Demadis 2004). The most promising inhibition method is the pH adjustment to retard the polymerization and aggregation of silica (Bourcier et al. 2005, Finster et al. 2015, Gallup 2002,1, Kiyota and Uchiyama 2011,

Rothbaum et al. 1979, Sigfusson and Gunnarsson 2011). In the framework of mineral extraction further cooling or concentration processes are required that may increase the SI$\gg$0 (Gunnarsson and Arnórsson 2005). In this case, even the pH adjustment will not prevent silica precipitation.

Milne et al. (2014) provide an overview of the state-of-the-art techniques for silica removal. Techniques like electrocoagulation and ion exchange can be excluded in this study due to high investment costs. A.1 provides an overview of the most promising silica removal techniques. The lime precipitation method is by far the most common method and has shown good applicability in geothermal settings (A.1). The use of metal salt addition techniques is not desired since the metal ions remain in solution and can affect potential raw material extraction processes and - depending on the used metal - may be a raw or economically interesting material itself and hence the use of metal cations is neither economic nor ecologic reasonable (Milne et al. 2014). The lime, the caustic, and the seed-induced precipitation processes are considered as most promising, because required materials are widely distributed and easily accessible. For the lime precipitation method (Borrmann and Johnston 2017, Cairns et al. 2006) and the silica seeding method (Setiawan et al. 2019) analyses of the chemical composition of the precipitates exist, but the behavior of lithium and other raw material were not considered. The analysis of the precipitates with a focus on lithium behavior is therefore emphasized in this study.

A.1.2.2 Geothermal fluid synthesis

A synthetic, trace-element-free geothermal fluid was used to study the effectiveness of various silica removal techniques and their impact on the lithium concentration in solution. A complex natural geothermal fluid was used to validate the applicability of a selected silica removal process with a special focus on the behavior of trace elements.

A.1.2.3 Synthetic geothermal fluid

Silica removal experiments were conducted with a synthetic geothermal fluid for comparability and reproducibility. The composition of the fluid was synthesized based on the chemical composition of the El Tatio geothermal waters, Northern Chile (Section 1, Table A.2 Ellis and Mahon 1977, Giggenbach 1978, Tassi et al. 2010). Hereby, only the main and redox-insensitive anions and cations were used for the synthesis of the synthetic geothermal fluid. Experimental conditions as well as silica concentration were adapted to simulate the cooled thermal fluid (cooled down from $\simeq$210 °C) of a geothermal power plant considered for reinjection with a temperature of 70 °C, leading to a supersaturation regarding silica.

For synthesis, both a salt solution and a silica solution were prepared separately to avoid unintended immediate precipitation during dissolution of the components. The salt solution

contains NaCl (Merck EMSURE, assay 99.5 %), KCl (Merck EMSURE, assay 99.5 %), Na_2SO_4 (Merck EMSURE, assay 99 %), LiOH (Merck EMSURE, assay 98 %), and $CaCl_2$ (VWR Chemicals, assay 94 %), dissolved in double-distilled water. The pH was adjusted to pH 6.7 using HCl (Merck Supelco, 37 %). The silica solution was prepared by mixing double distilled water with silica (Merck, extra pure) and NaOH (Merck EMSURE, assay 99 %) to obtain a solution with pH > 12. For complete dissolution we performed magnetic stirring with c. 500 rpm at 70 °C in an oven for more than 12 hours. Before mixing the solutions, the pH of the silica (+NaOH) solution was adjusted to pH 6.7 using HCl. The quantity of added salts was adjusted to yield the concentrations shown in Table A.2 after mixing. HDPE vessels were used during the whole synthesis process to exclude contamination by amorphous silica from glass containers. For each experiment, the synthetic silica solution was freshly prepared to exclude polymerization effects that may occur with time.

Table A.2: Chemical composition of the El Tatio well T5 geothermal fluid (Giggenbach 1978), the synthetic geothermal fluid, the Baden-Baden Fettquelle (FQ) thermal spring (Sanjuan et al. 2016) and the adapted natural geothermal fluid (twice the concentration of the natural FQ fluid). For the synthetic fluid and the adapted natural fluid mean values and standard deviations of ion concentrations are given.

Parameter	Unit	El Tatio T5	Synthetic geothermal fluid	Baden-Baden FQ	Adapted natural geothermal fluid
pH	-	6.7	6.7 ± 0.1	7.82	8.0 ± 0.1
Temperature	°C	212	69 ± 1	61	70.2 ± 0.3
TDS	mg/L	11,813	10,725± 280.8	2900	n.d.
Li^+	mg/L	32	32 ± 0.15	8.0	95.02 ± 1.53
Na^+	mg/L	3760	3686 ± 162	827	1815 ± 71.05
K^+	mg/L	519	518 ± 2.4	86.7	169.07 ± 6.43
Cs^+	mg/L	13.1	n.a.	0.7	10
Ca^{2+}	mg/L	219	215 ± 10.7	122	174.35 ± 4.32
Mg^{2+}	mg/L	n.d.	n.a.	3.96	7.78 ± 0.17
SiO_2	mg/L	343	343 ± 0.6	131	290.56 ± 3.48
Cl^-	mg/L	6690	6136 ± 280	1480	n.d.
SO_4^{2-}	mg/L	34	34.5 ± 0.7	140	n.d.

n.d. not determined, n.a. not added

A.1.2.4 Adapted natural geothermal fluid

For the experiments using a natural geothermal fluid, the Baden-Baden hot spring fluid ("Fettquelle", FQ) was selected due to its public accessibility. The Na-Cl-rich geothermal fluid contains a TDS of 2.9 g/L (Sanjuan et al. 2016) and 131 mg/L SiO_2 (Table A.5). As the

SiO_2 concentration deviates from deep geothermal fluids from URG (Sanjuan et al. 2016), the natural geothermal fluid was modified before the experiments (Table A.2). The concentration was increased twice by evaporation. Additionally, the concentration of Li was raised to about 100 mg/L by addition of LiCl (Sigma Aldrich, assay 99 %) and the concentration of Cs was raised to 10 mg/L by addition of CsCl (Merck Suprapur, assay 99.5 %) to be in the range of geothermal fluids of the URG and also enable a detectability in the precipitates. Both elements are of economic value and therefore of particular interest.

A.1.2.5 Additives

Four different additives were used for the silica removal experiments (A.1): Silica seeds (Merck, extra pure), $Ca(OH)_2$ (Merck EMSURE, assay 96 %), $CaCl_2$ (VWR Chemicals, assay 94 %), and NaOH (Merck EMSURE, assay 99 %). Silica seeds and $Ca(OH)_2$ proved to be effective for the removal of silica according to literature (Section A.1.2.1, A.1). $CaCl_2$ and NaOH are chosen to identify respective effects of Ca-ions and pH separately. The following experiments were conducted using synthetic geothermal fluid:

- Addition of silica seeds to the synthetic solution with a 10x higher concentration of the silica seeds to the SiO_2 content in solution. The geothermal fluid was synthesized without Ca to eliminate a possible impact on the removal mechanism.
- $Ca(OH)_2$ was added with a special focus on the impact of the molar calcium-to-silicon-ratio (Ca/Si ratio). Note that addition of $Ca(OH)_2$ affects the Ca/Si ratio and the pH at the same time.
- To study the sole impact of the pH value, different concentrations and amounts of NaOH were used to adjust the pH. The Ca/Si ratio was set to 2.0 by addition of $CaCl_2$.
- The sole impact of the Ca/Si ratio was studied by adjusting the ratio with different amount of $CaCl_2$. In this case, the pH was fixed at 10.5 by addition of NaOH.

Out of the four additives, the most effective one is chosen to validate the batch experiments using an adapted natural geothermal fluid.

A.1.2.6 Experimental setup

The experimental setup is similar for the experiments using synthetic geothermal fluid and for the experiments using adapted natural geothermal fluid. The precipitation experiments were carried out at 70 °C in an oven under magnetic stirring at 500 rpm in 1L-HDPE vessels. About 600 mL of the geothermal fluids (Section A.1.2.2) were used for each experiment. Solution samples were taken before adding the seeding material (Fig. A.1) and after the addition selectively in a 120 minutes time interval. The fluid samples were taken according

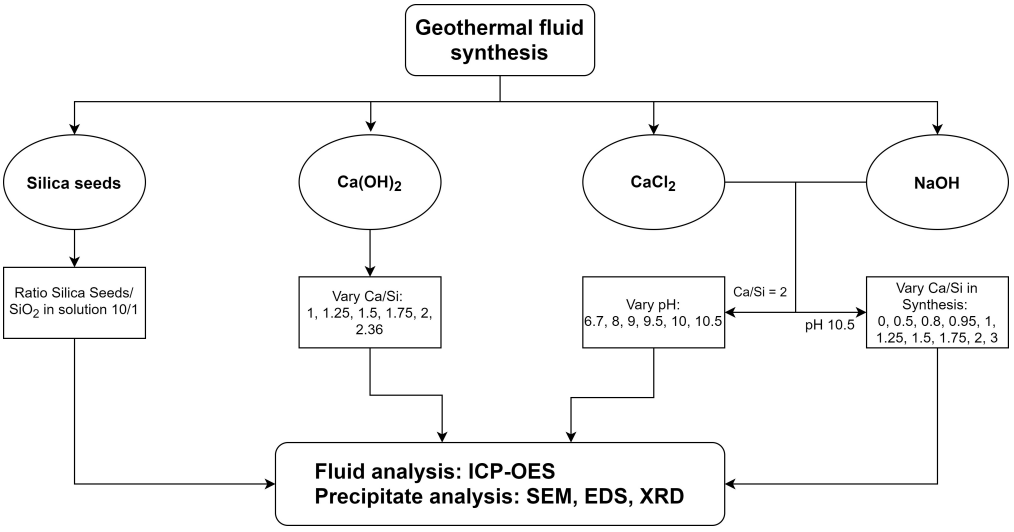

Figure A.1: Experimental scheme from synthesis of a synthetic geothermal fluid to analysis. The different additives are marked bold. The fluid analysis (ICP-OES results) show a time series of a 120 minutes reaction time interval for each experiment, whereas the precipitate analysis is performed solely for the precipitates after the reaction time interval. Ca/Si is the (initial) molar calcium-to-silicon-ratio

to the following procedure. 1 mL of the solution was filtered through a syringe using a cellulose acetate filter (0.45 µm) to remove solids. By diluting the aliquot 1:100 with double distilled water further reactions were prevented. Temperature and pH of the solution were measured during sampling. After 120 minutes of reaction time, the geothermal fluid was filtered using a vacuum pump and a 0.45 µm cellulose acetate filter. The precipitates were collected and dried overnight in the oven at 70 °C. The fluid samples were measured focusing on the cations using an ICP-OES (Varian 715-ES). The uncertainty was determined from the deviations of the standard solutions. The analyses of the dried precipitates were performed with XRD (Bruker D8), SEM (Tescan Vega), and EDS (Inca X Act). Additionally, the precipitates of the experiments with natural geothermal fluid are washed with double distilled water and collected by centrifugation (6000 rpm, 30 minutes). This step is performed to remove potential salt crust layers which may have formed during the drying process. The precipitates are dissolved using a HNO_3-HF-$HClO_4$-acid mixture and measured with an ICAP-RQ Thermo Fischer ICP-MS.

A.1.3 Results

A.1.3.1 Removal experiments using synthetic geothermal fluid

23 experiments were carried out following the experimental scheme shown in Fig. A.1. Selected results are presented in this section to emphasize the trend observed in the experiments. Detailed results are listed in Table A.4. A special focus is on the silica removal effectiveness

and the conservation of the Li concentration. The results of the precipitation experiments depicting on the SiO_2 and the Li concentration are shown in Fig. A.2. These experiments contribute to assess and to compare the methods (Section A.1.2). Fig. A.2A compares the residual SiO_2 concentrations, while Fig. A.2B displays the Li concentration. Addition of $Ca(OH)_2$ and NaOH caused an effective reduction of the silica concentration while the Li concentration has remained constant. In contrast, the addition of silica seeds as well as the addition of $CaCl_2$ did not show a significant reduction of the residual SiO_2 concentration. Furthermore, the Li concentration was reduced by 19 % in the silica seeding experiment.

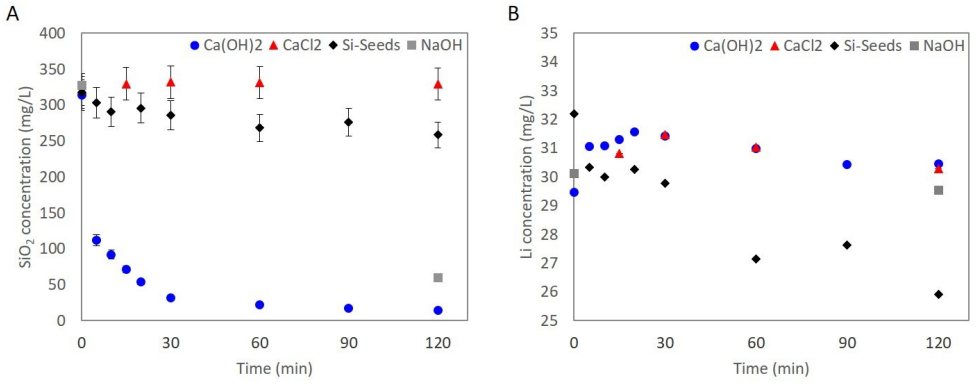

Figure A.2: Comparison of the residual SiO_2 (A) and Li (B) concentration after precipitation experiments with $Ca(OH)_2$, $CaCl_2$, silica seeds, and NaOH (Exs. 16, 2, 1, 23, Table A.4). For the $CaCl_2$ and NaOH experiments, not each time step has been sampled. The error bars represent the percentage error of the ICP-OES analysis and are calculated by the deviation from the standard solution. The errors are unique for each experimental trial and each cation.

Fig. A.3 shows the usage of $Ca(OH)_2$ as precipitation agent (A.3A) and the addition of silica seeds (Fig. A.3B) in more detail. After the addition of $Ca(OH)_2$ the pH raised immediately from initial 6.7 to 10.5 $\pm$ 0.1. The temperature remained constant at 69 °C. The molar Ca/Si ratio was raised from an initial Ca/Si ratio of 0.95 to 2.36 after the addition of 590 mg $Ca(OH)_2$ per liter. The SiO_2 concentration was reduced below the saturation concentration of 230 mg/L (reference at 70 °C and pH 6.7, PHREEQC LLNL database) within minutes and maintained constantly below 20 mg/L. Within 120 minutes, about 96 % of the initial silica concentration was removed, whereby 68 % was removed within the first 5 minutes and 94 % within 30 minutes after the addition of $Ca(OH)_2$. The concentrations of Li, K, and Na were not affected by the addition of the precipitation agent. The Ca concentration was raised due to the addition of $Ca(OH)_2$, but the theoretical maximum concentration of 539 mg/L Ca, which would comprise the initial plus the added Ca, was not reached. Fig. A.3B shows the results of the addition of silica seeds. In contrast to the precipitation experiment with $Ca(OH)_2$, the SiO_2 concentration could not be reduced below the saturation concentration of 230 mg/L. Furthermore, the Li concentration decreases about 19 % to 25.93 mg/L, the

K concentration decreases about 17 % to 444 mg/L and the Na concentration is reduced by 17 % to 3139 mg/L (Table A.4). Therefore, the silica seeding method did not prove to be effective in terms of effective and selective silica removal.

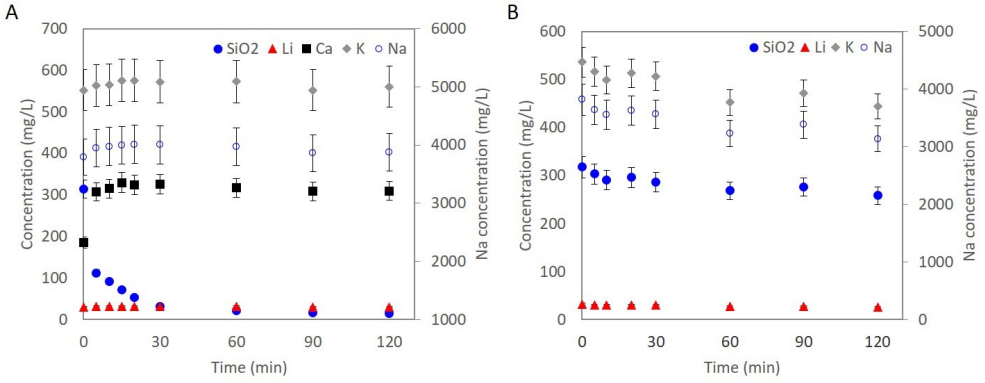

Figure A.3: ICP-OES results of the precipitation experiments with $Ca(OH)_2$ (A) and silica seeds (B) (Exs. 16, 1, Table A.4). Samples were taken over a time of 120 minutes after addition of the additive. Note that he Na concentration is shown on the 2nd y-axis. The error bars represent the percentage error of the ICP-OES analysis and are calculated by the deviation from the standard solution. The errors are unique for each experimental trial and each cation.

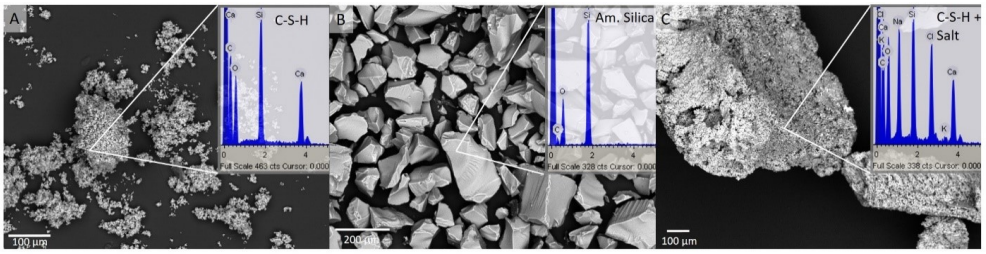

Figure A.4: SEM and EDS spectra of the precipitates. After the $Ca(OH)_2$ (A) and the NaOH (C) treatment, C-S-H is observed as precipitate in form of small, porous flakes, whereas in the silica seeding experiments (B) the output products look similar to silica seed input.

Fig. A.4 shows the SEM images and the EDS spectra of the precipitates from the different experiments (Exs. 1, 16, 23, Table A.4). The precipitates from the experiments with $Ca(OH)_2$ and NaOH (Fig. A.4A & C) have, according to the EDS spectra, Si and Ca as the main components. In accordance with the XRD analysis patterns, the precipitates can be classified as calcium-silicate-hydrates (C-S-H). The C-S-H phases have porous structures as reported in the literature (Borrmann and Johnston 2017, Cairns et al. 2006). The EDS spectra for the precipitate resulting from the addition of NaOH (Fig. A.4C) possess higher Na, K, and Cl concentrations compared to the EDS spectra of the precipitate adding $Ca(OH)_2$ (Fig. A.4A). Furthermore, the precipitates have a more solid morphology than the porous flakes resulting from the $Ca(OH)_2$ treatment. This indicates coverage of the C-S-H with salts. In accordance

with the XRD analysis patterns, halite and sylvite are expected. Furthermore, the XRD patterns reveal the presence of calcite in the precipitates resulting from the $Ca(OH)_2$ and the NaOH treatment. Calcite as carbonate can not be analyzed with EDS spectra due to the coverage of the samples with carbon. Furthermore, calcite was not visible in the SEM imaging, which indicates a microcrystalline structure.

The silica seeds (Fig. A.4B) could be analyzed with SEM and EDS, but due to the amorphous structure, no XRD analysis could be performed. The silica seeds do not show a difference between the recovered and the initial morphology.

A.1.3.2 Process validation using adapted natural geothermal fluid

The methods developed in this study were tested with synthetic geothermal fluids in batch experiments to analyze the driving forces behind silica precipitation. The general applicability for complex geothermal fluids was examined by further experiments with an adapted natural geothermal fluid from the Baden-Baden spring (Section A.1.2.2). Besides the silica removal, the focus of this experiment series was on the incorporation of trace elements in the precipitates that could not be investigated using a synthetic, trace-element-free fluid. The experiments shall determine a possible impact of trace elements on the removal mechanism and the selectivity of the precipitation mechanism. The previously described batch experiments with $Ca(OH)_2$ as additive have shown the highest removal effectiveness (Fig. A.2). Therefore, this method was selected to treat the Baden-Baden geothermal fluid. For verification, three similar samples of the natural geothermal fluid from FQ were prepared separately by evaporative concentration. The samples are denoted as Bad 1, Bad 2, and Bad 3.

Fig. A.5 shows the ICP-OES results of the fluid phase of the $Ca(OH)_2$ precipitation experiments. Three similar trials were performed following the experimental setup described in Section A.1.2. Detailed results can be found in Table A.5. A.5 A shows the evolution of the SiO_2 concentration within the 120 minutes reaction time interval in the fluid phase. For all samples tested, the decrease of the SiO_2 concentration occurs immediately after the addition of the $Ca(OH)_2$. Li (Fig. A.5 B), as well as Na (Fig. A.5 D), remain unaffected, whereas Mg is reduced below the detection limit during the experiment (Fig. A.5 C). Sr and Rb show a slight decrease (Fig. A.5 C). The precipitates consist in the majority of calcite and C-S-H phases as measured in the XRD. SEM and EDS identify the presence of Ca and Si (Fig. A.7). Due to the low initial concentration of Mg, it was not detected in the EDS or SEM. Clear identification of the incorporation process of trace elements and hence the purity of the product can be derived from the analysis of precipitates using ICP-MS. The results are shown in Fig. A.8. Mn and Sr show the highest incorporation in the precipitates with concentrations of 170-600 ppm and 450-600 ppm respectively. However, the incorporation of trace elements accounts only for a smaller amount (<0.25 %, Table A.1.6).

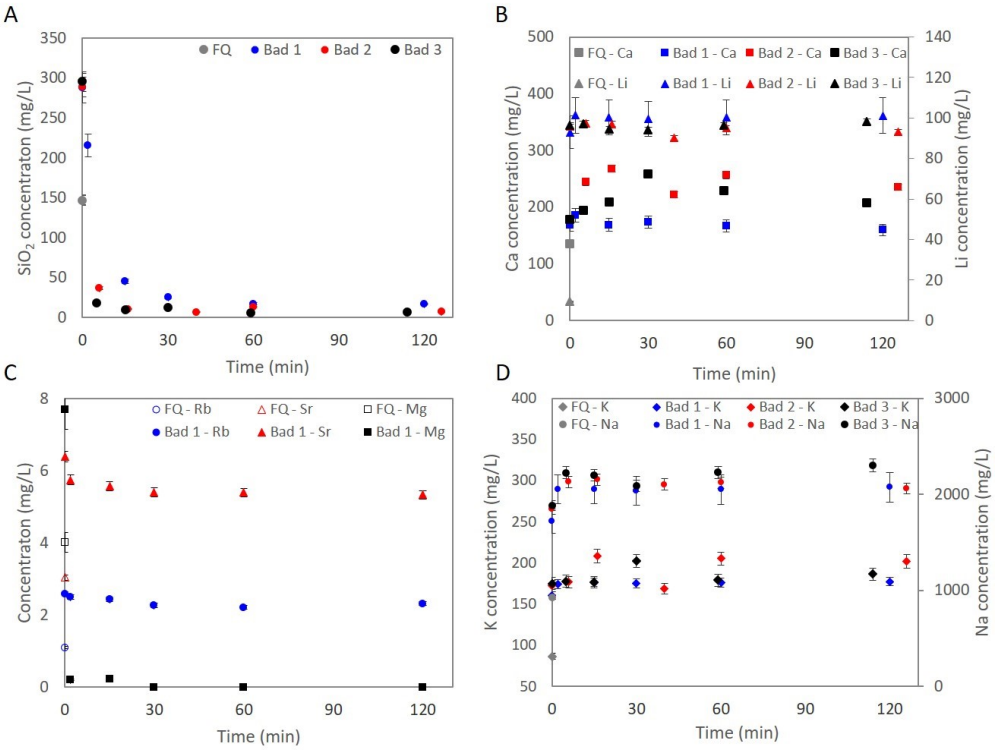

Figure A.5: ICP-OES results of the precipitation experiments with the thermal water from Baden-Baden. FQ shows the initial contents before concentrating the fluid. The precipitation was achieved by addition of $Ca(OH)_2$ and NaOH to raise the pH over 10.5. Note the different y_2-axis scaling at B and D. C only shows the results of Bad 1. Mg was below detection limit after 30 minutes (C).

A.1.4 Discussion

This study aims to develop a selective, element-specific silica removal process that does not affect the raw material concentration in geothermal fluids and is therefore suitable for mineral extraction purposes. Three different existing silica removal techniques were tested focusing on their removal effectiveness and their impact on raw materials.

A.1.4.1 Silica seeding

As indicated in the ICP-OES results (Fig. A.3), the EDS and SEM analysis (Fig. A.4B), the silica seeds did not show significant incorporation of other elements aside from silica itself. The reduction of the SiO_2 concentration is achieved by interaction between silicic acid (H_4SiO_4) and the silica seed surface leading to precipitation (Bremere et al. 2000, Sugita et al. 2000). The ability of amorphous silica seeds to induce the nucleation and polymerization of silicic acid is already well known and is applied in some geothermal power

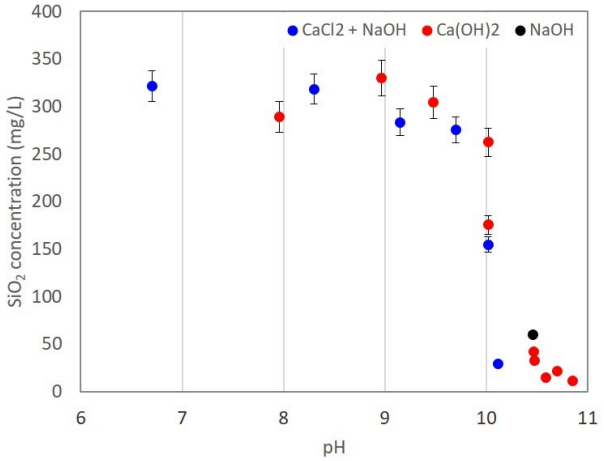

Figure A.6: Impact of the pH on the reduction of the SiO_2 concentration. Three different methods to raise the pH are shown (Exs. 3-7, 16-21, 23, Table A.4). They all prove to be effective at pH > 10, unaffected by the additive.

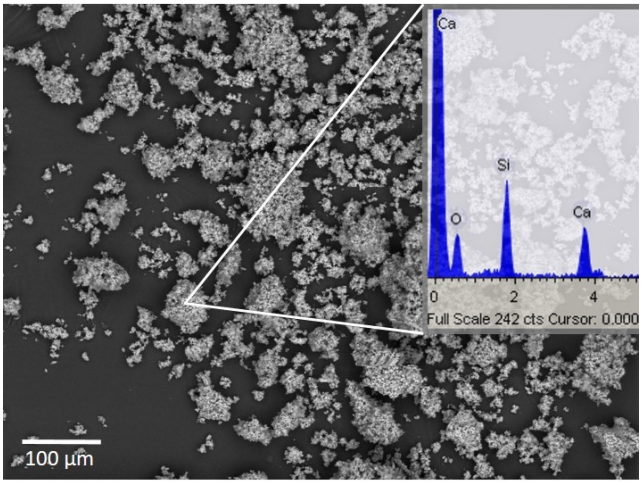

Figure A.7: SEM and EDS spectra of the Baden-Baden precipitate after treatment with $Ca(OH)_2$. The small, porous flakes show a C-S-H composition and have a similar morphology as the precipitates shown in Fig. A.4.

plants (Bremere et al. 2000, Setiawan et al. 2019, Sugita et al. 1999). The major disadvantage of the method can be observed in the experiments: The removal effectiveness of the method is dependent on the difference between the initial silica concentration and the saturation concentration (Bremere et al. 2000, Sugita et al. 1999). Below the saturation concentration, no further removal of SiO_2 occurs. Since geothermal fluid concentrating would cause again supersaturation of silica, it is not sufficient to reduce the concentration to saturation. For a concentration of raw materials in the geothermal fluid by a factor of 5 to 10 the silica content must be reduced to 1/5 to 1/10 of the saturation concentration to avoid unwanted precipitation.

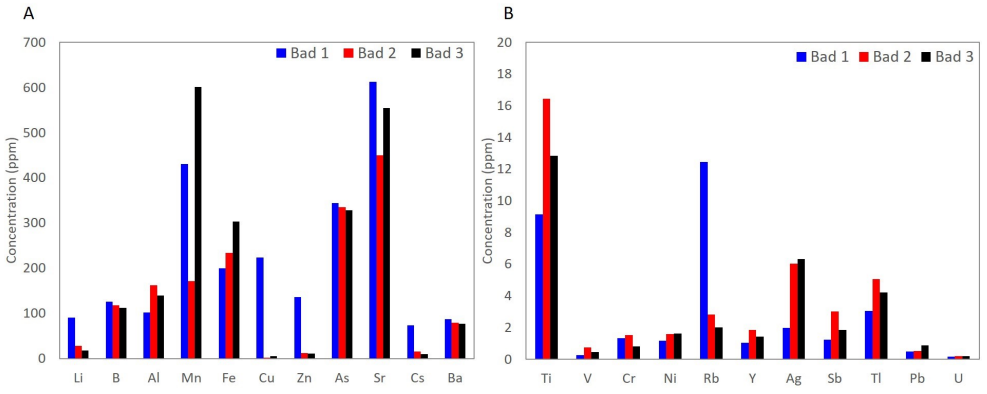

Figure A.8: Trace element content of the precipitates Bad 1, Bad 2 and Bad 3 analyzed with ICP-MS. Mn and Sr show the highest incorporation in the precipitates with concentrations of 170-600 ppm (Mn) and 450-600 ppm (Sr). However, the total amount of incorporated trace elements is summed up to less than 0.25 %.

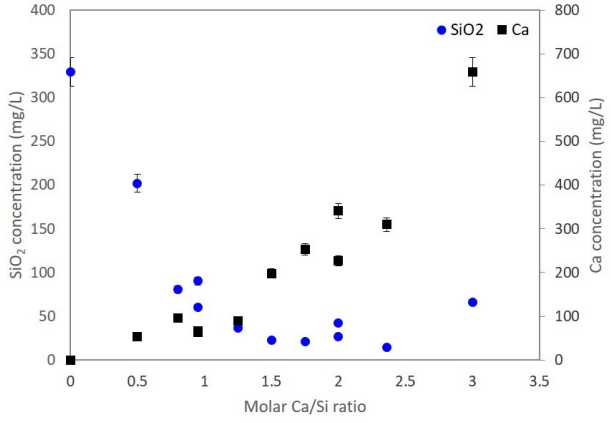

Figure A.9: Impact of the molar Ca/Si ratio on the removal of SiO_2 and the residual Ca concentration. The pH is set to 10.5 by addition of NaOH (Exs. 7-16, 22, 23, Table 4).

A.1.4.2 C-S-H formation

The precipitation mechanism for the experiments with $Ca(OH)_2$, NaOH and $CaCl_2$ + NaOH can be identified as the formation of C-S-H phases (Fig. A.4A & C). Two factors are crucial for the SiO_2 removal via C-S-H-phases: alkaline pH values and the availability of Ca. The interaction of both factors favors the formation of C-S-H phases. The addition of $Ca(OH)_2$ yields SiO_2 concentrations much below similar experiments with NaOH (Fig. A.2). Although both experiments were performed at the same pH of 10.5, the Ca/Si ratio differs: for NaOH it was the initial Ca/Si ratio of 0.95 (A.2), for the trial with $Ca(OH)_2$ addition the Ca/Si was raised to 2.36. Vice versa, the increase of the Ca/Si ratio with $CaCl_2$ did not show similar results to the $Ca(OH)_2$ experiments, even though the experiments with $CaCl_2$ were performed at an identical Ca/Si ratio of 2.36. Unlike $Ca(OH)_2$, the addition of $CaCl_2$ did not increase

the pH. As a conclusion, it can be stated that for an effective removal of Si via C-S-H phases formation, an alkaline pH value as well as a sufficiently high Ca/Si ratio need to be reached.

To examine the impact of the Ca/Si ratio on the removal effectiveness, experiments with different Ca/Si ratios were analyzed at a constant pH value. The Ca/Si ratio was set by the addition of $CaCl_2$ without affecting the pH (Fig. A.1). The pH value of each experiment was fixed to 10.5 using NaOH. The initial SiO_2 concentrations were 340 mg/L. Fig. A.9 shows the residual SiO_2 and the residual Ca concentration after 60 to 120 minutes of reaction time for different molar Ca/Si ratios. According to Greenberg (1954), not all Ca in solution reacts with the SiO_2, therefore molar Ca/Si ratios > 1 would improve the effectiveness of the precipitation methods significantly. This behavior is confirmed by the lab experiments (Fig. A.9). Minimum residual SiO_2 concentrations are reached at a Ca/Si ratio > 1.25. At higher ratios, no further significant decrease is observed. For applications in raw material extraction and power plant operations, the residual Ca concentration also needs to be minimized to avoid e.g. calcite scaling. Therefore, the optimal method yields both, minimal residual SiO_2 and Ca concentrations. As the residual Ca concentrations increase with higher initial molar Ca/Si ratios and the residual SiO_2 concentration does not further significantly decrease, Ca/Si ratios between 1.25 and 1.5 are favorable.

Fig. A.6 illustrates the impact of the pH on the residual SiO_2 concentration. The initial SiO_2 concentration was 340 mg/L (A.2, Table A.4) for all experiments, which results in an initial Ca/Si ratio of 0.95. Fig. A.6 clearly states that the removal of SiO_2 is independent of the precipitation method used. The decisive factor is the increase of the pH to values > 10 for a more effective reduction of the SiO_2 concentration underneath the silica saturation. Explications can be provided by the silica species distribution. At pH > 10 the H_3SiO_4-species becomes the predominant species (Alexander et al. 1954, Eikenberg 1990, Iler 1979). The H_3SiO_4-species favors the adsorption of divalent ions on the surface (Greenberg 1956). The adsorbed Ca^{2+} ion enhances the interparticle bridging and leads to agglomeration and formation of aqueous C-S-H phases (Gaboriaud et al. 1999, Iler 1975,7, Maraghechi et al. 2016, Santschi and Schindler 1973). The C-S-H phases are supersaturated at alkaline pH; hence they start to precipitate.

For the understanding of the incorporation process in the natural geothermal fluid experiments, the element enrichment in the precipitates is calculated with respect to the concentration in the fluid (Fig. A.10). Monovalent elements (Li, Rb, Cs) are depleted in the precipitate in comparison to the fluid, while divalent or higher valent elements are enriched in the precipitates. Hence, the incorporation of the trace elements seems to be dependent on the valence of the ions. However, the incorporation of trace elements is summed up to below 0.25 % (Fig. A.8). The only element which is clearly affected by the precipitation process is Mg. Mg could not be detected in ICP-MS analysis, because the measurement setup was focused on the trace element detection. However, the decrease in the fluid samples (Fig. A.5)

hints on the incorporation of Mg in the precipitation process resulting in the simultaneous formation of M-S-H and C-S-H phases.

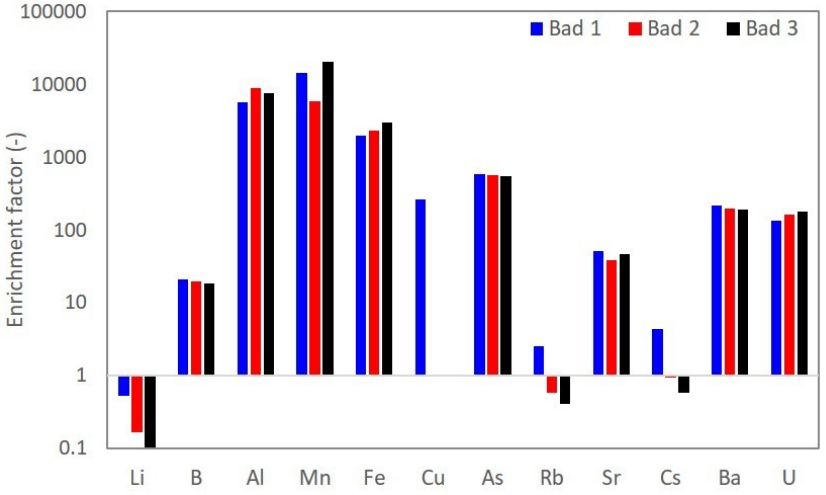

Figure A.10: Enrichment factors of the trace elements. The enrichment factors are calculated by dividing the percentage of the element in the solid phase by the percentage in the fluid. Enrichment factors greater than 1 indicate an accumulation of the element in the solid phase, whereas factors minor 1 indicate an accumulation in the fluid phase.

C-S-H phases are well known and commonly used in the cement and concrete industries. Furthermore, there exist some studies on chemisorption of phosphate in C-S-H phases, leading to potential application of these phases either as fertilizers or for environmental remediation (Johnston et al. 2019, Southam et al. 2004). However, careful analysis of the geothermal fluid and the C-S-H precipitates must be conducted to identify possible coprecipitation and incorporation of potentially harmful elements.

The residual high pH value of the spent geothermal fluids facilitates Li extraction. The most common Li extraction processes; Manganese ion sieves and Lithium carbonate precipitation, show higher effectiveness when operated at high pH (Han et al. 2020, Weng et al. 2020). However, the resulting high pH geothermal fluid must be neutralized before reinjection. To minimize the cost for neutralization, an approach could be to use pre-separated Non-Condensable Gases (NCGs Finster et al. 2015).

Fig. A.11 compares the removal effectiveness of our experimental setting with comparable results found in literature. To ensure comparability with the laboratory experiments, only experiments with similar SiO_2 and TDS concentrations and a comparable amount of additive used are taken into account (A.3). Precipitation methods with $Ca(OH)_2$, Zn, and Al as additives appear to be most effective. The silica seeding method in this study is less effective than the comparative methods described in the literature. The deviation can be explained by the experimental setup: The experiments in the literature were performed with a higher initial SiO_2 concentration and a lower temperature (Setiawan et al. 2019). This leads to higher

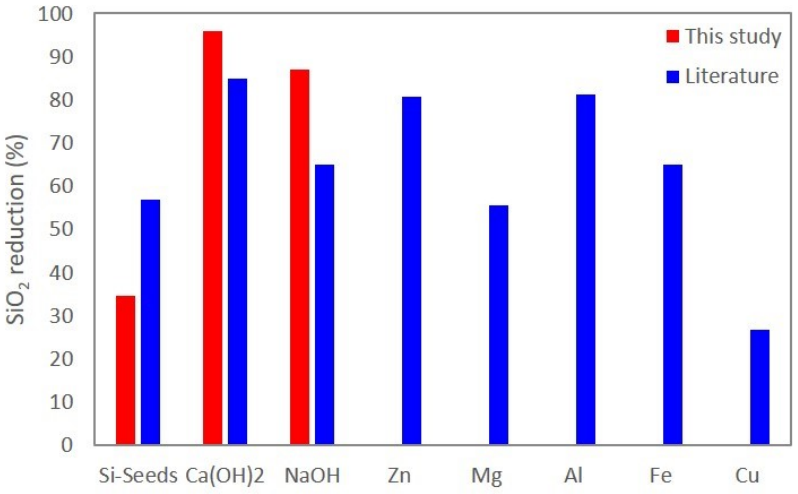

Figure A.11: Comparison of the removed SiO_2 in the experiments with results found in literature for different precipitation methods. Silica Seeds: Setiawan et al. (2019), Ex.1 (Table A.4), $Ca(OH)_2$: Badruk and Matsunaga (2001), Ex. 16 (Table A.4), NaOH: Gallup et al. (2003), Ex. 23 (Table A.4), Zn: Zeng et al. (2007), Mg: Lin et al. (2003), Al: Yokoyama et al. (2002), Fe: Renew and Hansen (2017), Cu: Gallup et al. (2003).

removal effectiveness, although the method is not able to reduce the SiO_2 concentration below saturation. As indicated in literature, silica removal processes using $Ca(OH)_2$ and NaOH are highly effective. In comparison with the literature data, our batch experiments with $Ca(OH)_2$ show even a higher removal effectiveness. Furthermore, our results indicated that also the addition of NaOH yields similar SiO_2 reduction rates, if the solution contains sufficient high Ca/Si ratios.

Table A.3: Comparison of the SiO_2 removal effectiveness of different precipitation methods from literature data (mg/L, unless otherwise noted).

Method	SiO_2 initial	SiO_2 residual	SiO_2 removed (%)	TDS	Reference
Silica seeds	418	180	57	24,153	Setiawan et al. (2019)
$Ca(OH)_2$	400	60	85	5093	Badruk and Matsunaga (2001)
NaOH	600	210	65	15,455	Gallup et al. (2003)
Zn	140	27	81	2830	Zeng et al. (2007)
Mg	450	200	56	n.d.	Lin et al. (2003)
Al	532	100	81	1688	Yokoyama et al. (2002)
Fe	240	84	65	4752	Renew and Hansen (2017)
Cu	600	440	27	15,455	Gallup et al. (2003)

n.d. not determined

A.1.5 Conclusions

Within this study, the removal of silica out of geothermal fluids was investigated. The aim was to minimize the risk of silica scaling which extends the use of geothermal fluids as a new source for raw materials. Effective silica removal is achieved via formation of C-S-H phases. The precipitation occurs within minutes and the residual silica concentration remains significantly below the saturation concentration of SiO_2. The reduction below the saturation concentration is reached in under 5 minutes and after 30 minutes after addition of the precipitation agent, the silica removal process is almost completed. For integration of a silica removal processing unit in geothermal power plants fast reaction kinetics are advantageous since it allows a plant design with short hydraulic residence times and as a consequence lower investment costs and smaller space requirement. The developed removal process depends on two major factors that need to be adapted to induce an effective and fast precipitation process:

1. The increase of the pH value > 10 favors the formation of C-S-H phases. The mechanism is hereby independent of the additives and trace elements
2. Molar Ca/Si ratios > 1.25 lead to an effective removal of silica.

Further optimizations of the molar Ca/Si ratio need to be performed, to yield maximal silica removal and simultaneously minimal residual calcium concentrations to prevent latter stage calcite scaling. However, the experiments have shown that the silica removal process by formation of C-S-H phases is element-specific. The concentration of Li, as a raw material of current economic interest, remains constant in solution. Additional experiments performed with complex, natural geothermal fluid confirm the element-specific removal process, which mechanism is also not disturbed by the presence of additional elements in the solution. In general, monovalent ions (Li, Rb, Cs) are not affected by the removal mechanism, while higher valent ions can be incorporated in the precipitates, which is confirmed by ICP-MS analysis of the precipitates. However, the incorporation of trace elements only accounts to a lesser amount (<0.25 %). The precipitates show elevated incorporation of Mg that is quantitatively removed from the solution. Mg, having the same valence as Ca, is presumably forming M-S-H-phases; in analogy with the C-S-H-phases. Therefore, it is likely that sufficient high molar Mg/Si ratios can also lead to effective removal of both Si and Mg.

These findings demonstrate that in silica-rich geothermal fluids the removal of silica by the formation of C/M-S-H-phases is suitable for fluid mining purposes. By reducing the SiO_2 concentration, the risk of silica scaling during further treatment processes is negligible. This is a first important step towards integrating mineral extraction in geothermal systems worldwide and thus enabling local raw material production in Germany again.

Acknowledgments

The authors gratefully acknowledge research funding by BMBF Client II for the BrineMine Project (Federal Ministry of Education and Research, FKZ: 033R190B). The authors appreciate the department of Geochemistry & Economic Geology (Karlsruhe Institute of Technology, Division of Applied Geosciences) for access to laboratories and equipment, and fruitful discussions.

A.1.6 Supplementary material

Table A.4: Overview of the experimental parameters and ICP-OES results of the experiments with synthetic produced water (mg/L, unless otherwise noted). The names of the experiments are used to differ between different experimental parameters. The reference is linked to the Figures in which the results are shown. For further explanation, the reader is referred to Section A.1.2

Ex.	Sample ID	Method	$t_{reac.}$ (min)	Temp. (°C)	pH (-)	Ca/Si (molar)	SiO_2	Li	Na	Ca	K	Reference
1	Ex. 1.0	Si-Seeds	0				317.65	32.19	3818.89	3.65	536.10	A.2, A.3
1	Ex. 1.1	Si-Seeds	5				303.06	30.34	3614.59	5.02	516.49	A.2, A.3
1	Ex. 1.2	Si-Seeds	10				290.76	30.01	3559.11	4.04	499.45	A.2, A.3
1	Ex. 1.3	Si-Seeds	20				295.82	30.25	3627.75	4.09	513.11	A.2, A.3
1	Ex. 1.4	Si-Seeds	30				286.02	29.78	3563.84	4.85	506.63	A.2, A.3
1	Ex. 1.5	Si-Seeds	60				268.30	27.15	3227.38	5.45	452.28	A.2, A.3
1	Ex. 1.6	Si-Seeds	90				276.13	27.62	3382.34	4.47	471.02	A.2, A.3
1	Ex. 1.7	Si-Seeds	120				258.63	25.93	3139.87	5.05	444.38	A.2, A.3, A.9, A.11
2	Ex. 2.0	$CaCl_2$	0	69.9	6.7	0.95	321.65	30.11	3693.88	205.04	537.03	A.2
2	Ex. 2.1	$CaCl_2$	15	68.5	6.86	2	329.88	30.83	3768.89	515.36	555.93	A.2
2	Ex. 2.2	$CaCl_2$	30	68.3	7.15	2	332.11	31.48	3832.11	521.70	567.77	A.2
2	Ex. 2.3	$CaCl_2$	60	69.3	6.7	2	331.21	31.04	3821.46	520.78	563.69	A.2
2	Ex. 2.4	$CaCl_2$	120	70	6.45	2	329.38	30.29	3722.04	501.82	561.46	A.2
3	Ex. 3	$CaCl_2$ + NaOH	120	69.7	7.96	2	288.91	26.49	3277.49	369.81	491.92	A.6
4	Ex. 4	$CaCl_2$ + NaOH	120	69.5	8.97	2	330.28	30.74	3822.48	429.27	554.70	A.6
5	Ex. 5	$CaCl_2$ + NaOH	120	70.1	9.48	2	304.11	28.35	3619.62	398.01	510.76	A.6
6	Ex. 6	$CaCl_2$ + NaOH	120	70.3	10.02	2	262.43	28.99	3771.95	385.48	527.45	A.6
7	Ex. 7	$CaCl_2$ + NaOH	120	70.4	10.47	2	42.28	25.76	3389.37	226.72	460.91	A.9, A.6

Ex.	Sample ID	Method	$t_{reac.}$ (min)	Temp. (°C)	pH (-)	Ca/Si (molar)	SiO_2	Li	Na	Ca	K	Reference
8	Ex. 8	$CaCl_2$ + NaOH	120	69.9	10.34	0.5	201.95	34.0	3974	53	567	A.9
9	Ex. 9	$CaCl_2$ + NaOH	120	69.5	10.46	0.8	80.65	34	4378	96	580	A.9
10	Ex. 10	$CaCl_2$ + NaOH	60	68.7	10.52	0.95	90.13	96.19		63.15		A.9
11	Ex. 11	$CaCl_2$ + NaOH	60	68.9	10.57	1.25	36.17	99.79		89.69		A.9
12	Ex. 12	$CaCl_2$ + NaOH	60	65.8	10.53	1.5	23	95.75		198.17		A.9
13	Ex. 13	$CaCl_2$ + NaOH	60	67.9	10.52	1.75	20.91	95.62		252.92		A.9
14	Ex. 14	$CaCl_2$ + NaOH	60	65.7	10.52	2	26.4	111.73		340.63		A.9
15	Ex. 15	$CaCl_2$ + NaOH	60	67.9	10.49	3	66.11	94.01		658.69		A.9
16	Ex. 16.0	Ca(OH)2	0	69.5	6.7	0	314.26	29.48	3787.95	185.71	551.78	A.2, A.3, A.9
16	Ex. 16.1	$Ca(OH)_2$	5	68.9	10.46	2.36	111.90	31.05	3943.58	307.01	563.70	Fig. 3, A.9
16	Ex. 16.2	$Ca(OH)_2$	10	67.8	10.36	2.36	91.81	31.08	3975.59	315.02	565.30	Fig. 3, A.9
16	Ex. 16.3	$Ca(OH)_2$	15	68.1	10.45	2.36	71.87	31.31	3995.13	329.73	575.49	Fig. 3, A.9
16	Ex. 16.4	$Ca(OH)_2$	20	68	10.44	2.36	53.77	31.57	4008.48	324.68	575.48	Fig. 3, A.9
16	Ex. 16.5	$Ca(OH)_2$	30	67.7	10.42	2.36	32.10	31.42	4001.58	326.10	572.31	Fig. 3, A.9
16	Ex. 16.6	$Ca(OH)_2$	60	68.8	10.47	2.36	21.93	31.00	3971.89	316.99	572.35	Fig. 3, A.9
16	Ex. 16.7	$Ca(OH)_2$	90	69.4	10.5	2.36	16.96	30.44	3861.12	308.19	552.18	Fig. 3, A.9
16	Ex. 16.8	$Ca(OH)_2$	120	69.2	10.59	2.36	14.75	30.45	3876.67	309.82	560.50	A.3, A.4, A.9, A.6, A.11
17	Ex. 17	$Ca(OH)_2$	120	70.8	8.3	1	318.27	32.26	3997.84	229.33	557.74	A.6
18	Ex. 18	$Ca(OH)_2$	120	70.3	9.15	1.25	283.41	30.13	3771.99	257.48	530.20	A.6
19	Ex. 19	$Ca(OH)_2$	120	71.2	9.7	1.5	275.16	31.10	3997.25	318.17	560.53	A.6
20	Ex. 20	$Ca(OH)_2$	120	71.4	10.02	1.75	154.79	31.44	3968.33	312.97	552.68	A.6
21	Ex. 21	$Ca(OH)_2$	120	71.6	10.12	2	29.43	31.51	4006.27	298.07	562.08	A.6
22	Ex. 22	NaOH	120	69.6	10.5	0	329.05	30.54	4098.99	1	562.33	A.9
23	Ex. 23.0	NaOH	0			0.95	327.81	30.12	3860.50	2.35	540.30	A.2

Ex.	Sample ID	Method	$t_{reac.}$ (min)	Temp. (°C)	pH (-)	Ca/Si (molar)	SiO_2	Li	Na	Ca	K	Reference
23	Ex. 23.1	NaOH	120	69.5	10.46	0.95	60.11	29.53	4039.48	66.57	543.04	A.2, A.6, A.11

Table A.5: ICP-OES results (mg/L, unless otherwise noted) and experimental parameters of the precipitation experiments using the Baden-Baden brine (Fettquelle "FQ"). For further explanation, the reader is referred to Section A.1.2.

Name	Reaction time (min)	Temp. (°C)	pH (-)	SiO_2	Li	Na	Ca	K	Mg	Rb	Sr	As	Ba
FQ		61		146.9	9.38	928.48	135.44	86.52	4.08	1.10	3.03	0.28	0.16
Bad 1	0	69.8	8.11	287.42	92.90	1717.68	168.48	160.14	7.55	2.59	6.39	0.44	0.32
Bad 1	2	71.4	9.44	215.66	101.28	2051.29	186.15	174.13	0.21	2.49	5.75	0.21	0.28
Bad 1	15	72.1	10.85	45.06	100.38	2051.53	168.78	176.31	0.23	2.43	5.57	0.19	0.25
Bad 1	30	69.4	10.93	24.96	99.61	2033.93	173.35	175.02	<0.1	2.26	5.41	0.16	0.25
Bad 1	60	70.2	10.87	17.17	100.25	2048.81	166.77	175.86	<0.1	2.21	5.39	0.09	0.25
Bad 1	120	69.9	10.89	16.43	101.13	2072.44	159.52	177.36	<0.1	2.32	5.33	0.11	0.25
Bad 2	0	70	7.9	288.84	95.69	1845.15	175.80	172.01	7.83				
Bad 2	6	70.1	11.34	36.60	97.49	2129.40	244.03	176.61	<0.1				
Bad 2	16	70.2	11.44	10.40	97.09	2152.00	267.87	208.43	<0.1				
Bad 2	40	70.2	11.39	6.61	90.29	2101.62	221.28	168.58	<0.1				
Bad 2	60	69.6	11.4	12.98	95.00	2120.99	256.46	205.13	<0.1				
Bad 2	126	69.4	11.26	6.92	93.30	2060.75	235.42	201.86	<0.1				
Bad 3	0	70.9	7.97	295.42	96.47	1884.04	178.77	175.06	7.97				
Bad 3	5	71.2	11.36	18.15	97.03	224.40	194.56	177.82	<0.1				
Bad 3	15	69.5	11.41	9.20	94.45	2198.45	208.42	176.69	<0.1				
Bad 3	30	68.8	11.38	12.88	94.16	2086.15	258.39	202.46	<0.1				

Name	Reaction time (min)	Temp. (°C)	pH (-)	SiO_2	Li	Na	Ca	K	Mg	Rb	Sr	As	Ba
Bad 3	59	67.9	11.37	5.83	96.51	2227.50	229.45	178.90	<0.1				
Bad 3	114	73.2	11.32	6.89	98.02	2301.61	207.15	186.91	<0.1				

Table A.6: ICP-MS results of the precipitates. For FQ the water analysis of Sanjuan et al. (2016) is used. (ppm, unless otherwise noted).

Component	FQ[1] (µg/L)	Bad-1 Precipitate	Bad-2 Precipitate	Bad-3 Precipitate
Li[2]	100,000	90.7	28.4	17.4
B	3600	126	118	113
Al	10.78	102	163	139
Ti	n.d.	9.13	16.4	12.8
V	n.d.	0.27	0.74	0.82
Cr	<1	1.32	1.51	0.82
Mn	17.62	431	172	601
Fe	60	200	234	304
Co	<0.5	0.06	0.1	0.08
Ni	<1	1.16	1.6	1.63
Cu[3]	<1	224	1.99	5.5
Zn	<5	136.2	12.1	11.1
As	352	344	335	329
Rb	2880	12.4	2.83	2
Sr	7000	613	450	555
Y	n.d.	1.04	1.86	1.44

Component	FQ[1] (µg/L)	Bad-1 Precipitate	Bad-2 Precipitate	Bad-3 Precipitate
Mo	n.d.	0.03	0.01	0.02
Ag	<0.1	1.97	6.02	6.31
Cd	<0.1	0.05	0.07	0.06
Sb	n.d.	1.24	3.01	1.84
Cs[4]	10,000	74	15.8	9.82
Ba	238	87.3	78.8	76.6
Tl	n.d.	3.03	5.05	4.2
Pb	<0.5	0.49	0.52	0.89
U	0.66	0.15	0.18	0.2

[1] Twice the concentration obtained by Sanjuan et al. (2016)

[2] Addition of 84 mg/L Li by LiCl

[3] Addition of 0.5 mg/L Cu by $CuSO_4$ in Bad-1

[4] Addition of 10 mg/L Cs by CsCl

List of Figures

List of Tables

Bibliography

Abdelfatah, E. R., Kang, K., Pournik, M., Shiau, B., and Harwell, J. (2017). Study of nanoparticle adsorption and release in porous media based on DLVO theory. *Journal of Petroleum Science and Engineering*, 157. https://doi.org/10.1016/j.petrol.2017.08.003.

Abdelrady, A., Tang, Y., Bogaard, T., and Foppen, J. W. (2024). The use of silica encapsulated DNA particles with a supermagnetic iron core (SiDNAMag) in sand filtration system: Effect of water chemistry. *Journal of Water Process Engineering*, 62. https://doi.org/10.1016/j.jwpe.2024.105316.

Adams, M. C. and Davis, J. (1991). Kinetics of fluorescein decay and its application as a geothermal tracer. *Geothermics*, 20. https://doi.org/10.1016/0375-6505(91)90005-G.

Adamzyck, Z. and Weroński, P. (1999). Application of DLVO theory for particle deposition problems. *Advances in Colloid and Interface Science*, 83. https://doi.org/10.1016/S0001-8686(99)00009-3.

Agasti, S. S., Chompoosor, A., You, C.-C., Ghosh, P., Kim, C. K., and Rotello, V. M. (2009). Photoregulated release of caged anticancer drugs from gold nanoparticles. *Journal of the American Chemical Society*, 131. https://doi.org/10.1021/ja900591t.

Agenet, N., Perriat, P., Brichart, T., Crowther, N., Martini, M., and Tillement, O. (2012). Fluorescent nanobeads: a first step towards intelligent water tracers. *SPE International Oilfield Nanotechnology Conference*, https://doi.org/10.2118/157019-MS.

Agmo Hernández, V. (2023). An overview of surface forces and the DLVO theory. *ChemTexts*, 9. https://doi.org/10.1007/s40828-023-00182-9.

Ahualli, S., Iglesias, G. R., Wachter, W., Dulle, M., Minami, D., and Glatter, O. (2011). Adsorption of anionic and cationic surfactants on anionic colloids: Supercharging and destabilization. *Langmuir*, 27. https://doi.org/10.1021/la201242d.

Akhter, F., Rao, A. A., Abbasi, M. N., Wahocho, S. A., Mallah, M. A., Anees-ur Rehman, H., and Chandio, Z. A. (2022). A comprehensive review of synthesis, applications and future prospects for silica nanoparticles (SNPs). *Silicon*, 14. https://doi.org/10.1007/s12633-021-01611-5.

Al Mahrouqi, D., Vinogradov, J., and Jackson, M. D. (2017). Zeta potential of artificial and natural calcite in aquoeus solutions. *Advances in Colloid and Interface Science*, 240. https://doi.org/10.1016/j.cis.2016.12.006.

Alaskar, M. (2013). *In-Situ Multifunctional Nanosensors for Fractured Reservoir Characterization*. PhD thesis, Stanford Universiy.

Alaskar, M., Ames, M., Chong, L., Li, K., and Horne, R. (2015a). Temperature nanotracers for fractured reservoirs characterization. *Journal of Petroleum Science and Engineering*, 127. https://doi.org/1016/j.petrol.2015.01.021.

Alaskar, M., Li, K., and Horne, R. (2015b). Silica particles mobility through fractured rock. *Arabian Journal for Science and Engineering*, 40. https://doi.org/10.1007/s13369-015-1577-1.

Ale, A., Gutierrez, M. F., Rossi, A. S., Bacchetta, C., Desimone, M. F., and Cazenave, J. (2021). Ecotoxicity of silica nanoparticles in aquatic organisms: An updated review. *Environ. Toxicol. Pharmacol.*, 87. https://doi.org/10.1016/j.etap.2021.103689.

Alexander, G. B., Heston, W. M., and Iler, R. K. (1954). The solubility of amorphous silica in water. *J. Phys. Chem.*, 58. https://doi.org/10.1021/j150516a002.

Alroudhan, A., Vinogradov, J., and Jackson, M. D. (2016). Zeta potential of intact natural limestone: Impact of potential-determining ions Ca, Mg and SO_4. *Colloids and Surfaces A: Physicochemical and Engineering Aspects*, 490. https://doi.org/10.1016/j.colsurfa.2015.11.068.

Anderson, M. P. (2005). Heat as ground water tracer. *Groundwater*, 43. https://doi.org/10.1111/j.1745-6584.2005.00052.x.

Andersson, J., Rosenholm, J., Areva, S., and Lindén, M. (2004). Influences of material characteristics on ibuprofen drug loading and release profiles from ordered micro- and mesoporous silica matrices. *Chem. Mater.*, 16. https://doi.org/10.1021/cm0401490.

Arkles, B., Pan, Y., Larson, G. L., and Singh, M. (2014). Enhanced hydrolytic stability of siliceous surfaces modified with pendant dipodal silanes. *Chemistry*, 20. https://doi.org/10.1002/chem.201402757.

Arnórsson, S. (1975). Application of the silica geothermometer in low temperature hydrothermal areas in Iceland. *Am. J. Sci.*, 275. https://doi.org/10.2475/ajs.275.7.763.

Arriagada, F. J. and Osseo-Assare, K. (1999). Synthesis of nanosize silica in a nonionic water-in-oil microemulsion: Effects of the water/surfactant molar ratio and ammonia concentration. *Journal of Colloid and Interface Science*, 211. https://doi.org/10.1006/jcis.1998.5985.

Atkins, P. and de Paula, J. (2006). *Physical Chemistry*. Oxford University Press, 8th edition.

Auger, A., Samuel, J., Poncelet, O., and Raccurt, O. (2011). A comparative study of non-covalent encapsulation methods for organic dyes into silica nanoparticles. *Nanoscale Research Letters*, 6. https://doi.org/10.1186/1556-276X-6-328.

Auset, M. and Keller, A. A. (2006). Pore-scale visualization of colloid straining and filtration in saturated porous media using micromodels. *Water Resources Resarch*, 42. https://doi.org/10.1029/2005WR004639.

Avnir, D., Levy, D., and Reisfeld, R. (1984). The nature of the silica cage as reflected by spectral changes and enhanced photostability of trapped rhodamine 6G. *J. Phys. Chem.*, 88. https://doi.org/10.1021/j150668a042.

Ayling, B. F. and Rose, P. E. (2006). Geochemical tracers: capabilities and potential for geothermal reservoir characterisation. In *35th New Zealand Geothermal Workshop*.

Azaroual, M., Fouillac, C., and Matray, J. M. (1997). Solubility of silica polymorphs in electrolyte solutions, II. Activity of aqueous silica and solid silica polymorphs in deep solutions from the sedimentary Paris Basin. *Chemical Geology*, 140. https://doi.org/10.1016/S0009-2541(97)00047-8.

Aznar, E., Mondragón, L., Ros-Lis, J. V., Sancenén, F., Marcos, M. D., Martínez-Manéz, R., Soto, J., Pérez-Payá, E., and Amorós, P. (2011). Finely tuned temperature-controlled cargo release using paraffin-capped mesoporous silica nanoparticles. *Angew Chem. Int. Ed. Engl.*, 18. https://doi.org/10.1002/anie.201102756.

Badruk, M. and Matsunaga, I. (2001). Experimental results of silica removal from simulated solutions of geothermal brine of Kizildere field, Turkey. *Geothermics*, 30. https://doi.org/10.1016/S0375-6505(01)00013-X.

Baeza, A., Guisasola, E., Ruiz-Hernández, E., and Vallet-Regí, M. (2012). Magnetically triggered multidrug release by hybrid mesoporous silica nanoparticles. *Chemistry of Materials*, 24. https://doi.org/10.1021/cm203000u.

Baeza, A. and Vallet-Regí, M. (2020). Mesoporous silica nanoparticles as theranostic antitumoral nanomedicines. *Pharmaceutics*, 12. https://doi.org/10.3390/pharmaceutics12100957.

Bagwe, R. P., Hilliard, L. R., and Tan, W. (2006). Surface modification of silica nanoparticles to reduce aggregation and nonspecific binding. *Langmuir*, 22. https://doi.org/10.1021/la052797j.

Bagwe, R. P., Yang, C., Hilliard, L. R., and Weihong, T. (2004). Optimization of dye-doped silica nanoparticles prepared using a reverse microemulsion method. *Langmuir*, 20. https://doi.org/10.1021/la049137j.

Bakshi, M. S. (2017). Nanotoxicity in systemic circulation and wound healing. *Chem. Res. Toxicol.*, 30. https://doi.org/10.1021/acs.chemrestox.7b00068.

Balboa, A., Partch, R. E., and Matjevic, E. (1987). Preparation of uniform colloidal dispersions by chemical reactions in aerosols IV. Mixed silica/titania particles. *Colloids and Surfaces*, 27. https://doi.org/10.1016/0166-6622(87)80332-3.

Barandeh, F., Nguyen, P. L., Kumar, R., Iacobucci, G. J., Kuznicki, M. L., Kosterman, A., Bergey, E. J., Prasad, P. N., and Gunawardena, S. (2012). Organically modified silica nanoparticles are biocompatbile and can be targeted to neurons in vivo. *PLoS One*, 7. https://doi.org/10.1371/journal.pone.0029424.

Barbier, E. (2002). Geothermal energy technology and current status: an overview. *Renewable and Sustainable Energy Reviews*, 6. https://doi.org/10.1016/S1364-0321(02)00002-3.

Barton, I. (2019). The effects of temperature and pressure on the stability of mineral colloids. *American Journal of Science*.

Baxter, S. and Bryant, K. C. (1952). Silica sols. Part II. Conditions of Stability. *Journal of the Chemical Society (Resumed)*, https://doi.org/10.1039/JR9520003021.

Bayda, S., Adeel, M., Tuccinardi, T., Cordani, M., and Rizzolio, F. (2020). The history of nanoscience and nanotechnology: from chemical-physical applications to nanomedicine. *Molecules*, 25. https://doi.org/10.3390/molecules25010112.

Beck, J. S., Vartuli, J. C., Roth, W. J., Leonowicz, M. E., Kresge, C. T., Schmitt, K. D., Chu, C. T.-W., Olson, D. H., Sheppard, E. W., McCullen, S. B., Higgins, J. B., and Schlenker, J. L. (1992). A new family of mesoporous molecular sieves prepared with liquid crystal templates. *J. Am. Chem. Soc.*, 114. https://doi.org/10.1021/ja00053a020.

Behrens, H., Ghergut, I., Licha, T., Orzol, J., and Sauter, M. (2006). Reactive behaviour of uranine (fluorescein) in a deep geothermal-reservoir tracer test. *Geophyiscal Research Abstracts*, 8. https://doi.org/1607-7962/gra/EGU06-A-10448.

Behrens, H., Ghergut, I., Sauter, M., and Licha, T. (2009). Tracer properties and spiking results (from geothermal reservoirs). In *Thirty-Fourth Workshop on Geothermal Reservoir Engineering*.

Bergna, H. E. (1994). Colloid chemistry of silica. *Advances in Chemistry*.

Bergström, L. (1997). Hamaker constants of inorganic materials. *Advances in Colloid and Interface Science*, 70. https://doi.org/10.1016/S0001-8686(97)00003-1.

Berson, J., Rudolph, B., Spitzmüller, L., Kohl, T., and Schimmel, T. (2024). Reporting nanoparticle tracers: Validation of performance in flow-through experiments simulating reservoir conditions. *Journal of Hydrology*, 637. https://doi.org/10.1016/j.jhydrol.2024.131429.

Bharti, C., Nagaich, U., Pal, A. K., and Gulati, N. (2015). Mesoporous silica nanoparticles in target drug delivery system. *Int. J. Pharm. Investig.*, 5. https://doi.org/10.4103/2230-973X.160844.

Bhattacharjee, S. (2016). DLS and zeta potential - what they are and what they are not? *Journal of Controlled Release*, 235. https://doi.org/10.1016/j.jconrel.2016.06.017.

Bhavsar, D., Patel, V., and Sawant, K. (2019). Systematic investigation of in vitro and in vivo safety, toxicity and degradation of mesoporous silica nanoparticles synthesized using commercial sodium silicat. *Microporous and Mesoporous Materials*, 284. https://doi.org/10.1016/j.micromeso.2019.04.050.

Blum, A. E., Yund, R. A., and Lasaga, A. C. (1990). The effect of dislocation density on the dissolution rate of quartz. *Geochimica et Cosmochimica Acta*, 54. https://doi.org/10.1016/0016-7037(90)90318-F.

Bogush, G. H. and Zukoski, C. F. I. (1991). Studies of the kinetics of the precipitation of uniform silica particles through the hydrolysis and condensation of silicon alkoxides. *Journal of Colloid and Interface Science*, 142. https://doi.org/10.1016/0021-9797(91)90029-8.

Borhan, M. Z. and Lee, T. Y. (2015). Synthesis of TiO_2 nanopowders from red gypsum using EDTA as complexing agent. *Journal of Nanostructure in Chemistry*, 5. https://doi.org/10.1007/s40097-014-0137-7.

Bork, M., Lange, J., Graf-Rosenfellner, M., and Lang, F. (2020). Controls of fluorescent tracer retention by soils and sediments. *Hydrol. Earth Syst. Sci.*, 24. https://doi.org/10.5194/hess-24-977-2020.

Borrmann, T. and Johnston, J. H. (2017). Transforming silica into silicate - pilot scale removal of problematic silica from geothermal brine. In *GRC Transactions*.

Borrmann, T., Johnston, J. H., and McBrearty, R. (2009). Nano-structured calcium silicate - a solution to the formation of silica scale in geothermal water. In *GRC Transactions*.

Bouchoucha, M., Côté, M.-F., Gaudreault, R. C., Fortin, M.-A., and Kleitz, F. (2016). Size-controlled functionalized mesoporous silica nanoparticles for tunable drug release and enhanced anti-tumoral activity. *Chemistry of Materials*, 28. https://doi.org/10.1021/acs.chemmater.6b00877.

Bourcier, W., Martin, S., Viani, B., and Bruton, C. (2001). Developing a process for commercial silica production from geothermal brines. In *GRC Transactions*.

Bourcier, W., Ralph, W., Johnson, M., Bruton, C., and Gutierrez, P. (2006). Silica extraction at the Mammoth Lakes geothermal site. *GRC*.

Bourcier, W. L., Lin, M., and Nix, G. (2005). Recovery of minerals and metals from geothermal fluids. Technical report, Lawrence Livermore National Laboratory (LLNL).

Bradford, S. A., Yates, S. R., Bettahar, M., and Simunek, J. (2002). Physical factors affecting the tranpsort and fate of colloids in saturated porous media. *Water Resourc. Res.*, 38. https://doi.org/10.1029/2002WR001340.

Braun, K., Pochert, A., Beck, M., Fiedler, R., Gruber, J., and Lindén, M. (2016). Dissolution kinetics of mesoporous silica nanoparticles in different simulated body fluids. *Journal of Sol-Gel Science and Technology*, 79. https://doi.org/10.1007/s10971-016-4053-9.

Brauser, E., Bartl, M., and Rose, P. (2013). Thermal stability and chemistry of fluorescent nanocrystals for use as novel geothermal tracer. In *Thirty-Eighth Workshop on Geothermal Reservoir Engineering*.

Bremere, I., Kennedy, M., Mhyio, S., Jaljuli, A., Witkamp, G.-J., and Schippers, J. (2000). Prevention of silica scale in membrane systems: removal of monomer and polymer silica. *Desalination*, 132. https://doi.org/10.1016/S0011-9164(00)00138-7.

Brown, K. (2011). Thermodynamics and kinetics of silica scaling. In *International workshop on mineral scaling*, volume https://doi.org/10.1007/978-981-10-7335-9_2.

Bultreys, T., van Offenwert, S., Goethals, W., Boone, M. N., Aelterman, J., and Cnudde, V. (2022). X-ray tomographic micro-particle velocimetry in porous media. *Physics of Fluids*, 34. https://doi.org/10.1063/5.0088000.

Buoyer, F., Robben, A., Yu, W. L., and Borkovec, M. (2001). Aggregation of colloidal particles in the presence of oppositely charged polyelectrolytes: Effect of surface charge heterogeneities. *Langmuir*, 17. https://doi.org/10.1021/la010548z.

Cairns, M., Borrmann, T., Höll, W., and Johnston, J. (2006). A study of the uptake of copper ions by nanostructured calcium silicate. *Microporous and Mesoporous Materials*, 95. https://doi.org/10.1016/j.micromeso.2006.05.009.

Caldelas, F., Murphy, M. J., Huh, C., and Bryant, S. L. (2011). Factors governing distance of nanoparticle propagation in porous media. In *SPE Production and Operations Symposium*.

Cao, V., Schaffer, M., Jin, Y., and Licha, T. (2017). Preservation of commonly applied fluorescent tracers in complex water samples. *Grundwasser*, 22. https://doi.org/10.1007/s00767-017-0356-1.

Cao, V., Schaffer, M., Taherdangkoo, R., and Licha, T. (2020). Solute reactive tracers for hydrogeological applications: A short review and future prospects. *Water*, 12. https://doi.org/10.3390/w12030653.

Carstens, J. F., Bachmann, J., and Neuweiler, I. (2019). A new approach to determine the relative importance of DLVO and non-DLVO colloid retention mechanisms in porous media. *Colloids and Surfaces A: Physicochemical and Engineering Aspects*, 560. https://doi.org/10.1016/j.colsurfa.2018.10.013.

Cauda, V., Schlossbauer, A., and Bein, T. (2010). Bio-degradation study of colloidal mesoporous silica nanoparticles: Effect of surface functionalization with organosilanes and poly(ethylene glycol). *Microporous and Mesoporous Materials*, 132. https://doi.org/10.1016/j.micromeso.2009.11.015.

Cauda, V., Szeifert, J. M., Merk, K., Fattakhova-Rohfling, D., and Bein, T. (2011). All-inorganic core-shell silica-titania mesoporous colloidal nanoparticles showing orthogonal functionality. *J. Mater. Sci.*, 21. https://doi.org/10.1039/C0JM04528D.

Cedervall, T., Lynch, I., Lindman, S., Berggord, T., Thulin, E., Nilsson, H., Daswon, K. A., and Linse, S. (2007). Understanding the nanoparticle–protein corona using methods to quantify exchange rates and affinities of proteins for nanoparticles. *PNAS*, 104. https://doi.org/10.1073/pnas.0608582104.

Chakraborty, S., Elhaj, R., Foppen, J. W., and Schijven, J. (2023). Effect of injection water ionic strength on estimating hydraulic parameters in a 3D sand tank using silica encapsulated magnetic DNA particles. *Advances in Water Resources*, 179. https://doi.org/10.1016/j.advwatres.2023.104507.

Chakraborty, S. and Panigrahi, P. K. (2020). Stability of nanofluid: A review. *Applied Thermal Engineering*, 174. https://doi.org/10.1016/j.applthermaleng.2020.115259.

Chan, S. H. (1989). A review on solubility and polymerization of silica. *Geothermics*, 18. https://doi.org/10.1016/0375-6505(89)90009-6.

Chang, C.-L. and Fogler, H. S. (1996). Kinetics of silica particle formation in nonionic w/o microemulsions from TEOS. *AIChE Journal*, 42. https://doi.org/10.1002/aic.690421115.

Chang, J.-S., Chang, K. L. B., Hwang, D.-F., and Kong, Z.-L. (2007). In vitro cytotoxicity of silica nanoparticles at high concentrations strongly depends on the metabolic activity type of the cell line. *Environ. Sci. Technol.*, 41. https://doi.org/10.1021/es062347t.

Chen, C.-T. and Marshall, W. L. (1982). Amorphous silica solubilities IV. Behavior in pure water and aqueous sodium chloride, sodium sulfate, magnesium chloride, and magnesium sulfate solutions up to 350°C. *Geochimica et Cosmochimica Acta*, 46. https://doi.org/10.1016/0016-7037(82)90255-1.

Chen, L. and Kibbey, T. C. G. (2008). Transport of nanomaterials in unsaturated porous media. In *Nanoscience and Nanotechnology: Environmental and Health Impacts*. John Wiley & Sons.

Chen, L., Liu, J., Zhang, Y., Zhang, G., Kang, Y., Chen, A., Feng, X., and Shao, L. (2018). The toxicity of silica nanoparticles to the immune system. *Nanomedicine*, 13. https://doi.org/10.2217/nnm-2018-0076.

Cheng, S.-H., Lee, S.-H., Chen, M.-C., Souris, J. S., Tseng, F.-G., Yang, C.-S., Mou, C. Y., Chen, C.-T., and Lo, L.-W. (2010). Tri-functionalization of mesoporous silica nanoparticles for comprehensive cancer theranostics—the trio of imaging, targeting and therapy. *Journal of Materials Chemistry*, 20. https://doi.org/10.1039/C0JM00645A.

Chequer, L., Bedrikovetsky, P., Carageorgos, T., Badalyan, A., and Gitis, V. (2019). Mobilization of attached clustered colloids in porous media. *Water Resources Research*, 55. https://doi.org/10.1029/2018WR024504.

Christenson, H. K. (1988). Non-DLVO forces between surfaces - solvation, hydration and capillary effects. *J. Dispersion Science and Technology*, 9. https://doi.org/10.1080/01932698808943983.

Chrysikopoulos, C. V. (1993). Artificial tracer for geothermal reservoir studies. *Environmental Geology*, 22. https://doi.org/10.1007/BF00775286.

Chrysikopoulos, C. V. and Katzourakis, V. E. (2015). Colloid particle size-dependent dispersivity. *Water Resources Research*, 51. https://doi.org/10.1002/2014WR016094.

Clemente, A., Moreno, N., Lobera, M. P., Balas, F., and Santamaria, J. (2016). Fluorescently labelled SiO_2 nanoparticles as tracers in natural waters: dependence of detection limits on environmental conditions. *Environmental Science: Nano*, 3. https://doi.org/10.1039/C6EN00014B.

Cobos, J. E. and Søgaard, E. G. (2022). Chelating agents for diluted geothermal brine reinjection. *Geothermal Energy*, 10. https://doi.org/10.1186/s40517-022-00227-1.

Corapcioglu, M. Y. and Jiang, S. (1993). Colloid-facilitated groundwater contaminant transport. *Water Resources Research*, 29. https://doi.org/10.1029/93WR00404.

Corbalan, J. J., Medina, C., Jacoby, A., Malinski, T., and Radomski, M. W. (2011). Amorphous silica nanoparticles trigger nitric oxide/peroxynitrite imbalance in human endothelial cells: inflammatory and cytotoxic effects. *Int. J. Nanomedicine*, 6. https://doi.org/10.2147/IJN.S25071.

Corbalan, J. J., Medina, C., Jacoby, A., Malinski, T., and Radomski, M. W. (2012). Amorphous silica nanoparticles aggregate human platelets: potential implications for vascular homeostasis. *Int. J. Nanomedicine*, 7. https://doi.org/10.2147/IJN.S28293.

Cozma, A. I., Baciu, C., Moldovan, M., and Pop, I.-C. (2016). Using natural tracers to track the groundwater flow in a mining area. *Procedia Environmental Sciences*, 32. https://doi.org/10.1016/j.proenv.2016.03.026.

Crear, D. A., Axtmann, E. V., and Axtmann, R. C. (1981). Growth and ripening of silica polymers in aqueous solutions. *Geochmicia et Cosmochimica Acta*, 45. https://doi.org/10.1016/0016-7037(82)90260-5.

Croissant, J. G. and Brinker, C. J. (2018). Biodegradble silica-based nanoparticles: Dissolution kinetics and selective bond cleavage. *Enzymes*, 43. https://doi.org/10.1016/bs.enz.2018.07.008.

Croissant, J. G., Butler, K. S., Zink, J. I., and Brinker, C. J. (2020). Synthetic amorphous silica nanoparticles: toxicity, biomedical and environmental implications. *Nature Reviews Materials*, 5. https://doi.org/10.1038/s41578-020-0230-0.

Croissant, J. G., Fatieiev, Y., and Khashab, N. M. (2017). Degradability and clearance of silicon, organosilica, silsesquioxane, silica mixed oxide, and mesoporous silica nanoparticles. *Advanced Materials*, 29. https://doi.org/10.1002/adma.201604634.

Crundwell, F. K. (2017). On the mechanism of the dissolution of quartz and silica in aqueous solutions. *ACS Omega*, 2. https://doi.org/10.1021/acsomega.7b00019.

Cui, Y., Tian, S., Zoras, S., and Zhou, J. (2024). Recent advances in various nanomaterials utilized in geothermal heaet exchangers. *Nano Energy*, 122. https://doi.org/10.1016/j.nanoen.2024.109309.

Cypryk, M. and Apeloig, Y. (2002). Mechanism of the acid-catalyzed Si-O bond cleavage in siloxanes and siloxanols. a theoretical study. *Organometallics*, 21. https://doi.org/10.1021/om011055s.

Dashti, A., Gholami Korzani, M., Geuziane, C., Egert, R., and Kohl, T. (2023). Impact of structural uncertainty on tracer test design in faulted geothermal reservoirs. *Geothermics*, 107. https://doi.org/10.1016/j.geothermics.2022.102607.

Davies, J. H. and Davies, D. R. (2010). Earth's surface heat flux. *Solid Earth*, 1. https://doi.org/10.5194/sed-1-1-2009.

Davis, S. N., Thompson, G. M., Bentley, H. W., and Stiles, G. (2006). Ground-water tracers — a short review. *Groundwater*, 18. https://doi.org/10.1111/j.1745-6584.1980.tb03366.x.

de la Torre, C., Agostini, A., Mondragon, L., Orzaez, M., Sancenon, F., Martinez-Manez, R., Marcos, M. D., Amoros, P., and Perez-Paya, E. (2014). Temperature-controlled release by changes in the secondary structure of peptides anchored onto mesoporous silica supports. *Chem Commun (Camb)*, 50. https://doi.org/10.1039/c3cc49421g.

Derjaguin, B. and Landau, L. (1941). Theory on the stability of strongly charged lyophobic sols and of the adhesion of strongly charged particles in solutions of electrolytes. *Acta Physico Chemica URSS*, 14. https://doi.org/10.1016/0079-6816(93)90013-L.

Diedrich, T., Dybowska, A., Schott, J., Valsami-Jones, E., and Oelkers, E. H. (2012). The dissolution rates of SiO_2 nanoparticles as a function of particle size. *Environ. Sci. Technol.*, 46. https://doi.org/10.1021/es2045053.

Dietzel, M. (2000). Dissolution of silicates and stability of polysilicic acid. *Geochmicia et Cosmochimica Acta*, 64. https://doi.org/10.1016/S0016-7037(00)00426-9.

Dole, R. B. (1906). Use of fluorescein in the study of underground waters. *Underground-Water Paper*.

Dong, Z., Yang, H., Wu, D., Ni, J., Kim, H., and Tong, M. (2014). Influence of silicate on the transport of bacteria in quartz sand and iron mineral-coated sand. *Colloids and Surfaces B: Biointerfaces*, 123. https://doi.org/10.1016/j.colsurfb.2014.10.052.

Dove, P. M., Han, N., Wallace, A. F., and De Yoreo, J. J. (2008). Kinetics of amorphous silica dissolution and the paradox of the silica polymorphs. *PNAS*, 105. https://doi.org/10.1073/pnas.0803798105.

Drees, L. R., Wilding, L. P., Smeck, N. E., and Senkayi, A. L. (1989). *Minerals in Soil Environments*, chapter 19: Silica in Soils: Quartz and Disordered Polymorphs. SSSA Book Series.

Durack, P. J., Wijffels, S. E., and Boyer, T. P. (2013). Long-term salinity changes and implications for the global water cycle. *Ocean Circulation and Climate - A 21st Century Perspective*.

Duy Thanh, L. and Sprik, R. (2015). Zeta potential measurement using streaming potential in porous media. *VNU Journal of Science: Mathematics – Physics,*, 31(4):10.

Eikenberg, J. (1990). On the problem of silica solubility at high pH. Technical report, Paul Scherrer Institut "PSI".

EL Mekkawi, D. and Abdel Mottaleb, M. S. A. (2005). The interaction and photostability of some xanthenes and selected azo sensitizing dyes with TiO_2 nanoparticles. *International Journal of Photoenergy*, 7. https://doi.org/10.1155/S1110662X05000140.

Elimelech, M., Gregory, J., Jia, X., and Williams, R. A. (1995). *Particle deposition & Aggregation - Mesaurement, Modeling and Simulation*. Butterworth-Heinemann.

Elimelech, M., Nagai, M., Ko, C.-H., and Ryan, J. N. (2000). Relative insignificance of mineral grain zeta potential to colloid transport in geochemically heterogeneous porous media. *Environmental Science and Technology*, 34. https://doi.org/10.1021/es9910309.

Elimelech, M. and O'Melia, C. R. (1990). Kinetics of deposition of colloidal particles in porous media. *Environ. Sci. Technol.*, 24. https://doi.org/10.1021/es00080a012.

Ellis, A. J. and Mahon, W. A. J. (1977). *Chemistry and geothermal systems*. Academic press.

Energy Institute (2024). Statistical review of world energy 73rd edition. Technical report, https://www.energyinst.org/.

Erzuah, S., Aggrey, W. N., Tetteh, J. T., Bodi, V., Adenutsi, C. D., Sokama-Neuyam, Y. A., Sarkodie, K., Ampomah, W., Ohemeng-Boahen, G., and Nyarko, K. B. (2023). Zeta potential prediction of dominant sandstone minerals via surface complexation modelling. *Scientific African*, 20. https://doi.org/10.1016/j.sciaf.2023.e01721.

Fan, K.-C., Gao, P.-J., Chen, B.-H., Han, Y.-L., and Cheng, C.-L. (2024). Development and application of a geothermal bio-tracer resistant to extreme environments. *Geothermics*, 119. https://doi.org/10.1016/j.geothermics.2024.102982.

Farooq, A., Shukur, A., Astley, C., Tosheva, L., Kelly, P., Whitehead, D., and Azzawi, M. (2018). Titania coating of mesoporous silica nanoparticles for improved biocompatibility and drug release within blood vessels. *Acta Biomater*, 76. https://doi.org/10.1016/j.actbio.2018.06.024.

Finster, M., Clark, C., Schroeder, J., and Martino, L. (2015). Geothermal produced fluids: Characteristics, treatment technologies, and management options. *Renewable and Sustainable Energy Reviews*, 50. https://doi.org/10.1016/j.rser.2015.05.059.

Fitts, D. D. (1966). Statistical mechanics: A study of intermolecular forces. *Annual Review of Physical Chemistry*, 17. https://doi.org/10.1146/annurev.pc.17.100166.000423.

Fleming, B. A. (1986). Kinetics of reaction between silicic acid and amorphous silica surfaces in NaCl solutions. *Journal of Colloid and Interface Science*, 110. https://doi.org/10.1016/0021-9797(86)90351-6.

Fleming, B. A. and Crear, D. A. (1982). Silicic acid ionization and calculation of silica solubility at elevated temperature and pH. application to geothermal fluid processing and reinjection. *Geothermics*, 11. https://doi.org/10.1016/0375-6505(82)90004-9.

Flury, M. and Qiu, H. (2008). Modeling colloid-facilitated contaminant transport in the vadose zone. *Vadose Zone Journal*, 7. https://doi.org/10.2136/vzj2007.0066.

Flury, M. and Wai, N. N. (2003). Dyes as tracers for vadose zone hydrology. *Reviews of Geophysics*, 41. https://doi.org/10.1029/2001RG000109.

Foppen, J. W. (2023). Artificial DNA in hydrology. *Water*, 10. https://doi.org/10.1002/wat2.1681.

Fournier, R. O. and Rowe, J. J. (1966). Estimation of unterground temperature. *AJS*, 264. https://doi.org/10.2475/ajs.264.9.685.

Fournier, R. O. and Rowe, J. J. (1977). The solubility of amorphous silica in water at high temperatures and high pressures. *American Mineralogist*, 62:1052–1056.

Franks, G. V. (2002). Zeta potentials and yield stresses of silica suspensions in concentrated monovalent electrolytes: isoelectric point shift and additional attraction. *J Colloid Interface Sci*, 249. https://doi.org/10.1006/jcis.2002.8250.

Franks, G. V., Johnson, S. B., Scales, P. J., Boger, D. V., and Healy, T. W. (1999). Ionic-specific strength of attractive particle networks. *Langmuir*, 15. https://doi.org/10.1021/la9815345.

French, R. H., Winey, K. I., Yang, M. K., and Qiu, W. (2007). Optical properties and van der Waals–London dispersion interactions of polystyrene determined by vacuum ultraviolet spectroscopy and spectroscopic ellipsometry. *Australian Journal of Chemistry*, 60. https://doi.org/10.1071/CH06222.

Fu, X. and Qutubuddin, S. (2001). Synthesis of titania-coated silica nanoparticles using a nonionic water-in-oil microemulsion. *Colloids and Surfaces A: Physicochemical and Engineering Aspects*, 179. https://doi.org/10.1016/S0927-7757(00)00723-8.

Gaboriaud, F., Nonat, A., Chaumont, D., and Craievich, A. (1999). Aggregation and gel formation basic silico-calco-alkaline solutions studied: A SAXS, SANS, and ELS study. *J. Phys. Chem. B*, 103. https://doi.org/10.1021/jp990151s.

Gallup, D., Sugiaman, F., Capuno, V., and Manceau, A. (2003). Laboratory investigation of silica removal from geothermal brines to control silica scaling and produce usable silicates. *Applied Geochemistry*, 18. https://doi.org/10.1016/S0883-2927(03)00077-5.

Gallup, D. L. (2002). Investigations of organic inhibitors for silica scale control in geothermal brines. *Geothermics*, 31. https://doi.org/10.1016/S0375-6505(02)00004-4.

Gallup, D. L. (2011). pH modification scale control technology. In *Proceedings International Workshop on Mineral Scaling*.

Gallup, D. L. and Barcelon, E. (2005). Investigations of organic inhibitors for silica scale control from geothermal brines-II. *Geothermics*, 34. https://doi.org/10.1016/j.geothermics.2005.09.002.

Gazem, A., Patel, H., Sreenivasan, H., Sahu, C., and Krishna, S. (2024). Combined effect of silica nanoparticles and binary surfactants in enhancing oil recovery: An experimental investigation. *Colloids and Surfaces A: Physicochemical and Engineering Aspects*, https://doi.org/10.1016/j.colsurfa.2024.134980.

Gerke, K. M., Sidle, R. C., and Mallants, D. (2013). Criteria for selecting fluorescent dye tracers for soil hydrological applications using uranine as an example. *Journal of Hydrology and Hydromechanics*, 61. https://doi.org/10.2478/johh-2013-0040.

Ghosh, S. K., Alargova, R. G., Deguchi, S., and Tsujii, K. (2006). Dispersion stability of colloids in sub- and supercritical water. *Journal of Physical Chemistry B*, 110. https://doi.org/10.1021/jp0656328.

Giggenbach, W. (1978). The isotopic composition of waters from the El Tatio geothermal field, Northern Chile. *Geochimica et Cosmochimica Acta*, 39. https://doi.org/10.2343/geochemj.39.547.

Gimenez, C., de la Torre, C., Gorbe, M., Aznar, E., Sancenon, F., Murguia, J. R., Martinez-Manez, R., Marcos, M. D., and Amoros, P. (2015). Gated mesoporous silica nanoparticles for the controlled delivery of drugs in cancer cells. *Langmuir*, 31. https://doi.org/10.1021/acs.langmuir.5b00139.

Goto, K. (1956). Effect of pH on polymerization of silicic acid. *Journal of Physical Chemistry*, 60. https://doi.org/10.1021/j150541a046.

Gratz, A. J. and Bird, P. (1993). Quartz dissolution: Theory of rough and smooth surfaces. *Geochimica et Cosmochimica Acta*, 57. https://doi.org/10.1016/0016-7037(93)90034-T.

Greenberg, S. A. (1956). The chemisorption of calcium hydroxide by silica. *J. Phys. Chem.*, 60. https://doi.org/10.1021/j150537a019.

Greenberg, S. A. and Price, E. W. (1957). The solubility of silica in solutions with electrolytes. *J. Phys. Chem.*, 61. https://doi.org/10.1021/j150557a019.

Gregory, J. (1970). The calculation of Hamaker constants. *Advances in Colloid and Interface Science*, 2. https://doi.org/10.1016/0001-8686(70)80002-1.

Gregory, J. (1981). Approximate expressions for retarded van der Waals interaction. *Journal of Colloid and Interface Science*, 83. https://doi.org/10.1016/0021-9797(81)90018-7.

Gregory, J. (1988). Polymer adsorption and flocculation in sheard suspensions. *Colloids and Surfaces*, 31. https://doi.org/10.1016/0166-6622(88)80196-3.

Grimmer, J., Ritter, J., Eisbacher, G., and Fielitz, W. (2017). The late variscan control on the location and asymmetry of the Upper Rhine Graben. *Int. J. Earth Sci.*, 106. https://doi.org/10.1007/s00531-016-1336-x.

Gubala, V., Giovannini, G., Kunc, F., Monopoli, M. P., and Moore, C. J. (2020). Dye-doped silica nanoparticles: synthesis, surface chemistry and bioapplications. *Cancer Nanotechnology*, 11. https://doi.org/10.1186/s12645-019-0056-x.

Gunnarsson, I. and Arnórsson, S. (2000). Amorphous silica solubility and the thermodynamic properties of H_4SiO_4 in the range of 0° to 350°C at p_{sat}. *Geochimica et Cosmochimica Acta*, 64. https://doi.org/10.1016/S0016-7037(99)00426-3.

Gunnarsson, I. and Arnórsson, S. (2003). Silica scaling: The main obstalce in efficient use of high-temperature geothermal fluids. In *International Geothermal Conference*.

Gunnarsson, I. and Arnórsson, S. (2005). Treatment of geothermal waste water to prevent silica scaling. In *Proceedings World Geothermal Congress*.

Guo, X.-C. and Dong, P. (1999). Multistep coating of thick titania layers on monodisperse silica nanospheres. *Langmuir*, 15. https://doi.org/10.1021/la990220u.

Gíslason, S. R., J., H. P., Veblen, D. R., and Livi, K. J. T. (1993). The difference between the solubility of quartz and chalcedony: the cause? *Chemical Geology*, 107.

Göppert, N. and Goldscheider, N. (2019). Improved understanding of particle transport in karst groundwater using natural sediments as tracers. *Water Reserach*, 166. https://doi.org/10.1016/j.watres.2019.115045.

Haghighatzadeh, A., Mazinani, B., and Abdolahpour Salari, M. (2017). Coating of ordered-large pore mesoporous silica with TiO_2 nanoparticles and evaluation of its photocatalytic activity. *Acta Phys. Pol. A*, 132. https://doi.org/10.12693/APhysPolA.132.420.

Hajareh Haghighi, F., Mercurio, M., Cerra, S., Salamone, T. A., Bianymotlagh, R., Palocci, C., Romano Spica, V., and Fratoddi, I. (2023). Surface modification of TiO_2 nanoparticles with organic molecules and their biological applications. *J Mater Chem B*, 11. https://doi.org/10.1039/d2tb02576k.

Halperin, M. L., Kamel, K. S., and Goldstein, M. B. (2010). Fluid, electrolyte & acid-base physiology. *Elsevier*.

Hamaker, H. C. (1937). The London—van der Waals attraction between spherical particles. *Physica*, 4. https://doi.org/10.1016/S0031-8914(37)80203-7.

Han, B., Anwar Ul Haq, R., and Louhi-Kultanen, M. (2020). Lithium carbonate precipitation by homogeneous and heterogeneous reactive crystallization. *Hydrometallurgy*, 195. https://doi.org/10.1016/j.hydromet.2020.105386.

Han, S., Kim, J., and Ko, S. H. (2021). Advances in air filtration technologies: structure-based and interaction-based approaches. *Materials Today Advances*, 9. https://doi.org/10.1016/j.mtadv.2021.100134.

Hanprasopwattana, A., Srinivasan, S., Sault, A. G., and Datye, A. K. (1996). Titania coatings on monodisperse silica spheres (characterization using 2-propanol dehydration and TEM). *Langmuir*, 12. https://doi.org/10.1021/la950808a.

Hardy, W. B. (1900). A preliminary investigation of the conditions which determine the stability of irreversible hydrosols. *Proceedings of the Royal Society of London*, 66. https://doi.org/10.1098/rspl.1899.0081.

Harris, M. T., Brunson, R. R., and Byers, C. H. (1992). The base catalyzed hydrolysis and condensation reactions of dilute and concentrated TEOS solutions. *Journal of Non-Crystalline Solids*, 121. https://doi.org/10.1016/0022-3093(90)90165-I.

Hartmann, R., Kinnunen, P., and Illikainen, M. (2018). Cellulose-mineral interactions based on the DLVO theory and their correlation with flotability. *Minerals Engineering*, 122. https://doi.org/10.1016/j.mineng.2018.03.023.

Hawkins, A. J., Becker, M. W., and Tester, J. W. (2018). Inert and adsorptive tracer tests for field measurement of flow-wetter surface area. *Water Resources Resarch*, 54. https://doi.org/10.1029/2017WR021910.

Hawkins, A. J., Bender, J. T., Grooms, R. D., Schissel, C. J., and Tester, J. W. (2021). Temperature-responsive smart tracers for field-measurement of inter-well thermal evolution: Heterogeneous kinetics and field demonstration. *Geothermics*, 92. https://doi.org/10.1016/j.geothermics.2021.102046.

He, Q., Shi, J., Zhu, M., Chen, Y., and Chen, F. (2010). he three-stage in vitro degradation behavior of mesoporous silica in simulated body fluid. *Microporous Mesoporous Mater*, 10. https://doi.org/10.1016/j.micromeso.2010.01.009.

He, X., Nie, H., Wang, K., Tan, W., Wu, X., and Zhang, P. (2008). In vivo study of biodistribution and urinary extrection of surface-modified silica nanoparticles. *Anal. Chem.*, 80. https://doi.org/10.1021/ac801882g.

Healy, T. W. and La Mer, V. K. (1964). The energetics of flocculation and redispersion by polymers. *Journal of Colloid Science*, 19. https://doi.org/10.1016/0095-8522(64)90034-0.

Hema, M., Yelil Arasi, A., Tamilselvi, P., and Anbarasan, R. (2013). Titania nanoparticles synthesized by sol-gel technique. *Chem. Sci. Trans.*, 2. https://doi.org/10.7598/cst2013.344.

Henley, W. R. (1983). pH and silica scaling control in geothermal field development. *Geothermics*, 12. https://doi.org/10.1016/0375-6505(83)90004-4.

Higgo, J. J. W., Williams, G. M., Harrison, I., Warwick, P., Gardiner, M. P., and Longworth, G. (1993). Colloid transport in a glacial sand aquifer. laboratory and field studies. *Colloids and Surfaces A: Physicochemical and Engineering Aspects*, 73. https://doi.org/10.1016/0927-7757(93)80015-7.

Hirayama, H., Amolegbe, S. A., Islam, M. S., Rahman, M. A., Goto, N., Sekine, Y., and Hayami, S. (2021). Encapsulation and controlled release of an antimalarial drug using surface functionalized mesoporous silica nanocarriers. *J. Mater. Chem. B*, 9. https://doi.org/10.1039/D1TB00954K.

Hogg, R., Healy, T. W., and Fuersteka, D. W. (1966). Mutual coagulation of colloidal dispersions. *Transactions of the Faraday Society*, 62. https://doi.org/10.1039/TF9666201638.

Holt, P. F. and King, D. T. (1955). The chemistry of silica surfaces. *Journal of the Chemical Society*, https://doi.org/10.1039/JR9550000773.

Hotze, E. M., Phenrat, T., and Lowry, G. V. (2010). Nanoparticle aggregation: Challenges to understanding transport and reactivity in the environment. *Journal of Environmental Quality*, 39. https://doi.org/10.2134/jeq2009.0462.

Hsu, W. P., Yu, R., and Matjevic, E. (1992). Paper whiteners: titania coated silica. *Journal of Colloid and Interface Science*, 156. http://dx.doi.org/10.1006/jcis.1993.1080.

Hu, J.-L., Qian, H.-S., Li, J.-J., Li, Z.-Q., and Yu, S.-H. (2013). Synthesis of mesoporous SiO_2@TiO_2 core/shell nanospheres with enhanced photocatalytic properties. *Part. Part. Syst. Character.*, 30. https://doi.org/10.1002/ppsc.201200110.

Huang, X., Teng, X., Chen, D., Tang, F., and He, J. (2010). The effect of the shape of mesoporous silica nanoparticles on cellular uptake and cell function. *Biomaterials*, 31. https://doi.org/10.1016/j.biomaterials.2009.09.060.

Hull, M. and Kitchener, J. A. (1969). Interaction of spherical colloidal particles with planar surfaces. *Trans. Faraday Soc.*, 65. https://doi.org/10.1039/TF9696503093.

Hájek, M., Jiménez-Alfaro, B., Hájek, O., Brancaleoni, L., Cantonati, M., Carbognani, M., Dedić, A., Díte, D., Gerdol, R., Hájková, P., Horsáková, V., Jansen, F., Kamberović,

J., Kapfer, J., Kolari, T., Lamentowicz, M., Lazarević, P., Masić, E., Moeslund, J., Pérez-Haase, A., Peterka, T., Petraglia, A., Pladevall-Izard, E., Plesková, Z., Segadelli, S., Semeniuk, Y., Singh, P., Símová, A., Smerdová, E., Tahvanainen, T., Tomaselli, M., Vystavna, Y., Bita-Nicolae, C., and Horsák, M. (2021). European map of groundwater pH and calcium. *Earth System Science Data*, 13. https://doi.org/10.5194/essd-13-1089-2021.

Icopini, G. A., Brantley, S. L., and Heaney, P. J. (2005). Kinetics of silica oligomerization and nanocolloid formation as a function of pH and ionic strength at 25°c. *Geochmicia et Cosmochimica Acta*, 69. https://doi.org/10.1016/j.gca.2004.06.038.

Iler, R. K. (1975). Coagulation of colloidal silica by calcium ions, mechanism, and effect of particle size. *Journal of Colloid and Interface Science*, 53.

Iler, R. K. (1979). *The chemistry of silica. Solubility, polymerization, colloid and surface properties, and biochemistry*. John Wiley & Sons.

Iler, R. K. and Dalton, R. L. (1956). Degree of hydration of particles of colloidal silica in aqueous solution. *Journal of Physical Chemistry*, 60. https://doi.org/10.1021/j150541a031.

IRENA and IGA (2023). Global geothermal market and technology assessment. Technical report, International Renewable Energy Agency, Abu Dhabi and International Geothermal Association, The Hague.

Ishida, N. and Craig, V. S. J. (2019). Direct measurement of interaction forces between surfaces in liquids using atomic force microscopy. *KONA Powder and Particle Journal*, 36. https://doi.org/10.14356/kona.2019013.

Ishido, T. and Mizutani, H. (1981). Experimental and theoretical basis of electrokinetic phenomena in rock-water systems and its applications to geophysic. *Journal of Geophysical Research*, 86. https://doi.org/10.1029/jb086ib03p01763.

Islam, S., Alshoaibi, A., Bakhtiar, H., Mazher, J., and Elshikeri, N. (2023). Solvent-assisted titania nanoparticles based fiber optic pH sensor: structural, optical, and sensing characteristics. *Journal of Sol-Gel Science and Technology*, 105. https://doi.org/10.1007/s10971-023-06037-6.

Ismail, M., Yahya, M. S., Idris, N. H., Mustafa, N. S. M., and Yap, M. F. A. A. H. (2020). *New Dimensions in Production and Utilization of Hydrogen*, chapter 14 Novel Materials and technologies for hydrogen storage. Elsevier.

Israelachvili, J. and Pashley, R. (1982). The hydrophobic interaction is long range, decaying exponentially with distance. *Nature*, 300. https://doi.org/10.1038/300341a0.

Izrael-Živković, L. T., Živković, L., Jokić, B. M., Savić, A. V., and Karadžić, I. M. (2015). Adsorption of *Candida rugosa* lipase onto alumina: effect of surface charge. *Journal of the Serbian Chemical Society*, 80. https://doi.org/10.2298/JSC150222035I.

Jafari, S., Derakhshankhah, H., Alaei, L., Fattahi, A., Varnamkhasti, B. S., and Saboury, A. A. (2019). Mesoporous silica nanoparticles for therapeutic/diagnostic applications. *Biomedicine & Pharmacotherapy*, 109. https://doi.org/10.1016/j.biopha.2018.10.167.

Jahanbin, A., Semprini, G., and Pulvirenti, B. (2022). Performance evaluation of U-tube borehole heat exchangers employing nanofluids as the heat carrier fluid. *Applied Thermal Engineering*, 212. https://doi.org/10.1016/j.applthermaleng.2022.118625.

Jeelani, P. G., Mulay, P., Venkat, R., and Ramalingam, C. (2020). Multifaceted application of silica nanoparticles. a review. *Silicon*, 12. https://doi.org/10.1007/s12633-019-00229-y.

Jia, F., Li, H., Liu, Z., Li, Y., Ma, X., Zhang, G., and Zhang, Q. (2024). Study on the adsorption mechanism of fluorescent nano-tracer in sandstone core. *Journal of Environmental Chemical Engineering*, 12. https://doi.org/10.1016/j.jece.2024.113560.

Jiang, L., Yu, Y., Li, Y., Yu, Y., Duan, J., Zou, Y., Li, Q., and Sun, Z. (2016). Oxidative damage and energy metabolism disorder contribute to the hemolytic effect of amorphous silica nanoparticles. *Nanoscale Res. Lett.*, 11. https://doi.org/10.1186/s11671-016-1280-5.

Johnston, J., Borrmann, T., Schweig, M., and Cairns, M. (2019). Developments in the nanostructured calcium silicate technology for preventing silica deposition and opening new business opportunities. In *GRC Transactions*.

Joo, J. B., Zhang, Q., Lee, I., Dahl, M., Zaera, F., and Yin, Y. (2012). Mesoporous anatase titania hollow nanostructures through silica-protected calcination, advanced functional materials. *Advanced Functional Materials*, 22. https://doi.org/10.1002/adfm.201101927.

Jorge, J., Castro, G. R., and Martines, M. A. U. (2013). Comparison among different pH values of rhodamine B solution impregnated into mesoporous silica. *Orbital: The Electronic Journal of Chemistry*, 5.

Jódar-Reyes, A. B., Martín-Rodríguez, A., and Ortega-Vinuesa, J. L. (2006). Effect of the ionic surfactant concentration on the stabilization/destabilization of polystyrene colloidal particles. *Journal of Colloid and Interface Science*, 298. https://doi.org/10.1016/j.jcis.2005.12.035.

Kahlenberg, L. and Lincoln, A. T. (1898). Solutions of silicates in the alkalies. *Journal of Physical Chemistry*, 2. https://doi.org/10.1021/j150002a001.

Kango, S., Kalia, S., Celli, A., Njuguna, J., Habibi, Y., and Kumar, R. (2013). Surface modification of inorganic nanoparticles for development of organic–inorganic nanocomposites—a review. *Progress in Polymer Science*, 38. https://doi.org/10.1016/j.progpolymsci.2013.02.003.

Karkare, M. M. (2014). Choice of precursor not affecting the size of anatase TiO_2 nanoparticles but affecting morphology under broader view. *International Nano Letters*, 4. https://doi.org/10.1007/s40089-014-0111-x.

Karni, M., Zidon, D., Zalevsky, Z., and Shefi, O. (2013). Thermal degradation of DNA. *DNA and Cell Biology*, 32. https://doi.org/10.1089/dna.2013.2056.

Kashpura, V. N. and Potapov, V. V. (2000). Study of the amorphous silica scales formation at the Mutnovskoe hydrothermal field (Russia). In *Proceedings 25th Workshop on Geothermal Reservoir Engineering*.

Kasnavia, T., Vu, D., and Sabatini, D. A. (1999). Fluorescent dye and media properties affecting sorption and tracer selection. *Ground Water*, 37. https://doi.org/10.1111/j.1745-6584.1999.tb01114.x.

Kato, K., Ueda, A., Mogi, K., Nakazawa, H., and Shimizu, K. (2003). Silica recovery from Sumikawa and Ohnuma geothermal brines (Japan) by addition of CaO and cationic precipitants in a newly developed seed circulation device. *Geothermics*, 32. https://doi.org/10.1016/S0375-6505(03)00019-1.

Kaya, A. and Yukselen-Aksoy, Y. (2011). Zeta potential of clay minerals and quartz contaminated by heavy metals. *Canadian Geotechnical Journal*, 42. https://doi.org/10.1139/t05-048.

Kersting, M., Olejnik, M., Rosenkranz, N., Loza, K., Breisch, M., Rostek, A., Westphal, G., Bunger, J., Ziegler, N., Ludwig, A., Koller, M., Sengstock, C., and Epple, M. (2020). Subtoxic cell responses to silica particles with different size and shape. *Sci. Rep.*, 10. https://doi.org/10.1038/s41598-020-78550-5.

Kesler, S., Gruber, P., Medina, P., Keoleian, G., Everson, M., and Wallington, T. (2012). Global lithium resources: Relative importance of pegmatite, brine and other deposits. *Ore Geology Reviews*, 48. https://doi.org/10.1016/j.oregeorev.2012.05.006.

Kessler, J. H. and Hunt, J. R. (1994). Dissolved and colloidal contaminant transport in a partially clogged fracture. *Water Resources Research*, 30. https://doi.org/10.1029/93WR03555.

Khlebovich, M. L. (2015). Applied aspects of the concept of critical salinity. *Biology Bulletin Reviews*.

Kianfar, B., Hassanizadeh, S., Abdelrady, A., Bogaard, T., and Foppen, J. W. (2023). Natural organic matter and ionic strength ($CaCl_2$) affect transport, retention and remobilization of silica encapsulated DNA colloids (DNAcol) in saturated sand columns. *Colloids and Surfaces A: Physicochemical and Engineering Aspects*, 678. https://doi.org/10.1016/j.colsurfa.2023.132476.

Kianfar, B., Tian, J., Rozemeijer, J., van der Zaanm B, Bogaard, T. A., and Foppen, J. W. (2022). Transport characteristics of DNA-tagged silica colloids as a colloidal tracer in saturated sand columns; role of solution chemistry, flow velocity, and sand grain size. *Journal of Contaminant Hydrology*, 246. https://doi.org/10.1016/j.jconhyd.2022.103954.

Kim, J., Kim, H. S., Lee, N., Kim, T., Kim, H., Yu, T., Song, I. C., Moon, W. K., and Hyeon, T. (2008). Multifunctional uniform nanoparticles composed of a magnetite nanocrystal core and a mesoporous silica shell for magnetic resonance and fluorescence imaging and for drug delivery. *Angew Chem Int Ed Engl*, 47. https://doi.org/10.1002/anie.200802469.

Kittilä, A., Jalali, M. R., Evans, K. F., Willmann, M., Saar, M. O., and Kong, X.-Z. (2019). Field comparison of DNA-labeled nanoparticle and solute tracer transport in a fracture crystalline rock. *Water Resources Research*, 55. https://doi.org/10.1029/2019WR025021.

Kiyota, Y. and Uchiyama, N. (2011). Silica scale prevention effects of brine pH modification at Hatchobaru power station, Japan. In *Proceedings International Workshop on Mineral Scaling.*

Klaine, S. J., Alvarez, P. J. J., Batley, G. E., Fernandes, T. F., Handy, R. D., Lyon, D. Y., Mahendra, S., McLaughlin, M. J., and Lead, J. R. (2009). Nanomaterials in the environment: Behavior, fate, bioavailability and effects. *Environmental Toxicology and Chemistry*, 27. https://doi.org/10.1897/08-090.1.

Kley, M., Kempter, A., Boyko, V., and Huber, K. (2017). Silica polymerization from supersaturated dilute aqueous solutions in the presence of alkaline earth salts. *Langmuir*, 33. https://doi.org/10.1021/acs.langmuir.7b00887.

Klonis, N. and Sawyer, W. H. (1996). Spectral properties of the prototropic forms of fluorescein in aqueous solution. *Journal of Fluorescence*, 6. https://doi.org/10.1007/BF00732054.

Knop, A. (1878). Ueber die hydrographischen Beziehungen zwischen der Donau und der Aachquelle im Badischen Oberlande (Schluss). *Neues Jahrbuch für Mineralogie, Geologie und Paläontologie*.

Koch, J., Doswald, S., Mikutis, G., Stark, W. J., and Grass, R. N. (2021). Ecotoxicological assessment of DNA-tagged silica particles for environmental tracing,. *Environ. Sci. Technol.*, 18. https://doi.org/10.1021/acs.est.0c07968.

Kong, X.-Z., Deuber, C. A., Kittilä, A., Somogyvári, M., Mikutis, G., Bayer, P., Stark, W. J., and Saar, M. O. (2018). Tomographic reservoir imaging with DNA-labeled silica nanotracers: The first field validation. *Environ. Sci. Technol.*, 52. https://doi.org/10.1021/acs.est.8b04367.

Korom, S. F. and Seaman, J. C. (2012). When "conservative" anionic tracers aren't. *Groundwater*, https://doi.org/10.1111/j.1745-6584.2012.00950.x.

Korzeniowska, B., Nooney, R., Wencel, D., and McDonagh, C. (2013). Silica nanoparticles for cell imaging and intracellular sensing. *Nanotechnology*, 24. https://doi.org/10.1088/0957-4484/24/44/442002.

Krauskopf, K. B. (1956). Dissolution and precipitation of silica at low temperatures. *Geochimica et Cosmochimica Acta*, 10. https://doi.org/10.1016/0016-7037(56)90009-6.

Kresge, C. T., Leonowicz, M. E., Roth, W. J., Vartuli, J. C., and Beck, J. S. (1992). Ordered mesoporous molecular sieves synthesized by liquid-crystal template mechanism. *Letters to Nature*, 359. https://doi.org/10.1038/359710a0.

Kristjánsson, B. R., Axelsson, G., Gunnarsson, G., Gunnarsson, I., and Óskarsson, F. (2016). Comprehensive tracer testing in the Hellideidi geothermal field SW-Iceland. In *41st Workshop on Geothermal Reservoir Engineering*.

Kristmannsdóttir, H. (1989). Types of scaling occuring by geothermal utilization in Iceland. *Geothermics*, 18. https://doi.org/10.1016/0375-6505(89)90026-6.

Kumar, P. S. M., Francis, A. P., and Devasena, T. (2014). Biosynthesized and chemically synthesized titania nanoparticles: Comparative analysis of antibacterial activity. *J. Environ. Nanotechnol.*, 3. https://doi.org/10.13074/jent.2014.09.143098.

Kwon, S., Singh, R. K., Perez, R. A., Abou Neel, E. A., Kim, H. W., and Chrzanowski, W. (2013). Silica-based mesoporous nanoparticles for controlled drug delivery. *J. Tissue Eng.*, 4. https://doi.org/10.1177/2041731413503357.

Käß, W. (2004). *Geohydrologische Markierungstechnik*. Borntraeger.

LaMer, V. K. and Dinegar, R. H. (1950). Theory, production and mechanism of formation of monodispersed hydrosols. *Journal of the American Chemical Society*, 72. https://doi.org/10.1021/ja01167a001.

Lau, H. C., Yu, M., and Nguyen, Q. P. (2017). Nanotechnology for oilfield applications: Challenges and impact. *Journal of Petroleum Science and Engineering*, 157. https://doi.org/10.1016/j.petrol.2017.07.062.

Lebedev, V. A., Kozlov, D. A., Kolesnik, I. V., Poluboyarinov, A. S., Becerikli, A. E., Grünert, W., and Garshev, A. V. (2016). The amorphous phase in titania and its influence on photocatalytic properties. *Applied Catalysis B: Environmental*, https://doi.org/10.1016/j.apcatb.2016.05.010.

Lee, C.-G., Alvarez, P., Kim, H.-G., Jeong, S., Lee, S., Lee, K., Lee, S.-H., and Choi, J.-W. (2018). Phosphorous recovery from sewage sludge using calcium silicate hydrates. *Chemosphere*, 193. https://doi.org/10.1016/j.chemosphere.2017.11.129.

Lefèvre, G. and Jolivet, A. (2009). Calculation of Hamaker constants applied to the deposition of metallic oxide particles at high temperature. In *Proceedings of International Conference on Heat Exchanger Fouling and Cleaning VIII*.

Leibundgut, C. (1974). Fluoreszierende Markierfarbstoffe in der Hydrologie: ein Beitrag zur Methodik und praktischen Anwendung. *Mitteilungen der Naturforschenden Gesellschaft in Bern*, 31. https://doi.org/10.5169/seals-319586.

Li, J. and Yuan, Y. J. (2014). Physisorption and chemisorption of a self-assembled monolayer by the quartz crystal microbalance. *Langmuir*, 30. https://doi.org/10.1021/la5020187.

Li, S., Ng, Y. H., Lau, H. C., Torsaeder, O., and Stubbs, L. P. (2020). Experimental investigation of stability of silica nanoparticles at reservoir conditions for Enhanced Oil-Recovery applications. *Nanomaterials*, 10. https://doi.org/10.3390/nano10081522.

Li, Y. and Kim, S.-J. (2005). Synthesis and characterization of nano titania embedded in mesoporous silica with both high photocatalytic activity and adsorption capability. *J. Phys. Chem. B*, 109. https://doi.org/10.1021/jp0512917.

Li, Y. V., Cathles, L. M., and Archer, L. A. (2014). Nanoparticle tracers in calcium carbonate porous media. *Journal of Nanoparticle Research*, 16. https://doi.org/10.1007/s11051-014-2541-9.

Li, Z., Hou, B., Xu, Y., Wu, D., Sun, Y., Hu, W., and Deng, F. (2005). Comparative study of sol-gel-hydrothermal and sol-gel synthesis of titania-silica composite nanoparticles. *Journal of Solid State Chemistry*, 178. https://doi.org/10.1016/j.jssc.2004.12.034.

Li, Z., Zhang, Y., and Feng, N. (2019). Mesoporous silica nanoparticles: synthesis, classification, drug loading, pharmacokinetics, biocompatibility, and application in drug delivery. *Expert Opinion on Drug Delivery*, https://doi.org/10.1080/17425247.2019.1575806.

Liao, R., P., Y., Wu, W., Luo, D., and Yang, D. (2018). A DNA tracer system for hydrological environment investigations. *Environ. Sci. Technol.*, 52. https://doi.org/10.1021/acs.est.7b02928.

Liberman, A., Mendez, N., Trogler, W. C., and Kummel, A. C. (2014). Synthesis and surface functionalization of silica nanoparticles in nanomedicine. *Surf. Sci. Rep.*, 69. https://doi.org/10.1016/j.surfrep.2014.07.001.

Lin, B. and Zhou, S. (2017). Poly(ethylene glycol)-grafted silica nanoparticles for highly hydrophilic acrylic-based polyurethane coatings. *Progress in Organic Coatings*, 106. https://doi.org/10.1016/j.porgcoat.2017.02.008.

Lin, M., Premuzic, E., Dong, B., Zhou, W., and Johnson, S. (2003). Recent advances in the development and commercialisation of geothermal silica products. In *GRC Transactions*.

Lin, M., Premuzic, E., Zhou, W., Dong, B., DeRocher, T., and Johnson, S. (2002). Silica recovery: A promising option to reduce geothermal power plant production costs. In *GRC Transaction*.

Lin, W., Huang, Y.-W., Zhou, X. D., and Ma, Y. (2006). In vitro toxicity of silica nanoparticle sin human lung cancer cells. *Toxicol. Appl. Pharamocl.*, 217. https://doi.org/10.1016/j.taap.2006.10.004.

Lin, Y. S., Abadeer, N., and L., H. C. (2011). Stability of small mesoporous silica nanoparticles in biological media. *Chem. Commun. (Camb.)*, 47. https://doi.org/10.1039/C0CC02923H.

Lin, Y. S., Hurley, K. R., and Haynes, C. L. (2012). Critical considerations in the biomedical use of mesoporous silica nanoparticles. *J Phys Chem Lett*, 3. https://doi.org/10.1021/jz2013837.

Lindén, M. (2018). Biodistribution and excretion of intravenously injected mesoporous silica nanoparticles: Implications for drug delivery efficiency and safety. *Enzymes*, 43. https://doi.org/10.1016/bs.enz.2018.07.007.

Liong, M. L., Kovochich, M., Xia, T., Ruehm, S. G., Nel, A. E., Tamanoi, F., and Zink, J. I. (2008). Multifunctional inorganic nanoparticles for imaging, targeting and drug delivery,. *ACS Nano*, 2. https://doi.org/10.1021/nn800072t.

Liu, D., Johnson, P. R., and Elimelech, M. (1995). Colloid deposition dynamics in flow through porous media: Role of electrolyte concentration. *Environ. Sci. Technol.*, 29. https://doi.org/10.1021/es00012a012.

Liu, G., Zhong, H., Ahmad, Z., Yang, X., and Huo, L. (2020). Transport of engineered nanoparticles in porous media and its enhancement for remediation of contaminated groundwater. *Critical Reviews in Environmental Science and Technology*, 50. https://doi.org/10.1080/10643389.2019.1694823.

Liu, Q., Sun, Z., and Santamarina, J. C. (2019). Transport and adsorption of silica nanoparticles in carbonate reservoirs: A sand column study. *Energy & Fuels*, 33. https://doi.org/10.1021/acs.energyfuels.9b00057.

Liu, T., Li, L., Teng, X., Huang, X., Liu, H., Chen, D., Ren, J., and Tang, F. (2011). Single and repeated dose toxicity of mesoporous hollow silica nanoparticles in intravenously exposed mice. *Biomaterials*, 32. https://doi.org/10.1016/j.biomaterials.2010.10.035.

Loosli, F. and Stoll, S. (2017). Effect of surfactants, pH and water hardness on the surface properties and agglomeration behavior of engineered TiO_2 nanoparticles. *Environmental Science: Nano*, 4. https://doi.org/10.1039/c6en00339g.

Lucas, C. C. and Dolan, M. E. (1939). Studies on the solubility of quartz and silicates. *The Canadian Medical Association Journal*, 40.

Lund, J. W., Bjelm, L., Bloomquist, G., and Mortensen, A. K. (2008). Characteristics, development and utilization of geothermal resources - a Nordic perspective. *Episodes*, 31. https://doi.org/10.18814/epiiugs/2008/v31i1/019.

Lunevich, L. (2019). Aqueous silica and silica polymerization. *Desalination - Challenges and Opportunities*, https://doi.org/10.5772/intechopen.84824.

Lunge, C. and Millberg, C. (1897). Über das Verhalten der verschiedenen Arten von Kieselsäure zu kaustischen und kohlensauren Alkalien. *Zeitschrift für Angewandte Chemie*, 14.

Luttrell, T., Halpegamage, S., Tao, J., Kramer, A., Sutter, E., and Batzill, M. (2014). Why is anatase a better photocatalyst than rutile? Model studies on epitaxial TiO_2 films. *Sci Rep*, 4. https://doi.org/10.1038/srep04043.

Ma, X.-K., Lee, N.-H., Oh, H.-J., Kim, J.-O., Rhee, C.-K., Park, K.-S., and Kim, S.-J. (2010). Surface modification and characterization of highly dispersed silica nanoparticles by a cationic surfactant. *Colloids and Surfaces A: Physicochemical and Engineering Aspects*, 358. https://doi.org/10.1016/j.colsurfa.2010.01.051.

Magal, E., Weisbrod, N., Yakirevich, A., and Yechieli, Y. (2008). The use of fluorescent dyes as tracers in highly saline groundwater. *Journal of Hydrology*, 358. https://doi.org/10.1016/j.jhydrol.2008.05.035.

Maggini, L., Cabrera, I., Ruiz-Carretero, A., Prasetyanto, E. A., Robinet, E., and de Cola, L. (2016). Breakable mesoporous nanoparticles for targeted drug delivery. *Nanoscale*, 8. https://doi.org/10.1039/C5NR09112H.

Mahmud, H. B., Tan, B. C., Giwelli, A., Al-Rubaye, A. F., and Shafiq, M. U. (2021). Numerical analysis of SiO_2-SDS surfactant effect on oil recovery in sandstone reservoirs. *Energy Geoscience*, 2. https://doi.org/10.1016/j.engeos.2021.06.003.

Mahon, E., Hristov, D. R., and Dawson, K. A. (2012). Stabilising fluorescent silica nanoparticles against dissolution effects for biological studies. *Chemical Communications*, 48. https://doi.org/10.1039/C2CC34023B.

Mahtabani, A., Rytölutu, I., Anyszka, R., He, X., Saarimäki, E., Lahti, K., M., P., Dierkes, W., and Blume, A. (2020). On the silica surface modification and its effect on charge trapping and transport in PP-based dielectric nanocomposites. *ACS Appl. Polym. Mater.*, 2. https://doi.org/10.1021/acsapm.0c00349.

Maier, F., Schaffer, M., , and Licha, T. (2015). Temperature determination using thermosensitive tracers. Experimental validation in an isothermal column heat exchanger. *Geothermics*, 53. https://doi.org/10.1016/j.geothermics.2014.09.007.

Maimoni, A. (1982). Minerals recovery from salton sea geothermal brines: A literature review and proposed cementation process. *Geothermics*, 11. https://doi.org/10.1016/0375-6505(82)90031-1.

Manzano, M. and Vallet-Regí, M. (2020). Mesoporous silica nanoparticles for drug delivery. *Advanced Functional Materials*, 30. https://doi.org/10.1002/adfm.201902634.

Maraghechi, H., Rajabipour, F., Pantano, C., and Burgos, W. (2016). Effect of calcium on dissolution and precipitation reactions of amorphous silica at high alkalinity. *Cement and Concrete Research*, 87. https://doi.org/10.1016/j.cemconres.2016.05.004.

Marshall, J. K. and Kitchener, J. A. (1966). The deposition of colloidal particles on smooth solids. *Journal of Colloid and Interface Science*, 22. https://doi.org/10.1016/0021-9797(66)90014-2.

Marshall, W. L. (1980a). Amorphous silica solubilities-I. Behavior in aqueous sodium nitrate solutions; 25-300°C, 0-6 molal. *Geochmicia et Cosmochimica Acta*, 44. https://doi.org/10.1016/0016-7037(80)90280-X.

Marshall, W. L. (1980b). Amorphous silica solubilities-III. Activity coefficient relations and predictions of solubility behavior in salt solutions, 0-350°C. *Geochmicia et Cosmochimica Acta*, 44. https://doi.org/10.1016/0016-7037(80)90282-3.

Marshall, W. L. and Chen, C.-T. A. (1982). Amorphous silica solubilities V. Predictions of solubility behavior in aqueous mixed electrolyte solutions to 300°C. *Geochimica et Cosmochimica Acta*, 46. https://doi.org/10.1016/0016-7037(82)90256-3.

Marshall, W. L. and Warakomski, J. M. (1980). Amorphous silica solubilities - II Effect of aqueous salt solutions at 25°C. *Geochimica et Cosmochimica Acta*, 44. https://doi.org/10.1016/0016-7037(80)90281-1.

Mathieux, F., Ardente, F., Bobba, S., Nuss, P., Blengini, G., Alves, P., Blagoeva, D., Torres de Matos, C., Wittmer, D., Pavel, C., and Solar, S. V. (2017). Critical raw materials and the circular econocmics: JRC science for policy report: background report. Technical report, Publication Office of the European Union.

Małoszewski, P. and Zuber, A. (1985). On the theory of tracer experiments in fissured rocks with a porous matrix. *Journal of Hydrology*, 79. https://doi.org/10.1016/0022-1694(85)90064-2.

McDowell, L. M., Hunt, J. R., and Sitar, N. (1986). Particle transport through porous media. *Water Resources Resarch*, 22. https://doi.org/10.1029/WR022i013p01901.

Mendiratta, S., Hussein, M., Nasser, H. A., and Ali, A. A. A. (2019). Multidisciplinary role of mesoporous silica nanoparticles in brain regeneration and cancers: From crossing the blood–brain barrier to treatment. *Particle & Particle Systems Characterization*, 36. https://doi.org/10.1002/ppsc.201900195.

Mikutis, G., Deuber, C. A., Schmid, L., Kittilä, A., Lobsiger, N., Puddu, M., Asgeirsson, D. O., Grass, R. N., Saar, M. O., and Stark, W. J. (2018). Silica-encapsulated DNA-based tracers for aquifer characterization. *Environ. Sci. Technol.*, 52. https://doi.org/10.1021/acs.est.8b03285.

Milne, N., O'Reilly, T., Sanciolo, P., Ostarcevic, E., Beighton, M., Taylor, K., Mullett, M., Tarquin, A., and Gray, S. (2014). Chemistry of silica scale mitigation for RO desalination with particular reference to remote operations. *Water Research*, 65. https://doi.org/10.1016/j.watres.2014.07.010.

Missana, T. and Adell, A. (2000). On the applicability of DLVO theory to the prediction of clay colloids stability. *Journal of Colloid and Interface Science*, 230. https://doi.org/10.1006/jcis.2000.7003.

Mohammadpour, R., Cheney, D. L., Grunberger, J. W., Yazdimamaghani, M., Jedrzkiewicz, J., Isaacson, K. J., Dobrovolskaia, M. A., and Ghandehari, H. (2020). One-year chronic toxicity evaluation of single dose intravenously administered silica nanoparticles in mice and their ex vivo human hemocompatibility,. *J. Control. Release*, 324. https://doi.org/10.1016/j.jconrel.2020.05.027.

Mohammadpour, R., Yazdimamaghani, M., Cheney, D. L., Jedrzkiewicz, J., and Ghandehari, H. (2019). Subchronic toxicity of silica nanoparticles as a function of size and porosity. *J. Control. release*, 304. https://doi.org/10.1016/j.jconrel.2019.04.041.

Molengraf, G. A. F. (1888). Studien über Quarz. *Zeitschrift für Kristallographie*, 14. https://doi.org/10.1524/zkri.1888.14.1.173.

Morey, G. W., Fournier, R. O., and Rowe, J. J. (1962). The solubility of quartz in water in the temperature interval from 25° to 300°C. *Geochimica et Cosmochimica Acta*, 26. https://doi.org/10.1016/0016-7037(62)90027-3.

Mori, U., Unami, S., Yanaze, T., Yokoyama, T., Tsukamoto, K., Kusakabe, M., Marumo, K., and Ueda, A. (2019). Observation of silica nanoparticle growth in saline geothermal brine from the Yamagawa geothermal power station, Japan, using dynamic light

scattering. *Geothermics*, 82. https://doi.org/10.1016/j.geothermics.2019.06.010.

Morita, M., Goto, Y., Motoda, S., and Fujino, T. (2017). Thermodynamic analysis of silica-based scale precipitation induced by magnesium ion. *Journal of the Geothermal Research Society of Japan*, 39. https://doi.org/10.11367/grsj.39.191.

Mozafarinia, M., Karimi, S., Farrokhnia, M., and Esfandiari, J. (2021). In vitro breast cancer targeting using trastuzumab-conjugated mesoporous silica nanoparticles: towards the new strategy for decreasing size and high drug loading capacity for drug delivery purposes in msn synthesis. *Microporous and Mesoporous Mater.*, 316. https://doi.org/10.1016/j.micromeso.2021.110950.

Mpelwa, M. and Tang, S. F. (2019). State of the art of synthetic threshold scale inhibitors for mineral scaling in the petroleum industry: a review. *Petroleum Science*, 2. https://doi.org/10.1007/s12182-019-0299-5.

Mroczek, E., Climo, M., Li, Y., Evans, D., Carey, B., and Gao, W. (2015). From waste to wealth: Mineral extraction from geothermal brines. In *World Geothermal Congress*.

Mueller, R., Mädler, L., and Pratsinis, S. E. (2003). Nanoparticle synthesis at high production rates by flame spray pyrolysis. *Chemical Engineering Science*, 58. https://doi.org/10.1016/S0009-2509(03)00022-8.

Muneer, R., Rehan Hashmet, M., and Pourafshary, P. (2020). Fine migration control in sandstones: Surface force analysis and application of DLVO theory. *ACS Omega*, 5. https://doi.org/10.1021/acsomega.0c03943.

Murashkevich, A. N., Lavitskaya, A. S., Barannikvoa, T. I., and Zharskii, I. M. (2008). Infrared absorption spectra and structure of TiO_2-SiO_2 composites. *Journal of Applied Spectroscopy*, 75. https://doi.org/10.1007/s10812-008-9097-3.

Murugadoss, S., Lison, D., Godderis, L., van den Brule, S., Mast, J., Brassinne, F., Sebaihi, N., and Hoet, P. H. (2017). Toxicology of silica nanoparticles: an update. *Arch. Toxicol.*, 91. https://doi.org/10.1007/s00204-017-1993-y.

Möller, K. and Bein, T. (2019). Degradable drug carriers: Vanishing mesoporous silica nanoparticles. *Chem. Mater.*, 31. https://doi.org/10.1021/acs.chemmater.9b00221.

Müller, Y. K., Goldscheider, N., Eiche, E., Emberger, H., and Göppert, N. (2023). From cave to spring: Understanding transport of suspended sediment particles in a fully phreatic karst conduit using particle analysis and geochemical methods. *Hydrological Processes*, 37. https://doi.org/10.1002/hyp.14979.

Napper, D. H. (1977). Steric stabilization. *Journal of Colloid and Interface Science*, 58. https://doi.org/10.1016/0021-9797(77)90150-3.

Napper, D. H. and Netschey, A. (1971). Studies of the steric stabilization of colloidal particles. *Journal of Colloid and Interface Science*, 37. https://doi.org/10.1016/0021-9797(71)90330-4.

Nasralla, R. A. and Nasr-El-Din, H. A. (2012). Double-layer expansion: Is it a primary mechanism of improved oil recovery by low-salinity waterflooding? In *SPE Improved Oil Recovery Symposium,*, volume https://doi.org/10.2118/154334-MS.

Natarajan, S. K. and Selvaraj, S. (2014). Mesoporous silica nanoparticles: importance of surface modifications and its role in drug delivery. *RSC Adv.*, 4. https://doi.org/10.1039/c4ra00781f.

Nayl, A. A., Abd-Elhamid, A. I., Aly, A. A., and Bräse, S. (2022). Recent progress in the applications of silica-based nanoparticles. *RSC Adv.*, 12. https://doi.org/10.1039/d2ra01587k.

Neofotistou, E. and Demadis, K. D. (2004). Silica scale inhibition by polyaminoamide STARBURST® dendrimers. *Colloids and Surfaces A: Physicochemical and Engineering Aspects*, 242. https://doi.org/10.1016/j.colsurfa.2004.04.067.

Neupane, G. and Wendt, D. S. (2017). Assessment of mineral resources in geothermal brines in the US. In *Proceedings 42nd Workshop on Geothermal Reservoir Engineering*.

Ninham, B. W. (1999). On progress in forces since the DVLO theory. *Advances in Colloid and Interface Science*, 83. https://doi.org/10.1016/S0001-8686(99)00008-1.

Nitschke, F., Held, S., Villalon, I., Neumann, T., and Kohl, T. (2017). Asessment of performance and parameter sensitivity of multicomponent geothermometry applied to a medium enthalpy geothermal system. *Geothermal Energy,*, 5. https://doi.org/10.1186/s40517-017-0070-3.

Nitschke, F., Scheiber, J., Kramar, U., and Kohl, T. (2014). Formation of alternating layered Ba-Sr-sulfate and Pb-sulfide scaling in the geothermal plant of Soultz-sous-Forêts. *N. Jb. Miner. Abh. (J. Min. Geochem.)*, 191. https://doi.org/10.1127/0077-7757/2014/0253.

Nordström, J., Nilsson, E., Jarvol, P., Nayeri, M., Palmqvist, A., Bergenholtz, J., and matic, A. (2011). Concentration- and pH-dependence of highly alkaline sodium silicate solutions. *Journal of Colloid and Interface Science*, 356. https://doi.org/10.1016/j.jcis.2010.12.085.

Nottebohm, M., Licha, T., and Sauter, M. (2012). Tracer design for tracking thermal fronts in geothermal reservoirs. *Geothermics*, 43. https://doi.org/10.1016/j.geothermics.2012.02.002.

Okamoto, G., Okura, T., and Goto, K. (1957). Properties of silica in water. *Geochimica et Cosmochimica Acta*, 12. https://doi.org/10.1016/0016-7037(57)90023-6.

Ow, H., Larson, D. R., Srivastava, M., Baird, B. A., Webb, W. W., and Wiesner, U. (2005). Bright and stable core-shell fluorescent silica nanoparticles. *Nano Letters*, 5. https://doi.org/10.1021/nl0482478.

Paris, J. L., Colilla, M., Izquierdo-Barba, I., Manzano, M., and Vallet-Regí, M. (2017). Tuning mesoporous silica dissolution in physiological environments: a review. *Journal of Material Science*, 52. https://doi.org/10.1007/s10853-017-0787-1.

Paris, J. L., Manzano, M., Cabañas, M. V., and Vallet-Regí, M. (2018). Mesoporous silica nanoparticles engineered for ultrasound-induced uptake by cancer cells. *Nanoscale*, 10. https://doi.org/10.1039/C8NR00693H.

Park, C., Lee, K., and Kim, C. (2009). Photoresponsive cyclodextrin-covered nanocontainers and their sol-gel transition induced by molecular recognition. *Angewandte Chemie International Edition*, 48. https://doi.org/10.1002/anie.200803880.

Park, J. T., Seo, J. A., Ahn, S. H., Kim, J. H., and Kang, S. W. (2010). Surface modification of silica nanoparticles with hydrophilic polymers. *Journal of Industrial and Engineering Chemistry*, 16. https://doi.org/10.1016/j.jiec.2010.03.030.

Park, M. V. D. Z., Lynch, I., Ramírez-García, S., Dawson, K. A., de la Fonteyne, L., Gremmer, E., Slob, W., Briedé, J. J., Elsaesser, A., Howard, C. V., van Loveren, H., and de Jong, W. H. (2011). In vitro evaluation of cytotoxic and inflammatory properties of silica nanoparticles of different sizes in murine RAW 264.7 macrophages. *Journal of Nanoparticle Research*, 13. https://doi.org/10.1007/s11051-011-0586-6.

Parsons, D. F., Bostrom, M., Maceina, T. J., Salis, A., and Ninham, B. W. (2010). Why direct or reversed Hofmeister series? Interplay of hydration, non-electrostatic potentials, and ion size. *Langmuir*, 26. https://doi.org/10.1021/la903061h.

Pashley, R. M. and Israelachvili, J. N. (1984). Molecular layering of water in thin films between mica surfaces and its relation to hydration forces. *Journal of Colloid and Interface Science*, 101. https://doi.org/10.1016/0021-9797(84)90063-8.

Paunescu, D., Puddu, M., Soellner, J. O., Stoessel, P. R., and Grass, R. N. (2013). Reversible DNA encapsulation in silica to produce ROS-resistant and heat-resistant synthetic DNA 'fossils'. *Nat. Protoc.*, 8. https://doi.org/10.1038/nprot.2013.154.

Phenrat, T., Saleh, N., Sirk, K., Tilton, R. D., and Lowry, G. V. (2007). Aggregation and sedimentation of aqueous nanoscale zerovalent iron dispersions. *Environ. Sci. Technology*, 41. https://doi.org/10.1021/es061349a.

Phillips, S., Mathur, A., and Garrison, W. (1980). Treatment methods for geothermal brines. *American Society for Testing and Materials*, https://doi.org/10.1520/stp30074s.

Pianegonda, S., Barbosa, M. C., and Levin, Y. (2005). Charge reversal of colloidal particles. *Europhysics Letters (EPL)*, 71. https://doi.org/10.1209/epl/i2005-10150-y.

Pinchuk, P. and Jiang, K. (2015). Size-dependent Hamaker constant for silver and gold nanoparticles. In *Proceedings Volume 9549, Physical Chemistry of Interfaces and Nanomaterials XIV*, volume https://doi.org/10.1117/12.2187282.

Pineda-Aguilar, N., Garza-Tovar, L. L., Sánchez-Cervantes, E. M., and Sánchez-Domínguez, M. (2018). Preparation of TiO_2–(B) by microemulsion mediated hydrothermal method: effect of the precursor and its electrochemical performance. *Journal of Material Science: Materials in Electronics*, 29. https://doi.org/10.1007/s10854-018-9085-1.

Pochapski, D. J., Carvalho Dos Santos, C., Leite, G. W., Pulcinelli, S. H., and Santilli, C. V. (2021). Zeta potential and colloidal stability predictions for inorganic nanoparticle

dispersions: Effects of experimental conditions and electrokinetic models on the interpretation of results. *Langmuir*, 37. https://doi.org/10.1021/acs.langmuir.1c02056.

Pradel, A., Catrouillet, C., and Gigault, J. (2023). The environmental fate of nanoplastics: what we know and what we need to know about aggregation. *NanoImpact*, 29. https://doi.org/10.1016/j.impact.2023.100453.

Proksch, E. (2018). pH in nature, humans and skin. *J. Dermatol.*, 45. https://doi.org/10.1111/1346-8138.14489.

Puddu, M., Mikutis, G., Stark, W. J., and Grass, R. N. (2016). Submicrometer-sized thermometer particles exploiting selective nucelic acid stability. *Small*, 12. https://doi.org/10.1002/smll.201502883.

Putera, A. D. P., Wiranda, A., Meriana, S., Perdana, I., and Olvianas, M. (2018). Assessing silica precipitation using calcium hydroxide addtion on Dieng's geothermal brine. In *IOP Conference Series: Earth and Environmental Science 200*.

Pérez, H., Miranda, R., Saavedra-Leos, Z., Zarraga, R., Alonso, P., Moctezuma, E., and Martínez, J. (2020). Green and facile sol–gel synthesis of the mesoporous SiO_2–TiO_2 catalyst by four different activation modes. *RSC Adv.*, https://doi.org/10.1039/D0RA07569H.

Qiao, B., Liang, Y., Wang, T.-J., and Jiang, Y. (2016). Surface modification to produce hydrophobic nano-silica particles using sodium dodecyl sulfate as a modifier. *Applied Surface Science*, 364. https://doi.org/10.1016/j.apsusc.2015.12.116.

Qiao, Z.-A., Zhang, L., Guo, M., Liu, Y., and Huo, Q. (2009). Synthesis of mesoporous silica nanoparticles via controlled hydrolysis and condensation of silicon alkoxide. *Chemistry of Materials*, 21. https://doi.org/10.1021/cm901335k.

Qiu, S., Chu, H., Zou, Y., Zhang, H., Sun, L., and Xu, F. (2015). Thermochemical studies of rhodamine B and rhodamine 6G by modulated differential scanning calorimetry and thermogravimetric analysis. *J. Therm. Anal. Calorim.*, 123. https://doi.org/10.1007/s10973-015-5055-5.

Quignard, S., Coradin, T., Powell, J. J., and Jugdaohsingh, R. (2017). Silica nanoparticles as sources of silicic acid favoring wound healing in vitro. *Colloids Surf. B Biointerfaces*, 155. https://doi.org/10.1016/j.colsurfb.2017.04.049.

Radilla, G., Sausse, J., Sanjuan, B., and Fourar, M. (2012). Interpreting tracer tests in the enhanced geothermal system (EGS) of Soultz-sous-Forêts using the equivalent stratified medium approach. *Geothermics*, 44. https://doi.org/10.1016/j.geothermics.2012.07.001.

Ravbar, N., Barberá, J. A., Petric, M., Kogovsek, J., and Andreo, B. (2012). The study of hydrodynamic behaviour of a complex karst system under low-flow conditions using natural and artificial tracers (the catchment of the Unica river, SW Slovenia). *Environmental Earth Sciences*, 65. https://doi.org/10.1007/s12665-012-1523-4.

Ren, Y., Kong, Y., Pang, Z., and Wang, J. (2023). A comprehensive review of tracer tests in enhanced geothermal systems. *Renewable and Sustainable Energy Reviews*, 182. https://doi.org/10.1016/j.rser.2023.113393.

Renew, J. and Hansen, T. (2017). Geothermal thermoelectric generation (G-TEG) with integrated temperature driven membrane distillation and novel manganese oxide for lithium extraction. Technical report, Southern Research Inst. Birmingham.

Richard, B., Lemyre, J. L., and Ritcey, A. M. (2017). Nanoparticle size control in microemulsion synthesis. *Langmuir*, 33. https://doi.org/10.1021/acs.langmuir.7b00773.

Rieger, J. (1996). The glass transition temperature of polystyrene. *Journal of Thermal Analysis*, 46. https://doi.org/10.1007/BF01983614.

Rimer, J. D., Trofymluk, O., Navrotsky, A., Lobo, R. F., and Vlachos, D. G. (2007). Kinetic and thermodynamic studies of silica nanoparticle dissolution. *Chem. Mater.*, 19. https://doi.org/10.1021/cm070708d.

Rimstidt, J. D. and Barnes, H. L. (1980). Kinetics of silica water reactions. *Geochimica et Cosmochimica Acta*, 44. https://doi.org/10.1016/0016-7037(80)90220-3.

Robertson, W. G. (1982). The solubility concept. *Biological Mineralization and Demineralization*, 23. https://doi.org/10.1007/978-3-642-68574-3_2.

Rodriguez, K. and Araujo, M. (2006). Temperature and pressure effects on zeta potential values of reservoir minerals. *J Colloid Interface Sci*, 300. https://doi.org/10.1016/j.jcis.2006.04.030.

Rose, P. and Clausen, S. (2014). The use of amino G as a thermally reactive tracer for geothermal applications. In *Proceedings 39th Workshop on Geothermal Reservoir Engineering, Stanford*.

Rose, P., Goranson, C., Salls, D., and Kilbourn, P. (1999). Tracer testing at Steamboat Hills, Nevada, using fluorescein and 1,5-naphthalene disulfonate. In *PROCEEDINGS, 24th Workshop on Geothermal Reservoir Engineering, Stanford University*.

Rose, P., Riasetto, D., Siy, J., Bartl, M., Reimus, P., Mella, M., Leecaster, K., and Petty, S. (2011). Quantum dots as tracers in geothermal and EGS reservoirs. In *Thirty-Sixth Workshop on Geothermal Reservoir Engineering*.

Rose, P. E., Benoit, W. R., and Kilbourn, P. M. (2001). The application of the polyaromatic sulfonates as tracers in geothermal reservoirs. *Geothermics*, 30. https://doi.org/10.1016/S0375-6505(01)00024-4.

Rose, P. E., Johnson, S. D., Kilbourn, P., and Kasteler, C. (2002). Tracer testing at Dixie valley, Nevada using 1-naphthalene sulfonate and 2,6-naphthalene disulfonate. In *Twenty-Seventh Workshop on Geothermal Reservoir Engineering*.

Rothbaum, H., Anderton, B., Harrison, R., Rohde, A., and Slatter, A. (1979). Effect of silica polymerisation and pH on geothermal scaling. *Geothermics*, 8. https://doi.org/10.1016/0375-6505(79)90062-2.

Rothbaum, H. P. and Anderton, B. H. (1975). Removal of silica and arsenic from geothermal discharge waters by precipitation of useful calcium silicates. In *Second United Nations Symposium on the development and use of geothermal resources*.

Roy, C. J. (1945). Silica in natural waters. *Am. Jour. Sci.*, 243. https://doi.org/10.2475/ajs.243.7.393.

Ruckenstein, E. and Prieve, D. C. (1976). Adsorption and desorption of particles and their chromatographic separation. *AIChE*, 22. https://doi.org/10.1002/aic.690220209.

Rudolph, B. (2021). *Reporting Nanoparticle Tracers - Entwicklung von thermoresponsiven Tracern für geothermische Anwendungen*. PhD thesis, Karlsruhe Institute of Technology (KIT).

Rudolph, B., Berson, J., Held, S., Nitschke, F., Wenzel, F., Kohl, T., and Schimmel, T. (2020). Development of thermo-reporting nanoparticles for accurate sensing of geothermal reservoir conditions. *Sci Rep*, 10. https://doi.org/10.1038/s41598-020-68122-y.

Ryan, J. N. and Elimelech, M. (1996). Colloid mobilization and transport in groundwater. *Colloids and Surfaces A: Physicochemical and Engineering Aspects*, 107. https://doi.org/10.1016/0927-7757(95)03384-X.

Ryu, D. H., Kim, S. C., and Koo, S. M. (2003). Deposition of titania nanoparticles on spherical silica. *Journal of Sol-Gel Science and Technology*, 26, https://doi.org/10.1023/A:1020791130557.

Ryu, T., Haldorai, Y., Rengaraj, A., Shin, J., Hong, H.-J., Lee, G.-W., Han, Y.-K., Huh, Y., and Chung, K.-S. (2016). Recovery of lithium ions from seawater using a continuous flow adsorption column packed with granulated chitosan lithium manganese oxide. *Ind. Eng. Chem. Res.*, 55. https://doi.org/10.1021/acs.iecr.6b01632.

Sabatini, D. A. and Austin, T. A. (1991). Characteristics of rhodamine WT and fluorescein as adsorbing ground-water tracers. *Ground Water*, 29. https://doi.org/10.1111/j.1745-6584.1991.tb00524.x:341–349.

Salopek, B., Krasic, D., and Filipovic, S. (1992). Measurement and application of zeta-potential. *Rudarsko-geoloiko-naftni zbornik*, 4:5.

Samari-Kermani, M., Jafari, S., Rahnama, M., and Raoof, A. (2021). Ionic strength and zeta potential effects on colloid transport and retention processes. *Colloid and Interface Science Communications*, 42. https://doi.org/10.1016/j.colcom.2021.100389.

San Andrés, E., del Prado, A., Martínez, F. L., Mártill, I., Bravo, D., and López, F. J. (2000). Rapid thermal annealing effects on the structural properties and density of defects in SiO_2 and SiN_x:H films deposited by electron cyclotron resonance. *Journal of Applied Physics*, 87. https://doi.org/10.1063/1.371996.

Sanjuan, B., Millot, R., Innocent, C., Dezayes, C., Scheiber, J., and Brach, M. (2016). Major geochemical characteristics of geothermal brines from the Upper Rhine Graben granitic

basement with constraints on temperature and circulation. *Chemical Geology*, 428. https://doi.org/10.1016/j.chemgeo.2016.02.021.

Sanjuan, B., Pinault, J.-L., Rose, P., Gérard, A., Brach, M., Braibant, G., Crouzet, C., Foucher, J.-C., Gautier, A., and Touzelet, S. (2006). Tracer testing of the geothermal heat exchanger at Soultz-sous-Forêts (France) between 2000 and 2005. *Geothermics*, 35. https://doi.org/10.1016/j.geothermics.2006.09.007.

Santschi, P. H. and Schindler, P. W. (1973). Complex formation in the ternary system Ca^{II}-H_4SiO_4-H_2O and Mg^{II}-H_4SiO_4-H_2O. *J. C. S. Dalton*, https://doi.org/10.1039/DT9740000181.

Schaffer, M., Maier, F., Licha, T., and Sauter, M. (2013). A new generation of tracers for the characterization of interfacial areas during supercritical carbon dioxide injections into deep saline aquifers: Kinetic interface-sensitive tracers (KIS tracer). *International Journal of Greenhouse Gas Control*, 14. https://doi.org/10.1016/j.ijggc.2013.01.020.

Schenkel, J. H. and Kitchener, J. A. (1960). A test of the Derjaguin-Verwey-Overbeek theory with a colloidal suspension. *Transactions of the Faraday Society*, 56. https://doi.org/10.1039/TF9605600161.

Schimmel, T., Berson, J., and Rudolph, B. (2022). Threshold-triggered tracer particles. *US patent US20220276217A1*.

Schmidt, J. and Vogelsberger, W. (2009). Aqueous long-term solubility of titania nanoparticles and titanium(IV) hydrolysis in a sodium chloride system studied by adsorptive stripping voltammetry. *Journal of Solution Chemistry*, 38. https://doi.org/10.1007/s10953-009-9445-9.

Schmidt, M. (2017). Rohstoffrisikobewertung - Lithium. Technical report, DERA Rohstoffinformationen.

Schudel, B., Biaggi, D., Dervey, T., Kozel, R., Müller, I., Ross, J. H., and Schindler, U. (2002). Einsatz künstlicher Tracer in der Hydrogeologie - Praxishilfe.

Schulze, H. (1882). Schwefelarsen in wässriger Lösung. *Journal für Praktische Chemie*, 25. https://doi.org/10.1002/prac.18820250142.

Scientific Committee on Consumer Safety (2019). Opinion on solubility of synthetic amorphous silica (SAS). Technical report, European Commission.

Scott, S., Galeczka, I. M., Gunnarsson, I., Arnórsson, S., and Stefánsson, A. (2024). Silica polymerization and nanocolloid nucleation and growth kinetics in aqueous solutions. *Geochimica et Cosmochimica Acta*, 371. https://doi.org/10.1016/j.gca.2024.02.017.

Sekigushi, K., Yamaguchi, S., and Tahara, T. (2006). Formation and dissociation of rhodamine 800 dimers in water: Steady-state and ultrafast spectroscopic study. *J. Phys. Chem. A*, 110. https://doi.org/10.1021/jp055027p.

Setiawan, F. A., Rahayuningsih, E., Murti Petrus, H. T. B., Nurpratama, M. I., and Perdana, I. (2019). Kinetics of silica precipitation in geothermal brine with seeds addition:

minimizing silica scaling in a cold re-injection system. *Geothermal Energy*, 7. https://doi.org/10.1186/s40517-019-0138-3.

Shehata, A. M. and Nasr-El-Din, H. A. (2015). Zeta potential measurements: Impact of salinity on sandstone minerals. In *SPE International Symposium on Oilfield Chemistry*, volume https://doi.org/10.2118/173763-MS.

Sheikholeslami, R. and Bright, J. (2002). Silica and metals removal by pretreatment to prevent fouling of reverse osmosis membranes. *Desalination*, 143. https://doi.org/10.1016/S0011-9164(02)00264-3.

Sieren, B., Baker, J., Wang, X., Rozzoni, S. J., Carlson, K., McBain, A., Kerstan, D., Allen, L., Liao, L., and Li, Z. (2020). Sorptive removal of color dye safranin O by fibrous clay minerals and zeolites. *Advances in Materials Science and Engineering*, https://doi.org/10.1155/2020/8845366.

Sigfusson, B. and Gunnarsson, I. (2011). Scaling prevention experiments in the Hellisheiði power plant, Iceland. In *Proceedings Thirty-Sixth Workshop on Geothermal Reservoir Engineering*.

Silencieux, F., Bouchoucha, M., Mercier, O., Turgeon, S., Chevallier, P., Kleitz, F., and Fortin, M.-A. (2015). Mesoporous silica nanoparticles under sintering conditions: a quantitative study. *Langmuir*, 31. https://doi.org/10.1021/acs.langmuir.5b02961.

Smart, P. L. and Laidlaw, I. M. S. (1977). Evaluation of some fluorescent dyes for water tracing. *Water Resources Research*, 13. https://doi.org/10.1029/WR013i001p00015.

Smitha, V. S., Athulya, P., Kochu, J. K., and Remsi, T. R. (2024). Fluorescent carbon dots embedded silica nanocomposites as tracers for hydrogeological investigations; a sustainable approach. *Environ. Sci. Adv.*, https://doi.org/10.1039/D4VA00156G.

Socrates, G. (2001). *Infrared and Raman Characteristic Group Frequencies*. John Wiley & Sons, third edition.

Sola, F., Canonico, B., Montanari, M., Volpe, A., Barattini, C., Pellegrino, C., Cesarini, E., Guescini, M., Battisetlli, M., Ortolani, C., Ventola, A., and Papa, S. (2021). Uptake and intracellular trafficking studies of multiple dye-doped core-shell silica nanoparticles in lymphoid and myeloid cells. *Nanotechnol. Sci. Appl.*, 14. https://doi.org/10.2147/NSA.S290867.

Soltani, M., Kashkooli, F. M., Fini, M. A., Gharapetian, D., Nathwani, J., and Dusseault, M. B. (2022). A review of nanotechnology fluid applications in geothermal energy systems. *Renewable and Sustainable Energy Reviews*, 167. https://doi.org/10.1016/j.rser.2022.112729.

Sondi, I., Bišćan, J., Vdović, N., and Škapin, S. D. (2009). The electrokinetic properties of carbonates in aqueous media revisited. *Colloids and Surfaces A: Physicochemical and Engineering Aspects*, 342. https://doi.org/10.1016/j.colsurfa.2009.04.012.

Song, Y., Li, Y., Xu, Q., and Liu, Z. (2017). Mesoporous silica nanoparticles for stimuli-resonsive controlled drug release. *Int. J Nanomedicine*, 12. https://doi.org/10.2147/IJN.S117495.

Southam, D., Lewis, T., McFarlane, A., and Johnston, J. (2004). Amorphous calcium silicate as a chemisorbent for phosphate. *Current Applied Physics*, 4. https://doi.org/10.1016/j.cap.2003.11.047.

Sperling, R. A. and Parak, W. J. (2010). Surface modification, functionalization and bioconjugation of colloidal inorganic nanoparticles. *Philosophical Transactions of the Royal Society A*, 368. https://doi.org/10.1098/rsta.2009.0273.

Spitzmüller, L., Berson, J., Nitschke, F., Kohl, T., and Schimmel, T. (2024a). Titania-mediated stabilization of fluorescent dye encapsulation in mesoporous silica nanoparticles. *Nanoscale Advances*, 6. https://doi.org/10.1039/D4NA00242C.

Spitzmüller, L., Berson, J., Schimmel, T., Kohl, T., and Nitschke, F. (2024b). Temperature stability and enhanced transport properties by surface modifications of silica nanoparticle tracers for geo-reservoir exploration. *Scientific Reports*, 14. https://doi.org/10.1038/s41598-024-70132-z.

Spitzmüller, L., Goldberg, V., Held, S., Grimmer, J. C., Winter, D., Genovese, M., Koschikowski, J., and Kohl, T. (2021). Selective silica removal in geothermal fluids: Implications for applications for geothermal power plant operation and mineral extraction. *Geothermics*, 95. https://doi.org/10.1016/j.geothermics.2021.102141.

Spitzmüller, L., Nitschke, F., Maercks, A., Berson, J., Rudolph, B., Schimmel, T., and Kohl, T. (2023a). Nanoparticle-based tracing techniques in geothermal reservoirs: Advances, challenges and prospects. In *48th Workshop on Geothermal Reservoir Engineering*.

Spitzmüller, L., Nitschke, F., Rudolph, B., Berson, J., Schimmel, T., and Kohl, T. (2023b). Dissolution control and stability improvement of silica nanoparticles in aqueous media. *Journal of Nanoparticle Research*, 25. https://doi.org/10.1007/s11051-023-05688-4.

Stephens, D. B., Hsu, K.-C., Prieksat, M. A., Ankeny, M. D., Blandford, N., Roth, T. L., Kelsey, J. A., and Whitworth, J. R. (1998). A comparison of estimated and calculated effective porosity. *Hydrogeology Journal*, 6. https://doi.org/10.1007/s100400050141.

Stober, I. (2002). Geologie und Geschichte der Mineral- und Thermalquellen im Schwarzwald. Technical report, Ber. Naturf. Ges. Freiburg i. Br.

Stokes, R. H. and Robinson, R. A. (1948). Ionic hydration and activity in electrolyte solutions. *J. Am. Chem. Soc*, 5. https://doi.org/10.1021/ja01185a065.

Stricker, K., Grimmer, J. C., Egert, R., Bremer, J., Korzani, M. G., Schill, E., and Kohl, T. (2020). The potential of depleted oil reservoirs for high-temperature storage systems. *Energies*, 13. https://doi.org/10.3390/en13246510.

Stöber, W. (1967). Formation of silicic acid in aqueous suspensions of different silica modifications. *Equilibrium Concepts in Natural Water Systems*, https://doi.org/10.1021/ba-1967-0067.

Stöber, W., Fink, A., and Bohn, E. (1968). Controlled growth of monodisperse silica spheres in the micron size range. *Journal of Colloid and Interface Science*, 26. https://doi.org/10.1016/0021-9797(68)90272-5.

Sugita, H., Kato, K., Ueda, A., Matsunaga, I., Sakurai, Y., Yasuda, K., Bando, Y., and Nakamura, M. (1999). Field tests on silica removal from geothermal brines in Sumikawa and Onuma geothermal areas. *Journal of chemical engineering of Japan*, https://doi.org/10.1252/jcej.32.696.

Sugita, H., Matsunaga, I., and Yamaguchi, T. (2000). Silica scale prevention method using seed made from geothermal brine. In *Proceedings World Geothermal Congress*.

Sugita, H., Matsunaga, I., Yamaguchi, T., Kato, K., and Ueda, A. (2003). Silica removal performance of seed from geothermal fluids. *Geothermics*, 32. https://doi.org/10.1016/S0375-6505(03)00013-0.

Sun, L., Sogo, Y., Wang, X., and Ito, A. (2021). Biosafety of mesoporous silica nanoparticles: a combined experimental and literature study. *J. Mater. Sci. Mater. Med.*, 32. https://doi.org/10.1007/s10856-021-06582-y.

Suzuki, A., Cui, J., Zhang, Y., Uehara, S., Li, K., Horne, R. N., and Ito, T. (2020). Experimental study on nano-/microparticles transport to characterize structures in fractured porous media. *Rock Mechanics and Rock Engineering*, 53. https://doi.org/10.1007/s00603-020-02081-8.

Suzuki, Y., Ioka, S., and Muraoka, H. (2017). Geothermal resource exploration by stream pH mapping in Mutsu Hiuchi Dake volcano, Japan. *Energies*, 10. https://doi.org/10.3390/en10071009.

Tamura, R., Inoue, H., Hanajima, E., Ikeda, R., Osaka, Y., Yanaze, T., Kusakabe, M., Yonezu, K., Yokoyama, T., Tsukamoto, K., Marumo, K., and Ueda, A. (2019). In situ observations of silica nanoparticle growth in geothermal brine at the Sumikawa geothermal station, Japan, by dynamic light scattering. *Geothermics*, 77. https://doi.org/10.1016/j.geothermics.2018.10.008.

Tang, Y., Zhang, F., Boogard, T., Chassagne, C., Ali, Z., Bandyopadhyay, S., and Foppen, J. W. (2023). Settling of superparamagnetic silica encapsulated DNA microparticles in water. *Hydrological Processes*, 37. https://doi.org/10.1002/hyp.14801.

Tannock, L. F. and Rotin, D. (1989). Acid pH in tumors and its potential in therapeutic exploitation. *Cancer Research.*

Tassi, F., Aguilera, F., Darrah, T., Vaselli, O., Capaccioni, B., Poreda, R., and Delgado Huertas, A. (2010). Fluid geochemistry of hydrothermal systems in the Arica-Parinacota, Tarapacá and Antofagasta regions (northern Chile). *Journal of Volcanology and Geothermal Resarch*, 192. https://doi.org/10.1016/j.jvolgeores.2010.02.006.

Taylor, G. (1953). Dispersion of soluble matter in solvent flowing slowly through a tube. *Proceedings of the Royal Society of London. Series A: Mathematical and Physical Sciences*, 219. https://doi.org/10.1098/rspa.1953.0139.

Teamsinsungvon, A., Ruksakulpiwat, C., Amonpattaratkit, P., and Ruksakulpiwat, Y. (2022). Structural characterization of titanium-silica oxide using synchrotron radiation X-ray absorption spectroscopy. *Polymers*, 14. https://doi.org/10.3390/polym14132729.

Thi, T. T. H., Cao, V. D., Nguyen, T. N. Q., Hoang, D. T., Ngo, V. C., and Nguyen, D. H. (2019). Functionalized mesoporous silica nanoparticles and biomedical applications. *Materials Science and Engineering: C*, 99. https://doi.org/10.1016/j.msec.2019.01.129.

Tian, Y., Gao, B., Silvera-Batista, C., and Ziegler, K. J. (2010). Transport of engineered nanoparticles in saturated porous media. *Journal of Nanoparticle Research*, 12. https://doi.org/10.1007/s11051-010-9912-7.

Tikhonov, A. M. (2007). Compact layer of alkali ions at the surface of colloidal silica. *J. Phys. Chem. C*, 111. https://doi.org/10.1021/jp065538r.

Tobler, D. J. and Benning, L. G. (2013). In situ and time resolved nucleation and growth of silica nanoparticles forming under simulated geothermal conditions. *Geochimica and Cosmochimica Acta*, 114. https://doi.org/10.1016/j.gca.2013.03.045.

Tonelli, F. M. P., Tonelli, F. C. P., Ferreira, D. R. C., da Silva, E., Cordeiro, H. G., Ouchida, A. T., and de Melo Nunes, N. A. (2020). Biocompatibility and functionalization of nanomaterials. *Intelligent Nanomaterials for Drug Delivery Applications*, https://doi.org/10.1016/B978-0-12-817830-0.00005-9.

Torkzaban, S., Bradford, S. A., and Walker, S. L. (2007). Resolving the coupled effects of hydrodynamics and DLVO forces on colloid attachment in porous media. *Langmuir*, 23. https://doi.org/10.1021/la700995e.

Tosha, T., Matsushima, N., and Ishido, T. (2003). Zeta potential measured for an intact granite sample at temperatures to 200°C. *Geophysical Research Letters*, 30. https://doi.org/10.1029/2002GL016608.

Tourne-Peteilh, C., Begu, S., Lerner, D. A., Galarneau, A., Lafont, U., and Devoisselle, J.-M. (2011). Sol–gel one-pot synthesis in soft conditions of mesoporous silica materials ready for drug delivery system. *Journal of Sol-Gel Science and Technology*, 61. https://doi.org/10.1007/s10971-011-2646-x.

Tran, E. and Richmond, G. L. (2021). Interfacial steric and molecular bonding effects contributing to the stability of neutrally charged nanoemulsions. *Langmuir*, 37. https://doi.org/10.1021/acs.langmuir.1c02020.

Tufenkji, N. and Elimelech, M. (2004). Correlation equation for predicting single-collector efficiency in physicochemical filtration in saturated porous media. *Environmental Science & Technology*, 38. https://doi.org/10.1021/es034049r.

Ueda, A., Kato, K., Mogi, K., Mroczek, E., and Thain, I. A. (2003). Silica removal from Mokai, New Zealand, geothermal brine by treatment with lime and a cationic precipitant. *Geothermics*, 32. https://doi.org/10.1016/S0375-6505(02)00050-0.

Ullattil, S. G. and Periyat, P. (2017). *Sol-Gel Synthesis of Titanium Dioxide*, book section 9. Springer International. https://doi.org/10.1007/978-3-319-50144-4_9.

U.S. Department of Energy (2011). Federal interagency geothermal activities. Technical report, U.S. Department of Energy - Energy Efficiency & Renewable Energy.

Vallet-Regí, M., Rámila, A., del Real, R. P., and Pérez-Pariente, J. (2001). A new property of mcm-41: Drug delivery system. *Chemistry of Materials*, 13. https://doi.org/10.1021/cm0011559.

Valmacco, V., Elzbieciak-Wodka, M., Besnard, C., Maroni, P., Trefalt, G., and Borkovec, M. (2016). Dispersion forces acting between silica particles across water: influence of nanoscale roughness. *Nanoscale Horizons*, 4. https://doi.org/10.1039/C6NH00070C.

van Blaaderen, A., van Geest, J., and Vrij, A. (1992). Monodisperse colloidal silica spheres from tetraalkoxysilanes: Particle formation and growth mechanism. *Journal of Colloid and Interface Science*, 154. https://doi.org/10.1016/0021-9797(92)90163-G.

van den Heuvel, D. B., Gunnlaugsson, E., Gunnarsson, I., Stawski, T. M., Peacock, C., and Benning, L. G. (2018). Understanding amorphous silica scaling under well-constrained conditions inside geothermal pipelines. *Geothermics*, 76. https://doi.org/10.1016/j.geothermics.2018.07.006.

van Lier, J. A., de Bruyn, P. L., and Overbeek, J. T. G. (1960). The solubility of quartz. *The Journal of Physical Chemistry*, 64. https://doi.org/10.1021/j100840a017.

van Oss, C. J. (2008). The extended DLVO theory. *Interface Science and Technology*, 16. https://doi.org/10.1016/s1573-4285(08)00203-2.

van Rijt, S. H., Bölükbas, D. A., Argyo, C., Datz, S., Lindner, M., Eickelberg, O., Königshoff, M., Bein, T., and Meiners, S. (2015). Protease-mediated release of chemotherapeutics from mesoporous silica nanoparticles to ex vivo human and mouse lung tumors. *ACS Nano*, 9. https://doi.org/10.1021/nn5070343.

Vdović, N. (2001). Electrokinetic behaviour of calcite—the relationship with other calcite properties. *Chemical Geology*, 177. https://doi.org/10.1016/S0009-2541(00)00397-1.

Verwey, E. J. W. and Overebeek, J. T. G. (1948). *Theory of the stability of lyophobic colloids; the interaction of sol particles having an electric double layer*. Elsevier.

Vincent, B., Edwards, J., Emmett, S., and Jones, A. (1986). Depletion flocculation in dispersions of sterically-stabilised particles ("soft spheres"). *Colloids and Surfaces*, 18. https://doi.org/10.1016/0166-6622(86)80317-1.

Visser, J. (1981). The concept of negative Hamaker coefficients. Part 1 history and present status. *Adv. Colloid Interface Sci*, 15. https://doi.org/10.1016/0001-8686(81)80007-3.

Vitolo, S. and Cialdella, M. L. (1994). Silica separation from reinjection brines at Monte Amiata geothermal plants, Italy. *Geothermics*, 23. https://doi.org/10.1016/0375-6505(94)90003-5.

Vitorge, E., Szenknect, S., Martins, J. M. F., Barthès, V., and Gaudet, J.-P. (2014). Comparison of three labeled silica nanoparticles used as tracers in transport experiments in porous

media. Part II: Transport experiments and modeling. *Environmental Pollution*, 184. https://doi.org/10.1016/j.envpol.2013.07.031.

Vogelsberger, W., Seidel, A., and Rudakoff, G. (1992). Solubility of silica gel in water. *J. Chem. Soc. Faraday Trans.*, 88. https://doi.org/10.1039/FT9928800473.

Volmer, M. and Weber, A. (1925). Keimbildung in übersättigten Gebilden. *Zeitschrift für physikalische Chemie*, 119. https://doi.org/10.1515/zpch-1926-11927.

von Baeckmann, C., Guillet-Nicolas, R., Renfer, D., Kahlig, H., and Kleitz, F. (2018). A toolbox for the synthesis of multifunctionalized mesoporous silica nanoparticles for biomedical applications. *ACS Omega*, 3. https://doi.org/10.1021/acsomega.8b02784.

von Baeckmann, C., Kahlig, H., Lindén, M., and Kleitz, F. (2021). On the importance of the linking chemistry for the PEGylation of mesoporous silica nanoparticles. *J Colloid Interface Sci*, 589. https://doi.org/10.1016/j.jcis.2020.12.004.

Vuluga, Z., Radovici, C., Serban, S., Potarniche, C. G., Danciu, V., Trandafir, V., Vuluga, D. M., and Vasile, E. (2008). Titania modified layered silicate for polymer/inorganic nanocomposites. *Mol. Cryst. Liq. Cryst.*, 483. https://doi.org/10.1080/15421400801913998.

Walker, E. and Glover, P. W. J. (2018). Measurements of the relationship between microstructure, pH, and the streaming and Zeta potential of sandstones. *Transp. Porous Media*, 121. https://doi.org/10.1007/s11242-017-0954-5.

Wang, F., Tan, W. B., Zhang, Y., Fan, X., and Wang, M. (2006). Luminescent nanomaterials for biological labelling. *Nanotechnology*, 17. https://doi.org/10.1088/0957-4484/17/1/R01.

Wang, P., Du, M., Zhang, M., Zhu, H., and Bao, S. (2013a). The preparation of tubular heterostructures based on titanium dioxide and silica nanotubes and their photocatalytic activity. *Dalton Trans.*, 43. https://doi.org/10.1039/C3DT51959G.

Wang, Y., Wang, L., Hampton, M. A., and Nguyen, A. V. (2013b). Atomic Force Microscopy study of forces between a silica sphere and an oxidized silicon wafer in aqueous solutions of NaCl, KCl, and CsCl at concentrations up to saturation. *The Journal of Physical Chemistry C*, 117. https://doi.org/10.1021/jp3092495.

Wang, Y., Zhao, Q., Han, N., Bai, L., Li, J., Liu, J., Che, E., Hu, L., Zhang, Q., Jiang, T., and Wang, S. (2015). Mesoporous silica nanoparticles in drug delivery and biomedical applications. *Nanomedicine*, 11. https://doi.org/10.1016/j.nano.2014.09.014.

Warring, S. L., Beattie, D. A., and McQuillan, A. J. (2016). Surficial siloxane-to-silanol interconversion during room-temperature hydration/dehydration of amorphous silica films observed by ATR-IR and TIR-Raman spectroscopy. *Langmuir*, 32. https://doi.org/10.1021/acs.langmuir.5b04506.

Washburn, E. W. and Navias, L. (1922). The relation of chalcedony to other the forms of silica. *Proceedings of the National Academy*, 8. https://doi.org/10.1073/pnas.8.1.1.

Watanabe, N., Abe, H., Okamoto, A., Nakamura, K., and Komai, T. (2021a). Formation of amorphous silica nanoparticles and its impact on permeability of fractured granite in superhot geothermal environments. *Scientific Reports*, 11. https://doi.org/10.1038/s41598-021-84744-2.

Watanabe, Y., Amitani, N., Yokoyama, T., Ueda, A., Kusakabe, M., Unami, S., and Odashima, Y. (2021b). Synthesis of mesoporous silica from geothermal water. *Scientific Reports*, 11. https://doi.org/10.1038/s41598-021-03133-x.

Weidner, C., Naurath, L., Rüde, T. R., and Banning, A. (2011). Parameters affecting Na-fluorescein (uranine) detection in mine water tracer tests. In Rüde, Freund, and Wolkersdorfer, editors, *IMWA*.

Weng, D., Duan, H., Hou, Y., Huo, J., Chen, L., Zhang, F., and Wang, J. (2020). Introduction of manganese based lithium-ion sieve - a review. *Progress in Natural Science: Materials International*, 30. https://doi.org/10.1016/j.pnsc.2020.01.017.

Widjornako, D. M., Jumina, J., Kartini, I., and Nuryono, N. (2014). Phosphonate modified silica for adsorption of Co(II), Ni(II), Cu(II), and Zn(II). *Indo. J. Chem.*, 14. https://doi.org/10.22146/ijc.21251.

Wilhelm, P. and Stephan, D. (2006). On-line tracking of the coating of nanoscaled silica with titania nanoparticles via zeta-potential measurements. *J Colloid Interface Sci*, 293. https://doi.org/10.1016/j.jcis.2005.06.047.

Wilhelm, S. and Kind, M. (2015). Influence of pH, temperature and sample size on natural and enforced syneresis of precipitated silica. *Polymers*, 7. https://doi.org/10.3390/polym7121528.

Williams, L. A. and Crear, D. A. (1985). Silica diagenesis, II. General mechanisms. *Journal of Sedimentary Petrology*, 55. https://doi.org/10.1306/212f86b1-2b24-11d7-8648000102c1865d.

Wolf, S. and Feldmann, C. (2016). Microemulsions: Options to expand the synthesis of inorganic nanoparticles. *Angew Chem Int Ed Engl*, 55. https://doi.org/10.1002/anie.201604263.

Worthen, A. J., Tran, V., Cornell, K. A., Truskett, T. M., and Johnston, K. P. (2016). Steric stabilization of nanoparticles with grafted low molecular weight ligands in highly concentrated brines including divalent ions. *RSC Soft Matter*, 12. https://doi.org/10.1039/C5SM02787J.

Wu, J., Xu, H., Xiong, B., Fang, C., Wang, S., Zong, P., Liu, D., and Xin, F. (2024). A new method for investigating the impact of temperature on in-situ reservoir properties using high-temperature afm. *Geothermics*, 120. https://doi.org/10.1016/j.geothermics.2024.103006.

Wu, S. H., Mou, C. Y., and Lin, H. P. (2013). Synthesis of mesoporous silica nanoparticles. *Chem Soc Rev*, 42. https://doi.org/10.1039/c3cs35405a.

Wu, Y. and Zhou, X. (2024). Source and influencing factors of metasilicic acid in mixed geothermal waters. *Geothermics*, 123. https://doi.org/10.1016/j.geothermics.2024.103098.

Xie, Q., Saeedi, A., Pooryousefy, E., and Liu, Y. (2016). Extended DLVO-based estimates of surface force in low salinity water flooding. *Journal of Molecular Liquids*, 221. https://doi.org/10.1016/j.molliq.2016.06.004.

Xu, S., Gao, B., and Saiers, J. E. (2006). Straining of colloidal particles in saturated porous media. *AGU Water Resources Research*, 42. https://doi.org/10.1029/2006WR004948.

Xu, Z., Ma, X., Gao, Y.-E., Hou, M., Xue, P., Li, C. M., and Kang, Y. (2017). Multifunctional silica nanoparticles as a promising theranostic platform for biomedical applications. *Mater. Chem. Front.*, 1. https://doi.org/10.1039/C7QM00153C.

Yamada, H., Urata, C., Aoyama, Y., Osada, S., Yamauchi, Y., and Kuroda, K. (2012). Preparation of colloidal mesoporous silica nanoparticles with different diameters and their unique degradation behavior in static aqueous systems. *Chemistry of Materials*, 24. https://doi.org/10.1021/cm3001688.

Yamamoto, E. and Kuroda, K. (2016). Collodial mesoporous silica nanoparticles. *Bulletin of the Chemical Society of Japan*, 89. https://doi.org/10.1246/bcsj.20150420.

Yan, F., Jiang, J., Chen, X., Tian, S., and Li, K. (2014a). Synthesis and characterization of silica nanoparticles preparing by low-temperature vapor-phase hydrolysis of $SiCl_4$. *Industrial and Engineering Chemistry Research*, 53. https://doi.org/10.1021/ie501759w.

Yan, G., Andersen, P. O., Qiao, Y., Hatzignatiou, D. G., Nitschke, F., Spitzmüller, L., and Kohl, T. (2024). Numerical modeling of temperature-reporting nanoparticle tracer for fractured geothermal reservoir characterization. *Geoenergy Science and Engineering*, 237. https://doi.org/10.1016/j.geoen.2024.212787.

Yan, W., Petkov, V., Mahurin, S. M., Overbury, S. H., and Dai, S. (2005). Powder XRD analysis and catalysis characterization of ultra-small gold nanoparticles deposited on titania-modified SBA-15. *Catalysis Communications*, 6. https://doi.org/10.1016/j.catcom.2005.04.004.

Yan, Z., Huang, X., and Yang, C. (2014b). Deposition of colloidal particles in a microchannel at elevated temperatures. *Microfluid Nanofluid*, https://doi.org/10.1007/s10404-014-1448-1.

Yanagisawa, K. and Ovenstone, J. (1999). Crystallization of anatase from amorphous titania using the hydrothermal technique: Effects of starting material and temperature. *J. Phys. Chem. B*, 103. https://doi.org/10.1021/jp990521c.

Yang, X., Liu, X., Zhang, A., Lu, D., Li, G., Zhang, Q., Liu, Q., and Jiang, G. (2019). Distinguishing the sources of silica nanoparticles by dual isotopic fingerprinting and machine learning. *Nature Communications*, 10. https://doi.org/10.1038/s41467-019-09629-5.

Ye, Y., Liu, J., Chen, M., Sun, L., and Lan, M. (2010). In vitro toxicity of silica nanoparticles in myocardial cells. *Environ. Toxicol. Pharmacol.*, 29. https://doi.org/10.1016/j.etap.2009.12.002.

Yokoyama, T., Takahashi, Y., Yamanaka, C., and Tarutani, T. (1989). Effect of aluminium on the polymerization silicic acid in aqueous solution and the deposition of silica. *Geothermics*, 18. https://doi.org/10.1016/0375-6505(89)90042-4.

Yokoyama, T., Ueda, A., Kato, K., Mogi, K., and Matsuo, S. (2002). A study of the alumina-silica gel adsorbent for the removal of silicic acid from geothermal water: increase in adsorption capacity of the adsorbent due to formation of amorphous aluminosilicate by adsorption of silicic acid. *Journal of Colloid and Interface Science*, 252. https://doi.org/10.1006/jcis.2002.8382.

Yotsumoto, H. and Yoon, R.-H. (1993). Application of Extended DLVO theory - II. stability of silica suspensions. *Journal of Colloid and Interface Science*, 157. https://doi.org/10.1006/jcis.1993.1206.

You, Y.-Z., Kalebaila, K. K., Brock, S. L., and Oupicky, D. (2008). Temperature-controlled uptake and release in PNIPAM-modified porous silica nanoparticles. *Chemistry of Materials*, 20. https://doi.org/10.1021/cm703363w.

Yusuf, S., Manan, M., and Jaafar, M. Z. (2013). Aqueous foams stabilized by hydrophilic silica nanoparticles via in-situ physisorption of nonionic TX100 surfactant. *Iranica Journal of Energy & Enviornment*, 4.

Zareei, M., Yoozbashizadeh, H., and Madaah Hosseini, H. R. (2018). Investigating the effects of pH, surfactant and ionic strength on the stability of alumina/water nanofluids using DLVO theory. *Journal of Thermal Analysis and Calorimetry*, 135. https://doi.org/10.1007/s10973-018-7620-1.

Zaucha, M., Adamczyk, Z., and Barbasz, J. (2011). Zeta potential of particles bilayers on mica: A streaming potential study. *Journal of Colloid and Interface Science*, 360. https://doi.org/10.1016/j.jcis.2011.02.025.

Zeitler, V. A. and Brown, C. A. (1957). The infrared spectra of some Ti-O-Si, Ti-O-Ti and Si-O-Si compounds. *The Journal of Physical Chemistry*, 61. https://doi.org/10.1021/j150555a010.

Zeng, Y., Yang, C., Pu, W., and Zhang, X. (2007). Removal of silica from heavy oil wastewater to be reused in a boiler by combining magnesium and zinc compounds with coagulation. *Desalination*, 216. https://doi.org/10.1016/j.desal.2007.01.005.

Zhang, H., Finnegan, M., and Banfield, J. F. (2001). Preparing single-phase nanocrystalline anatase from amorphous titania with particle sizes tailored by temperature. *Nano Letters*, 1. https://doi.org/10.1021/nl0055198/.

Zhang, Y. and Huang, T. (2022). DNA-based tracers for the characterization of hydrogeological systems—recent advances and new frontiers. *Water*, 14. https://doi.org/10.3390/w14213545.

Zhang, Y., Manley, T. S., Li, K., and Horne, R. N. (2016). Uniquely identifiable DNA-embedded silica nanotracer for fractured reservoir characterization. In *Proceedings 41st Workshop on Geothermal Reservoir Engineering, Stanford University*.

Zhao, D., Huo, Q., Feng, J., Chmelkam, B. F., and Stucky, G. D. (1998). Nonionic triblock and star diblock copolymer and oligomeric surfactant syntheses of highly ordered, hydrothermally stable, mesoporous silica structures. *J. Am. Chem. Soc.*, 120. https://doi.org/10.1021/ja974025i.

Zhao, S., Zhang, S., Ma, J., Fan, L., Yin, C., Lin, G., and Li, Q. (2015). Double loaded self-decomposable SiO_2 nanoparticles for sustained drug release. *Nanoscale*, 7. https://doi.org/10.1039/C5NR03029C.

Zhao, Y.-L., Li, Z., Kabehie, S., Botros, Y. Y., Stoddard, J. F., and Zink, J. I. (2010). pH-operated nanopistons on the surface of mesoporous silica nanoparticles. *J. Am. Chem. Soc.*, 132. https://doi.org/10.1021/ja105371u.

Zhu, H., Derksen, R. C., Krause, C. R., Fox, R. D., Brazee, R. D., and Ozkan, H. E. (2005). Fluorescent intensity of dye solutions under different pH conditions. *Journal of ASTM International*, 2. https://doi.org/10.1520/JAI12926.

Zhulina, E. B., Borisov, O. V., and Priamitsyn, V. A. (1990). Theory of steric stabilization of colloid dispersions by grafted polymers. *Journal of Colloid and Interface Science*, 137. https://doi.org/10.1016/0021-9797(90)90423-L.

Zhuravlev, L. T. (2000). The surface chemistry of amorphous silica: Zhuravlev model. *Colloids and Surfaces A: Physicochemical and Engineering Aspects*, 173. https://doi.org/10.1016/S0927-7757(00)00556-2.

Zu, G., Shen, J., Wang, W., Zou, L., Lian, Y., and Zhang, Z. (2015). Silica–titania composite aerogel photocatalysts by chemical liquid deposition of titania onto nanoporous silica scaffolds. *ACS Appl. Mater. Interfaces*, 7. https://doi.org/10.1021/am5089132.

Declaration of Authorship

In Chapter 3: 3.3 Nanoparticle-based tracing techniques in geothermal reservoirs: Advances, challenges and prospects

Published as: Laura Spitzmüller, Fabian Nitschke, Annika Maercks, Jonathan Berson, Bastian Rudolph, Thomas Schimmel, Thomas Kohl (2023): Nanoparticle-based tracing techniques in geothermal reservoirs: Advances, challenges and prospects. *Proceedings 48th Workshop on Geothermal Reservoir Engineering*, Stanford, CA. https://doi.org/10.5445/IR/1000156430.

This study was conducted within the Helmholtz topic "Geoenergy" in the program "MTET - Materials and Technologies for the Energy Transition". In this study, I carried out the laboratory work with input by Annika Maercks, Jonathan Berson and Bastian Rudolph. I visualized and interpreted the results and wrote the manuscript.

Chapter 4 Dissolution Control and Stability Improvement of Silica Nanoparticles in Aqueous Media

Published as: Spitzmüller, L., Nitschke, F., Rudolph, B., Berson, J., Schimmel, T. and Kohl, T. (2023): Dissolution Control and Stability Improvement of Silica Nanoparticles in Aqueous Media. *J. Nanopart. Res.* 25, 40. https://doi.org/10.1007/s11051-023-05688-4. This paper is published open access under the Creative Commons license CC BY 4.0.

This study was conducted within the Helmholtz topic "Geoenergy" in the program "MTET - Materials and Technologies for the Energy Transition". In this study, I developed the concept, carried out the laboratory work, visualized and interpreted the results and wrote the manuscript.

Chapter 5 Titania-Mediated Stabiliziation of Fluorescent Dye Encapsulation in Mesoporous Silica Nanoparticles

Published as: Spitzmüller, L., Berson, J., Nitschke, F., Kohl T. and Schimmel, T. (2024a): Titania-Mediated Stabilization of Fluorescent Dye Encapsulation in Mesoporous Silica Nanoparticle. *Nanoscale Advances*, 6, 13. `https://doi.org/10.1039/D4NA00242C`. This paper is published open access under the Creative Commons license CC BY 3.0.

This study was conducted within the Helmholtz topic "Geoenergy" in the program "MTET - Materials and Technologies for the Energy Transition". In this study, I developed the concept with input by Jonathan Berson, carried out the laboratory work (assistance for STEM, XRD, BET and TGA measurements as indicated in the Acknowledgments), visualized and interpreted the results and wrote the manuscript.

Chapter 6 Temperature stability and enhanced transport properties by surface modifications of silica nanoparticle tracers for geo-reservoir exploration

Published as: Spitzmüller, L., Berson, J., Schimmel, T., Kohl, T. and Nitschke, F. (2024b): Temperature stability and enhanced transport properties by surface modifications of silica nanoparticle tracers for geo-reservoir exploration. *Scientific Reports*, 14. `https://doi.org/10.1038/s41598-024-70132-z`. This paper is published open access under the Creative Commons license CC BY 4.0.

This study was conducted within the Helmholtz topic "Geoenergy" in the program "MTET - Materials and Technologies for the Energy Transition".

CRediT-Statement: LS: Conceptualization, Methodology, Validation, Formal Analysis, Investigation, Writing – Original Draft, Writing – Review & Editing, Visualization. JB: Conceptualization, Methodology, Validation, Writing – Review & Editing. TS: Resources, Supervision. TK: Resources, Supervision, Funding acquisition. FN: Conceptualization, Methodology, Writing – Review & Editing, Supervision, Project administration.

Chapter 7 Design of silica nanoparticle tracers with optimized dispersion stability, sorption and deposition properties based on (X)DLVO and filtration theory

Under review at Geothermics.

This study was conducted within the Helmholtz topic "Geoenergy" in the program "MTET - Materials and Technologies for the Energy Transition". In this study, I developed the concept, carried out the experimental investigations with help by Jonathan Berson, performed the formal analysis, interpreted and visualized the result and wrote the manuscript.

In Chapter A: A.1 Selective Silica Removal in Geothermal Fluids: Implications for Applications for Geothermal Power Plant Operation and Mineral Extraction

Published as: Spitzmüller, L., Goldberg, V., Held, S., Grimmer, J. C., Winter, D., Genovese, M., Koschikowski, J., Kohl, T. (2021): Selective Silica Removal in Geothermal Fluids: Implications for Applications for Geothermal Power Plant Operation and Mineral Extraction. *Geothermics* 95. https://doi.org/10.1016/j.geothermics.2021.102141. As author of this publication, I retain the right to include it in a thesis.

This study was conducted within the BrineMine Project (BMBF Client II Federal Ministry of Education and Research, FKZ: 033R190B) and is partially based on my master thesis (L. Spitzmüller 2020: Entwicklung eines elementspezifischen Fällungsprozesses zur Reduktion der Siliziumdioxidkonzentration im Vorfeld der Rohstoffextraktion aus geothermalen Fluiden - Development of an Element-Specific Precipitation Process for the Reduction of the Silicon Dioxide Concentration Prior to the Extraction of Raw Materials from Geothermal Fluids). In this study, I developed the concept with discussion input by Sebastian Held and Valentin Goldberg. I carried out the laboratory work, visualized and interpreted the results and wrote the manuscript.

List of Publications

Publications in peer-reviewed journals

Berson, J., Rudolph, B., **Spitzmüller, L.**, Kohl, T., and Schimmel, T. (2024). Reporting nanoparticle tracers: Validation of performance in flow-through experiments simulating reservoir conditions. *Journal of Hydrology*, 637. https://doi.org/10.1016/j.jhydrol.2024.131429.

Goldberg, V., Winter, D., Nitschke, F., Rath, M., Held, S., **Spitzmüller, L.**, Budach, I., Pavez, M., Morata, D., Koschikowski, J., and Kohl, T. (2021). The potential of raw material extraction from thermal brines – successful milestones of the BrineMine project. *Oil Gas*, 1. https://geothermics.agw.kit.edu/downloads/OGA_001_21_026-033_Goldberg_et_al_HP-Liz.pdf.

Spitzmüller, L., Berson, J., Kohl, T., Schimmel, T., and Nitschke, F. (202x). Design of silica nanoparticle tracers with optimized dispersion stability, sorption and deposition properties based on (X)DLVO and filtration theory. *Under review*.

Spitzmüller, L., Berson, J., Nitschke, F., Kohl, T., and Schimmel, T. (2024a). Titania-mediated stabilization of fluorescent dye encapsulation in mesoporous silica nanoparticles. *Nanoscale Advances*, 6. https://doi.org/10.1039/D4NA00242C.

Spitzmüller, L., Berson, J., Schimmel, T., Kohl, T., and Nitschke, F. (2024b). Temperature stability and enhanced transport properties by surface modifications of silica nanoparticle tracers for geo-reservoir exploration. *Scientific Reports*, 14. https://doi.org/10.1038/s41598-024-70132-z.

Spitzmüller, L., Goldberg, V., Held, S., Grimmer, J. C., Winter, D., Genovese, M., Koschikowski, J., and Kohl, T. (2021). Selective silica removal in geothermal fluids: Implications for applications for geothermal power plant operation and mineral extraction. *Geothermics*, 95. https://doi.org/10.1016/j.geothermics.2021.102141.

Spitzmüller, L., Nitschke, F., Rudolph, B., Berson, J., Schimmel, T., and Kohl, T. (2023). Dissolution control and stability improvement of silica nanoparticles in aqueous media. *Journal of Nanoparticle Research*, 25(40). https://doi.org/10.1007/s11051-023-05688-4.

Yan, G., Andersen, P. O., Qiao, Y., Hatzignatiou, D. G., Nitschke, F., **Spitzmüller, L.**, and Kohl, T. (2024). Numerical modeling of temperature-reporting nanoparticle tracer for fractured geothermal reservoir characterization. *Geoenergy Science and Engineering*, 237. https://doi.org/10.1016/j.geoen.2024.212787.

Conference contributions

Goldberg, V., Held, S., Winter, D., **Spitzmüller, L.**, Nitschke, F., Morata, D., Kohl, T., Budach, I., and Koschikowski, J. (2020). Nachhaltige Rohstoffgewinnung aus Thermalwässern: das BrineMine Projekt. In *Der digital Geothermiekongress (DGK), online.*

Spitzmüller, L., Berson, J., Rudolph, B., Nitschke, F., Schimmel, T., and Kohl, T. (2021a). Design and application of messenger nanoparticle tracers for multi-parameter reservoir exploration. In *9th European Geothermal Workshop (EGW), online.*

Spitzmüller, L., Berson, J., Rudolph, B., Nitschke, F., Schimmel, T., and Kohl, T. (2021b). Design und Anwendung von Messenger Nanopartikeltracern zur Exploration geothermischer Reservoire. In *Symposium Nano-BW, online.*

Spitzmüller, L., Berson, J., Rudolph, B., Nitschke, F., Schimmel, T., and Kohl, T. (2021c). Design und Anwendung von Messenger Nanopartikeltracern zur Exploration geothermischer Reservoire. In *Symposium Nano-BW, Bad Herrenalb, Germany.*

Spitzmüller, L., Goldberg, V., Held, S., Grimmer, J. C., Winter, D., Koschikowski, J., and Kohl, T. (2020a). Entwicklung eines elementspezifischen Fällungsprozesses zur Reduktion der Siliziumdioxidkonzentartion aus geothermalen Wässern. In *Der digital Geothermiekongress (DGK), online.*

Spitzmüller, L., Goldberg, V., Held, S., Grimmer, J. C., Winter, D., Koschikowski, J., and Kohl, T. (2020b). Removal of silica from geothermal water by addition of $Ca(OH)_2$. In *Student Technical Congress - German Section (STC), online.*

Spitzmüller, L., Nitschke, F., Berson, J., Maercks, A., Rudolph, B., Schimmel, T., and Kohl, T. (2023a). Nanoparticle-based tracing techniques in geothermal reservoirs: Advances, challenges and prospects. In *48th Workshop on Geothermal Reservoir Engineering, Stanford, California.*

Spitzmüller, L., Nitschke, F., Berson, J., Maercks, A., Rudolph, B., Schimmel, T., and Kohl, T. (2023b). Nanoparticle-based tracing techniques in geothermal reservoirs: Advances, challenges and prospects. In *Proceedings: 48th Workshop on Geothermal Reservoir Engineering, Stanford, California.* https://doi.org/10.5445/IR/1000156430.

Spitzmüller, L., Nitschke, F., Berson, J., Rudolph, B., Schimmel, T., and Kohl, T. (2022a). Design and application of nanoparticle tracer for multiparameter-reservoir-exploration. In *Symposium Nano-BW, Bad Herrenalb, Germany.*

Spitzmüller, L., Nitschke, F., Berson, J., Rudolph, B., Schimmel, T., and Kohl, T. (2022b). Nanoparticle tracer development for subsurface reservoir exploration. In *Symposium Nano-BW, Bad Herrenalb, Germany.*

Spitzmüller, L., Nitschke, F., Berson, J., Rudolph, B., Schimmel, T., and Kohl, T. (2023c). Development of thermo-reporting nanoparticle tracer for geothermal reservoir characterization. In *Helmholtz Energy Conference, Koblenz, Germany.*

Yan, G., Andersen, P. O., Qiao, Y., Hatzignatiou, G., Nitschke, F., **Spitzmüller, L.**, and Kohl, T. (2024). Simulation of temperature-reporting nanoparticle tracers for fractured geothermal reservoir characterization. In *85th EAGE Annual Conference & Exhibition*.

Acknowledgments

During my PhD, I had the chance to meet a variety of people who inspired, motivated, and supported me along the way. I want to thank all of them, and in particular thank you to:

... Thomas Kohl for supporting me throughout my entire research journey, from the project study and master's thesis all the way to my dissertation. I appreciate the opportunity you gave me to cross disciplines — it was a game-changer.

... Thomas Schimmel, for co-supervising my thesis and for letting me dive into nanotechnology.

... Fabian and Jonathan, a big thank you to both of you for all the discussions, advice, motivation, and support. It really meant a lot.

... the people at MZE, past and present. Annika, Bastian, and Mojgan — thank you for being awesome collaborators in our nanotracer working group. And thanks to Annabell, Harald, Kai, and Lea for the friendly atmosphere and for helping me out when I needed another measurement device.

... the APH/INT group for their uncomplicated support and for sharing your insights into nanoscience.

... the geothermal research team at AGW — thank you! Especially thank you Carola, Lars, Michael, and Valentin from the geothermal hydrochemistry subgroup for the helpful discussions during our ASLWS meetings. And Silke, thank you for your help with the KIT administration.

A special thanks to the KHYS research travel grant for making my research stay in France possible. Thank you, Sophie Roman and Cyprien Soulaine, for welcoming me into your group and giving me the chance to explore microfluidics and OpenFOAM modeling. Also, thanks to the ISTO porous media group, especially Nathan, Victor, and Walid, for the hospitality, great coffee, and interesting conversations.

Lastly, a huge thank you to my family and friends for their constant support and encouragement.

And Alex — thank you. I can't put into words what it means to have you by my side. Thanks for being there through all the ups and downs and for your love and support.

Dedicated to my father

How
I wish
you were here

Pink Floyd 1975